ULB Faculté des Sciences

Synthetic gauge fields, relativistic Landau levels and local valley Hall response in artificially-strained honeycomb lattices

Thesis submitted by Maxime JAMOTTE

in fulfilment of the requirements of the PhD Degree in Physics

Academic year 2024-2025

Supervisor: Professor Nathan GOLDMAN

Centre pour les phénomènes non-linéaires et systèmes complexes

Thesis jury:

Grégory KOZYREFF (Université libre de Bruxelles, Chair)
Pierre GASPARD (Université Libre de Bruxelles, Secretary)
Nathan GOLDMAN (Université Libre de Bruxelles)
Verònica AHUFINGER BRETO (Universitat Autònoma de Barcelona)
Grazia SALERNO (Aalto University)

fnrs LA LIBERTÉ DE CHERCHER

Résumé

Cette thèse s'inscrit dans la continuité des avancées récentes dans le domaine des simulations quantiques pour la physique fondamentale, notamment pour l'étude de théories de champs de jauge sur réseau. Le réseau envisagée ici est un réseau bidimensionnel en nid d'abeille dans lequel sont piégées des particules quantiques. Les déformations de ce réseau entraînent des pseudo-champs magnétiques effectifs qui ne rompent pas la symétrie de renversement temporel, mais génèrent tout de même une physique de quasi-niveaux de Landau. Ceci est exploité de deux manières. Premièrement, grâce à une adaptation de la formule de Widom-Středa, nous montrons que l'effet Hall de vallée émergeant dans ce système peut être mesuré à partir des réponses d'un gaz fermionique aux variations de d'étirement dans le réseau. Nous démontrons que notre proposition est valable pour différentes configurations de déformation, pour diverses terminaisons du réseau, et est indépendante de la présence d'états de bord hélicoïdaux. De plus, elle est robuste contre le désordre. Deuxièmement, nous présentons une nouvelle méthode pour créer un étirement artificiel, et le champ magnétique effectif associé, dans des réseaux hexagonaux optiques rigides dans lesquels sont piégés des gaz de deux espèces d'atomes ultrafroids. Ici, seule l'une des espèces, notée A, fait l'expérience de l'étirement généré au travers de l'interaction avec l'autre espèce B. Cela est réalisé par un couplage atypique, appelé effet tunnel quantique assisté par densité, où la probabilité que l'espèce A subisse un effet tunnel entre deux sites du réseau en nid d'abeille dépend de la différence de nombre de particules B à ces deux sites. Nous démontrons la concordance de cette proposition avec les modèles d'étirements habituels et comment ce couplage exotique peut être généré par un forçage périodique (Floquet) de l'interaction entre les deux espèces.

Abstract

This thesis builds on recent advancements in the field of quantum simulations for fundamental physics, particularly in the study of lattice gauge theories. The lattice considered here is a two-dimensional honeycomb lattice in which quantum particles are trapped. Deformations of this lattice lead to effective pseudo-magnetic fields that do not break time-reversal symmetry but still generate physics resembling quasi-Landau levels. This is exploited in two ways. First, using an adaptation of the Widom-Středa formula, we show that the valley Hall effect emerging in this system can be measured from the responses of a fermionic gas to variations in the stretching of the lattice. We demonstrate that our proposal holds for different deformation configurations, various lattice terminations, and is independent of the presence of helical edge states. Furthermore, it is robust against disorder. Secondly, we present a novel method to create an artificial stretching, and the associated effective magnetic field, in rigid optical hexagonal lattices in which gases of two species of ultracold atoms are trapped. Here, only one of the species, denoted A, experiences the stretching generated through interaction with the other species B. This is achieved via an atypical coupling known as density-assisted quantum tunneling, where the probability of species A tunneling between two sites on the honeycomb lattice depends on the difference in the number of B particles at those two sites. We demonstrate the consistency of this proposal with conventional stretching models and how this exotic coupling can be generated by periodic driving (Floquet) of the interaction between the two species.

Acknowledgments

First, I would like to thank my supervisor Nathan Goldman and Marco Di Liberto for their kindness, patience and help during these four years. I am proud of the work we have accomplished. I would also like to thank my group for all the interesting discussions we had. I am incredibly lucky to have worked with you, in such a positive and motivating environment. I hope to find even half of what I experienced with you all in the future. Thanks to you, working was not really working.

Ensuite, je tiens à remercier ma famille, ma compagne et mes amis. Maman, Papa, merci de m'avoir permis de faire ses études, de m'avoir incondtionnellment soutenu. Ceci est également le fruit de votre travail et de vos efforts. C'est grâce à vous que j'ai pu me focaliser sur mes études et en arriver là où je suis. Marine, merci pour ta patience et ta tendresse qui m'ont permis d'arriver au bout de ce long chemin. Cédric, merci pour notre profonde amitié et toutes nos discussions quotidiennes à propos de tout, chaque jour. Merci aussi pour ton aide et ta patience durant nos études, qui ont tant contribué à ma réussite. René, tu es celui qui, depuis dix ans, a le plus entendu"*désolé mais ce week-end je dois étudier, je ne pourrai pas venir*", mais malgré tout, tu es resté l'ami que chacun rêverait d'avoir. À tous, je sais que les sacrifices que j'ai dû faire sont aussi les vôtres. Sans vous tous, je n'en serais pas là. Merci.

I thank the members of the jury for their questions and helpful comments during the defense and for their careful reading of the manuscript.

Finally, I am grateful to the Belgian National Fund for Scientific Research (FRS-FNRS) for funding this work under FRIA Grant No. FC 38756.

Publications

The original results presented in this thesis can be found in the following published articles:

- *Strain and pseudo-magnetic field in optical lattices from density-assisted tunneling*,
  M. Jamotte, N. Goldman, M. Di Liberto,
  Communications Physics, **5** (1), 2022.

- *Quantized valley Hall response from local bulk density variations*,
  M. Jamotte, L. Peralta Gavensky, C. Morais Smith, M. Di Liberto and N. Goldman,
  Communications Physics, **6** (1), 2023.

Contents

Chapter 1

General introduction

Simulating quantum many-body systems is extremely challenging as it requires immense computational resources to store their quantum state and to accurately simulate their time-evolution. The complexity arises from the exponential growth in the amount of information needed as the number of particles in the system increases, a scale at which even the most advanced supercomputers are quickly outpaced. To address this, scientists have proposed the use of quantum simulators that fully harness the quantum properties of their components [1]. Quantum simulators are highly-controllable devices that can be used to emulate the physics of less manageable or accessible quantum systems. Their applications extend to many-body problems across a wide range of domains, such as condensed-matter physics, high-energy physics, quantum chemistry, cosmology, *etc.* Among other things, these simulators aim to deepen our understanding of quantum phase transitions, high-temperature superconductivity, quark confinement, and quantum gravity, while also contributing to the development of fault-tolerant quantum computers [2, 3].

Quantum simulators have been implemented on a wide variety of atomic, molecular, optical and solid-state platforms [2, 4, 5]. Examples of solid state platforms are Dirac materials, like graphene, a two-dimensional carbon allotrope. These systems have been proposed or employed as experimental laboratories for testing quantum field theory (QFT): Klein tunneling [6, 7], Andreev reflection [8], Schwinger effect [9] and consequences of curved space in QFT [10, 11]. This is due to their peculiar spectra characterized by conical structures around special points of the Brillouin zone, called *valleys*, at which the conduction and valence bands touch – which gives them the name of semi-metals. Close to these points, low-energy excitations near half-filling are described by an effective (relativistic) QFT, where the speed of light is replaced by the Fermi velocity of the material.

Furthermore, in mono- and multilayer graphene, relativistic Landau level physics [12–14] as well as (anomalous) integer [15, 16] and fractional [17] quantum Hall phases have been observed. Besides, when the valleys are well separated in momentum space as in graphene and

transition-metal-dichalcogenides (TMDs), they can be manipulated as a new degree of freedom, known as valley pseudo-spin, for processing and storing information, akin to the role of charge in electronics and spin in spintronics. The manipulation of the valley pseudo-spin in graphene, TMDs and other 2D materials, opens up possibilities for exploiting the valley Hall effect [18] and developing valleytronics [19, 20], thus opening new avenues beyond the paradigmatic electronics on silicon. To these days, however, only indirect measurements of the valley Hall conductivity have been performed [21–26], some of which are still highly debated [27–30].

As mentioned earlier, engineered (or *synthetic*) platform have also been developed beyond traditional solid state systems [2, 4, 5]. In particular, taking advantage of important developments in trapping and advanced cooling techniques (down to near the absolute zero), ultracold atomic gases in optical lattices constitute one of these synthetic platforms for quantum simulation that are extremely versatile [31–36]. Indeed, one can choose the disorder or the dimension of the lattice (from 1D to 3D or more if synthetic dimensions are exploited [37]), pick fermionic or bosonic atoms, tune the sign and intensity of their interactions, as well as vary their mobility on the lattice. This platform is well suited for realizing Hubbard-type models and therefore allows to study a wide variety of condensed-matter phenomena, such as high-temperature superconductivity [38, 39], superfluid-to-Mott-insulator quantum phase transition [40], BEC-BCS crossover [41] and topologically non-trivial insulators [42–44]. It can emulate the physics of electrons in strong magnetic fields such as (fractional) quantum Hall phases [45, 46], or simulate tunable long-range interacting systems [47–49], quantum magnetism [50, 51], and (non-Abelian) gauge lattice gauge theories (LGT) [52–56].

Gauge fields are core ingredients of many of the aforementioned effects and phenomena. Methods for incorporating these fields into quantum simulators depend on the platform to implement them. On the one hand, for solid states materials, where the matter field is represented by the electrons, $U(1)$ gauge fields are the typical electromagnetic fields, carried by lasers, magnets, *etc.*, or can be induced by voltage biases (gates, onsite electrical potentials). Particularly appealing are the existing alternatives for generating effective magnetic fields (that do not break time-reversal symmetry), *e.g.* by deforming (or straining) the lattice, which is modeled by space-dependent hopping amplitudes of the electrons in the lattice. As a result, strain may generate intense pseudo-gauge fields (up to hundreds of Teslas), therefore allowing to mimic pseudo-Landau levels [57–59] or flat bands physics [60–62]. On the other hand, for neutral cold atoms in optical lattices, gauge fields have to be engineered. They are typically incorporated into models through Peierls phases for the atoms, which describe the Aharonov-Bohm effect experienced by the atoms circulating around a plaquette of the lattice. Hence, one aims at engineering these phases, thanks to different mechanisms [63–66], such as laser-assisted-tunneling of internal states [43, 67, 68], lattice acceleration [69], lattice depth modulations [70], radio-frequency fields (combined with Raman coupling) [71], current-

carrying wires on a chip [72] or immersion into a rotating BEC [73].

Instead of directly generating such phases, alternative methods allow to emulate strain and pseudo-magnetic fields. As an example, starting from a standard configuration of three Gaussian laser beams that form a honeycomb optical lattice by intersecting at 120°, the hexagonal lattice is deformed by simply displacing the beams, which therefore emulates strain and a uniform, static pseudo-magnetic field [74].

This thesis builds upon these advances and aims at answering two questions. The first one is: *for cold atoms, can we find another way of creating pseudo-magnetic fields by artificially straining an optical lattice and hence producing Landau levels?* To address this, we propose to employ a cold mixture of two atomic species that is trapped in a honeycomb lattice. Their coupling occurs through density-assisted tunneling processes, where the hopping amplitudes of one species depends on the density operators of the other species. Such density-dependent hopping parameters are realized by periodically driving in time parameters of the model, and tailored such that a desired space-dependence is introduced into the hopping amplitudes. As a result, it mimics strain and reproduces the Landau level physics. By incorporating the strain into the model in this way, the second species actually carries the pseudo-magnetic field's degrees of freedom. While, in this thesis, we assumed that the second species are bosons that form a static Bose-Einstein condensate (BEC), the analysis of this system can naturally be extended by including its low-energy quantum excitations, which take the form of phononic modes, known as Bogoliubov quasi-particles. As they will interact with the atoms of the other species, considered as the matter field, the pseudo-magnetic field experiences their back-action, allowing to add the gauge field's dynamics to the model, which is an essential block of proper LGTs.

The second question is: *can the quantum valley Hall conductivity of a fermionic gas be directly and locally probed in synthetic platforms in order to detect Landau levels physics resulting from artificial strain?* To answer it, we propose a new probing method for *in situ* measurements of the quantum valley Hall effect through local bulk responses of a fermionic gas to strain variations in a honeycomb lattice. It consists in comparing two density distributions at equilibrium for two (infinitesimally) different strain intensities. For that, we adapt the Widom-Středa formula, originally derived for fermions in real magnetic fields, to strain-induced pseudo-magnetic fields. Then, we analytically determine the (quantized) values taken by the valley Hall conductivity in this context and numerically show to which extend our probing scheme agrees with these predictions. Moreover, we prove the robustness of our findings to disorder (impurities and lattice imperfections). We anticipate that our approach is well suited for synthetic platforms such as cold atoms in optical lattices or molecular graphene, where direct and local density measurements can be performed. Furthermore, these measurements should be realized in the bulk. Hence, the quantization of the valley Hall response does not rely on the

presence or absence of edge currents, which are not topologically protected and thus fragile to disorder.

The next chapters are organized as follows:

Chapter 2 develops the theoretical concepts encountered in the rest of this thesis. We begin with Hall effects, Landau levels and derive the Widom-Středa formula. We introduce the honeycomb lattice found in Dirac materials like graphene, and deduce its low-energy spectrum. We then deduce the relativistic Landau levels, found when the honeycomb lattice is pierced by a real magnetic field. After that, we detail how straining this lattice is analogous to immerse it into a pseudo-magnetic field. In particular, we discuss the relativistic Landau level physics found in such systems. The valley Hall effect is then presented, along with some methods employed to probe it. Afterwards, we continue with time-periodically driven systems and two relevant examples on how it can serve for renormalizing tunneling amplitudes of particles in double-wells. One of the examples illustrates the emergence of density-assisted tunneling. We then discuss weakly-interacting bosonic gases and derive the Gross-Pitaevskii equation. Eventually,we end the chapter with the physics of trapped bosonic atoms in optical lattices.

Chapter 3 presents the original results from our published article [75]. It starts with the adaptation of the Widom-Středa formula to the valley Hall effect and the proves that weakly-strained honeycomb lattices possess quantized valley Hall responses. This is numerically shown for two types of strained lattices of different geometries and terminations. We also prove that its robustness against disorder.

Chapter 4 presents the original results from our published article [76]. We show that density-assisted tunneling processes can reproduce space-dependent hopping amplitudes and, in particular, how employing Bose-Einstein condensates in harmonic traps as a second species allows for mimicking strain. Then, we analytically and numerically analyze the physics of this artificially strained honeycomb optical lattice. We prove the excellent agreement between the spectrum of this system to the Landau level spectrum obtained for typical strained systems, as those encountered in the previous chapter. We then show how the density-assisted tunneling amplitudes relevant for our model are derived from Floquet engineering. The chapter ends with further remarks on neglected effects and insights for potential experiments.

Chapter 5 draws the conclusions and outlines the perspectives emanating from this thesis.

Chapter 2

Theoretical background

This chapter provides the reader with the theoretical background invoked in the rest of the thesis. In section 2.1, we first describe the physics of classical charges in a two-dimensional plane pierced by a magnetic field. We then briefly discuss quantum Hall effects and derive the Widom-Středa formula from Maxwell's equations. We find the Landau level spectrum of quantum particles in a uniform magnetic field. In section 2.2, we discuss the tight-binding approximation of graphene and show how low-energy excitations near half-filling can be described by an effective Dirac theory. Section 2.3 discusses three fundamental symmetries of topological insulators and some of their consequences that are relevant for the remaining sections. Then, section 2.4 focuses on the honeycomb lattice in the presence of a magnetic field, on its description by the Dirac theory and on the derivation of its (relativistic) Landau-level-like spectrum near half-filling. The section 2.5 expands on the effects of strain in the honeycomb lattice and unveils its (dis)similarities with the Landau level physics. Along the way, we show that strain produces an effective magnetic field that do not break time reversal symmetry. Section 2.6 discusses the existence of propagating edge states in strained honeycomb lattices depending on the edge terminations and the sign of the strain intensity. Section 2.7 introduces the valley Hall effect and summarizes some of existing probing methods to detect it.

While the preceding sections are common to the remaining chapters, the following introductory sections focus on notions that are central only to the chapter 4. Section 2.8 presents Floquet engineering and how time-periodic driving can be employed to generate new exotic terms (in the Hamiltonian) expressing effective hopping processes or interactions, namely leading to pair-hopping or density-assisted tunnelings. In section 2.9, we focus on Bose-Einstein condensates and on the conditions for reducing the bosonic many-body wavefunction to an order-parameter that solves the Gross-Pitaevskii equation. In section 2.10, we briefly explain how lasers can be employed to trap atoms into optical lattices and deduce the Bose-Hubbard model.

2.1 Particles in a magnetic field

2.1.1 Classical Hall effect: Drude model

The trajectory of a moving charge in a 2D material along a given direction is deflected in the presence of a uniform, constant magnetic field due to the Lorentz force applied to it,

$$\mathbf{F} = q\left(\mathbf{E} + \mathbf{v} \times \mathbf{B}\right), \tag{2.1}$$

where q is the charge value, $\mathbf{E}$ is the electric field that sets the charge in motion (say along x), $\mathbf{v}$ its velocity and $\mathbf{B}$ the magnetic field. The accumulation of opposite charges at opposite edges of the material results in an electric field $\mathbf{E}_{\mathrm{H}}$ perpendicular to $\mathbf{E}$ and $\mathbf{B}$. This generates a Hall voltage V_{H} and a Hall current I_{H}. This is the classical Hall effect, first described by E. Hall in 1879 [77]. This situation is depicted in Figure 2.1 for an electron (e^-) in a two-dimensional plane of width L pierced by a magnetic field. Notice that without any electric field, the charges would simply follow in-plane circular trajectories of radius $\ell_B \equiv v_0/\omega_B$, called the magnetic length, where v_0 is the velocity of the charge and Ω_B is the cyclotron frequency $\omega_B \equiv eB/m$.

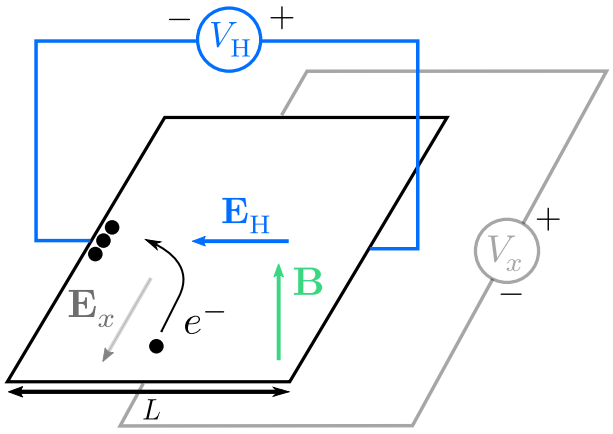

Figure 2.1: Sketch of the Hall effect. Electrons (e^-) are accelerated by an electric field $\mathbf{E}_x$ and their trajectory is deflected by the magnetic field $\mathbf{B}$ perpendicular to the plane. An accumulation of opposite charges occurs at opposite edges, resulting into a Hall voltage V_{H} and its associated Hall electric field $\mathbf{E}_{\mathrm{H}}$.

The *Drude model* captures the impedance of a material, due to impurities, lattice effect, or interactions with other electrons, through a simple linear friction term,

$$m\dot{\mathbf{v}} = q\left(\mathbf{E} + \mathbf{v} \times \mathbf{B}\right) - m\frac{\mathbf{v}}{\tau}, \tag{2.2}$$

where τ is the scattering time – average time between consecutive collisions (of the charge q). The resistivity tensor $\bar{\bar{\rho}}$ is deduced in the stationary regime ($\dot{\mathbf{v}} = \mathbf{0}$) for $\mathbf{J} = nq\mathbf{v}$,

$$\bar{\bar{\rho}} \cdot \mathbf{J} = \mathbf{E}, \tag{2.3}$$

where

$$\rho_{xx} = \rho_{yy} = \frac{m}{e^2 n\tau}, \qquad \rho_{yx} = -\rho_{xy} = \frac{B}{ne}, \tag{2.4}$$

with $n = N/S$ being the density of N particles of mass m in a system of area S. Inverting the resistivity tensor to the right hand side of (2.3), one obtains the Ohm's law,

$$\mathbf{J} = \bar{\bar{\sigma}}\mathbf{E}, \tag{2.5}$$

where $\bar{\bar{\sigma}} = \bar{\bar{\rho}}^{-1}$ is the conductivity tensor, whose off-diagonal element σ_{xy}^{H} is responsible for the Hall effect. Notice that the transversal resistivity ρ_{xy} does not depend on microscopic properties of the material (embodied by τ) but only on the charge and density of the particles. The so-called Hall resistance is defined as

$$R_{\mathrm{H}} = \frac{V_{\mathrm{H}}}{I_x} = \frac{LE_y}{LJ_x} = -\rho_{xy}, \tag{2.6}$$

and, therefore, has the same units as the resistivity. Note that *Hall resistance* is a misnomer as no dissipation of energy is associated to the Hall current. Indeed, the second term of the Lorentz force $q\mathbf{v} \times \mathbf{B}$, responsible for the deflection of the electrons' trajectory, is always perpendicular to the change in position, hence no work is produced.

2.1.2 Integer quantum Hall effect

In 1980, K. von Klitzing made a ground breaking discovery: in strong magnetic fields (several teslas) at temperatures around $1.5\,\mathrm{K}$, the Hall resistance R_{H} of a silicon MOSFET (metal-oxide-semiconductor field effect transistor), prepared by G. Dorda and M. Pepper [78], sits on a plateau for a range of B, before jumping to the next plateau – see Figure 2.2, accompanied with sudden drops of the longitudinal resistivity ρ_{xx}. Hence, R_{H} is quantized according to

$$R_{\mathrm{H}} = \frac{B}{ne} = \frac{h}{\nu e^2} \qquad (\nu \in \mathbb{N}), \tag{2.7}$$

at a strikingly high precision. The integer ν is called the filling factor[1], defined as the ratio between the number of particles N and the total number of magnetic flux quanta,

$$\nu = \frac{N}{BS/\phi_0} \quad \left(\phi_0 \equiv \frac{h}{e}\right) \qquad \text{then} \qquad \nu = \frac{nh}{eB}. \tag{2.8}$$

This discovery became a cornerstone in the field of metrology as it provided an electrical resistance standard based on fundamental physical constants (the elementary charge of an electron e and the Planck constant h). Its incredible precision is explained by the robustness of the R_{H} plateaus to imperfections, such as impurities, dislocations and vacancies. This robustness relies on the topological origin of the IQHE, symbolized by the so-called TKNN invariant, introduced

[1] In a Landau level system, ν corresponds to the number of filled Landau levels.

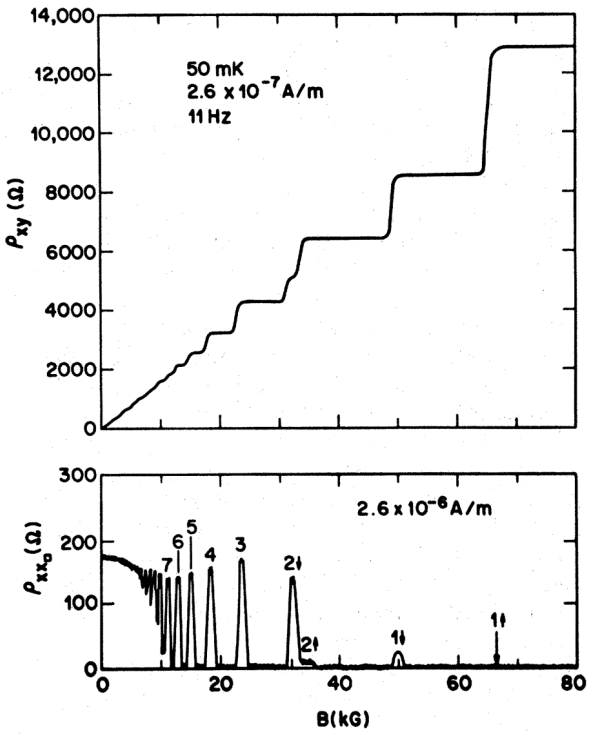

Figure 2.2: Image taken from [79]. Hall (top) and longitudinal (bottom) resistivities as a function of the magnetic field.

by Thouless, Kohmoto, Nightingale and den Nijs [80]. This invariant unveiled a profound bond between the energy bands of a system and the mathematical field of topology. Indeed, when the Fermi level lies in an energy gap, the quantum Hall conductivity σ_{xy}^{H} of occupied bands is proportional to the sum of the integral topological invariants, called Chern numbers and denoted by $\mathcal{C}_n$, associated to these filled bands [80, 81] as

$$\sigma_{xy}^{\mathrm{H}} = \frac{e^2}{h} \sum_{n \text{ filled}} \mathcal{C}_n. \tag{2.9}$$

The analog of the IQHE in spintronics, called the quantum spin Hall effect (QSHE), results in a spin accumulation along the boundaries of a topological insulator. It has been predicted to occur in graphene by Kane *et al.* [82] but the spin-orbit coupling at the origin of the QSHE in this material is too weak to open a sufficiently large energy gap. To remedy this problem, Bernevig *et al.* [83] proposed to vary the width of HgTe quantum wells to induce a topological phase transition from a trivial insulator to a quantum spin Hall phase. The QSHE was successfully measured by König *et al.* [84]. They observed that the transverse conductivity of spin currents is quantized and related to a $\mathbb{Z}_2$ topological invariant.

At even lower temperatures and in stronger magnetic fields, the Hall conductivity takes fractional values, as initially discovered by Stormer *et al.* [85] in 1982, who measured

$$\sigma_{xy}^{\mathrm{H}} = \frac{1}{3}\frac{e^2}{h}. \tag{2.10}$$

Subsequent studies measured other rational values and therefore confirmed the discovery of the fractional quantum Hall effect. It cannot be explained by single-body physics but by including Coulomb interactions between electrons. As described by Laughlin [86] one year later, the excitations of this new quantum liquid exhibit fractional statistics and possess fractional charges. Hence, fractional quantum Hall systems were considered as good candidates for experimental observation of anyons [87, 88]. These are neither bosons nor fermions as the many-body wavefunction of two Abelian anyons takes a phase $\mathrm{e}^{2\pi q}$ ($q \in \mathbb{Q}$) when they are braided [89, 90]. The non-Abelian counterpart of anyons brings a unitary matrix to the many-body wavefunction after braiding. Due to their long-range correlations and topological protection, they constitute a promising route towards fault-tolerant quantum gates for quantum computers [91].

2.1.3 Widom-Středa formula

A few years after the discovery by von Klitzing et al. [78] of a robust quantization of the Hall conductivity for a 2D gas of electrons in a uniform magnetic field, Středa [92] found, from linear response theory, that the quantum Hall conductivity could be expressed as the derivative of the fermionic density of an insulator with respect to the intensity of the magnetic field, and that it gets quantized when the Fermi energy μ_{F} lies within a spectral gap[2], that is

$$\sigma_{xy}^{\mathrm{H}} = e\left(\frac{\partial n}{\partial B}\right)\bigg|_{\mu_{\mathrm{F}}}, \tag{2.11}$$

where e is the charge of the electric carrier. A few months apart, Widom used very general thermodynamics relations to obtain the same formula [93]. Recent theoretical and experimental works have extended its domain of application to any insulating phase of matter, including strongly-correlated ones, enabling to measure integer and fractional quantum Hall responses in Chern insulators [46, 94–96].

The Widom-Středa formula can be obtained by following the reasoning presented in Ref. [97]. We take electrons in a 2D plane and adiabatically vary an external uniform magnetic field, perpendicular to the insulator. Note that this magnetic field could be added to another magnetic field already present in the system, or only be there as a probe. As the magnetic field changes in time, it induces an electric field $\mathbf{E}$. The electric and magnetic fields are related by Faraday's induction law,

[2] Since the fermionic gas rearranges itself under variations of the magnetic field, one has to ensure that the Fermi level remains in a gap when the field strength is changed. This prescribes adiabatic variations of the external magnetic field, assumed from the linear response theory.

$$\nabla \times \mathbf{E} = -\frac{\partial \mathbf{B}}{\partial t}. \tag{2.12}$$

Assuming that the system is in its insulating phase, which occurs when the Fermi level lies in a spectral gap (*e.g.* in the Haldane model or Landau level systems), no longitudinal current is produced, *i.e.* $\sigma_{xx} = 0$. Hence, from the Ohm's law deduced in section 2.1.1, the current resulting from the action of the electric fields inside the insulator is given by

$$\mathbf{J} = \sigma_{xy}^{\mathrm{H}} \hat{\mathbf{n}} \times \mathbf{E}, \tag{2.13}$$

where $\hat{\mathbf{n}}$ indicates the direction of opposite to the magnetic field. The charge conservation is expressed by the continuity equation,

$$-e\frac{\partial n}{\partial t} = -\nabla \cdot \mathbf{J}. \tag{2.14}$$

All together,

$$\frac{\partial n}{\partial t} = \frac{\sigma_{xy}^{\mathrm{H}}}{e} \nabla \cdot (\hat{\mathbf{n}} \times \mathbf{E}) = -\frac{\sigma_{xy}^{\mathrm{H}}}{e} \hat{\mathbf{n}} \cdot (\nabla \times \mathbf{E}) = \frac{\sigma_{xy}^{\mathrm{H}}}{e} \frac{\partial \mathbf{B} \cdot \hat{\mathbf{n}}}{\partial t}, \tag{2.15}$$

Therefore,

$$\sigma_{xy}^{\mathrm{H}} = e\frac{\Delta n}{\Delta B}. \tag{2.16}$$

when the Fermi level lies in a gap. For infinitesimal variations of the magnetic field piercing the insulator, we recover the relation (2.11).

2.1.4 Landau levels

The quantum mechanics of a free electron in a 2D plane pierced by a magnetic field is described by the Hamiltonian

$$\hat{H} = \frac{1}{2m_e}(\hat{\mathbf{p}} + e\mathbf{A}(\hat{\mathbf{x}}))^2, \tag{2.17}$$

where $\mathbf{A}$ is the vector potential related to the magnetic field $\mathbf{B} = \nabla \times \mathbf{A}$. The operators $\hat{\mathbf{x}}$ and $\hat{\mathbf{p}}$ are canonical conjugates [98]:

$$[\hat{x}_i, \hat{p}_j] = \mathrm{i}\hbar\delta_{ij}. \tag{2.18}$$

The energy spectrum of this system can easily be calculated by rewriting (2.17) in terms of creation and annihilation operators. Indeed, by defining $\boldsymbol{\pi} \equiv \mathbf{p} + e\mathbf{A}$ and then

$$\hat{a} = \frac{1}{\sqrt{2}e\hbar B}(\pi_x - \mathrm{i}\pi_y), \qquad \hat{a}^\dagger = \frac{1}{\sqrt{2}e\hbar B}(\pi_x + \mathrm{i}\pi_y), \tag{2.19}$$

the Hamiltonian (2.17) becomes

$$\hat{H} = \frac{1}{2m_e}\boldsymbol{\pi}\cdot\boldsymbol{\pi} = \hbar\omega_B\left(\hat{a}^\dagger\hat{a} + \frac{1}{2}\right), \tag{2.20}$$

which is the Hamiltonian of a harmonic oscillator, where $\omega_B = eB/m_e$ is the cyclotron frequency. Therefore, the eigenstates are those of the number operator $\hat{N}_a = \hat{a}^\dagger\hat{a}$, denotes by $|n\rangle$ ($n \in \mathbb{N}$). Their associated energies read

$$\epsilon_n = \hbar\omega_B\left(n + \frac{1}{2}\right), \qquad n \in \mathbb{N}. \tag{2.21}$$

Hence, the spectrum of charged particles in a magnetic field consists of equally spaced energy levels, called *Landau levels*. Importantly, those have a large degeneracy, expressed by a degree of freedom that has been overlooked on the way from the 2D Hamiltonian to the 1D harmonic oscillator. In order to take this degree of freedom into account, one introduces an operator that commutes with the Hamiltonian. In the symmetric gauge $\mathbf{A} = (-By/2, Bx/2, 0)$, the operator

$$\tilde{\pi} = \mathbf{p} - e\mathbf{A}, \tag{2.22}$$

commutes with $\boldsymbol{\pi}$. Consequently, it allows to define other raising and lowering operators

$$\hat{b} = \frac{1}{\sqrt{2}e\hbar B}(\tilde{\pi}_x + \mathrm{i}\tilde{\pi}_y), \qquad \hat{b}^\dagger = \frac{1}{\sqrt{2}e\hbar B}(\tilde{\pi}_x - \mathrm{i}\tilde{\pi}_y), \tag{2.23}$$

whose commutation relation is $[\hat{b}, \hat{b}^\dagger] = 1$. The common eigenstates to $\hat{N}_a$ and $\hat{N}_b = \hat{b}^\dagger\hat{b}$ are written

$$|n, m\rangle = \frac{(\hat{a}^\dagger)^n(\hat{b}^\dagger)^m}{\sqrt{n!m!}}\,|0, 0\rangle\,. \tag{2.24}$$

The degeneracy of each Landau level, *i.e.* the number of values taken by m, is given by [99]

$$\mathcal{N} = \frac{eBS}{2\pi\hbar}, \tag{2.25}$$

meaning that it increases with the size of the system and the intensity of the magnetic field. Reintroducing the flux quantum $\phi_0 = h/e$, the degeneracy is also related to the number of flux quanta in the system,

$$\mathcal{N} = \frac{BS}{\phi_0}. \tag{2.26}$$

Finally, it is rather simple to deduce the (gauge-dependent) analytical expression of the eigenstates as they are those of the harmonic oscillator. In the Landau gauge $\mathbf{A} = (0, Bx, 0)$ (instead of the symmetric gauge), the wavefunction of $|n\rangle$ reads

$$\varphi_n^{k_y}(\mathbf{r}) = \langle\mathbf{r}|n\rangle = \frac{1}{\sqrt{2^n n!}}\left(\frac{1}{\pi\ell_B^2}\right)^{1/4} e^{\mathrm{i}k_y y}H_n(x)\mathrm{e}^{-(x-x_0(k_y))^2/2\ell_B^2}, \tag{2.27}$$

which assumes a periodicity along the y-axis. The function H_n is the n^{th}-Hermite polynomial and $x_0(k_y)$ is the center of $\varphi_n^{k_y}(\mathbf{r})$ along the x-axis. Importantly, it depends on k_y as

$$x_0(k_y) = x_{\text{c}} - k_y \ell_B^2, \tag{2.28}$$

meaning that changing the quasimomentum shifts the wavefunction, where x_{c} is the system's center. Figure 2.3 displays the wavefunctions of the three first Landau levels (for $k_y = 0$).

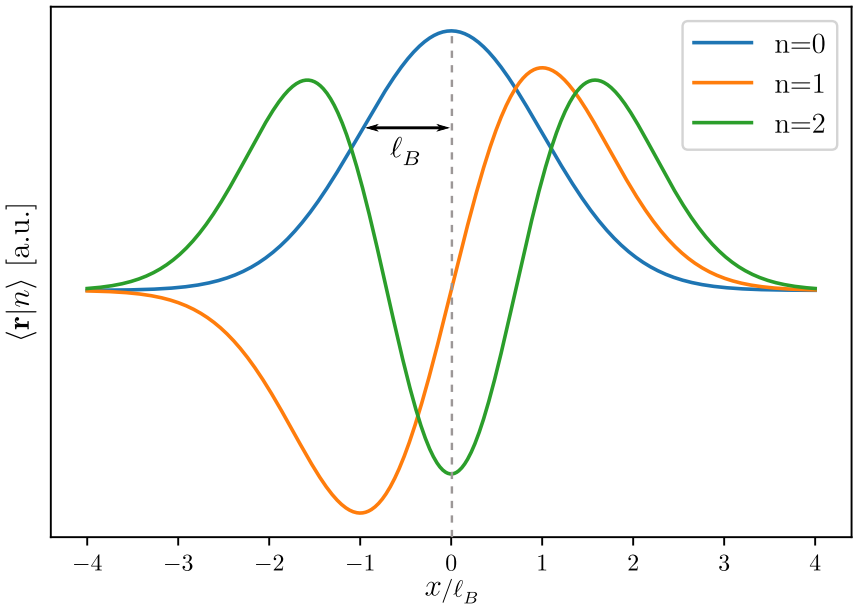

Figure 2.3: Wavefunctions of the three first Landau levels ($n = 0,\ 1$ and 2).

Interestingly, the Widom-Středa formula can easily be deduced from the relation (2.26). Indeed, if $\nu \in \mathbb{N}$ levels are filled, meaning that there are $N = \nu\mathcal{N}$ fermions in the system, then for a density of particles $\rho = N/S$,

$$\rho S = N = \nu\mathcal{N} = \nu \frac{eBS}{2\pi\hbar}, \tag{2.29}$$

hence

$$e\frac{\partial \rho}{\partial B} = \nu \frac{e^2}{h} \qquad \nu \in \mathbb{N}. \tag{2.30}$$

This is the Widom-Středa formula – see section 2.1.3 – when the Hall conductivity takes quantized values, which shows that Landau level systems exhibit the integer quantum Hall effect.

2.2 Tight-binding approximation of graphene in a magnetic field

Graphene is a two-dimensional sheet of carbon atoms, whose sp^2-hybridization imparts its honeycomb geometry. Three of the electrons per carbon atom are involved in the strong cova-

lent σ-bonds with its three nearest-neighbors. The fourth electron (π-electron) is responsible for the electronic properties near the charge neutrality point [99]. A spectrum of graphene, numerically obtained with density functional theory, is shown in Figure 2.4 [100]. The π-bands are highlighted in color, where orange and blue stand for the conduction and valence bands, respectively.

The physics of the π-bands is well predicted by a tight-binding model on a honeycomb lattice, that will be derived in the following section after a brief presentation of the honeycomb lattice and its Brillouin zone. Then, the low-energy spectrum of the tight-binding model on the honeycomb lattice is linked to the physics of massless, relativistic particles in 2D space. Finally, this effective description is exploited by including a (real) magnetic field through a Peierls substitution into the Dirac Hamiltonian and its spectrum is derived.

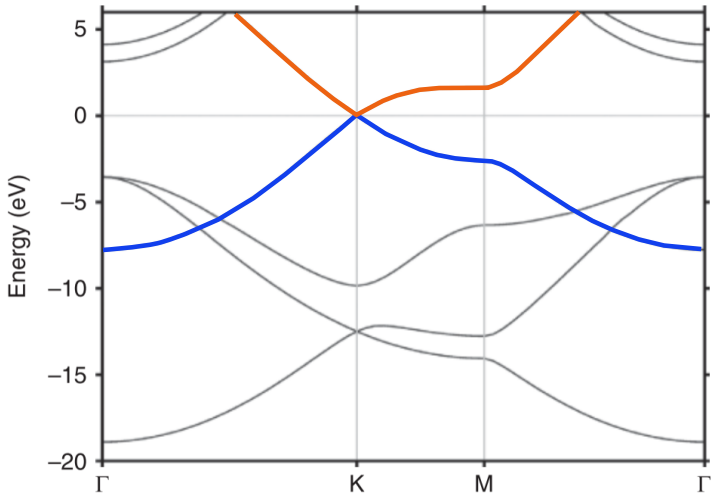

Figure 2.4: Image taken from Boukhvalov et *al.* [100]. The orange and blue lines stand for the conduction and valence bands of the π-orbital, respectively. The gray lines represent the σ-bonds orbitals, neglected in this work.

2.2.1 Honeycomb lattice and its Brillouin zone

The honeycomb lattice is an hexagonal bipartite lattice formed by a triangular Bravais lattice, spanned by two vectors $\mathbf{a}_1 = (3a/2, \sqrt{3}a/2)$ and $\mathbf{a}_2 = (3a/2, -\sqrt{3}a/2)$, of which each vertex is connected to three sites of another triangular lattice by the basis vectors $\boldsymbol{\delta}_1 = (-a, 0)$, $\boldsymbol{\delta}_2 = (a/2, \sqrt{3}a/2)$ and $\boldsymbol{\delta}_3 = (a/2, -\sqrt{3}a/2)$, where a is the lattice spacing. This is depicted in Figure 2.5**a**, where the lattice has $N_x = 4$ sites along x and $N_y = 5$ sites along y. This bipartite lattice, i.e. consisting of two sublattices denoted A and B, has an hexagonal Brillouin zone, shown in Figure 2.5**b**. In the first Brillouin zone, the summits are located at $(\pm 2\pi/3a, 2\pi/3\sqrt{3}a)$, $(0, -4\pi/3\sqrt{3}a)$, $(\pm 2\pi/3a, -2\pi/3\sqrt{3}a)$ and $(0, 4\pi/3\sqrt{3}a)$.

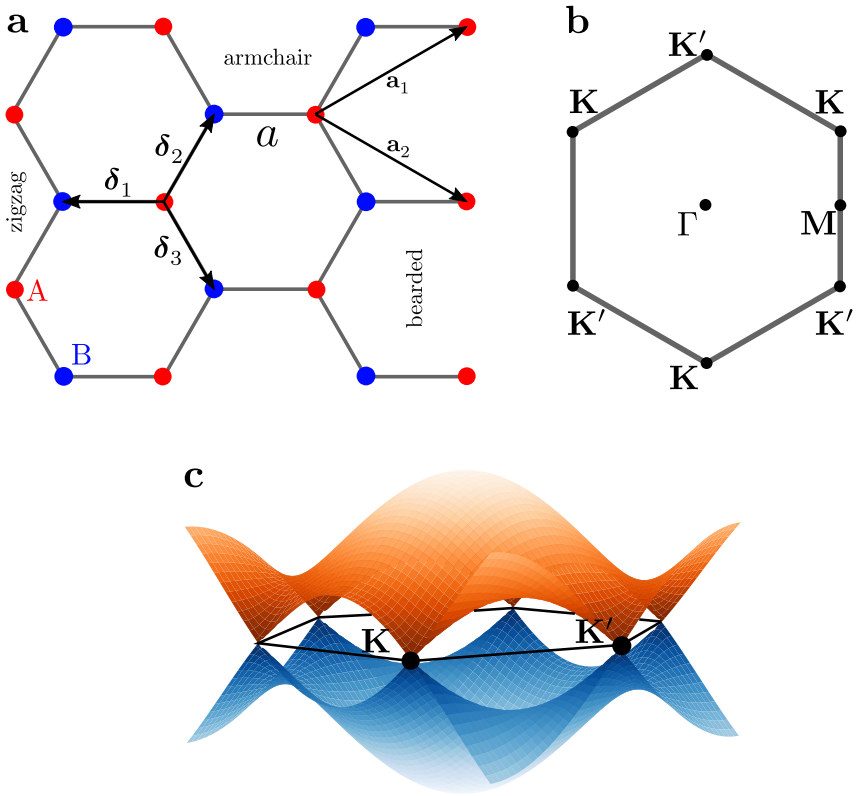

Figure 2.5: **a** Honeycomb lattice with $N_x = 4$ and $N_y = 5$ sites along the x and y-directions, respectively. This hexagonal bipartite lattice is formed by a triangular Bravais lattice, spanned from two vectors $\mathbf{a}_1 = (3a/2, \sqrt{3}a/2)$ and $\mathbf{a}_2 = (3a/2, -\sqrt{3}a/2)$, whose each vertex is connected to three sites of another triangular lattice by the nearest-neighboring vectors δ_j ($j = 1, 2, 3$) (all vectors are defined in the main text.). The lattice parameter is given by a. Pristine honeycomb lattice can have three different terminations called armchair, zigzag and bearded. **b** First Brillouin zone of the honeycomb lattice. **c** Valence (blue) and conduction (orange) bands of the tight-binding Hamiltonian (2.31) touching at the Dirac points **K** and **K′** that form the summits of the first Brillouin zone. The bands colors (orange and blue) correspond to those in Figure 2.4.

2.2.2 Tight-binding model

The physics of the π-bands of graphene is well captured by the tight-binding model defined on the honeycomb lattice [101]. The one-body Hamiltonian of this model reads

$$\hat{H} = -\sum_{\mathbf{r},j} t_j \, \hat{a}^\dagger_{\mathbf{r}} \hat{b}_{\mathbf{r}+\boldsymbol{\delta}_j} + \text{H.c.}, \tag{2.31}$$

when quantum tunneling (hopping) to the nearest-neighbor is the strongly dominant process in front of next-nearest-neighbor hopping, as in graphene. The operators $\hat{a}^{(\dagger)}_{\mathbf{r}}$, $b^{(\dagger)}_{\mathbf{r}}$ are the annihilation (creation) operators at a A, B site at position $\mathbf{r}$. The parameters t_j are the hopping amplitudes along the $\boldsymbol{\delta}_j$ basis vector, and result from the overlap between $2p_z$-orbitals of neighboring carbon atoms, $\psi_{\text{A}}(\mathbf{r})$ and $\psi_{\text{B}}(\mathbf{r} + \boldsymbol{\delta}_j)$ centered at a A and B sites, respectively:

$$t_j = \int d\mathbf{r}\, \psi_{\mathrm{A}}^*(\mathbf{r})\, V_{\mathrm{CC}}\, \psi_{\mathrm{B}}(\mathbf{r}+\boldsymbol{\delta}_j), \tag{2.32}$$

where V_{CC} is the potential produced by the two carbon (C) atoms between which the tunneling occurs. If the translational invariance is preserved, the quasi-momenta $\mathbf{k} = (k_x, k_y)$ are good quantum numbers. One applies Fourier transforms along both x and y-directions on the local creation and annihilation operators,

$$\begin{aligned} \hat{a}_{\mathbf{r}} &= \frac{1}{\sqrt{L_x L_y}} \sum_{\mathbf{k}} \hat{a}_{\mathbf{k}} \mathrm{e}^{-\mathrm{i}\mathbf{k}\cdot\mathbf{r}}, \qquad \hat{a}_{\mathbf{r}}^\dagger = \frac{1}{\sqrt{L_x L_y}} \sum_{\mathbf{k}} \hat{a}_{\mathbf{k}}^\dagger \mathrm{e}^{\mathrm{i}\mathbf{k}\cdot\mathbf{r}}, \\ \hat{b}_{\mathbf{r}} &= \frac{1}{\sqrt{L_x L_y}} \sum_{\mathbf{k}} \hat{b}_{\mathbf{k}} \mathrm{e}^{-\mathrm{i}\mathbf{k}\cdot\mathbf{r}}, \qquad \hat{b}_{\mathbf{r}}^\dagger = \frac{1}{\sqrt{L_x L_y}} \sum_{\mathbf{k}} \hat{b}_{\mathbf{k}}^\dagger \mathrm{e}^{\mathrm{i}\mathbf{k}\cdot\mathbf{r}}, \end{aligned} \tag{2.33}$$

where L_x and L_y are the projected length of the lattice in the x and y directions. In this new basis, $\hat{H}$ reads

$$\hat{H} = \bigoplus_{\mathbf{k}\in \mathrm{BZ}} \hat{H}(\mathbf{k}) = \sum_{\mathbf{k}} \begin{pmatrix} \hat{a}_{\mathbf{k}}^\dagger & \hat{b}_{\mathbf{k}}^\dagger \end{pmatrix} \begin{pmatrix} 0 & -\sum_{j=1}^3 t_j \mathrm{e}^{-\mathrm{i}\mathbf{k}\cdot\boldsymbol{\delta}_j} \\ -\sum_{j=1}^3 t_j \mathrm{e}^{\mathrm{i}\mathbf{k}\cdot\boldsymbol{\delta}_j} & 0 \end{pmatrix} \begin{pmatrix} \hat{a}_{\mathbf{k}} \\ \hat{b}_{\mathbf{k}} \end{pmatrix}. \tag{2.34}$$

By diagonalizing this 2×2 matrix, denoted $H(\mathbf{k})$, the dispersion relations for both the valence $(-)$ and the conduction $(+)$ bands of the model, read

$$\varepsilon(\mathbf{k}) = \pm t \sqrt{3 + 4\cos\left(\frac{3k_x a}{2}\right)\cos\left(\frac{\sqrt{3}k_y a}{2}\right) + 2\cos\left(\sqrt{3}k_y a\right)}, \tag{2.35}$$

when $t_j = t\ \forall j$. The two bands touch at the summits of the Brillouin zone in Figure 2.5, at the so-called *Dirac points* or *Dirac valleys*. The latter are split into two groups, denoted $\mathbf{K}$ or $\mathbf{K}'$. Note that Dirac points in the same group are physically equivalent; $\mathbf{K} = (0, -4\pi/3\sqrt{3}a)$ and $\mathbf{K}' = (0, 4\pi/3\sqrt{3}a) = -\mathbf{K}$ are chosen as their representatives.

2.2.3 Dirac theory near half-filling

When the system (2.31) is close to half-filling, the low-energy excitations, whose energy scale is much smaller than the bandwidth of order t, are analogous to massless, relativistic quantum particles in 2D, described by Dirac theory (even though the Fermi velocity is only around $10^6\ \mathrm{ms}^{-1}$ in graphene). To show this, one expands the elements of the matrix in (2.34) around $\zeta\mathbf{K}$ at first order in $\mathbf{q}a \equiv (\mathbf{k} - \zeta\mathbf{K})a \ll 1$, where $\zeta = \pm 1$ is the valley pseudospin. This leads to the Dirac Hamiltonian

$$h^\zeta(\mathbf{q}) = -\hbar v_{\mathrm{F}} \left(\zeta q_y \sigma_x - q_x \sigma_y\right), \tag{2.36}$$

where $v_{\mathrm{F}} \equiv 3at/2\hbar$ is the Fermi velocity and σ_x, σ_y are the Pauli matrices. The relativistic behavior of the low-energy excitations is revealed by their linear dispersion relation

$$\varepsilon(q) = \pm\hbar v_{\mathrm{F}} q, \qquad q = \|\mathbf{q}\|. \tag{2.37}$$

To describe the full theory of low-energy excitations jointly at both valleys, h^+ and h^- are recombined into a 4×4 matrix,

$$\mathfrak{h}(\mathbf{q}) = \begin{pmatrix} h^+(\mathbf{q}) & 0 \\ 0 & h^-(\mathbf{q}) \end{pmatrix}. \tag{2.38}$$

Then, one applies the following unitary transformation,

$$U = \left(\begin{array}{cc|cc} 1 & 0 & 0 & 0 \\ 0 & \mathrm{i} & 0 & 0 \\ \hline 0 & 0 & 0 & 1 \\ 0 & 0 & \mathrm{i} & 0 \end{array}\right), \tag{2.39}$$

resulting into a 4×4 Hamiltonian $\mathfrak{h}(\mathbf{q})$ that consists in two copies of the 2D Dirac Hamiltonian,

$$\bar{\mathfrak{h}}(\mathbf{q}) = U\,\mathfrak{h}(\mathbf{q})\,U^\dagger = -\hbar v_{\mathrm{F}} \tau_z \otimes \mathbf{q}\cdot\boldsymbol{\sigma}, \tag{2.40}$$

where τ_z is the z-Pauli matrix embodying the valley (pseudo-spin) degree of freedom. Notice that this compact notation in the form of a scalar product is only possible after the change of basis (2.39), where the two last components of the 4-spinor are interchanged, hence the A and B sublattices are switched: (A,B,A,B) $\rightarrow$ (A,B,B,A).

This description in terms of a Dirac Hamiltonian has led scientists to envisage graphene as an experimental platform to study quantum field theories (QFT) [102, 103]. Indeed, Klein tunneling have been theoretically predicted [6] and experimentally observed in doped graphene [7] and photonic graphene [104]. Other effects such as atomic collapse, Andreev reflection [8], the Schwinger effect [9] and consequences of curved space in QFT [10, 11] have also been proposed.

2.3 Symmetries and consequences

Following references [105, 106], three global symmetries that lead to the Altland-Zirnbauer classification of topological insulators and superconductors [107] are presented: time-reversal, particle-hole and chiral symmetries. When one (or more) of them is preserved, interesting features of lattice systems can be deduced, such as the uniformity of the density at half-filling as well as the obligation for states exclusively populating one sublattice to be zero-energy states. These will be useful to derive some of our results in the rest of this manuscript.

2.3.1 Time-reversal symmetry

By definition, a second-quantized Hamiltonian $\hat{H}$ preserves a symmetry if it commutes with the operator associated to this symmetry,

$$\hat{\mathcal{U}}\hat{H}\hat{\mathcal{U}}^{-1} = \hat{H}, \tag{2.41}$$

where $\hat{\mathcal{U}} = \hat{\mathcal{T}}, \hat{\mathcal{C}}$ or $\hat{\mathcal{S}}$ for the time-reversal, particle-hole or chiral symmetry, respectively.

The operator $\hat{\mathcal{T}}$ implementing time-reversal symmetry (TRS) on the Fermion Fock space of second quantization is defined by

$$\hat{\mathcal{T}}\,\hat{c}_i\,\hat{\mathcal{T}}^{-1} = \sum_j (U_T^\dagger)_{ij}\,\hat{c}_j, \qquad \hat{\mathcal{T}}\,\hat{c}_i^\dagger\,\hat{\mathcal{T}}^{-1} = \sum_j \hat{c}_j^\dagger\,(U_T)_{ji}, \qquad \hat{\mathcal{T}}\mathrm{i}\hat{\mathcal{T}}^{-1} = -\mathrm{i}, \tag{2.42}$$

where U_T is a unitary matrix. The third equality is derived from the sign change of the momentum $\hat{\mathbf{p}} \to -\hat{\mathbf{p}}$ under time-reversal,

$$\hat{\mathcal{T}}\,\mathrm{i}\hbar\delta_{ab}\,\hat{\mathcal{T}}^{-1} = \hat{\mathcal{T}}\,[\hat{x}_a, \hat{p}_b]\,\hat{\mathcal{T}}^{-1} = [\hat{x}_a, -\hat{p}_b] = -\mathrm{i}\hbar\delta_{ab}. \tag{2.43}$$

Consequently, by substituting (2.42) into (2.41) for $\hat{\mathcal{U}} = \hat{\mathcal{T}}$ and using the relation between the first-quantized Hamiltonian H and its second-quantized counterpart, that is $\hat{H} = \hat{c}_i^\dagger H_{ij}\hat{c}_j$, H transforms under TR as

$$U_\mathrm{T}^\dagger H U_\mathrm{T} = H^*. \tag{2.44}$$

Going to momentum space using the Fourier transform in both x and y directions (2.33), one deduces that, after block-diagonalizing with respect to $\mathbf{k}$,

$$u_\mathrm{T}^\dagger H(\mathbf{k}) u_\mathrm{T} = H^*(\mathbf{k}), \tag{2.45}$$

where u_T is a unitary matrix resulting from the reshaping of U_T due to the Fourier transform. Besides, the sign change of momentum from TRS results in an explicit expression of the action of TRS on $H(\mathbf{k})$, that is

$$u_\mathrm{T}^\dagger H(\mathbf{k}) u_\mathrm{T} = H(-\mathbf{k}), \tag{2.46}$$

meaning that, for each energy $\varepsilon(\mathbf{k})$, there is an eigenvalue $\varepsilon(-\mathbf{k})$ when TRS is preserved. Therefore, the spectrum of (2.34) is an even function of $\mathbf{k}$. TRS is preserved when the condition

$$H^*(\mathbf{k}) = H(-\mathbf{k}) \tag{2.47}$$

is fulfilled. Thanks to the equation (2.47), one deduces the expression of an eigenvector of $H(-\mathbf{k})$ from an eigenvector of $H(\mathbf{k})$ at the same energy $\varepsilon_\mathbf{k}$. Indeed, since $H(\mathbf{k})v_\mathbf{k} = \varepsilon_\mathbf{k} v_\mathbf{k}$ then $H(\mathbf{k})^* v_\mathbf{k}^* = \varepsilon_\mathbf{k} v_\mathbf{k}^*$ and $H(-\mathbf{k})v_{-\mathbf{k}} = \varepsilon_{-\mathbf{k}} v_{-\mathbf{k}} = H(\mathbf{k})^* v_{-\mathbf{k}} = \varepsilon_\mathbf{k} v_{-\mathbf{k}}$, where

$$v_{\mathbf{k}} = \begin{pmatrix} |\psi_{\mathrm{A}}^{\mathbf{k}}\rangle \\ |\psi_{\mathrm{B}}^{\mathbf{k}}\rangle \\ \vdots \\ 0 \\ 0 \\ \vdots \end{pmatrix} \qquad v_{\mathbf{k}}^{*} = \begin{pmatrix} |\psi_{\mathrm{A}}^{\mathbf{k}}\rangle^{*} \\ |\psi_{\mathrm{B}}^{\mathbf{k}}\rangle^{*} \\ \vdots \\ 0 \\ 0 \\ \vdots \end{pmatrix} \qquad v_{-\mathbf{k}} = \begin{pmatrix} 0 \\ 0 \\ \vdots \\ |\psi_{\mathrm{A}}^{\mathbf{k}}\rangle^{*} \\ |\psi_{\mathrm{B}}^{\mathbf{k}}\rangle^{*} \\ \vdots \end{pmatrix} \tag{2.48}$$

where the block-diagonal form of $\hat{H}$ – see (2.34) – has been reintroduced. Deductively, the distributions of particles on each sublattice at $\mathbf{k}$ are the same as those at $-\mathbf{k}$. In particular, this holds for the distributions at $\mathbf{K}$ and $\mathbf{K}' = -\mathbf{K}$.

2.3.2 Particle-hole symmetry

The particle-hole symmetry (PHS) transforms the fermionic creation and annihilation operators into one another, as

$$\hat{\mathcal{C}}\,\hat{c}_i\,\hat{\mathcal{C}}^{-1} = \sum_j (U_{\mathrm{C}}^{*})_{ij}^{\dagger}\,\hat{c}_j^{\dagger}, \qquad \hat{\mathcal{C}}\,\hat{c}_i^{\dagger}\,\hat{\mathcal{C}}^{-1} = \sum_j \hat{c}_j\,(U_{\mathrm{C}}^{*})_{ji}, \qquad \hat{\mathcal{C}}\mathrm{i}\hat{\mathcal{C}}^{-1} = \mathrm{i}, \tag{2.49}$$

where U_{C} is a unitary matrix. Consequently, by substituting (2.49) into (2.41) for $\hat{\mathcal{U}} = \hat{\mathcal{C}}$ and using the relation between the first-quantized Hamiltonian H and its second-quantized counterpart, that is $\hat{H} = \hat{c}_i^{\dagger} H_{ij} \hat{c}_j$, H transforms under

$$U_{\mathrm{C}} H^{*} U_{\mathrm{C}}^{\dagger} = -H, \qquad u_{\mathrm{C}} H(\mathbf{k})^{*} u_{\mathrm{C}}^{\dagger} = -H(\mathbf{k}), \tag{2.50}$$

where u_{C} is a unitary matrix resulting from the reshaping of U_{C} due to the Fourier transform. This means that each energy ε has a corresponding energy $-\varepsilon$ when the PHS is preserved [106]. Thus, there are as many positive energies as negative ones, therefore $\varepsilon = 0$ is the energy at half-filling of any Hamiltonian that preserves PHS. Taking again the example of the tight-binding Hamiltonian (2.34), where $H(\mathbf{k})^{*} = H(-\mathbf{k})$, then $U_{\mathrm{C}} H(\mathbf{k}) U_{\mathrm{C}}^{\dagger} = -H(-\mathbf{k})$. Therefore, the energy corresponding to $\varepsilon(\mathbf{k})$ through the PH operation is $-\varepsilon(-\mathbf{k})$. Note that this does not imply that the spectrum is symmetric with respect to the plane $\varepsilon = 0$ but instead to the central point $(\varepsilon = 0, \mathbf{k} = 0)$.

2.3.3 Chiral symmetry

The chiral symmetry (CS) arises from the combination of time-reversal and particle-hole operations $\hat{\mathcal{S}} = \hat{\mathcal{T}} \cdot \hat{\mathcal{C}}$. It acts as follows on the fermionic creation and annihilation operators:

$$\hat{\mathcal{S}}\,\hat{c}_i\,\hat{\mathcal{S}}^{-1} = \sum_j (U_{\mathrm{S}}^{*})_{ij}^{\dagger}\,\hat{c}_j^{\dagger}, \qquad \hat{\mathcal{S}}\,\hat{c}_i^{\dagger}\,\hat{\mathcal{S}}^{-1} = \sum_j \hat{c}_j\,(U_{\mathrm{S}}^{*})_{ji}, \qquad \hat{\mathcal{S}}\mathrm{i}\hat{\mathcal{S}}^{-1} = -\mathrm{i}. \tag{2.51}$$

where U_S is a unitary matrix. Consequently, by substituting (2.51) into (2.41) for $\hat{\mathcal{U}} = \hat{\mathcal{C}}$ and using the relation between the first-quantized Hamiltonian H and its second-quantized counterpart, that is $\hat{H} = \hat{c}_i^\dagger H_{ij} \hat{c}_j$, H transforms under

$$U_S H U_S^\dagger = -H, \qquad u_S H(\mathbf{k}) u_S^\dagger = -H(\mathbf{k}), \tag{2.52}$$

where u_S is a unitary matrix resulting from the reshaping of U_S due to the Fourier transform. The chiral symmetry implies that the spectrum is symmetric with respect to $\varepsilon = 0$ as the chiral symmetry operation sends $\varepsilon(\mathbf{k})$ to $-\varepsilon(\mathbf{k})$. Particularizing to the tight-binding Hamiltonian in real space (2.31) and assuming that the chiral operator acts on the creation and annihilation operators on A ($\hat{a}^{(\dagger)}$) and B ($\hat{b}^{(\dagger)}$) sublattices as

$$\begin{aligned} \hat{\mathcal{S}} \hat{a}_i \hat{\mathcal{S}}^{-1} &= \hat{a}_i^\dagger, & \hat{\mathcal{S}} \hat{b}_i \hat{\mathcal{S}}^{-1} &= -\hat{b}_i^\dagger, \\ \hat{\mathcal{S}} \hat{a}_i^\dagger \hat{\mathcal{S}}^{-1} &= \hat{a}_i, & \hat{\mathcal{S}} \hat{b}_i^\dagger \hat{\mathcal{S}}^{-1} &= -\hat{b}_i, \end{aligned} \tag{2.53}$$

then $(U_S)_{ij} = (-\delta_{ij})^i$, where even (odd) values of i stand for A (B) sites [106]. From this, one deduces that the wavefunctions associated to $\pm\varepsilon$ have related expressions. Any eigenstate $|\varepsilon_\lambda\rangle$, associated to an energy ε_λ (λ indices the eigenvalue), is related to the eigenstate $|\varepsilon_{\lambda'}\rangle$, corresponding to $\varepsilon_{\lambda'} = -\varepsilon_\lambda$, by $|-\varepsilon_\lambda\rangle = U_S |\varepsilon_\lambda\rangle$ such that their respective wavefunctions at the position $\mathbf{r}_i$ of the i^{th} site, $\psi_{\varepsilon_\lambda}(\mathbf{r}_i) = \langle \mathbf{r}_i | \varepsilon_\lambda \rangle$ and $\psi_{-\varepsilon_\lambda}(\mathbf{r}_i) = \langle \mathbf{r}_i | -\varepsilon_\lambda \rangle$ satisfy

$$\psi_{-\varepsilon_\lambda}(\mathbf{r}_i) = (-1)^i \psi_{\varepsilon_\lambda}(\mathbf{r}_i) \qquad \Longrightarrow \qquad |\psi_{-\varepsilon_\lambda}(\mathbf{r}_i)|^2 = |\psi_{\varepsilon_\lambda}(\mathbf{r}_i)|^2. \tag{2.54}$$

Before discussing the consequences of the chiral symmetry, Figure 2.6 shows a sketch that highlights the spectral symmetries resulting from the three global symmetries (TRS, PHS and CS). This is useful for identifying whether one of the global symmetries is satisfied as the spectrum has to possess the corresponding (geometric) symmetry.

Uniform density at half-filling

The interesting consequence of both the spectrum symmetry and the equation (2.54) is the exact uniformity of the fermionic density at half-filling, *i.e.* when half of the energy states are populated. Indeed, it first allows to deduce that the local density of states at energy ω at site[3] $\mathbf{r}$, denoted $\rho(\omega, \mathbf{r})$, is symmetric in ω, i.e. $\rho(-\omega, \mathbf{r}) = \rho(\omega, \mathbf{r})$. From its definition involving the

[3] Without loss of generality and for the sake of readability, the index i is removed for the derivation.

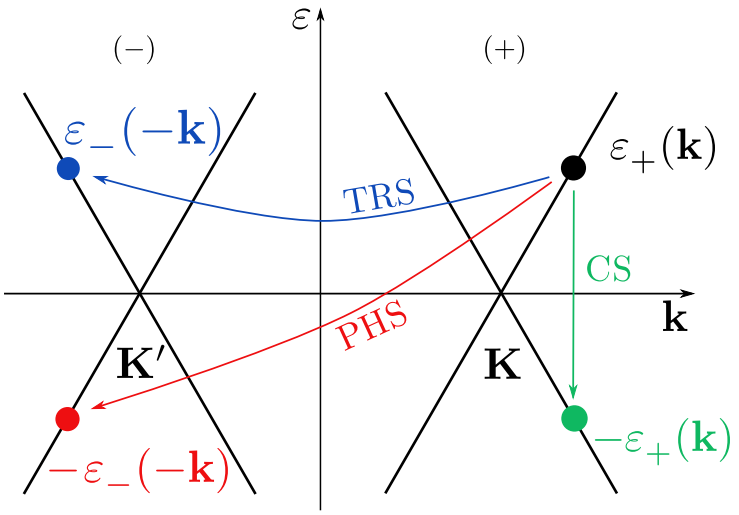

Figure 2.6: Summary sketch of the apparent spectral symmetries resulting from the time-reversal (TRS), particle-hole (PHS) and chiral (CS) symmetries. Note that these three spectral symmetries are necessary conditions for preserving their corresponding global symmetries, not sufficient ones.

retarded Green's function $\hat{G}^r(\omega) = (\omega - \hat{H} + \mathrm{i}\eta)^{-1}$,

$$
\begin{aligned}
\rho(\omega, \mathbf{r}) &= -\frac{1}{\pi} \operatorname{Im} \langle \mathbf{r} | \, \hat{G}^r(\omega) \, | \mathbf{r} \rangle \\
&= \frac{\eta}{\pi} \sum_\lambda \frac{|\psi_{\varepsilon_\lambda}(\mathbf{r})|^2}{(\omega - \varepsilon_\lambda)^2 + \eta^2} \qquad \left(\sum_{\lambda=-\mathcal{N}}^{\mathcal{N}} \left| \psi_{\varepsilon_\lambda} \right\rangle \left\langle \psi_{\varepsilon_\lambda} \right| = \mathbb{1}, \ \lambda \neq 0, \hat{H} \, |\varepsilon_\lambda\rangle = \varepsilon_\lambda \, |\varepsilon_\lambda\rangle \right) \\
&= \frac{\eta}{\pi} \sum_\lambda \frac{|\psi_{\varepsilon_\lambda}(\mathbf{r})|^2}{(-\omega + \varepsilon_\lambda)^2 + \eta^2} \\
&= \frac{\eta}{\pi} \sum_\lambda \frac{|\psi_{\varepsilon_{-\lambda}}(\mathbf{r})|^2}{(-\omega + \varepsilon_{-\lambda})^2 + \eta^2} \qquad \left(\lambda \to -\lambda, \ \sum_{-\lambda} = \sum_\lambda \right) \\
&= \frac{\eta}{\pi} \sum_\lambda \frac{|\psi_{\varepsilon_\lambda}(\mathbf{r})|^2}{(\omega + \varepsilon_\lambda)^2 + \eta^2} \qquad \left(\varepsilon_{-\lambda} = -\varepsilon_\lambda, \ |\psi_{\varepsilon_\lambda}(\mathbf{r})|^2 = |\psi_{\varepsilon_{-\lambda}}(\mathbf{r})|^2 \right) \\
&= \rho(-\omega, \mathbf{r})
\end{aligned}
$$

Then, since the local density of states on each site is normalized to 1, i.e.

$$\int_{-\infty}^{\infty} \rho(\omega, \mathbf{r}) d\omega = 1 \tag{2.55}$$

and since the energy at half-filling is $\varepsilon = 0$,

$$\begin{aligned} 1 &= \int_{-\infty}^{0} \rho(\omega, \mathbf{r}) d\omega + \int_{0}^{\infty} \rho(\omega, \mathbf{r}) d\omega \\ &= \int_{-\infty}^{0} \rho(\omega, \mathbf{r}) d\omega + \int_{0}^{\infty} \rho(-\omega, \mathbf{r}) d\omega \\ &= \int_{-\infty}^{0} \rho(\omega, \mathbf{r}) d\omega + \int_{-\infty}^{0} \rho(\omega, \mathbf{r}) d\omega \\ &= 2 \int_{-\infty}^{0} \rho(\omega, \mathbf{r}) d\omega. \end{aligned} \tag{2.56}$$

Secondly, the local density of particles at site $\mathbf{r}$, denoted $n_p(\mathbf{r})$, is related to the density of states by

$$n_p(\mathbf{r}) = \int_{-\infty}^{+\infty} f(\omega, T) \rho(\omega, \mathbf{r}) d\omega, \tag{2.57}$$

where $f(\omega, T)$ is the Fermi-Dirac distribution at temperature T (in the grand canonical ensemble), which gives the occupation number of the energy ω. Its expression is

$$f(\omega, T) = \frac{1}{\mathrm{e}^{(\omega - \mu_{\mathrm{F}})/k_{\mathrm{B}}T} + 1}, \tag{2.58}$$

where μ_{F} is the Fermi energy and k_{B} is the Boltzmann constant. At zero temperature, $f(\omega, 0)$ is the Heaviside function, thus, at half-filling ($\mu_{\mathrm{F}} = 0$),

$$n_p^{\mathrm{hf}}(\mathbf{r}) = \int_{-\infty}^{0} \rho(\omega, \mathbf{r}) d\omega = \frac{1}{2}. \tag{2.59}$$

One concludes that the chiral symmetry imposes the density of particles at half-filling to be uniform in the whole system.

Zero-energy state from exclusive sublattice occupation

When chiral symmetry is preserved, if an eigenstate of $\hat{H}$ only occupies one of the two sublattices of a bipartite lattice (say A, without loss of generality), then its associate energy must be zero. Indeed, as the Hamiltonian matrix H anticommutes with the representation matrix of the chiral symmetry u_{S}, $Hu_{\mathrm{S}} = -u_{\mathrm{S}}H$, and due to the action of the chiral symmetry on creation/annihilation operators (2.54), one finds

$$\begin{aligned} H \begin{pmatrix} |\phi_A\rangle \\ |\phi_B\rangle \end{pmatrix} = \varepsilon \begin{pmatrix} |\phi_A\rangle \\ |\phi_B\rangle \end{pmatrix}, \qquad u_{\mathrm{S}} \begin{pmatrix} |\phi_A\rangle \\ |\phi_B\rangle \end{pmatrix} = \begin{pmatrix} |\phi_A\rangle \\ -|\phi_B\rangle \end{pmatrix}, \\ \Longrightarrow H u_{\mathrm{S}} \begin{pmatrix} |\phi_A\rangle \\ |\phi_B\rangle \end{pmatrix} = -\varepsilon u_{\mathrm{S}} \begin{pmatrix} |\phi_A\rangle \\ |\phi_B\rangle \end{pmatrix} = -\varepsilon \begin{pmatrix} |\phi_A\rangle \\ -|\phi_B\rangle \end{pmatrix}. \end{aligned} \tag{2.60}$$

When only the A sublattice is occupied, the first and second lines of (2.60) lead to

$$H\begin{pmatrix}|\phi_A\rangle\\0\end{pmatrix}=\varepsilon\begin{pmatrix}|\phi_A\rangle\\0\end{pmatrix},\qquad u_{\mathrm{S}}\begin{pmatrix}|\phi_A\rangle\\0\end{pmatrix}=\begin{pmatrix}|\phi_A\rangle\\0\end{pmatrix},$$

$$\begin{aligned}\implies Hu_{\mathrm{S}}\begin{pmatrix}|\phi_A\rangle\\0\end{pmatrix}&=-\varepsilon u_{\mathrm{S}}\begin{pmatrix}|\phi_A\rangle\\0\end{pmatrix}=-\varepsilon\begin{pmatrix}|\phi_A\rangle\\0\end{pmatrix}\\&=\varepsilon\begin{pmatrix}|\phi_A\rangle\\0\end{pmatrix},\end{aligned}\tag{2.61}$$

hence $\varepsilon=0$, which proves that when an eigenstate of an Hamiltonian that preserves CS only occupies one of the two sublattices of a bipartite lattice, then it is a zero-energy state.

2.4 Honeycomb lattice in a magnetic field: relativistic quantum Hall effect

In both of our articles [75, 76] – to which chapters 3 and 4 are dedicated respectively – we treat systems with pseudo-gauge fields generated by strain that are mathematically analog to real magnetic fields but that do not break time-reversal symmetry. For this reason and gaining intuition, we derive the spectrum and eigenstates of free particles in a honeycomb lattice pierced by a real magnetic field. We show that the spectrum displays relativistic Landau levels and provide their associated wavefunctions.

2.4.1 Relativistic Landau levels

When the honeycomb lattice is immersed into a magnetic field **B**, the Hamiltonian (2.31) becomes

$$\hat{H}=-t\sum_{\mathbf{r}}\hat{a}^\dagger_{\mathbf{r}}\left(\hat{b}_{\mathbf{r}+\boldsymbol{\delta}_1}+\hat{b}_{\mathbf{r}+\boldsymbol{\delta}_2}\mathrm{e}^{-\mathrm{i}\varphi x/\phi_0 a}+\hat{b}_{\mathbf{r}+\boldsymbol{\delta}_3}\mathrm{e}^{\mathrm{i}\varphi x/\phi_0 a}\right)+\mathrm{H.c.},\tag{2.62}$$

in the Landau gauge $\mathbf{A}=(0,-Bx,0)$, where $\varphi=BA_{\mathrm{c}}$ is the magnetic flux per hexagonal plaquette of area $A_{\mathrm{c}}=3\sqrt{3}a^2/2$ and $\phi_0=h/e$. For weak magnetic fields, the space-dependence in the phases can be neglected and the Fourier transform (2.33) can be performed. Exploiting the fact that the low-energy spectrum of particles in the honeycomb lattice (around the Dirac points) is well described by a Dirac Hamiltonian, the addition of a magnetic field **B** to the honeycomb lattice is introduced by a minimal substitution $\hbar\mathbf{q}\to\hbar\mathbf{q}+e\mathbf{A}$ in the effective Dirac Hamiltonian [99]. Note that, for this to hold, the intensity of the magnetic field must be such that the magnetic length ℓ_B is bigger than the lattice parameter a but smaller than the

system's size L_x, *i.e.* $a \ll \ell_B \ll L_x$. For spinless electrons, the Hamiltonian (2.40) becomes

$$\bar{\mathfrak{h}}(\mathbf{q}) = -v_{\mathrm{F}}\tau_z \otimes (\hbar\mathbf{q} + e\mathbf{A}) \cdot \boldsymbol{\sigma} = \begin{pmatrix} \bar{h}^{+}(\mathbf{q}, \mathbf{A}) & 0 \\ 0 & \bar{h}^{-}(\mathbf{q}, \mathbf{A}) \end{pmatrix}, \tag{2.63}$$

where $-e$ is the charge of the electron and $\mathbf{A}$ is the vector potential, such that $\mathbf{B} = \nabla \times \mathbf{A}$.

Importantly, the canonical momentum $\mathbf{p} = \hbar\mathbf{q}$ is no longer a physical observable as it is not gauge invariant, nor conserved as the blocks of the matrix $\bar{\mathfrak{h}}(\mathbf{q})$ are not translation invariant anymore. Therefore, to describe free electrons in a magnetic field, one needs to replace $\mathbf{p}$ by the gauge-invariant kinetic momentum $\Pi = (\Pi_x, \Pi_y) \equiv \hbar\mathbf{q} + e\mathbf{A}$. A quantum mechanical treatment of (2.63) requires the canonical quantization of $\mathbf{r}$ and $\mathbf{p}$, that have to satisfy the canonical commutation relations (2.18). Hence, the kinetic momenta $\hat{\Pi}_x$ and $\hat{\Pi}_y$ do not commute anymore,

$$[\hat{\Pi}_x, \hat{\Pi}_y] = -ie\hbar B = -i\frac{\hbar^2}{\ell_B^2}, \qquad \ell_B \equiv \sqrt{\frac{\hbar}{eB}}, \tag{2.64}$$

where ℓ_B is the magnetic length, a fundamental length scale for systems in the presence of a magnetic field. Introducing ladder operators similarly as for the harmonic oscillator in 1D in equation (2.19), the Hamiltonian $\bar{h}^{\zeta}(\mathbf{q}, \mathbf{A})$ – see (2.63) – becomes

$$\bar{h}^{\zeta}(\hat{\mathbf{q}}, \hat{\mathbf{A}}) = -\zeta\sqrt{2}\frac{\hbar v_{\mathrm{F}}}{\ell_B}\begin{pmatrix} 0 & \hat{a} \\ \hat{a}^{\dagger} & 0 \end{pmatrix}. \tag{2.65}$$

One obtains the eigenvalues and eigenvectors of $h(\zeta)$ by solving the eigenvalue equation $\bar{h}^{\zeta}\psi_n = \varepsilon_n\psi_n$, where $\psi_n = (|u_n\rangle, |v_n\rangle)$ is a two-spinor, whose first and second components occupy the A and B sublattice, respectively. Indeed, this equation forms the following system,

$$\begin{aligned} -\zeta\hbar\omega_B\hat{a}\,|v_n\rangle &= \varepsilon_n\,|u_n\rangle\,, \\ -\zeta\hbar\omega_B\hat{a}^{\dagger}\,|u_n\rangle &= \varepsilon_n\,|v_n\rangle\,, \end{aligned} \tag{2.66}$$

where $\omega_B \equiv \sqrt{2}v_{\mathrm{F}}/\ell_B$ plays the role of the cyclotron frequency in this relativistic setting and ζ indicates the valley. Substituting $|u_n\rangle$ in the first line in (2.66) yields

$$(\hbar\omega_B)^2\hat{a}^{\dagger}\hat{a}\,|v_n\rangle = \varepsilon_n^2\,|v_n\rangle\,, \tag{2.67}$$

meaning that $|v_n\rangle = |n\rangle$ is an eigenvector of the number operator $\hat{a}^{\dagger}\hat{a}$, whose eigenvalues are positive integers, $n \geq 0$. Therefore, one deduces the energies of the Landau levels,

$$\varepsilon_n = \pm\hbar\omega_B\sqrt{n} = \pm v_{\mathrm{F}}\sqrt{2n\hbar eB}, \tag{2.68}$$

where the $\pm$ sign indicates the valence (-) and conduction (+) band. Note that the energy gaps between the levels get smaller as n increases and exhibit the same ladder spectrum in both bands. The other component, $|u_n\rangle$, is readily derived, as

$$-\zeta\hat{a}\,|n\rangle = \lambda\sqrt{n}\,|u_n\rangle \tag{2.69}$$

where λ ($\lambda^2 = 1$) symbolizes the valence ($-$) or the conduction ($+$) band. Thus, $u_n = -\lambda\zeta\,|n-1\rangle$. An important distinction between $n = 0$ and $n > 0$ must be pointed out. From (2.69), $u_0 = 0$, meaning that the wavefunction of the zero-energy level only occupies one of the two sublattices,

$$\psi_0 = \begin{pmatrix} 0 \\ |0\rangle \end{pmatrix}. \tag{2.70}$$

For $n > 0$, the two-spinors, normalized to unity, read

$$\psi^{\zeta}_{n,\lambda} = \frac{1}{\sqrt{2}} \begin{pmatrix} -\lambda\zeta\,|n-1\rangle \\ |n\rangle \end{pmatrix}. \tag{2.71}$$

The analytical expressions of these eigenvectors' components in the Landau gauge are the same as those already given by equation (2.27) for the non-relativistic Landau levels. The degeneracy of the relativistic Landau levels is computed in the same way as their non-relativistic counterparts [99].

Importantly, from (2.40), one recalls that the components of the pseudo-spinor at the $\mathbf{K}'$-valley are exchanged with respect to the components of the pseudo-spinor at $\mathbf{K}$. Hence, the populations on the A and B sublattices of an eigenstate at $\mathbf{K}$ are the same populations as on the B and A sublattices at $\mathbf{K}'$. This is a sign of the TRS breaking. Indeed, a necessary condition for preserving TRS is the equality in populations of the same sublattice at both valleys – see section 2.3.1.

Relativistic quantum Hall effect

Subjecting graphene to strong magnetic fields (several teslas) have revealed an unusual quantization of its transversal conductivity. Instead of taking all integer values – see section 2.1.2 – the Hall conductivity follows the law

$$\sigma_{\mathrm{H}} = 2(2\nu+1)\sigma_0, \qquad \nu \in \mathbb{Z}, \tag{2.72}$$

where $\sigma_0 = e^2/h$ is the conductivity quantum. This was first measured by Zhang et *al.* [15], where a factor of 2 originating from the spin degree of freedom has to be taken into account. However, since our work does not deal with real magnetic fields but only with pseudo-magnetic field that do not couple to spin, this degree of freedom will be neglected.

2.5 Strain and pseudo-magnetic field in the honeycomb lattice

Mechanical deformations in solid states materials can emulate effective gauge field theories. As an example, strain is achieved by applying external forces or by engineering the growth conditions of the crystal such that the distance between its atoms are modified. The present section details how strain modifies the low-energy physics of the honeycomb lattice and converts into a minimal coupling to a pseudo-vector potential in the Dirac Hamiltonian (2.36), whose sign depends on the valley. In the following sections, similarly as the honeycomb lattice in a magnetic field, strain in graphene results in (pseudo) Landau levels around the Dirac points, as experimentally observed in real [57–59] and artificial [108–117] graphene. Their energy is deduced for two types of strain: uniaxial and trigonal (or triaxial). This section ends with a discussion on the conditions for the presence of non-propagating and helical edge states in the honeycomb lattice.

2.5.1 Effect of strain on the Dirac Hamiltonian: minimal coupling to a vector potential

For two atoms positioned at $\mathbf{r}$ and $\mathbf{s}$, where $\boldsymbol{\delta}_j = \mathbf{r} - \mathbf{s}$ ($j = 1, 2, 3$) is one of the nearest-neighbor vectors (defined in section 2.2.1) of norm $\|\boldsymbol{\delta}_j\| = a$, the displacement of these neighboring atoms to $\mathbf{r}'$ and $\mathbf{s}'$ can be assigned by new space-dependent nearest-neighbor vectors $\boldsymbol{\delta}'_j(\mathbf{r}) = \mathbf{r}'(\mathbf{r}) - \mathbf{s}'$. When restoring forces are non-linear in the displacement field $\mathbf{u}(\mathbf{r}) = \mathbf{r}'(\mathbf{r}) - \mathbf{r}$, the phonon frequency depends on the deformations of the lattice bonds [118, 119]. This modifies the electron-phonon coupling, resulting in a renormalization of the nearest-neighbor hopping amplitude t,

$$t \to t_j(\mathbf{r}) = t \exp\left[-\beta\left(\frac{\|\boldsymbol{\delta}'_j(\mathbf{r})\|}{a} - 1\right)\right], \tag{2.73}$$

where $\beta \equiv -\partial \ln(t)/\partial \ln(a)$ is the Grüneisen parameter. Hence, this initially uniform t in the Hamiltonian (2.31) might become space-dependent due to the strain, as prescribed by (2.73). Within the continuum elastic theory, the vectors $\boldsymbol{\delta}'_j(\mathbf{r})$ are expressed as a smooth function of the spatial coordinates. Therefore, the argument of the exponential can be related to the strain tensor $\boldsymbol{\epsilon}$ by

$$\frac{\|\boldsymbol{\delta}'_j(\mathbf{r})\|}{a} - 1 = \sum_{k,l=x,y} \frac{\delta_j^k \delta_j^l}{a^2} \epsilon_{kl}(\mathbf{r}) \equiv d_j, \tag{2.74}$$

where $\epsilon_{kl}(\mathbf{r}) \equiv 1/2(\partial_k u_l + \partial_l u_k)$, with the displacement field smoothly depending on $\mathbf{r}$. For an homogeneous strain, only function of the bond direction j, the hopping parameter along j reads

$$t_j = t \exp\left[-\beta d_j\right] = t(1 - \beta d_j), \tag{2.75}$$

for small displacements $d_j \ll 1$. The Fourier transform of the tight-binding Hamiltonian (2.31) in both directions x and y, expanded in linear order separately in q_x and q_y around $\mathbf{K}$, yields

$$h^+(\mathbf{q}) = \begin{pmatrix} 0 & (V^+(\mathbf{q}))^* \\ V^+(\mathbf{q}) & 0 \end{pmatrix} \tag{2.76}$$

where

$$\begin{aligned} V^+(\mathbf{q}) = &-\frac{1}{2}(2t_1 - t_2 - t_3) + \mathrm{i}\frac{\sqrt{3}}{2}(t_2 - t_3) \\ &- q_x\left[\frac{\sqrt{3}a}{4}(t_2 - t_3) - \mathrm{i}\frac{a}{4}(4t_1 + t_2 + t_3)\right] \\ &- q_y\left[\frac{3a}{4}(t_2 + t_3) - \mathrm{i}\frac{\sqrt{3}a}{4}(t_2 - t_3)\right] \\ &+ q_x q_y a^2\left[\frac{\sqrt{3}}{8}(t_2 - t_3) + \mathrm{i}\frac{3}{8}(t_2 + t_3)\right]. \end{aligned} \tag{2.77}$$

From the relations (2.75), one finds

$$\begin{aligned} V^+(\mathbf{q}) = &\mathrm{i}\hbar v_\mathrm{F}\left(\hbar q_x f_x(\boldsymbol{\epsilon}) - \frac{\beta}{a}\epsilon_{xy}\right) - \hbar v_\mathrm{F}\left(q_y f_y(\boldsymbol{\epsilon}) + \frac{\beta}{2a}(\epsilon_{yy} - \epsilon_{xx})\right) \\ &+ \hbar v_\mathrm{F} q_x q_y\left[-\frac{\beta a}{4}\epsilon_{xy} + \frac{\mathrm{i}a}{2}\left(1 - \frac{\beta}{4}(\epsilon_{xx} + 3\epsilon_{yy})\right)\right], \end{aligned} \tag{2.78}$$

where were introduced

$$\begin{aligned} f_x(\boldsymbol{\epsilon}) &\equiv 1 - \frac{\beta}{4}(3\epsilon_{xx} - \epsilon_{yy}) - \mathrm{i}\frac{\beta}{2}\epsilon_{xy}, \\ f_y(\boldsymbol{\epsilon}) &\equiv 1 - \frac{\beta}{4}(\epsilon_{xx} + 3\epsilon_{yy}) + \mathrm{i}\frac{\beta}{2}\epsilon_{xy}, \end{aligned} \tag{2.79}$$

for the sake of clarity. Eventually wrapping these results back into the matrix form, one obtains

$$\begin{aligned} h^+(\mathbf{q}) = &\hbar v_\mathrm{F}\left[q_x f_x(\boldsymbol{\epsilon}) - \frac{\beta}{a}\epsilon_{xy} + q_x q_y \frac{a}{2}\left(1 - \frac{\beta}{4}(\epsilon_{xx} + 3\epsilon_{yy})\right)\right]\sigma_y \\ &- \hbar v_\mathrm{F}\left[q_y f_y(\boldsymbol{\epsilon}) + \frac{\beta}{2a}(\epsilon_{yy} - \epsilon_{xx}) + q_x q_y \frac{\beta a}{4}\epsilon_{xy}\right]\sigma_x. \end{aligned} \tag{2.80}$$

This rewriting (2.80) unveils the analogy between the strain and an effective pseudo-vector potential. Indeed, as for a particle in a magnetic field, the space-derivatives undergo a minimal substitution

$$\hbar q_l \quad \rightarrow \quad \hbar q_l f_l(\boldsymbol{\epsilon}) - eA_l \qquad (l = x, y), \tag{2.81}$$

where the functions f_l indicate anisotropic derivatives along x and y due to the strain tensor [120]. The vector potential at the valley $\mathbf{K}$ (+) is defined as

$$\begin{aligned} A_x^+ &= \frac{\hbar\beta}{ea}\epsilon_{xy}, \\ A_y^+ &= \frac{\hbar\beta}{2ea}(\epsilon_{xx} - \epsilon_{yy}). \end{aligned} \tag{2.82}$$

In the literature, the terms in (2.80) proportional to $q_x q_y$ have usually been overlooked. These are necessary to correctly reproduce the spectrum of a system whose translational symmetry along one axis is broken and only one of the momenta remains a good quantum number [120]. The subsequent section conveys that the pseudo-vector potential, effectively created by the strain, has opposite signs at opposite valleys due to the preservation of time-reversal symmetry.

2.5.2 Vector potential with opposite sign at opposite valleys from time-reversal symmetry

As a consequence of the TRS, the Hamiltonian $h(\mathbf{q}, \mathbf{K}')$ at the other valley $\mathbf{K}'$ can be readily derived from the one at $\mathbf{K}$. Indeed, as in Section 2.2.3, the two Hamiltonians at opposite valleys are related to each other by

$$(h^-(-\mathbf{q}, \mathbf{A}^-))^* = h^+(\mathbf{q}, \mathbf{A}^+) \tag{2.83}$$

after the minimal substitution, or equivalently, $h^-(\mathbf{q}, \mathbf{A}^-) = h^+(-\mathbf{q}, \mathbf{A}^+)^*$. This allows to deduce the relation between the vector potential $\mathbf{A}^+$ at $\mathbf{K}$ and $\mathbf{A}^-$ at $\mathbf{K}'$. Indeed,

$$\begin{aligned} (h^+(-\mathbf{q}, \mathbf{A}^+))^* &= -v_{\mathrm{F}}\left[(-\hbar q_y f_y^* - eA_y^+)\sigma_x - (-\hbar q_x f_x^* - eA_x^+)\sigma_y^*\right] + \mathcal{O}(q_x q_y a^2) \\ &= -v_{\mathrm{F}}\left[-(\hbar q_y f_y^* + eA_y^+)\sigma_x - (\hbar q_x f_x^* + eA_x^+)\sigma_y\right] + \mathcal{O}(q_x q_y a^2) \\ &= h^-(\mathbf{q}, -\mathbf{A}^+) \\ &\equiv h^-(\mathbf{q}, \mathbf{A}^-), \end{aligned} \tag{2.84}$$

meaning that the pseudo vector potential must have opposite signs at opposite valleys. From

now on,

$$\begin{aligned} A_x^\zeta &= \zeta \frac{\beta}{ea} \epsilon_{xy} = -\zeta \frac{\hbar}{\sqrt{3}ta}(t_2 - t_3), \\ A_y^\zeta &= \zeta \frac{\beta}{2ea}(\epsilon_{xx} - \epsilon_{yy}) = -\zeta \frac{\hbar}{3ta}\left(2t_1 - t_2 - t_3\right). \end{aligned} \tag{2.85}$$

where the tunneling amplitudes were reintroduced thanks to the relations (2.73) and (2.74). As suggested by this rewriting in terms of a vector potential, each of the valley seems to host a magnetic field $\mathbf{B}_\tau^\zeta \equiv \boldsymbol{\nabla} \times \mathbf{A}_\tau^\zeta$, whose sign also depends on the valley ζ. Since it does not break TRS, $\mathbf{B}_\tau^\zeta$ is called a *pseudo*-magnetic field. Importantly, the resemblance of the Hamiltonians $h^+(\mathbf{q}, \mathbf{A}^+)$ and $h^-(\mathbf{q}, \mathbf{A}^-)$ imply similar eigenspinors expressions, with identical particle distributions per sublattice, *i.e.* $n^{\mathbf{K}}_{\mathrm{A(B)}} = n^{\mathbf{K}'}_{\mathrm{A(B)}}$. As previously announced in section 2.3, this is also a consequence of the TRS.

The rewriting of the Dirac Hamiltonian prompts us to ask whether the low-energy physics of a strained honeycomb lattice mimics the relativistic Landau levels physics encountered in section 2.4 for a real uniform magnetic field. As shown in the two following sections, this is the case when appropriate strain schemes leading to a uniform $\mathbf{B}_\tau^\zeta$ are chosen, *e.g.* when $t_j(\mathbf{r})$ depends linearly on x or y.

2.5.3 Uniaxial strain and pseudo-magnetic field

Before revealing the exact expression of the space dependence of the hopping amplitudes $t_j(\mathbf{r})$ needed to deduce the spectrum of the strained honeycomb lattice, here come some words of caution. According to the preceding section 2.5, when strain corresponds to real mechanical deformations[4] and is modeled through renormalized hopping amplitudes, one must ensure that these t_j can be derived from a displacement field leading to a desired strain tensor. Uniaxial, linear strain along the x-direction can be modeled by displacement fields that are function of x only, such that ϵ_{xx} is linear in x and $\epsilon_{xy} = \epsilon_{yy} = 0$. Then, for τ denoting the strain intensity [120],

$$\epsilon_{xx} = -\frac{\tau}{3\beta a}\, x, \tag{2.86}$$

the tunneling amplitudes reads

$$t_j(x) = t\left(1 + \tau \frac{x}{3a^3} |\hat{\mathbf{x}} \cdot \boldsymbol{\delta}_j|^2\right), \quad \hat{\mathbf{x}} = (1, 0). \tag{2.87}$$

Importantly, in the rest of this work, the strain that is envisaged does not rely on having a real, stretched material. Indeed, in the two papers [75, 76] on which is based the major part of the present manuscript, the models that were analyzed are aiming at synthetic platforms

[4] Instead of an effective strain as later envisaged in this work – see section 4.1.

where strain is an effective consequence of other intrinsic mechanisms of the system and not to actual mechanical deformations. Along this line, the artificial uniaxial strain, described in chapter 4 based our first paper [76], results from a exotic tunneling process – see section 4.4.1 – which yields a hopping amplitude

$$t_j(x) = t\left(1 + \tau\frac{x}{3a^2}|\hat{\mathbf{x}}\cdot\boldsymbol{\delta}_j|\right), \quad \hat{\mathbf{x}} = (1,0), \tag{2.88}$$

which is still linear in space but with a different dependence on the δ_j^x components. Deductively, the strain tensor element ϵ_{xx} (remember that $\epsilon_{xy} = \epsilon_{yy} = 0$) is unchanged.The corresponding Hamiltonian reads

$$\hat{H} = -\sum_{\mathbf{r},j} t\left(1 + \tau\frac{x - x_c}{3a^2}|\hat{\mathbf{x}}\cdot\boldsymbol{\delta}_j|\right)\hat{a}_{\mathbf{r}}^\dagger\hat{b}_{\mathbf{r}+\boldsymbol{\delta}_j} + \text{H.c.} \tag{2.89}$$

With this in mind, the formalism introduced in section 2.5.1 can also be applied. The Figures 2.7**a** and **b** respectively depict an unstretched lattice and a stretched one, where the area of a unit cell A_c remains identical or not, respectively. The former case is the situation of interest for the rest of this work. Also in panel **a**, notice the discrete x-position of the center of a link between two sites, denoted by x_l ($l \in [0, N_x - 1]$). For the rest of this work, unless specified, the x-variable is meant to take those discrete values and the index will be omitted.

Assuming small strain intensities, i.e. $\tau \ll 1$ in (2.88), one can reintroduce the space-dependence of the hopping amplitudes into the $t_j(\mathbf{r})$ in (2.77). Consequently, one obtains a uniform pseudo-magnetic field $\mathbf{B}_\tau^\zeta = \boldsymbol{\nabla}\times\mathbf{A}^\zeta$ from the pseudo vector potential (2.85) promoted to a space-dependent function:

$$v_F e\mathbf{A}^\zeta = \left(0, -\zeta\frac{\tau t}{6a}(x - x_c)\right) \qquad \Longrightarrow \qquad \mathbf{B}_\tau^\zeta = -\zeta\frac{\hbar\tau}{9ea^2}\hat{\mathbf{z}}. \tag{2.90}$$

The position of the system's center is denoted by $x_c = L_x/2$, where L_x is the projected length of the ribbon. For a ribbon with both zigzag terminations as shown Figure 2.8, $L_x = 3N_x/2 - 1$. To prevent any hopping term (2.88) from vanishing (breaking in the lattice) or exceeding $2t$ (leading to Lifshitz transition [121]) across the entire ribbon, the value of τ shall fulfill the condition $\tau L_x/6a < 1$.

Besides, while the translational invariance along x is broken by the uniaxial strain Eq (2.87), it is preserved along y. Therefore, the ribbon possesses cylindrical boundary conditions along y. The y-periodicity is emphasized in Figure 2.8 by matching the color of equivalent links (dashed lines) at each site. The thickening of the link $\boldsymbol{\delta}_1$ signals that the tunneling amplitude is increasing with x. The cylindrical geometry allows to block-diagonalize the Hamiltonian, where each block corresponds to one value of quasi-momentum k_y, i.e.

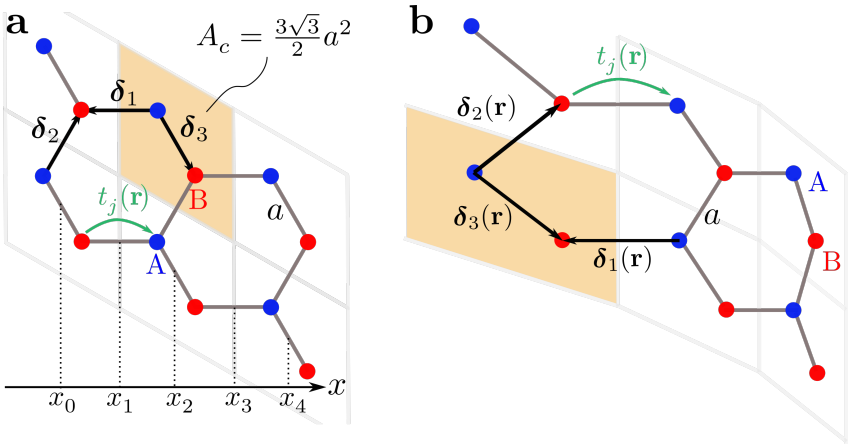

Figure 2.7: Schematic representation of strained honeycomb lattices. **a** Strain is directly imprinted on the tunneling amplitudes $t_j(\mathbf{r})$ without modifying the underlying structure of the lattice nor changing the area of the unit cell $A_c = 3\sqrt{3}a^2/2$. The vectors $\boldsymbol{\delta}_j$ remain uniform. **b** Strain is applied by mechanically stretching the lattice, making the vectors connecting neighboring sites $\boldsymbol{\delta}_j$ position-dependent.

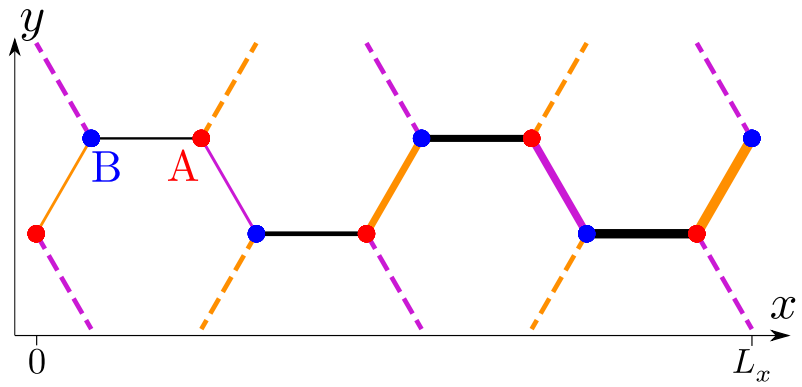

Figure 2.8: Ribbon of honeycomb lattice with $N_x = 5$ sites along the x-axis and $N_y = 2$ sites along y, with imposed cylindrical boundary conditions symbolized by dashed lines with matching colors for identical links. Notice the thickening of the link as the x-position increases.

$$\hat{H} = \bigoplus_{k_y \in BZ} \hat{H}(k_y), \tag{2.91}$$

where

$$\hat{H}(k_y) = \begin{pmatrix} \vdots \\ \hat{b}_{l-1,k_y} \\ \hat{a}_{l,k_y} \\ \hat{b}_{l,k_y} \\ \hat{a}_{l+1,k_y} \\ \vdots \end{pmatrix}^{\dagger} h(k_y) \begin{pmatrix} \vdots \\ \hat{b}_{l-1,k_y} \\ \hat{a}_{l,k_y} \\ \hat{b}_{l,k_y} \\ \hat{a}_{l+1,k_y} \\ \vdots \end{pmatrix},$$

$$h(k_y) = \begin{pmatrix} \cdots & \cdots & \cdots & \cdots \\ \cdots & \sum_{j=2,3} t_j(x_{l-1}) \mathrm{e}^{ik_y\delta_{j,y}} & \cdots & \cdots \\ \cdots & 0 & t_1(x_l) & \cdots \\ \cdots & t_1(x_l) & 0 & \cdots \\ \cdots & \cdots & \sum_{j=2,3} t_j(x_{l+1}) \mathrm{e}^{-ik_y\delta_{j,y}} & \ddots \\ \cdots & \cdots & \cdots & \cdots \end{pmatrix}. \tag{2.92}$$

The matrix $h(k_y)$ is found by Fourier transforming the local creation and annihilation operators $\hat{a}_i^{(\dagger)}$, $\hat{b}_i^{(\dagger)}$ in Eq. (2.89),

$$\begin{aligned} \hat{a}_{\mathbf{r}} &= \frac{1}{\sqrt{L_y}} \sum_{k_y} \hat{a}_{x,k_y} \mathrm{e}^{\mathrm{i}k_y y}, \qquad \hat{a}_{\mathbf{r}}^{\dagger} = \frac{1}{\sqrt{L_y}} \sum_{k_y} \hat{a}_{x,k_y}^{\dagger} \mathrm{e}^{-\mathrm{i}k_y y}, \\ \hat{b}_{\mathbf{r}} &= \frac{1}{\sqrt{L_y}} \sum_{k_y} \hat{b}_{x,k_y} \mathrm{e}^{\mathrm{i}k_y y}, \qquad \hat{b}_{\mathbf{r}}^{\dagger} = \frac{1}{\sqrt{L_y}} \sum_{k_y} \hat{b}_{x,k_y}^{\dagger} \mathrm{e}^{-\mathrm{i}k_y y}. \end{aligned} \tag{2.93}$$

By diagonalizing each block $h(k_y)$ for every value of k_y in the BZ, one obtains the energy spectrum ε (in units of t) shown in Figure 2.9 for $\tau = 0$ (gray lines) and $\tau \neq 0$ (colored lines), as a function of k_y. In the unstrained case, two Dirac cones are clearly visible and touch at the **K** and **K′** points.

Relativistic pseudo-Landau levels and wavefunctions

Uniaxial strain generates dispersive levels near the Dirac points ($q_y a \ll 1$) in the valence and conduction bands, as shown in Figure 2.9 that displays the spectrum of the Hamiltonian (2.89). While an analytical expression of their dispersion relation can be obtained by following the reasoning detailed in [120], we (only) numerically verify that, around the Dirac points, the dispersion relation in the valence (-) and the conduction bands (+) reads

$$\varepsilon_{\nu}^{\zeta}(q_y) = \pm t \sqrt{\frac{|\tau|\,\nu}{2}} \sqrt{1 - \zeta \frac{3 q_y a}{2}}, \qquad \nu \in \mathbb{N}. \tag{2.94}$$

with opposite slope at opposite valley. The analytical expression is indicated by black dashed lines in Figure 2.9 for the valley **K′** ($\zeta = -1$). In the same way as for a real magnetic field, the

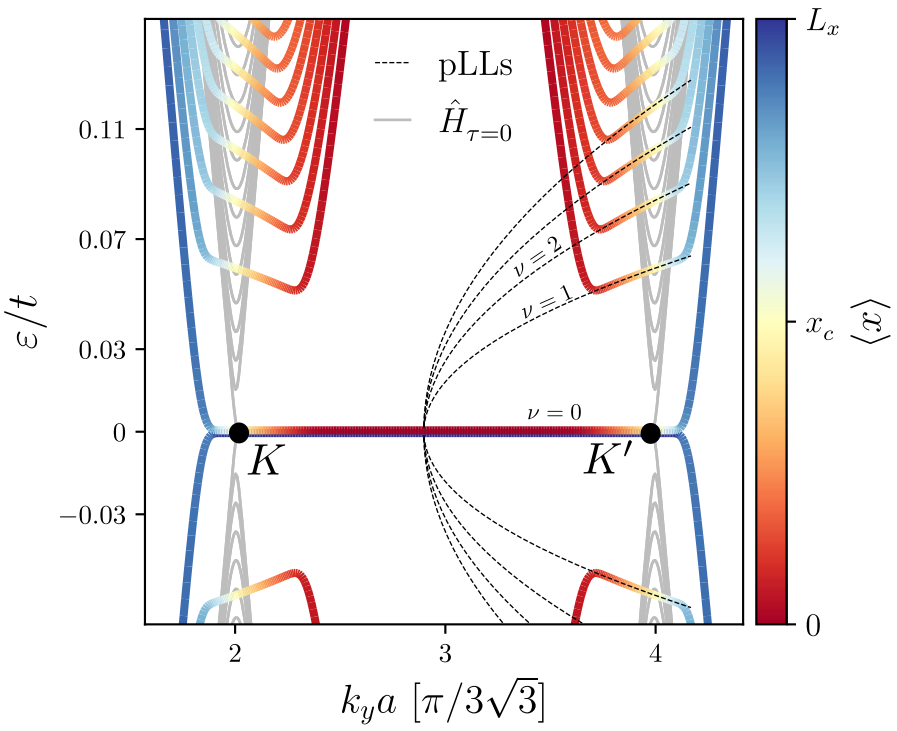

Figure 2.9: Spectrum of pristine ($\tau = 0$, gray lines) and uniaxially strained ($\tau \neq 0$, colored lines) honeycomb lattice (2.89) in units of hopping parameter t with zigzag terminations at both edges and cylindrical boundary conditions along y. For finite strain, the color scale indicates the mean position $\langle x \rangle$ of each state. The dashed black lines represent the pseudo-Landau levels (pLLs) whose approximate dispersion is given by (2.94).

centers of the pLLs ($q_y = 0$ or $k_y = \xi K_y$) occur at energies

$$\bar{\varepsilon}_\nu = \pm\hbar v_{\mathrm{F}}\sqrt{2\nu\hbar e|B_\tau|} = \pm t\sqrt{\frac{|\tau|\,\nu}{2}}, \qquad \nu \in \mathbb{N}, \tag{2.95}$$

following (2.90). For this reason, they are called relativistic *pseudo*-Landau levels (pLLs). Each point (ε, k_y) is colored respectively to the mean position of the corresponding eigenstates,

$$\langle \psi_\varepsilon^{k_y} | \hat{x} | \psi_\varepsilon^{k_y} \rangle = \sum_{x \in \mathrm{A,B}} x\, |\psi_\varepsilon^{k_y}(x)|^2. \tag{2.96}$$

One identifies that the pLLs eigenstates are located in the bulk of the system (in yellow). While deducing their exact analytical expressions is beyond the scope of this thesis, the wavefunctions of these pseudo-LLs states appear to be in appreciable agreement with the wavefunctions of the original LLs given by $\langle x|\nu\rangle$ in the Landau gauge (2.27). This is shown in Figures 2.10**a** and **b** for the two first levels $\nu = 1$ and $\nu = 2$, respectively, at $k_y = K_y$ ($q_y = K_y$). The particle distributions of the eigenstates of the strained honeycomb lattice on the A and B sublattices are plotted in blue and orange circles, respectively. The analytical LLs distributions on the A and B sublattice are represented by solid red and black lines, respectively.

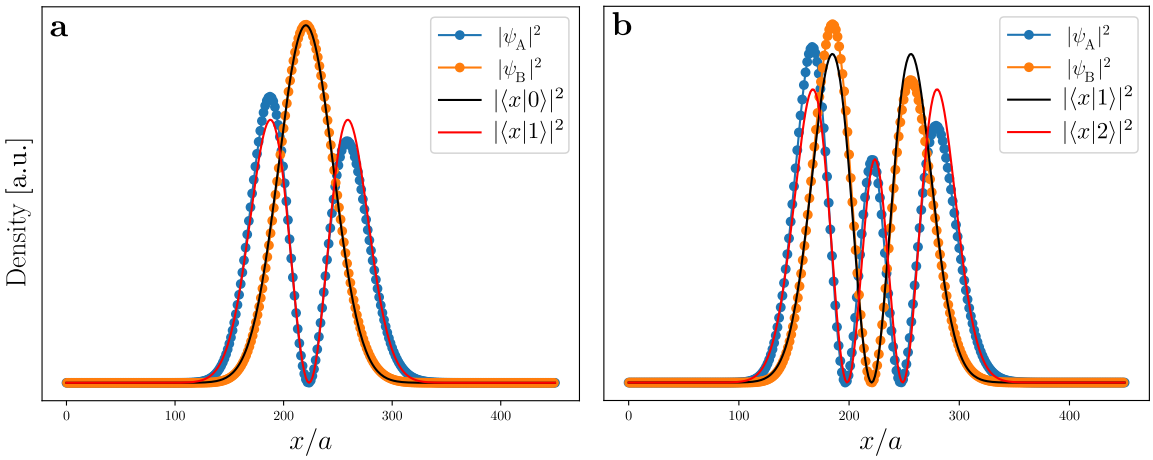

Figure 2.10: Particle distributions on the A and B sublattices (blue and orange circles, respectively) of the eigenstates of (2.89) at $k_y = K_y$ associated to the pLLs $\nu = 1$ in **a** and $\nu = 2$ in **b**. In each case, they are compared to the analytical LLs (2.27) for the corresponding ν on each sublattice.

2.5.4 Trigonal strain and pseudo-magnetic field

Another way of generating linearly space-dependent hopping amplitudes and consequently a uniform pseudo-magnetic, consists in (artificially or mechanically) straining the honeycomb lattice along its three main axes, preserving its $\mathcal{C}_3$-symmetry. This type of strain, called *trigonal* or *triaxial*, also leads to clear signatures of the expected effective Landau levels physics. It is encoded into the hopping amplitudes as

$$t_j(\mathbf{r}) = t\left(1 + \tau\frac{(\mathbf{r} - \mathbf{r}_c)\cdot\delta_j}{3a^2}\right), \tag{2.97}$$

therefore breaking the translational invariance along both the x and y directions. The corresponding Hamiltonian reads

$$\hat{H} = -\sum_{\mathbf{r},j} t\left(1 + \tau\frac{(\mathbf{r} - \mathbf{r}_c)\cdot\boldsymbol{\delta}_j}{3a^2}\right)\hat{a}^\dagger_{\mathbf{r}}\hat{b}_{\mathbf{r}+\boldsymbol{\delta}_j} + \text{H.c.}. \tag{2.98}$$

The pseudo-magnetic field is given by

$$\mathbf{B}^\zeta_\tau = \zeta\frac{2\hbar}{3ea^2}\tau\,\hat{\mathbf{z}}. \tag{2.99}$$

As shown in Figure 2.11, the spectrum of (2.98) also presents relativistic pseudo-Landau levels, much less dispersive than those formed with the previous strain scheme, encountered in section 2.5.3. The energies of the pLLs are given by

$$\bar{\varepsilon}_\nu = \pm t\sqrt{3|\tau|\nu}, \qquad \tau \in \mathbb{N}. \tag{2.100}$$

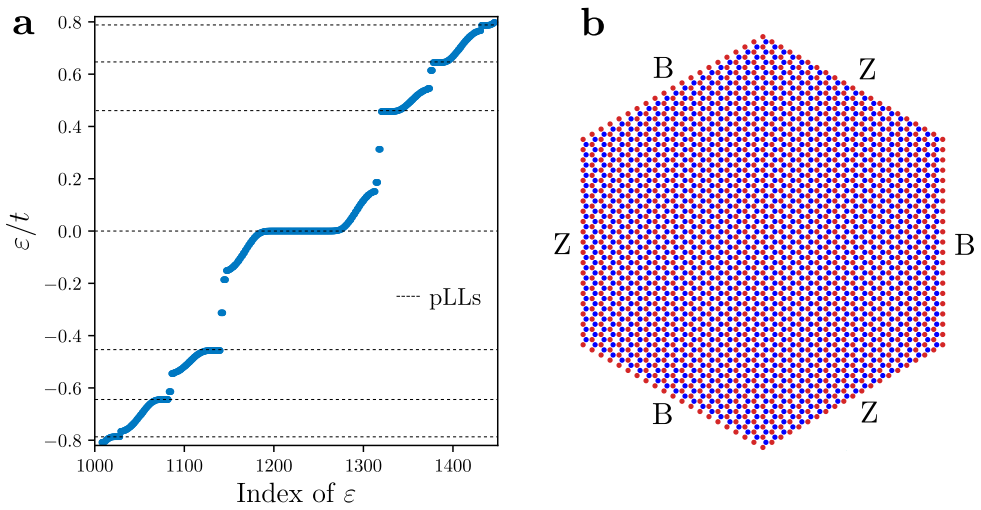

Figure 2.11: **a** Spectrum of a triaxially strained honeycomb flake of 2461 sites shown in panel **b**. The dashed black lines in **a** represent the pseudo-Landau levels (pLLs) whose approximate dispersion is given by (2.100). **b** The zigzag and bearded terminations are indicated by Z and B. The A and B sites are represented by red and blue dots, respectively

2.6 Terminations and edge states

Depending on the terminations of the ribbon (see Figure 2.5), a monolayer (unstrained) graphene might or might not possess non-propagating zero-energy edge states. More specifically, for chiral-symmetric honeycomb lattices, no boundary state is expected at edges with armchair terminations contrarily to edges with bearded and zigzag terminations. The presence or absence of non-propagating edge state is actually related to a topological quantity, called the *Zak phase* or *winding number* [122, 123], defined as the one-dimensional integral of the Berry connection over the first Brillouin zone. It allows to define another type of bulk-edge correspondence, different from the one encountered in quantum Hall systems or $\mathbb{Z}_2$ topological insulators associated to distinct topological invariants. Indeed, the latter reveals the (non-)existence of edge states in 2D systems independently of the edge terminations.

On their side, strained honeycomb lattices display helical currents localized at its edges depending on its terminations. Indeed, adding strain and changing its sign, switch on or off helical currents at the edges of the honeycomb lattice. This is relevant for explaining our results in section 3.2.2. For $\tau > 0$, when the honeycomb lattice is non-uniformly strained, for $q_y a > 0\,(< 0)$ – *i.e.* away from the **K**-valley – the wavefunction $\psi_\varepsilon^{q_y}$ is shifted to the left (right), as indicated by the red (blue) colorization in panels **a** and **c** of Figure 2.12. Stemming from the TRS preservation, the opposite mechanism takes place at the **K′**-valley. For $\tau < 0$, the inverse is true. Consequently, the edge states, living at the left and right boundaries of the ribbon, are helical instead of chiral: each edge hosts pairs of two counterpropagating modes, each of them belonging to a different valley. The sign of their group velocity $v(k_y) = \partial\varepsilon(k_y)/\partial k_y$ switches sign by going to the other valley.

As mentioned earlier, for an unstrained honeycomb lattice, a zero-energy non-propagating edge state exists when the ribbon has bearded and/or zigzag-terminations, but does not exist when it has armchair terminations. However, in the presence of uniform strain (*i.e.* for space-independent t_j), a zero-energy non-propagating edge state may appear for any type of termination [124, 125]. When non-uniform strain is applied, these edge states may propagate, but only when they populate both sublattices, as a consequence of the chiral symmetry – see section 2.3.3. To become propagative, a zero-energy edge state needs to mix with a 0^{th}-LL state such that the resulting state populates both sublattices.

In Figure 2.12, the presence or absence of such edge states is shown for several combinations of terminations and for different sign of the strain intensity. Panels **a** and **b** correspond to zigzag-bearded terminations with $\tau > 0$ and $\tau < 0$, respectively. Panel **c** corresponds to zigzag-zigzag terminations with $\tau > 0$. In the first case (panel **a**), no propagating edge states exists in the first gap which is agreement with the fact that only the A sublattice is populated. This is shown in panel **d** where is plotted the distribution n^0_α ($\alpha = $ A,B), defined as the sum of all particle densities associated to the zero-energy level (indicated by the green box in panel **a**), *i.e.*

$$n^0_\alpha(x) = \sum_{\varepsilon=0,k_y} |\psi^{k_y}_\alpha(x)|^2, \qquad \alpha = \text{A,B}. \tag{2.101}$$

Panel **e** shows the particle distributions of propagating modes at $(\varepsilon/t, k_y a) = (1.09, 0.03)$ and $(2.53, 0.03)$, whose markers correspond to those indicated by the empty circle and triangle in panel **b**. Notice that the color of the branch they are extracted from, reflects the region where they are localized in the system – to the left (L) in red and to the right (R) in blue. Panel **f** shows the particle density of the helical edge states localized to the right of the system, indicated in panel **c** by the empty circle at $(\varepsilon/t, k_y a) = (1.09, 0.03)$. The results are in perfect agreement[5] with those of Ref. [124]. In panel **e** for $\tau < 0$ with zigzag and bearded terminations on the left and right boundaries, respectively, or in panel **f** for $\tau > 0$ with both zigzag terminations, the corresponding propagating edge states from the branches in panels **b** and **c** are located on the A and B sublattices. Notice that for all higher pLLs, both valleys have propagating edge states as the pLLs-states all have a non-zero component on both sublattices.

[5] A word of caution is mandatory here: the nearest-neighbor vectors defined in Ref. [124] are opposite to those that were chosen for the current work. This simply corresponds to opposite strain intensities or, equivalently, to mirroring the lattice with respect to the axis $x = x_c$ in (2.88).

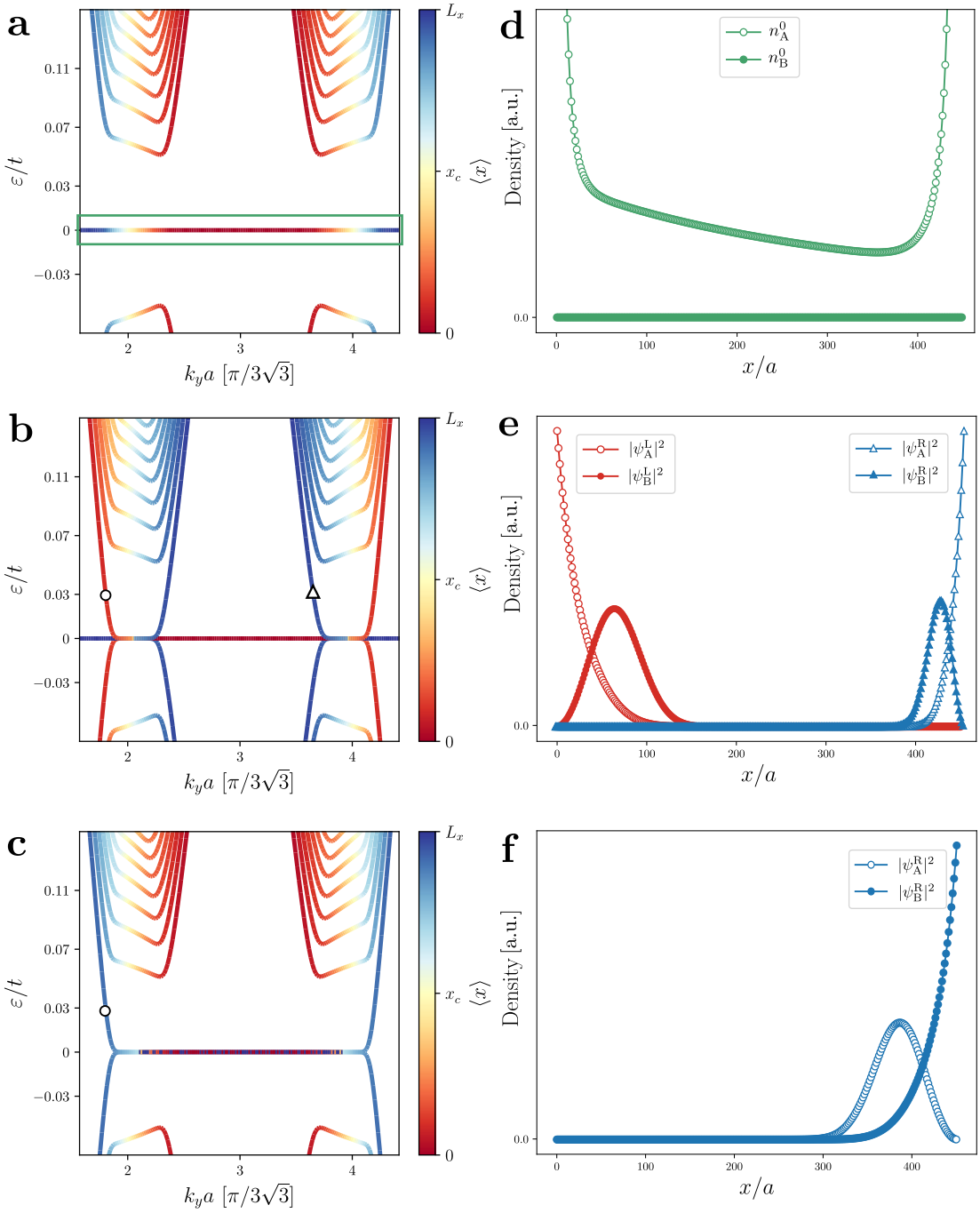

Figure 2.12: Panels **a** and **b** correspond to zigzag-bearded terminations with $\tau > 0$ and $\tau < 0$, respectively. Panel **c** corresponds to zigzag-zigzag terminations with $\tau > 0$. In the first case, no propagating edge states exists in the first gap since only the A sublattice is populated, as shown in panel **d**. The distribution n_α^0 ($\alpha =$ A,B) is defined as the sum of all particle densities associated to the zero-energy level – see (2.101) – indicated by the green box in panel **a**. In panel **e**, we show the particle distributions of propagating modes at $(k_y a, \varepsilon/t) = (1.09, 0.03)$ and $(2.53, 0.03)$, whose markers correspond to those indicated by the empty circle and triangle in panel **b**. Notice that the color of the branch they are extracted from, reflects the region where they are localized in the system – to the left (L) in red and to the right (R) in blue. Panel **f** shows the particle density of the helical edge states localized to the right of the system, indicated in panel **c** by the empty circle at $(k_y a, \varepsilon/t) = (1.09, 0.03)$.

2.7 Valley Hall effect and probing techniques

As introduced in section 2.2.1, the Brillouin zone of the honeycomb lattice presents two symmetry-nonequivalent Dirac points $\mathbf{K}$ and $\mathbf{K}'$, called valleys, which are the contact points of the conduction and valence bands. In materials where they are largely separated in momentum space, such as graphene, the intervalley scattering is strongly suppressed. Hence, in addition to their charge and spin, electrons in such systems possess a valley pseudospin, that can be manipulated to process and store information – referred to as valleytronics – in a way similar to the charge in electronics and the spin in spintronics [19, 20].

When the inversion symmetry is broken explicitly, as in graphene, or spontaneously as in transition metal dichalcogenides (TMDs) [22, 126] (*e.g.* MoS_2, $MoSe_2$, WS_2 and WSe_2) and ferroelectrics [127, 128] (*e.g* SnS, SnTe), the Berry curvature $\boldsymbol{\Omega}(\mathbf{k})$ of the Bloch band can be employed to distinguish populations of particles at nonequivalent valleys. Addressable with a magnetic or an electric field, a non-zero Berry curvature of a band causes the deflection of the trajectory of the electrons of that band. Indeed, in the semi-classical approximation, the velocity of an electron in the presence of an in-plane electric field $\mathbf{E}$ is given by [129]

$$\mathbf{v} = \boldsymbol{\nabla}_{\mathbf{k}}\varepsilon(\mathbf{k}) - \partial_t\mathbf{k} \times \boldsymbol{\Omega}(\mathbf{k}), \tag{2.102}$$

where $\partial_t\mathbf{k} = -e\mathbf{E}/\hbar$, $\varepsilon(\mathbf{k})$ is the energy dispersion, $\boldsymbol{\Omega}(\mathbf{k})$ is obtained from the Fourier-transformed Bloch functions $u(\mathbf{k})$,

$$\boldsymbol{\Omega}(\mathbf{k}) = \mathrm{i}\boldsymbol{\nabla}_{\mathbf{k}} \times \langle u(\mathbf{k})|\boldsymbol{\nabla}_{\mathbf{k}}u(\mathbf{k})\rangle\,. \tag{2.103}$$

While the inversion symmetry is broken in TMDs, graphene on substrates or voltage-biased graphene, time-reversal symmetry is preserved. Since the Berry curvature acquires opposite signs at opposite momenta when TRS is preserved, $\boldsymbol{\Omega}(-\mathbf{k}) = -\boldsymbol{\Omega}(\mathbf{k})$, it does at different valleys, $\Omega(\mathbf{K}) = -\Omega(\mathbf{K}')$. Looking at (2.102), electrons consequently undergo a deflection in one or the opposite direction depending on the valley they occupy, which is called the *valley Hall effect* [18, 130]. This creates a valley polarization within the material transversal to the applied electric field, instead of a charge separation taking place in a real magnetic field, which is the Hall effect – see section 2.1.

Several probing techniques exist for measuring the valley Hall effect. One of these relies on non-local resistance measurement in multiterminal Hall bar geometries [21], in a similar scheme as the one used to detect spin Hall currents [131]. Although early advances were made in understanding the non-local resistance as a hallmark of the valley Hall effect (VHE), simulations [23, 26, 27] and experiments [25, 28] showed that, along the possible contribution from the Berry curvature of the Fermi sea, several other effects (propagating edge-states, Joule's currents) were responsible for the strong non-local resistance signal observed by Gorbachev

et *al.* [21]. It therefore impedes to identify the exact role played by the valley Hall effect and extract its clear signature.

An alternative probing method, relying on valley-resolved measurements, exploits spatially-resolved optical Kerr signals [24]. First, an electric field perpendicular to the sample breaks the inversion symmetry and allows to tune the Berry curvature. Resulting from the interplay between the Berry curvature and a longitudinal electric field, the valley Hall effect causes a valley polarization near the device's edges. Then, a linearly-polarized light beam is shed onto the sample and transmitted as circularly-polarized light due to the optical Kerr effect. Its Kerr-rotation angle is eventually measured and is shown to depend on the population imbalance at the edges.

A third technique uses circular light to selectively excite valley-polarized carriers, again deflected due to the anomalous velocity, subsequently leading to a photo-induced anomalous Hall voltage [132]. While this also employs a valley-resolved preparation, their observations indicate that these signals arise from the bulk of the device. This is of great relevance as the VHE is not topological protected and edge measurements are peculiarly sensitive to local disorder, that leads to inter-valley scattering between counter-propagating edge states living at the same boundary. In chapter 3 is proposed another alternative for directly probing the valley Hall effect, that relies on locally measuring fermionic density responses upon external variations of strain applied to a honeycomb lattice.

2.8 Floquet driving

Adding time-periodic driving, or Floquet driving, to static systems allows to engineer effective Hamiltonians and leads to novel quantum phases of matter [133, 134]. From the growing interest on nonequilibrium states in condensed matter physics, Floquet driving has been increasingly employed in various fields, namely in cold atoms setups [133, 135–137], photonics [109, 138, 139], solid state materials [140], acoustic [141] and mechanical systems [142].

There are two typical types[6] of quantum systems: *i*) open quantum systems, coupled to the environment with dissipation, whose dynamics is governed by the von Neumann equation $\frac{d}{dt}\hat{\rho} = -\mathrm{i}[\hat{H}, \hat{\rho}]$, and *ii*) isolated quantum system driven, whose time evolution is entirely determined by the unitary dynamics. In the former case, when the energy absorbed from an external time-periodic fields is balanced with the dissipation into the environment, a time-periodic steady state can be reached. In the latter case, which will be of interest here, adding a periodic drive continuously supplies energy to the system. Consequently, it reaches infinite-

[6] Other types of non-trivial stationary states are expected to emerge in many-body localized systems, where strong disorder prevents the system from heating even without dissipation energy into its environment, or in time crystals [134].

temperature state at long times as particles can absorb energy from the driving field, resulting in excitations to higher Bloch bands, particle losses or dissipation of energy. As these effects develops over time, Floquet heating thus generally limits the duration of experiments that can be carried in driven systems and bounds (from below) the attainable temperatures in experiments [143]. Nonetheless, the system may stay in the so-called Floquet prethermalization phase for a certain time scale, that is exponentially long when the driving frequency is much larger than any other energy scale of the system [134, 143].

Floquet engineering allowed to realize (topological) quantum phase transitions [137, 144, 145], emulate artificial gauge fields, opening new routes for implementing lattice gauge theories [146, 147], chaos-assisted tunneling processes [148], superconductivity [149], and other exotic quantum states of matter [150]. To understand how these effective theories are constructed, the general idea of Floquet engineering is presented, with an emphasis on the separation of time scales, namely by distinguishing the fast from the slow dynamics. In particular, the focus will be set on deriving the stroboscopic Hamiltonian, that governs the slow dynamics of the system, therefore letting aside the micromotion. Along this line, in the high-frequency limit, a Magnus expansion allows to derive a new Hamiltonian, one or more parameters get renormalized by a function of the frequency. This can be exploited as a knob to tune the model. Then, two examples where the tunneling amplitudes get renormalized will be presented, as they are relevant for further derivations in chapter 4.

2.8.1 Floquet theory and quasi-energy spectrum

Floquet theory [151] was originally developed for solving ordinary differential equations of the type $\dot{x}_m(t) = \sum_n C_{mn}(t)x_n(t)$, where the coefficients C_{mn} are periodic functions. Adapted to quantum mechanics, the time evolution of isolated quantum systems is governed by the time-dependent Schrödinger equation,

$$\mathrm{i}\hbar\frac{d}{d\tau}\left|\psi\right\rangle = \hat{H}(\tau)\left|\psi\right\rangle, \tag{2.104}$$

where the Hamiltonian $\hat{H}(t)$ satisfies $\hat{H}(\tau) = \hat{H}(\tau + T)$, with T the drive period. The time translation from $|\psi(\tau_0)\rangle$ to $|\psi(\tau)\rangle$ is determined by the unitary operator $\hat{U}(\tau, \tau_0)$, *i.e.* $|\psi(\tau)\rangle = \hat{U}(\tau, \tau_0)\,|\psi(\tau_0)\rangle$, where

$$\hat{U}(\tau, \tau_0) := \mathcal{T}\exp\left(-\frac{\mathrm{i}}{\hbar}\int_{\tau_0}^{\tau} d\tau' \hat{H}(\tau')\right), \tag{2.105}$$

where $\mathcal{T}$ is the time-ordered product.

The essence of Floquet theory is to separate the overall dynamics into two evolutions corresponding to two time scales: one is stroboscopic and consists of a sequence of snapshots

taken at each period T at times $s \to s+T \to s+2T \to \ldots$ The other one is governed by the micromotion taking place within each period, *i.e.* at times $s \to s+t$, with $0 \leq t < T$. Hence, the first one captures the long-time and time-averaged dynamics, while the second contains information on the short-time scale. Besides, the Floquet theorem states that f*or each unitary operator $\hat{U}(\tau, \tau_0)$ associated to a periodic Hamiltonian $\hat{H}(\tau) = \hat{H}(\tau + T)$, there exist a time-independent hermitian operator $\hat{H}_{\mathrm{F}}$ and a time-periodic unitary operator $\hat{K}(\tau) = \hat{K}(\tau + T)$ (called the kick operator) such that*

$$\hat{U}(\tau, \tau_0) = \mathrm{e}^{\mathrm{i}\hat{K}(\tau)} \mathrm{e}^{-\mathrm{i}(\tau-\tau_0)\hat{H}_{\mathrm{F}}} \mathrm{e}^{-\mathrm{i}\hat{K}(\tau_0)}. \tag{2.106}$$

Note that the couple $\{\hat{H}_{\mathrm{F}}, \hat{K}(\tau)\}$ is not unique, but can be connected by a gauge transformation to any other couple that fulfills (2.106). The equation (2.106) simplifies by stroboscopically observing the system, *i.e.* at times $\tau = \tau_0 + nT$ $(n \in \mathbb{Z})$,

$$\begin{aligned} \hat{U}(\tau_0 + nT, \tau_0) &= \mathrm{e}^{-\mathrm{i}\hat{K}(\tau_0)} \mathrm{e}^{-\mathrm{i}\hat{H}_{\mathrm{F}} nT/\hbar} \mathrm{e}^{\mathrm{i}\hat{K}(\tau_0)} \\ &= \exp\left(\mathrm{e}^{-\mathrm{i}\hat{K}(\tau_0)} (-\mathrm{i}\hat{H}_{\mathrm{F}} nT/\hbar) \mathrm{e}^{\mathrm{i}\hat{K}(\tau_0)} \right) \\ &\equiv \mathrm{e}^{-\mathrm{i}\hat{H}_{\mathrm{F}}[\tau_0] nT/\hbar}. \end{aligned} \tag{2.107}$$

Note that the second line is obtained by using the fact that if A and B are operators and B is unitary, then $\exp\left(B^\dagger A B\right) = B^\dagger \exp(A) B$. With this rewriting, the (new) Floquet Hamiltonian depends on the initial time, but does not evolve within a period.

2.8.2 High-frequency Floquet driving and Magnus expansion of the stroboscopic Floquet Hamiltonian

The Floquet Hamiltonian $\hat{H}_{\mathrm{F}}[\tau_0]$ can be computed in the high-frequency limit using the Magnus expansion [143], which consists in rewriting $\hat{H}_{\mathrm{F}}[\tau_0]$ into a power series of $1/\Omega$,

$$\hat{H}_{\mathrm{F}}[\tau_0] = \sum_{k=0}^{\infty} \frac{1}{\Omega^k} \hat{H}_{\mathrm{F}}^{(k)}[\tau_0]. \tag{2.108}$$

By following the reasoning detailed in appendix A.1, one exactly computes the 0^{th} and 1^{st}-order terms of the Magnus expansion, that read

$$\begin{aligned} \hat{H}_{\mathrm{F}}^{(0)}[\tau_0] &= H_0 = \frac{1}{T} \int_{\tau_0}^{\tau_0+T} \hat{H}(t) d\tau, \\ \hat{H}_{\mathrm{F}}^{(1)}[\tau_0] &= \sum_{l=1}^{\infty} \frac{1}{\hbar l} \left([H_l, H_{-l}] + [H_0, H_l] \mathrm{e}^{\mathrm{i}l\Omega\tau_0} - [H_0, H_{-l}] \mathrm{e}^{-\mathrm{i}l\Omega\tau_0} \right), \end{aligned} \tag{2.109}$$

where H_l is defined by the Fourier transform of $\hat{H}(t)$ as

$$\hat{H}(t) = \sum_{l\in\mathbb{Z}} H_l \mathrm{e}^{\mathrm{i}l\Omega\tau}. \tag{2.110}$$

2.8.3 Resonant Floquet scheme

When a parameter of the Hamiltonian (*e.g.* the amplitude of the drive or an onsite potential) is proportional to the driving frequency, the Magnus expansion cannot be readily applied as its terms would diverge in the high-frequency limit ($\Omega \to \infty$) – see the example below. By performing a unitary transformation onto the Hamiltonian – commonly named rotation – similarly as a Schrieffer-Wolff transformation, its high-energy terms get reabsorbed into a renormalization of its other parameters. Henceforth, the high-frequency expansion is applicable. To operate this rotation, we apply $\hat{\mathcal{R}}(\tau) \equiv \exp\left(-\mathrm{i}\hat{K}(\tau)\right)$ on a state to the comoving (rotating) frame [143],

$$|\psi(\tau)\rangle \to \hat{\mathcal{R}}(\tau)\,|\psi(\tau)\rangle\,, \quad \hat{H}(\tau) \to \hat{H}_{\mathrm{rot}}(\tau). \tag{2.111}$$

Inserting the rotated state $\hat{\mathcal{R}}(\tau)\,|\psi(\tau)\rangle$ into the Schrödinger equation (2.104), the resulting rotated Hamiltonian $\hat{H}_{\mathrm{rot}}(\tau)$ reads

$$\hat{H}_{\mathrm{rot}}(\tau) = \hat{\mathcal{R}}\hat{H}(\tau)\hat{\mathcal{R}}^\dagger - \mathrm{i}\hbar\hat{\mathcal{R}}\partial_\tau\hat{\mathcal{R}}^\dagger \tag{2.112}$$

Example of resonant Floquet engineering in a double-well

The following example sets the ground for deriving the effective Hamiltonian analyzed in chapter 4. It shows how the tunneling amplitude t of a particle in a double-well, with time-periodically driven onsite potentials and an offset Δ, is renormalized by a Bessel function, that depends on the difference of amplitudes of the drives $\mathcal{K}_0 - \mathcal{K}_1$ and the frequency Ω. This situation is inspired by [143, 152] where, contrarily to here, only one well is driven. One starts from the time-dependent Hamiltonian $\hat{H}(\tau) = \hat{H}_0 + \hat{\mathcal{V}}(\tau)$, where

$$\begin{aligned} \hat{H}_0 &= -t\hat{c}_0^\dagger\hat{c}_1 - t\hat{c}_1^\dagger\hat{c}_0 + \Delta\hat{n}_1, \\ \hat{\mathcal{V}}(\tau) &= \mathcal{K}_0\cos(\Omega\tau)\hat{n}_0 + \mathcal{K}_1\cos(\Omega\tau)\hat{n}_1, \end{aligned} \tag{2.113}$$

with $\hat{c}_i^\dagger$ ($\hat{c}_i$) the creation (annihilation) operator of the particle. In the case of a resonance $\Delta = m\hbar\Omega$, performing a high-frequency expansion would cause the 0^{th}-order term H_0 to diverge. To circumvent the divergence, one applies a unitary transformation $\hat{\mathcal{R}}$ to the comoving frame (2.111) where, in the present case,

$$\hat{\mathcal{R}}(\tau) = \mathrm{e}^{\mathrm{i}\left[\frac{\mathcal{K}_0}{\hbar\Omega}\sin(\Omega\tau)\hat{n}_0 + \frac{\mathcal{K}_1}{\hbar\Omega}\sin(\Omega\tau)\hat{n}_1 + m\Omega\tau\hat{n}_1\right]}. \tag{2.114}$$

Therefore,

$$\hat{H}_{\mathrm{rot}}(\tau) = -t\mathrm{e}^{\mathrm{i}(\mathcal{K}_0-\mathcal{K}_1)\sin(\Omega\tau)/\hbar\Omega - \mathrm{i}m\Omega\tau}\hat{c}_0^\dagger\hat{c}_1 + \mathrm{H.c.} \tag{2.115}$$

The derivation of (2.115) is presented in appendix A.1. The Magnus expansion (2.108) can now be applied and converges to H_0 in the high-frequency limit. The zeroth-order term is obtained by taking the time-average of $\hat{H}_{\mathrm{rot}}(\tau)$ – see (2.109) – which reads

$$\hat{H}_{\mathrm{F}}^{(0)} = -t\mathcal{J}_m\left(\frac{\mathcal{K}_0 - \mathcal{K}_1}{\hbar\Omega}\right)\hat{c}_0^\dagger\hat{c}_1 + \mathrm{H.c.}, \tag{2.116}$$

for $\tau_0 = 0$, where $\mathcal{J}_m$ is the m^{th} Bessel function of the first kind. From this, we conclude that having control on the energy offset Δ between the wells allows to select the renormalizing Bessel function.

2.8.4 Floquet engineering of density-assisted tunneling processes

By modulating the onsite potential energy or the interaction parameters, the tunneling amplitudes are generally renormalized by a Peierls phase or a Bessel function, leading to non-standard effective Hubbard Hamiltonians [153], where exotic interaction terms arise. Examples of such processes are pair-tunneling, where particles hop by pair in the lattice, or density-assisted tunneling, where the hopping amplitude of a particle depends on the densities of these particles (or of another species) at the sites between which it tunnels. As a result, the parameters of the effective Hamiltonian are functions of particle density operators. In some cases, quantum gauge field theories on lattices [146, 147, 154] may emerge. This last scenario is realized when Peierls phase, or equivalently the gauge field, becomes an operator, which allows for its quantum fluctuations to be incorporated into the model.

Example of Floquet-engineered density-assisted tunneling:

We now derive a non-standard Hubbard model with *density-assisted tunneling*. The systems explored here is a simpler version of the model proposed in Ref. [155] and serves as a toy model for ours, later presented in chapter 4. Here, it consists of bosons in a double-well that can hop between sites 0 and 1 with an amplitude J and interact with each other (by pair) when they occupy the same site, with an energy $U(\tau) = U\cos(\Omega\tau)$, that is periodically driven in time (τ), where $T = 2\pi/\Omega$ is the drive period. As in the previous example in section 2.8.3, the

double-well presents an energy imbalance Δ that is also proportional to the frequency of the drive. The Hamiltonian reads

$$\hat{H}(\tau) = -J(\hat{b}_0^\dagger \hat{b}_1 + \hat{b}_1^\dagger \hat{b}_0) + \frac{U(\tau)}{2} \sum_{i=0}^{1} \hat{n}_i(\hat{n}_i - 1) + \Delta \hat{n}_1. \tag{2.117}$$

where $\hat{b}_i^{(\dagger)}$ and $\hat{n}_i$ are the annihilation (creation) and density operators of a boson at site i. The resonance between $\Delta = m\hbar\Omega$ and the drive requires to apply a rotation represented by the unitary operator

$$\hat{\mathcal{R}}(\tau) = \mathrm{e}^{\mathrm{i}\left[\frac{U\hat{n}_0}{\hbar\Omega}\sin(\Omega\tau)\hat{n}_0 + \frac{U\hat{n}_1}{\hbar\Omega}\sin(\Omega\tau)\hat{n}_1 + m\Omega\tau\hat{n}_1\right]}. \tag{2.118}$$

The rotated Hamiltonian derived from (2.112) is given by

$$\hat{H}_{\mathrm{rot}}(\tau) = -t\mathrm{e}^{2\mathrm{i}U(\hat{n}_0 - \hat{n}_1)\sin(\Omega\tau)/\hbar\Omega - \mathrm{i}m\Omega\tau}\hat{b}_0^\dagger \hat{b}_1 + \mathrm{H.c.} \tag{2.119}$$

As in the previous example, the Magnus expansion (2.108) can now be applied and converges to H_0 in the high-frequency limit. The zeroth-order term is obtained by taking the time-average of $\hat{H}_{\mathrm{rot}}(\tau)$ – see (2.109) – which reads

$$\hat{H}_{\mathrm{F}}^{(0)} = -t\mathcal{J}_m\left(\frac{2U}{\hbar\Omega}(\hat{n}_0 - \hat{n}_1)\right)\hat{b}_0^\dagger \hat{b}_1 + \mathrm{H.c.}, \tag{2.120}$$

for $\tau_0 = 0$, where we have used the identities (A.16) and (A.17). Hence, periodic modulations of the interaction result in nonlinear hopping terms, where the tunneling amplitudes from one well to the other depends on the difference in particles densities.

2.9 Weakly-interacting Bose gas

One building block of the model presented in our article [76] is a *Bose-Einstein condensate* (BEC). Moreover, one of the crucial steps of the model consists in calculating the density of the interacting, harmonically trapped BEC, whose distribution is obtained by solving a non-linear Schrödinger equation, the so-called *Gross-Pitaevskii equation* (GPE). We thus present the principal notions regarding weakly-interacting gases of bosons, based (to a great extend) on Refs. [34, 156, 157]. We start by describing how Bose-Einstein condensation takes place, *i.e.* how an eigenstate may be macroscopically occupied while the other states are barely populated. Then, by supposing that the dilute Bose gas has condensed into a BEC, the equation of motion of its stationary many-body wavefunction – the time-independent GPE – is derived. A discussion is given on how the BEC wavefunction can be interpreted as an order parameter through the mean-field and the Bogoliubov approximations.

2.9.1 Bose-Einstein condensation

One important feature of a Bose gas is the possibility that one of its energy state can be macroscopically occupied, thanks to a mechanism called Bose-Einstein condensation[7] [159] that occurs when a Bose gas is cooled down to near the absolute zero temperature. This is easily understood from the positivity of the number occupation $\bar{n}_i \geq 0$ of the i^{th} energy state, given by the Bose-Einstein statistics

$$\bar{n}_i(T,\mu) = \frac{1}{\mathrm{e}^{(\epsilon_i-\mu)/k_{\mathrm{B}}T}-1}, \tag{2.121}$$

in the grand-canonical ensemble formalism [157]. If ϵ_0 is set to 0 by convention, then $\mu(T,N)$ has to be negative. In order to avoid the number of particles in the ground state to become infinite when $T \to \infty$, one needs to have μ to also decrease in absolute value. If a critical temperature T_{c} exists such that $\mu(T \to T_{\mathrm{c}}) \to 0_-$, then $\bar{n}_0$ increases, possibly reaching the same order of magnitude as N, while the other occupation numbers $\bar{n}_{i\neq 0}$ are of the order of 1. This is known as *Bose-Einstein condensation*, whose experimental observation by the group of E. Cornell and C. Wieman [160] and independently by the group of W. Ketterle [161], was awarded the Nobel Prize in 2001. Importantly, while the number of bosons in an ideal condensate is $\bar{n}_0 = N$ at $T = 0$, interactions cause quantum fluctuations, thus $\bar{n}_0 < N$ even at $T = 0$ [156, 157, 162].

2.9.2 Gross-Pitaevskii equation

In a dilute gas, three-body (or higher) scattering processes are rare and their contributions are negligible in front of two-body processes. The Hamiltonian of a dilute gas of interacting bosons of mass m, trapped in an external potential[8] $V_{\text{ext}}(\mathbf{r},t)$ reads

$$\begin{aligned}\hat{H} = &\int d\mathbf{r}\left(-\frac{\hbar^2}{2m}\hat{\Psi}^\dagger(\mathbf{r})\nabla^2\hat{\Psi}(\mathbf{r}) + V_{\text{ext}}(\mathbf{r},t)\hat{\Psi}^\dagger(\mathbf{r})\hat{\Psi}(\mathbf{r})\right)\\ &+\frac{1}{2}\int \hat{\Psi}^\dagger(\mathbf{r}',t)\hat{\Psi}^\dagger(\mathbf{r},t)V(\mathbf{r}'-\mathbf{r})\hat{\Psi}(\mathbf{r}',t)\hat{\Psi}(\mathbf{r},t)d\mathbf{r}'d\mathbf{r},\end{aligned} \tag{2.122}$$

where $\hat{\Psi}$ and $\hat{\Psi}^\dagger$ are the bosonic annihilation and creation field operators, respectively. Pair-scattering with small energy in the center-of-mass frame is dominated by s-wave contribution to the wavefunction. It is reasonable to approximate $V(\mathbf{r}-\mathbf{r}')$ by a constant value U, symbolizing the effective scattering energy for all particles [156]. In this case, the physics is reasonably well described by a single parameter, called the s-wave scattering length and denoted by a_s. In the Born approximation, for uniform effective interacting potentials,

[7] Not only the ground state but higher states can be macroscopically occupied [158].

[8] As an example, this external trap may consist of multiple potentials, such as a smooth parabolic trap that keeps the bosons localized in the region of interest, in addition to an optical lattice.

$$V(\mathbf{r}-\mathbf{r}') = U\delta(\mathbf{r}-\mathbf{r}'), \qquad U = \frac{4\pi\hbar^2}{m}a_s. \tag{2.123}$$

Therefore, the Hamiltonian (2.122) becomes

$$\begin{aligned}\hat{H} = &\int d\mathbf{r}\left(-\frac{\hbar^2}{2m}\hat{\Psi}^\dagger(\mathbf{r},t)\nabla^2\hat{\Psi}(\mathbf{r},t) + V_{\text{ext}}(\mathbf{r},t)\hat{\Psi}^\dagger(\mathbf{r},t)\hat{\Psi}(\mathbf{r},t)\right)\\ &+\frac{U}{2}\int \hat{\Psi}^\dagger(\mathbf{r},t)\hat{\Psi}^\dagger(\mathbf{r},t)\hat{\Psi}(\mathbf{r},t)\hat{\Psi}(\mathbf{r},t)d\mathbf{r}.\end{aligned} \tag{2.124}$$

One can rewrite the bosonic field operator as a combination of single-body annihilation operators $\hat{a}_i$ that remove a particle in the state φ_i, i.e.

$$\hat{\Psi}(\mathbf{r},t) = \varphi_0(\mathbf{r},t)\hat{a}_0 + \sum_{i>0}\varphi_i(\mathbf{r},t)\hat{a}_i. \tag{2.125}$$

where we have separated the condensate term $i=0$ from the other components and where the wavefunctions φ_i are one-body wavefunctions related to the one-body density matrix $n^{(1)}(\mathbf{r},\mathbf{r}') = \langle\hat{\Psi}^\dagger(\mathbf{r})\hat{\Psi}(\mathbf{r}')\rangle$ by

$$n^{(1)}(\mathbf{r},\mathbf{r}') = \sum n_i\varphi_i^*(\mathbf{r})\varphi_i(\mathbf{r}'), \tag{2.126}$$

with n_i being the occupation number relative to the single-particle state φ_i. Substituting this expression into the Hamiltonian and neglecting $\hat{a}_i^{(\dagger)}$ contributions yield[9]

$$\hat{H} = \int d\mathbf{r}\left(-\frac{\hbar^2}{2m}\varphi_0^*\nabla^2\varphi_0 + V_{\text{ext}}(\mathbf{r},t)|\varphi_0|^2\right)\hat{a}_0^\dagger\hat{a}_0 + \frac{U}{2}\int d\mathbf{r}|\varphi_0|^4\hat{a}_0^\dagger\hat{a}_0^\dagger\hat{a}_0\hat{a}_0. \tag{2.127}$$

Notice that any term in $\hat{a}_i$ or $\hat{a}_i^\dagger$ is discarded if the ground state is massively populated ($N_0 \gg N - N_0$) thus only the quartic term in $\hat{a}_0$ is kept in (2.127). This assumption of large occupation allows to use the Hartree-Fock approximation, which prescribes to write the many-body wavefunction (for $N = N_0$) as a product of single-body ground state wavefunctions. Then, the many-body ground state and its wavefunction read

$$|\Phi_0\rangle = |\varphi_0\rangle^{\otimes N}, \qquad \Phi_0(\mathbf{r}_1,...,\mathbf{r}_N) = \varphi_0(\mathbf{r}_1)...\varphi_0(\mathbf{r}_N). \tag{2.128}$$

Its corresponding energy is given by[10]

$$\langle\Phi_0|\,\hat{H}\,|\Phi_0\rangle = N\int d\mathbf{r}\left(-\frac{\hbar^2}{2m}\varphi_0^*\nabla^2\varphi_0 + V_{\text{ext}}(\mathbf{r},t)|\varphi_0|^2\right) + \frac{U}{2}N(N-1)\int d\mathbf{r}|\varphi_0|^4. \tag{2.129}$$

[9] The space and time dependence of the fields φ_i ($i \geq 0$) have been omitted for the sake of clarity.

[10] The annihilation operator of an excited state $\hat{a}_i$ (for $i > 0$) applied onto the single-body ground state is zero, i.e. $\hat{a}_i\,|\varphi_0\rangle = 0$.

Notice the $N-1$ factor coming from the commutation relation $[\hat{a}_0, \hat{a}_0^\dagger] = 1$. Since $N \gg 1$, one obtains

$$E_0(t) \equiv \langle \Phi_0 | \hat{H} | \Phi_0 \rangle = N \int d\mathbf{r} \left(-\frac{\hbar^2}{2m} \varphi_0^* \nabla^2 \varphi_0 + V_{\text{ext}}(\mathbf{r}', t') |\varphi_0|^2 \right) + \frac{UN^2}{2} \int d\mathbf{r} |\varphi_0|^4. \tag{2.130}$$

By first absorbing $\sqrt{N}$ into $\Psi_0 = \sqrt{N}\varphi_0$ then minimizing this energy functional[11] with respect to Ψ_0^* with the constraint that all N bosons occupy the single-body ground state, i.e. $\int d\mathbf{r}' |\Psi_0|^2 = N$,

$$\begin{aligned} 0 &= \frac{\delta \left(E_0[\Psi_0, \Psi_0^*] - \mu(\int d\mathbf{r}' |\Psi_0(\mathbf{r}', t)|^2 - N) \right)}{\delta \Psi_0^*(\mathbf{r}, t)} \\ &= -\frac{\hbar^2}{2m} \nabla^2 \Psi_0(\mathbf{r}, t) + V_{\text{ext}}(\mathbf{r}, t) \Psi_0(\mathbf{r}, t) + U |\Psi(\mathbf{r}, t)|^2 \Psi_0 - \mu \Psi_0(\mathbf{r}, t) \\ \iff \quad \mu \Psi_0 &= -\frac{\hbar^2}{2m} \nabla^2 \Psi_0 + V_{\text{ext}} \Psi_0 + U |\Psi_0|^2 \Psi_0, \end{aligned} \tag{2.131}$$

one obtains the time-independent *Gross-Pitaevskii equation* where we omitted the dependence on space and time coordinates. Its solution is the ground state of (2.122) when all quantum fluctuations are neglected. Its associated energy is the chemical potential μ.

2.9.3 Thomas-Fermi limit

For a slowly varying density over space, the gradient of the BEC wavefunction can be neglected, i.e. the kinetic term in the energy functional (2.130) becomes small in front of the other energetic contributions. The GPE then reads

$$V_{\text{ext}}(\mathbf{r}) + Un(\mathbf{r}) = \mu, \tag{2.132}$$

which expresses the condition of local equilibrium. Equivalently, the density reads

$$n(\mathbf{r}) = \frac{1}{U}(\mu - V_{\text{ext}}(\mathbf{r})). \tag{2.133}$$

As an example, if the potential is a harmonic trap, $V_{\text{ext}} = V_0 r^2$, the BEC distribution is a simple inverted parabola.

Importantly, the Thomas-Fermi approximation fails at the boundary of the BEC cloud, where $V_{\text{ext}}(\mathbf{r}) = \mu$. Indeed, the Thomas-Fermi boundary sets a transition between two regions, one occupied by bosons and another without bosons, which undeniably implies the presence of an

[11] Remember $\frac{\delta \Psi_0^*(\mathbf{r}', t')}{\delta \Psi_0^*(\mathbf{r}, t)} = \delta(\mathbf{r} - \mathbf{r}', t' - t)$.

abrupt, nonphysical change in the density at the cloud edge that would lead to a divergence of the kinetic energy at the boundary of the Thomas-Fermi distribution. This is solved by rehabilitating the kinetic term at the first place and by performing an asymptotical analysis at the edge of the Thomas-Fermi cloud [156, 157], which is beyond the scope of this thesis. Therefore, the density profile is no more parabolic at the cloud edge but rather smoothly decreases to zero.

2.9.4 Mean-field and Bogoliubov approximations

The derivation of the GPE (2.131) suggests that the bosonic field operator could have been replaced by the many-body wavefunction Ψ_0 from the start in (2.124). This is the essence of a mean-field approximation, where Ψ_0 plays the role of an order parameter, that is a complex number

$$\Psi_0(\mathbf{r}) = |\Psi_0(\mathbf{r})| \mathrm{e}^{\mathrm{i}S(\mathbf{r})}. \tag{2.134}$$

The modulus represents the contribution of the condensate to the density $n^{(1)}(\mathbf{r})$, while the phase $S(\mathbf{r})$ is responsible for coherence (order at longer range, for $\mathbf{r} \neq \mathbf{r}'$) and superfluidity phenomena [157]. Note that the order parameter is only defined up to a uniform phase factor. This reflects a global $U(1)$ gauge symmetry of the system. Making an explicit choice of the phase corresponds to the breaking of this gauge symmetry.

An improved mean-field approximation, proposed by Bogoliubov, suggests to replace the field operator $\hat{\Psi}$ in (2.124) by its average value in the ground state $\langle \Psi_0 | \hat{\Psi} | \Psi_0 \rangle$ and an additional term that would take into account fluctuations around this average, that is

$$\hat{\Psi}(\mathbf{r}, t) = \Psi_0(\mathbf{r}, t) + \delta\hat{\Psi}(\mathbf{r}, t). \tag{2.135}$$

Regarding equation (2.125), this is equivalent to replacing $\hat{a}_0$ by $\sqrt{N_0}$ and relating the fluctuation term $\delta\hat{\Psi}$ to its non-condensed part, represented by the terms $\sum_{i\neq 0} \varphi_i \hat{a}_i$. Interestingly, in the limit $N_0 \simeq N$, neglecting the term $\delta\hat{\Psi}$ and directly replacing $\hat{\Psi}$ by the order parameter Ψ_0 in (2.124) would also lead to the Gross-Pitaevskii equation (after minimization).

Ground state as a coherent state

Since the population of the ground state largely dominates $N_0 \simeq N \gg 1$, one can make the physical assumption that adding or removing one particle from the BEC negligibly impacts any property of the system. This suggests that the ground state can be interpreted as a coherent state[12], i.e. an eigenstate of the annihilation field operator $\hat{\Psi}$, whose associated eigenvalue is the order parameter of the condensate,

[12] This assumption is equivalent to supposing that $\hat{a}_0$ can be replaced by $\sqrt{N_0}$.

$$\hat{\Psi}\left|\Psi_0\right\rangle = \Psi_0\left|\Psi_0\right\rangle. \tag{2.136}$$

The Gross-Pitaevskii equation can also be derived from the Schrödinger equation of this coherent ground state. Indeed, computing the average energy of $|\Psi_0\rangle$ with the Hamiltonian (2.124) would lead (after minimization) to the time-dependent Gross-Pitaevskii equation

$$i\hbar\frac{\partial}{\partial t}\Psi_0 = -\frac{\hbar^2}{2m}\nabla^2\Psi_0 + V_{\text{ext}}\Psi_0 + U|\Psi_0|^2\Psi_0. \tag{2.137}$$

Besides, since $|\Psi_0\rangle$ is expected to be the ground state which is stationary, its time-evolution is governed by a simple phase

$$\left|\Psi_0\right\rangle(t) = e^{-i\alpha t}\left|\Psi_0\right\rangle, \tag{2.138}$$

where α needs to be determined. From the Schrödinger equation of $|\Psi_0\rangle$ on which is applied $\langle\Psi_0|$, we deduce

$$\begin{aligned} & i\hbar\left\langle\Psi_0\right|\frac{\partial}{\partial t}\left|\Psi_0\right\rangle = \left\langle\Psi_0\right|\hat{H}\left|\Psi_0\right\rangle \\ \iff \quad & \alpha N = \int d\mathbf{r}\left[-\frac{\hbar^2}{2m}\Psi_0^*\nabla^2\Psi_0 + V_{\text{ext}}|\Psi_0|^2 + \frac{U}{2}|\Psi_0|^4\right] = E_{\text{MF}}, \end{aligned} \tag{2.139}$$

where we use the normalization condition $\int d\mathbf{r}|\Psi_0|^2 = N$ and exploit the fact that the energy functional in the mean-field approximation is given by $E_{\text{MF}} = \langle\Psi_0|\hat{H}|\Psi_0\rangle$. As a last step,we derive both sides with respect to N, remembering the definition of the chemical potential in the mean-field limit,

$$\alpha = \frac{\partial E_{\text{MF}}}{\partial N} = \mu. \tag{2.140}$$

Therefore, the time-dependence of the stationary state $|\Psi_0\rangle$ is given by $e^{-i\mu t/\hbar}$. Plugging this into the Schrödinger equation yields the GPE (2.131).

2.10 Bosonic atoms in lattices

In this section, we first briefly present the underlying mechanism of trapping atoms with interfering lasers that form periodic potentials viewed as *crystals of light*, called *optical lattices*. Then, by assuming that the optical lattice wells are sufficiently deep, taking the tight-binding approximation of the Hamiltonian (2.122) will lead us to the Bose-Hubbard model.

2.10.1 Ultracold atoms in optical lattices

Optical lattices are created by counter-propagating laser beams carrying electric fields of the form [163]

$$\mathbf{E}(\mathbf{r},t) = \mathbf{E}_0(\mathbf{r})\, \mathrm{e}^{-\mathrm{i}\omega_\mathrm{L} t} + \text{ c.c}, \tag{2.141}$$

where ω_L is the laser frequency. This electric field acting on an atom induces a time-dependent dipole moment $\mathbf{d}(\mathbf{r},t)$ for the atom that reads

$$\mathbf{d}(\mathbf{r},t) = \mathbf{d}_0(\mathbf{r})\, \mathrm{e}^{-\mathrm{i}\omega_\mathrm{L} t} + \text{ c.c}, \tag{2.142}$$

where

$$\mathbf{d}_0(\mathbf{r}) = \bar{\bar{\alpha}}(\omega_\mathrm{L})\, \mathbf{E}_0(\mathbf{r}), \tag{2.143}$$

with $\bar{\bar{\alpha}}(\omega_\mathrm{L})$ being the the polarizability tensor that characterizes the response of the atom to the applied electric field. The Hamiltonian of a single atom of mass m subjected to the electric field $\mathbf{E}_+(\mathbf{r},t)$ is given by

$$\hat{H} = \frac{\hat{\mathbf{p}}^2}{2m} + \sum_{j=1}^{N_I} \hbar\omega_j \left|e_j\right\rangle \left\langle e_j\right| - \mathbf{d}\cdot\mathbf{E}, \tag{2.144}$$

where $\left|e_j\right\rangle$ is the j^{th} out of the N_I internal atomic states and has a corresponding energy $\hbar\omega_j$. When the atom occupies a single internal state $|e_0\rangle$ and the laser is far-detuned from any atomic transition, the effect of the laser can be treated as a perturbation in second order of the electric field. Supposing that ω_L is much closer to the transition of energy $\hbar\omega_1$ (between the ground state $|e_0\rangle$ and the excited state $|e_1\rangle$), *i.e.* $\Delta\omega = \omega_\mathrm{L} - \omega_1 \ll \omega_\mathrm{L} - \omega_j$ ($j \neq 1$), the atom can be thought of as a two-level system since excitations to other states are much less probable. The perturbative energy shift of the internal state $|e_0\rangle$, known as the *AC Stark shift*, is quadratic in the electric field amplitude [163]. Moreover, under these assumptions, $\bar{\bar{\alpha}}$ only depends on $\Delta\omega$ [34,156,163]. As a result, the energy shift caused by the atom-light interaction therefore reads

$$V_\text{opt}(\mathbf{r}) \propto -\frac{\overline{E^2(\mathbf{r},t)}}{\Delta\omega}. \tag{2.145}$$

where the overline indicates a time average of the laser intensity $I(\mathbf{r}) = \overline{E^2(\mathbf{r},t)}$. The time averaging is valid since the typical frequency of the atomic motion is much slower than the frequency (ω) of the electric field of the laser [157]. As a result from the space dependence of the radiating field, the energy landscape around the atom creates more or less energetically favorable regions for the atom to localize. One can define a force as the gradient of the energy shift and the sign of the detuning determines if the atom is localized in the maxima or minima of the intensity. Employing a pair of counter-propagating lasers, with the same frequency,

that interfere will create standing waves and spatially periodic potential for the atom of the form

$$V(x) = V_0 \sin^2\left(\frac{2\pi}{\lambda}x\right), \tag{2.146}$$

where λ is the wavelength of the lasers and V_0 is the depth of the optical lattice, that is proportional to the laser intensity. By using multiple pairs of lasers pointing at different angles, one can build various lattice geometries in different dimensions [34]. A relevant example for the present work is the 2D honeycomb lattice, which is created by interfering three pairs of lasers at 120° [74].

2.10.2 Hubbard model for ultracold atoms

The Hubbard model describes the physics of interacting fermionic particles in lattices and has been envisioned as a promising candidate to investigate the quantum phase diagram of high-temperature superconductors [164]. Subsequent implementations have been achieved with ultracold fermionic atoms in optical lattices [39, 165–170]. On the other hand, its bosonic counterpart instead led to the prediction [31, 171] and the observation of the superfluid to Mott-insulator phase transition [40]. Recent theoretical and experimental advances for generating artificial gauge fields and synthetic spin-orbit coupling have further expanded the scope of the Hubbard model. These advancements have opened new avenues for exploring exotic quantum phases such as topological insulators [42–44, 46], (fractional) quantum Hall phases [45, 46], quantum magnetism [50, 51], and (non-Abelian) gauge field theories on lattices (LGT) [52–54, 56].

Here, the Bose-Hubbard model is derived from the Hamiltonian (2.124). The external potential consists of the optical lattice and a harmonic trap, $V_{\text{ext}} = V_{\text{opt}} + V_{\text{harm}}$. For a sufficiently deep optical lattice, *i.e.* $V_0 > 2E_{\text{R}}$ where $E_R = \hbar^2 k^2/2m$ is the recoil energy[13], and supposing that the system is confined to the lowest Bloch band, so-called s-band, the tight-binding approximation can be invoked. Then, the bosonic field operator can be expressed in terms of annihilation operators of bosons $\hat{b}_i$ at the i^{th} lattice site $\mathbf{r}_i$, weighted by Wannier[14] functions of the lowest band localized around this same site [34], *i.e.*

$$\hat{\Psi}(\mathbf{r}) = \sum_i \hat{b}_i w(\mathbf{r} - \mathbf{r}_i). \tag{2.147}$$

By plugging this expression into (2.124) and defining the parameters

[13] The recoil energy is the kinetic energy imparted to an atom at rest when it absorbs a photon of momentum $\hbar k$ [156].

[14] The Wannier functions form an orthonormal basis of wavefunctions $w(\mathbf{r}-\mathbf{r}_i)$ of a single atomic state localized around the lattice site $\mathbf{r}_i$. Note that for the Wannier expansion to be relevant, the external parabolic trap has to be smooth to preserve a quasi-periodicity and to enable the use of the same expression for the Wannier function $w(\mathbf{r} - \mathbf{r}_i)$ at all sites.

$$\tilde{J}_{ij} = -\int d\mathbf{r}\, w^*(\mathbf{r}-\mathbf{r}_i)\left[-\frac{\hbar^2}{2m}\nabla^2 + V_{\text{opt}}(\mathbf{r}) + V_{\text{harm}}(\mathbf{r})\right] w(\mathbf{r}-\mathbf{r}_j), \tag{2.148}$$

and

$$\tilde{U}_{ijkl} = U\int d\mathbf{r}\, w^*(\mathbf{r}-\mathbf{r}_i)w^*(\mathbf{r}-\mathbf{r}_j)w(\mathbf{r}-\mathbf{r}_k)w(\mathbf{r}-\mathbf{r}_l), \tag{2.149}$$

one obtains the *Bose-Hubbard model*,

$$\hat{H}_{\text{BH}} = -\sum_{i,j}\tilde{J}_{ij}\left(\hat{b}_i^\dagger\hat{b}_j + \text{H.c.}\right) + \frac{1}{2}\sum_{ijkl}\tilde{U}_{ijkl}\hat{b}_i^\dagger\hat{b}_j^\dagger\hat{b}_k\hat{b}_l, \tag{2.150}$$

The integrals involving Wannier functions localized at different sites are usually small [172]. Consequently, only the terms whose indices satisfy $|i-j| < 2$ are kept in the first sum and the parameter $\tilde{U}_{ijkl}$ is approximated by the onsite interaction $\tilde{U}$. By splitting the terms $i = j$ from the rest ($|i-j| \geq 1$), the Bose-Hubbard Hamiltonian becomes

$$\hat{H}_{\text{BH}} = -\sum_{\langle i,j\rangle}J_{ij}\left(\hat{b}_i^\dagger\hat{b}_j + \text{H.c.}\right) + \sum_i V_i\hat{n}_i + \frac{\tilde{U}}{2}\sum_i\hat{n}_i(\hat{n}_i-1), \tag{2.151}$$

where the parameter J_{ij} is the tunneling amplitude between two sites i and j, $\tilde{U} > 0$ is the on-site interaction energy and $V_i = V_0 i^2/2$ is an onsite energy resulting from the parabolic trap. The number operator on site i is denoted by $\hat{n}_i = \hat{b}_i^\dagger\hat{b}_i$. The notation $\langle i,j\rangle$ restricts the sum to nearest-neighboring sites. A term $-\mu\sum_i\hat{n}_i$ is usually added to (2.151) in order to control the average number of particles and thus determines the filling factor.

To compute the BEC distribution over the lattice, one needs to solve the discretized stationary Gross-Pitaevskii equation, obtained by replacing the operators $\hat{b}_i$ by the order parameter Ψ_i [34] at every site in (2.151) and minimizing the resulting energy functional with respect to Ψ_i^*. This assumes that each site hosts a BEC whose wavefunction is localized on the i^{th} site and takes the form of a coherent state, *i.e.* $\hat{b}_i|\varphi_i\rangle = \Psi_i|\varphi_i\rangle$. As explained in the previous section, it requires that the number of weakly-interacting bosons at each site is large, i.e. $N_i \gg 1$. Also, we impose that all global phases of Ψ_i are the same, enforcing a phase coherence over the whole system. For example, the stationary GPE at $T = 0$ for a 1D lattice reads

$$-J(\Psi_{i-1}+\Psi_{i+1}) + (V_i + \tilde{U}|\Psi_i|^2)\Psi_i = \mu\Psi_i, \tag{2.152}$$

where we assume that the tunneling amplitude is not site-dependent, which occurs when the external trapping is weak. Equation (2.152) can be solved with the imaginary-time evolution method [173], detailed in appendix B.3.

Chapter 3

Quantized valley Hall response from local bulk density variations

The following chapter is based on the original results presented in our published article [75]. We envisage an alternative method to those presented in section 2.7 for probing the quantum valley Hall effect (QVHE). It relies on locally testing the equilibrium particle density variations upon modifying the strength of strain. In section 3.1.1, we show this by adapting the Widom-Středa formula, which originally relates the electrical Hall conductivity to the response of a bulk density upon a change of an external magnetic field – see section 2.1.3. In the framework of strained lattices, pseudo-magnetic field perturbations, related to modifications of the strain intensity, result in density responses, directly reflecting the underlying valley Hall effect. Importantly, this approach suggests that the quantized valley Hall response can be cleanly extracted from a direct measurement within the system's bulk, in sharp contrast with more standard indirect methods relying on non-local transport or edge measurements. The quantization of the valley Hall response is analytically proved in section 3.1.2. In section 3.2, we numerically test our predictions for two geometries and strain configurations: a more idealized system with cylindrical boundary conditions along the y-axis and uniaxial strain along x in section 3.2.1, and a more realistic system with full open-boundary conditions and trigonal strain in section 3.2.2. Remarkably, it predicts that a quantized valley Hall response is expected regardless of the edge terminations of the sample and does not require any valley-resolution. Furthermore, as shown in section 3.3, this probing method displays an appreciable robustness against different types of disorder and lattice imperfections. Note that this approach relies on the low-energy Dirac model introduced in section 2.5.1, hence, it is valid for small strain intensities $\tau \ll 1$. This chapter ends with the conclusions and outlooks with an emphasis on synthetic platforms envisaged for testing our probing scheme.

3.1 Valley Hall response as a density response function

In this section, the Widom-Středa formula is adapted for the valley Hall conductivity in insulators. An extended proof of its quantization – when the chemical potential lies in a gap – is provided.

3.1.1 Adapting the Widom-Středa formula to the valley Hall effect

As introduced in section 2.1.3, the Widom-Středa formula relates the Hall conductivity of a two-dimensional fermionic gas to the response of its bulk-density to the variation of an external magnetic field. While the Hall conductivity remains strictly zero when time-reversal symmetry is preserved, this formula can be adapted to probe the valley Hall effect, occurring for example in a strained honeycomb lattice, when the modification of strain – equivalently of the pseudo-magnetic field – implies a response from the density in the insulating bulk. Indeed, at half-filling, the valley Hall response is defined as the difference between the contributions to the Hall conductivity at the valleys $\mathbf{K}$ and $\mathbf{K}'$, σ_{H}^{K} and $\sigma_{\mathrm{H}}^{K'}$ respectively, i.e.

$$\sigma_{\mathrm{V}} = \sigma_{\mathrm{H}}^{K} - \sigma_{\mathrm{H}}^{K'}. \tag{3.1}$$

As long as the inter-valley scattering remains negligible[1], the Hall conductivity at each valley can be separately calculated as

$$\sigma_{\mathrm{H}}^{K} \simeq e \left(\frac{\partial n_{\mathrm{bulk}}^{K}}{\partial B_{\tau}^{K}} \right) \Bigg|_{\mu_{\mathrm{F}}}, \qquad \sigma_{\mathrm{H}}^{K'} \simeq e \left(\frac{\partial n_{\mathrm{bulk}}^{K'}}{\partial B_{\tau}^{K'}} \right) \Bigg|_{\mu_{\mathrm{F}}}, \tag{3.2}$$

when the chemical potential μ_{F} lies in a spectral gap, where n^{ζ} stands for the contribution of the K ($\zeta = +1$) or the K' ($\zeta = -1$) valley to the density. From time-reversal symmetry – as explained in section 2.5.2 – we recall that $B_{\tau}^{K'} = -B_{\tau}^{K}$, such that the valley Hall response can be directly obtained in terms of the variation of the total bulk density $n_{\mathrm{bulk}} = n_{\mathrm{bulk}}^{K} + n_{\mathrm{bulk}}^{K'}$ upon strain perturbations. Indeed,

$$\begin{aligned} \sigma_{\mathrm{V}} &\simeq e \left(\frac{\partial n_{\mathrm{bulk}}^{K}}{\partial B_{\tau}^{K}} - \frac{\partial n_{\mathrm{bulk}}^{K'}}{\partial B_{\tau}^{K'}} \right) \Bigg|_{\mu_{\mathrm{F}}} \\ &= e \frac{\partial n_{\mathrm{bulk}}}{\partial B_{\tau}^{K}} \Bigg|_{\mu_{\mathrm{F}}}, \end{aligned} \tag{3.3}$$

eliminating the need for valley resolution.

[1] The inter-valley scattering might strongly alter the Landau level picture and prevent the separation in momentum of the two nonequivalent valleys.

3.1.2 Quantized valley Hall response in strained honeycomb lattice

This section proves that the valley Hall response is quantized when the chemical potential lies in a spectral gap and the Dirac model

$$h^{\zeta}(\mathbf{q}, \mathbf{A}_{\tau}^{\zeta}) = v_{\mathrm{F}} \left[\hbar q_x \sigma_y - \zeta(\hbar q_y + e A_y^{\zeta})\sigma_x\right], \tag{3.4}$$

describes the low-energy physics of a uniaxially strained honeycomb lattice near half-filling. This occurs for small strain intensities $\tau \ll 1$, for which the continuum limit and the small inter-valley scattering limit are both reached. Indeed, high strain intensities would deform and create scattering channels between pseudo-Landau levels from different valleys, invalidating the description (3.4).

Focusing separately on the valley $\zeta = \pm 1$, the Brillouin zone is split into two parts: around $\mathbf{K}'$, $k_y \in [-\pi/\sqrt{3}a, 0]$, and around $\mathbf{K}$, $k_y \in [0, \pi/\sqrt{3}a]$. The contribution of each valley to the bulk particle density is given by

$$n^{\zeta}(x) = \sum_{p=0}^{\zeta M/2} \sum_{\varepsilon} \theta(\mu_{\mathrm{F}} - \varepsilon) \, |\Psi_{\varepsilon}^{k_y}(x)|^2, \tag{3.5}$$

where θ is the Heaviside function, M is the number of values of k_y in the first Brillouin zone, $k_y = 2\pi p/L_y$, $p \in \{0, ..., \zeta M/2\}$ and $L_y = \sqrt{3}Ma$ is the length of the lattice in the y-direction. Here $\Psi_{\varepsilon}^{k_y}(x)$ is a two-component spinor describing an eigenstate of energy ε and quasimomentum k_y. Each of its components accounts for the weight of the corresponding state on the A and B sublattices, respectively. In the thermodynamic limit,

$$\frac{2\pi}{L_y} \sum_{p=0}^{\zeta M/2} \xrightarrow{M\to\infty} \zeta \int_0^{\zeta\pi/\sqrt{3}a} dk_y, \tag{3.6}$$

and hence

$$n^{\zeta}(x) = \frac{\zeta L_y}{2\pi} \int_0^{\zeta\pi/\sqrt{3}a} dk_y \sum_{\varepsilon} \theta(\mu_{\mathrm{F}} - \varepsilon) \, |\Psi_{\varepsilon}^{k_y}(x)|^2. \tag{3.7}$$

For $\mu_{\mathrm{F}} > 0$, $n^{\zeta}(x) = n_{-}^{\zeta}(x) + n_{+}^{\zeta}(x) + n_0^{\zeta}(x)$, where $n_{+}^{\zeta}(x)$ ($n_{-}^{\zeta}(x)$) is the density of particles in the states with $\varepsilon > 0$ ($\varepsilon < 0$) and $n_0^{\zeta}(x)$ is the density of particles in the state with zero energy. Note that this can be rewritten as $n^{\zeta}(x) = n_{\mathrm{hf}}^{\zeta}(x) + n_{+}^{\zeta}(x) + n_0^{\zeta}(x)/2$, where $n_{\mathrm{hf}}^{\zeta}(x)$ is the density of a half-filled system. As explained in section 2.3.3, the chiral symmetry imposes that if the system is exactly half-filled, the particle density at each cell $n_{\mathrm{hf}}(\mathbf{r}) = 1$, meaning that the density variations with respect to strain are exactly zero, thus the Hall conductivity is strictly zero,

$$\frac{\partial n^{\zeta}_{\rm hf}}{\partial B^{\zeta}_{\tau}} = 0. \tag{3.8}$$

The Hall conductivity at each valley can then be obtained as

$$\sigma^{\zeta}_{\rm H} = e\frac{\partial n^{\zeta}}{\partial B^{\zeta}_{\tau}}\bigg|_{\mu_{\rm F}>0} = e\frac{\partial}{\partial B^{\zeta}_{\tau}}\left(n^{\zeta}_{+}(x) + \frac{n^{\zeta}_{0}(x)}{2}\right)\bigg|_{\mu_{\rm F}>0}. \tag{3.9}$$

Close to each Dirac point $\zeta\mathbf{K}$ (i.e. $|q_y|a \ll 1$) and in the continuum limit $\ell_B \gg a$ (i.e. $\tau \ll 1$), the spinors in Eq. (3.7) can be approximated with the eigenstates of the Dirac Hamiltonian (2.65), which, in the case of $\tau > 0$, are given by

$$\Psi^{q_y}_{\nu}(x) = \frac{1}{\sqrt{L_y\ell_B}}\frac{\mathrm{e}^{\mathrm{i}q_y y}}{\sqrt{2-\delta_{\nu 0}}}\begin{pmatrix}\phi_{|\nu|}(X)\\ \mathrm{sign}(\nu)\phi_{|\nu|-1}(X)\end{pmatrix}, \tag{3.10}$$

where $\phi_{\nu}(X) = 1/(\sqrt{\pi}2^{\nu}\nu!)^{-1/2}\mathrm{e}^{-X^2/2}H_{\nu}(X)$ is the normalized harmonic oscillator wavefunction, $\ell_B^2 = \hbar/e|B^{\zeta}_{\tau}|$ and $X \equiv (x-x_{\rm c})/\ell_B - \zeta q_y\ell_B$. The index ν labels the discrete set of energies of the relativistic pseudo-Landau levels. In order to perform the derivative in Eq. (3.9), one can explicitly compute

$$\begin{aligned} n^{\zeta}_{+}(x) + \frac{n^{\zeta}_{0}(x)}{2} =& \frac{\zeta}{4\pi\ell_B}\sum_{\nu=1}^{\nu_{\rm max}}\int_{-\zeta\infty}^{\zeta\infty} dq_y\,\left[|\phi_{\nu}(X)|^2 + |\phi_{\nu-1}(X)|^2\right] \\ &+ \frac{\zeta}{4\pi\ell_B}\int_{-\zeta\infty}^{\zeta\infty} dq_y|\phi_0(X)|^2, \end{aligned} \tag{3.11}$$

where $\mu_{\rm F}$ lies between the levels $\nu_{\rm max}$ and $\nu_{\rm max}+1$. The index[2] $\nu_{\rm max}$ therefore indicates the last filled pseudo-Landau level. Note that the limits of the bounded integral in Eq. (3.7) are extended to $\pm\zeta\infty$ in the above equation. Since the eigenstates in Eq. (3.10) decay exponentially with q_y, this remains a fairly good approximation. By simply using the normalization of the wavefunctions, the integral in Eq. (3.11) can be readily performed to find that

$$n^{\zeta}_{+}(x) + \frac{n^{\zeta}_{0}(x)}{2} \simeq \frac{1}{4\pi\ell_B^2}(2\nu_{\rm max}+1) = \frac{e|B^{\zeta}_{\tau}|}{2\pi\hbar}\left(\nu_{\rm max}+\frac{1}{2}\right). \tag{3.12}$$

Notice that

[2] In the case of strained finite lattices, the largest value that $\nu_{\rm max}$ can take is set by the validity of the approximation of the eigenstates (close to the Dirac point) of the strained system by those of the Hamiltonian (3.4). The eigenstates of higher pseudo-Landau levels are more delocalized and undergo boundary effects, hence preventing $\nu_{\rm max}$ to be arbitrarily large.

$$B_\tau^\zeta = \text{sign}\left(B_\tau^\zeta\right)|B_\tau^\zeta| = \text{sign}\left(\frac{B_\tau^\zeta}{\zeta}\right)\zeta|B_\tau^\zeta|, \tag{3.13}$$

where we do not simplify ζ on purpose because the one at the numerator provides the '-' (at $\mathbf{K}'$) while the one at the denominator cancels the ζ inside of B_τ^ζ. For example, in the uniaxial and trigonal strain cases, $\text{sign}(B_\tau^\zeta/\zeta) = \text{sign}(-\tau)$ and $\text{sign}(\tau)$, respectively – see (2.90) and (2.99). Eventually, the Hall conductivity at each valley reads

$$\sigma_{\text{H}}^\zeta = e\frac{\partial n^\zeta}{\partial B_\tau^\zeta}\bigg|_{\mu_F} \simeq \text{sign}\left(\frac{B_\tau^\zeta}{\zeta}\right)\zeta\left(\nu_{\text{max}} + \frac{1}{2}\right)\sigma_0, \tag{3.14}$$

where $\sigma_0 = e^2/h$. The derivation of σ_{H}^ζ is similar for $\mu_{\text{F}} < 0$, where the values of ν_{max} will be taken negative. Therefore, the valley Hall response is quantized, as

$$\sigma_{\text{V}} \simeq e\frac{\partial n_{\text{bulk}}}{\partial B_\tau^\zeta}\bigg|_{\mu_F} \simeq \text{sign}\left(\frac{B_\tau^\zeta}{\zeta}\right)(2\nu+1)\sigma_0. \tag{3.15}$$

Remarkably, from Eq. (3.11), it is clear that each sublattice contributes with a quantized result. Indeed, the summation runs over A and B sites and can be separated into two sums. The sum over A sites contains the terms $|\phi_\nu(X)|^2$ and $|\phi_0(X)|^2$, while the sum over the B sites only contains the terms $|\phi_{\nu-1}(X)|^2$. Performing the integrals separately and using the wavefunction normalization, one gets

$$\begin{aligned} n_{\text{A}}^\zeta(x) &= \frac{e|B_\tau^\zeta|}{2\pi\hbar}\left(\frac{\nu_{\text{max}}}{2} + \frac{1}{2}\right), \\ n_{\text{B}}^\zeta(x) &= \frac{e|B_\tau^\zeta|}{2\pi\hbar}\frac{\nu_{\text{max}}}{2}. \end{aligned} \tag{3.16}$$

So,

$$\begin{aligned} e\frac{\partial n_{\text{A}}^\zeta}{\partial B_\tau^\zeta}\bigg|_{\mu_F} &= \text{sign}\left(\frac{B_\tau^\zeta}{\zeta}\right)\zeta\left(\frac{\nu_{\text{max}}}{2} + \frac{1}{2}\right)\sigma_0, \\ e\frac{\partial n_{\text{B}}^\zeta}{\partial B_\tau^\zeta}\bigg|_{\mu_F} &= \text{sign}\left(\frac{B_\tau^\zeta}{\zeta}\right)\zeta\frac{\nu_{\text{max}}}{2}\sigma_0, \end{aligned} \tag{3.17}$$

which means that

$$\sigma_V = e\frac{\partial n_{\text{bulk}}}{\partial B_\tau^K}\bigg|_{\mu_F} = \sigma_V^{\text{A}} + \sigma_V^{\text{B}}, \tag{3.18}$$

where $\sigma_V^{\mathrm{A}} = \mathrm{sign}(B_\tau^\zeta/\zeta)(\nu_{\max}+1)\sigma_0$ and $\sigma_V^{\mathrm{B}} = \mathrm{sign}(B_\tau^\zeta/\zeta)\nu_{\max}\sigma_0$.

3.2 Local probe for the valley Hall response

In the following, two types of boundary conditions are studied to test our analytical predictions (3.15): *i*) open along x and periodic along y and *ii*) fully open. The former is employed as a more ideal case, where the finite size and boundary effects are negligible (to some extent), contrarily to the latter case, which is more realistic. Intriguingly, as further explained, the local density response $\mathfrak{S}(\mathbf{r})$ is quantized regardless of whether the first pLLs gap support helical edge states or not.

3.2.1 Uniaxial strain in a cylindrical honeycomb lattice

The first scenario envisaged to test the predictions of (3.15) takes place in a ribbon of a honeycomb lattice with cylindrical boundary conditions: periodic along the y direction and open along x. The Hamiltonian reads

$$\hat{H} = -\sum_{\mathbf{r},j} t\left(1+\tau\frac{x-x_{\mathrm{c}}}{3a^2}|\hat{\mathbf{x}}\cdot\boldsymbol{\delta}_j|\right)\hat{a}_{\mathbf{r}}^\dagger\hat{b}_{\mathbf{r}+\boldsymbol{\delta}_j} + \mathrm{H.c.}, \tag{3.19}$$

and can be block-diagonalized thanks to a Fourier transform along y since k_y is a good quantum number, as explained in section 2.5.3. The ribbon used in this part has zigzag terminations at both edges, with $N_x = 301$ and $N_y = 2$. Its spectrum appears in Figure 3.1. As a reminder, the corresponding pseudo-magnetic field reads

$$\mathbf{B}_\tau^\zeta = -\zeta\frac{\hbar\tau}{9ea^2}\hat{\mathbf{z}}. \tag{3.20}$$

Computing the particle density per unit cell

The first required ingredient to obtain the valley Hall marker is the local particle density $\tilde{n}(x)$. After choosing the strain intensity $\tau = 70.84\cdot10^{-4}$ and fixing two chemical potentials $\mu_1 = 0.02t$ and $\mu_2 = 0.068t$ in the first and second spectrum gaps, respectively – represented by dotted blue and green line in Figure 3.1 – $\tilde{n}(x)$ is numerically calculated from the sum of all the occupied states in the Fermi sea ($\varepsilon \leq \mu_{\mathrm{F}}$), for all values of k_y and for both sublattices ($\alpha =$A, B),

$$\tilde{n}(x) = A_{\mathrm{c}}\sum_{k_y}\sum_{\varepsilon(k_y)\leq\mu_{\mathrm{F}}}\sum_{\alpha=\mathrm{A,B}}|\psi^\alpha_{\varepsilon(k_y)}(x)|^2, \tag{3.21}$$

where the area of a unit cell of the honeycomb lattice, denoted A_{c}, is used to obtain a dimen-

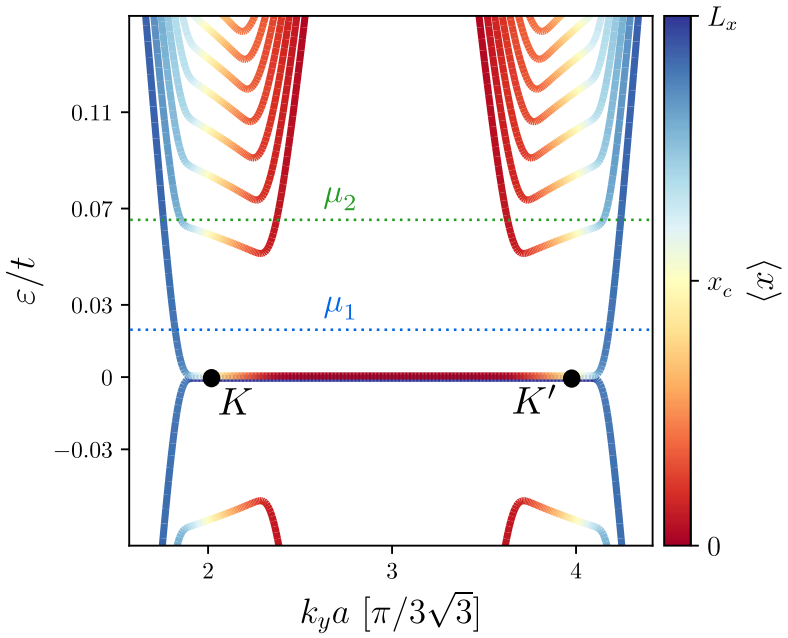

Figure 3.1: Energies ε of the Hamiltonian (3.19) in units of hopping parameter t for $\tau = 7.84 \times 10^{-4}$, $N_x = 301$ cells along the x-direction and zigzag terminations. The color scale indicates the mean position $\langle x \rangle$ of each state. The Fermi levels in the first and second gaps are indicated by the dotted blue and green line at $\mu_1 = 0.02t$ and $\mu_2 = 0.068t$, respectively.

sionless density per cell. The density distributions[3] are shown in Figure 3.2, colored according to their chemical potentials in Figure 3.1. These densities are compared with the ones of a honeycomb lattice in the presence of a homogeneous magnetic field of strength $B = B_\tau$, represented by dashed blue and green lines for the same chemical potentials μ_1 and μ_2. Interestingly, the difference between both models tends to zero at the center of the ribbon ($x = x_c$), hinting that the uniform magnetic field picture is accurate at the center of the sample. One also notices Friedel oscillations near the boundaries, that act as a scattering source, until the density peaks due to the edge states contribution.

While the density is uniform over a region of over 200 sites for the case of a homogeneous magnetic field, the presence of strain makes the particle density dependent on space, even deep in the bulk. Indeed, the space dependence of the hopping amplitudes actually reflects an increase of kinetic energy from the left to the right, where particles tend to localize or delocalize, respectively. Moreover, the imbalance in the particles distribution is a clear signature of the inversion symmetry breaking by strain. Besides, near x_c, the densities display deviations that are linear in space. Since these deviations are symmetric with respect to x_c, it is relevant to define a region around x_c over which the density is averaged, such that this average would be equal to $\tilde{n}_{\text{bulk}} \equiv \tilde{n}(x_c)$:

[3] As explained in section 2.3.3, the chiral symmetry imposes that $\tilde{n}(x)$ equals 1 at half-filling (1/2 on each single site) everywhere in the ribbon, hence $\tilde{n}(x)$ is plotted with respect to this reference value.

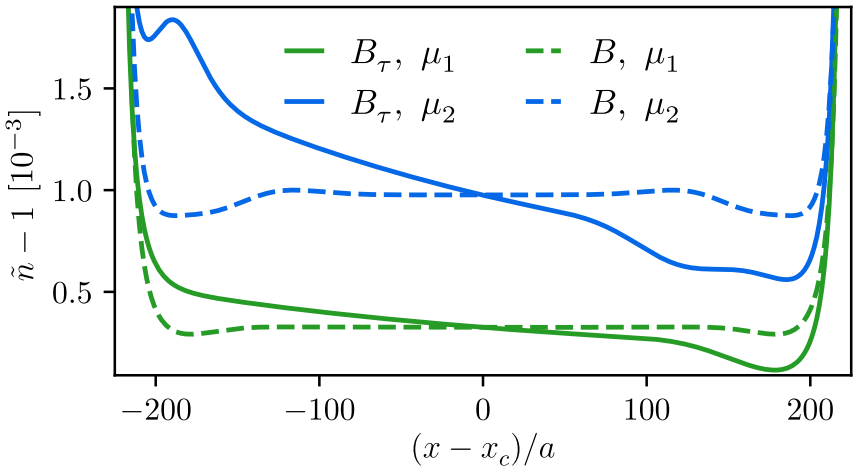

Figure 3.2: Particle density per cell for the same parameters as in Figure 3.1 for a strained sample (solid line) and for a lattice with a homogeneous external magnetic field $B = B_\tau^K$ (dashed line). Green and blue colors correspond to Fermi levels $\mu_1 = 0.02t$ (first gap) and $\mu_2 = 0.068t$ (second gap), respectively. Note that only the deviations of the dimensionless density of particles $\tilde{n}$ from unity are plotted, which are of the order of 10^{-3}.

$$\tilde{n}_{\text{bulk}} = \frac{1}{N_{\text{bulk}}} \sum_{x \in \text{bulk}} \tilde{n}(x), \tag{3.22}$$

where the bulk region, of width L_{bulk}, corresponds to $x \in [x_{\text{c}} - r_{\text{bulk}}, x_{\text{c}} + r_{\text{bulk}}]$, $r_{\text{bulk}} = L_{\text{bulk}}/2$ and N_{bulk} is the number of cells considered in the sum. As long as the bulk radius r_{bulk} is small compared to the system's size L_x, the linearity in space is ensured, thus $\tilde{n}_{\text{bulk}}$ should remain fairly close to the particle density in the presence of the real magnetic field, implying that the Středa formulation of the valley Hall conductivity (3.3) holds.

Computing the density of states in the bulk

As already mentioned in sections 2.1.3 and 3.1.1 when introducing and adapting the Widom-Středa formula, the valley Hall quantization is the property of an insulating bulk. As such, one needs to identify whether the Fermi energy lies in a spectrum gap or not. However, as the system has a finite size with propagating edge states, there are no true spectral gaps – except in some occasions[4]. Nevertheless, for sufficiently large systems ($L_x \gg L_{\text{bulk}}$), the bulk density should not be strongly affected by the edge modes, and therefore the Středa formulation should remain reasonably accurate. In order to determine the energy regions where the Widom-Středa formula can be applied for the strained honeycomb lattice, one can study the spectral properties of the system.

A first step in this direction consists in analyzing the density of states (DoS) of the sample,

[4] As explained in section 2.6, for a positive strain $\tau > 0$ with bearded (left) and zigzag (right) terminations, the first Landau gap has no propagating edge states but higher pLLs do.

calculated from the retarded Green's function $\hat{G}^{\mathrm{r}}(\varepsilon) = \lim_{\eta\to 0}(\varepsilon + \mathrm{i}\eta - \hat{H})^{-1}$ as

$$\begin{aligned}\rho(\varepsilon) &= -\frac{1}{\pi}\mathrm{Im}\left(\mathrm{Tr}\left[\hat{G}^{\mathrm{r}}(\varepsilon)\right]\right) \\ &= -\frac{1}{\pi}\lim_{\eta\to 0}\mathrm{Im}\sum_{\varepsilon_n}\langle\varepsilon_n|(\varepsilon+\mathrm{i}\eta-\hat{H})^{-1}|\varepsilon_n\rangle \\ &= \lim_{\eta\to 0}\frac{\eta}{\pi}\sum_{\varepsilon_n}\frac{1}{\eta^2+(\varepsilon_n-\varepsilon)^2}.\end{aligned} \tag{3.23}$$

The DoS is plotted in Figure 3.3**a** as a function of energy and α_τ where

$$\alpha_\tau = \frac{B_\tau A_{\mathrm{c}}}{\phi_0}, \tag{3.24}$$

is the magnetic flux per unit cell. For reference purposes, Figure 3.3**b** shows the DoS for $\alpha_\tau = 3.255\times10^{-4}$ ($\tau = 70.84\times10^{-4}$) – indicated by the vertical black dashed line in **a** – used to produce the Figure 3.1. In panel **a**, around the analytical energy of pLLs $\nu = 0,\ 1,\ 2$ (indicated by black solid lines) at the Dirac points ($q_y = 0$), one clearly identifies a continuum of states representing the pLLs for $|\nu| \geq 1$, caused by their finite drift velocity. Moreover, one discerns a set of discrete modes, stemming from the edge states of the system. As α_τ increases, their energies decreases until they merge with the lower continuum bulk states. Their spectral flow reflects the remoteness of their wavefunctions from the hard wall potential, due to both the translation of the wavefunctions towards the center and their localization in a tighter area. This can be easily understood from their (approximate) analytical expression,

$$\psi_\nu \propto \mathrm{e}^{-(x-x_{\mathrm{c}}+\zeta q_y \ell_B^2)^2/2\ell_B^2}, \tag{3.25}$$

where the magnetic length $\ell_B = \sqrt{\hbar/eB_\tau} = \sqrt{A_{\mathrm{c}}/2\pi\alpha_\tau}$, inversely proportional to the strain, dictates their width as well as their position center. Hence, thanks to the DoS, one clearly identifies the spectrum gaps (light color in Figure 3.3**a**), in which are also represented the aforementioned chemical potentials μ_1 and μ_2 by the green and blue dashed lines, respectively.

However, this is not the end of the story. Remember that the Středa theory is applicable for an insulating bulk, where, by definition, the density of states has to vanish. To evaluate how the density of states changes through the sample, one computes the local density of states (LDoS) per unit cell, defined as

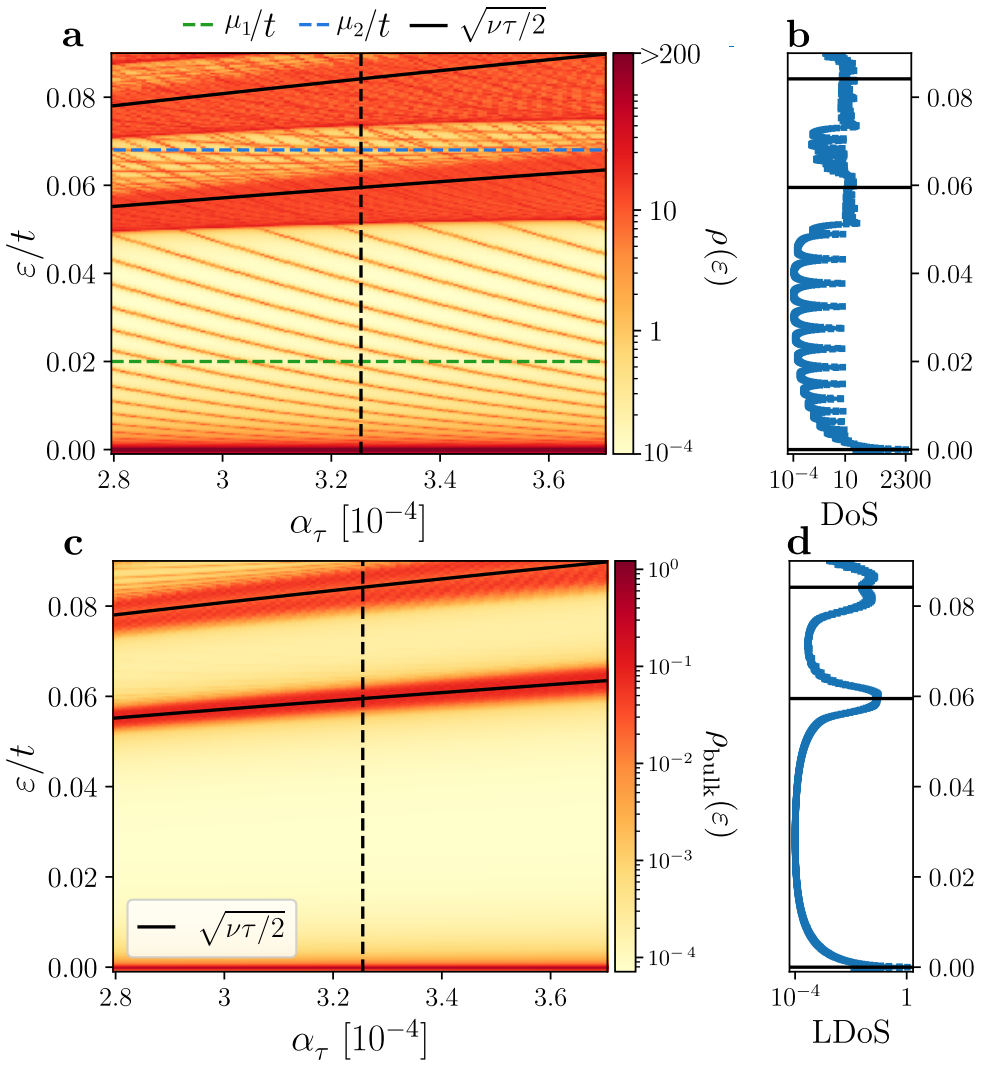

Figure 3.3: **a.** Total density of states $\rho(\varepsilon)$ in logarithmic scale as a function of energy ε and pseudomagnetic flux α_τ. The size of the sample is the same as in Figure 3.1, namely $L_x = 450.5\,a$. The dashed green and blue lines represent the chemical potentials $\mu_1 = 0.02t$ and $\mu_2 = 0.068t$, respectively. **c.** Bulk density of states $\rho_{\text{bulk}}(\varepsilon)$ in logarithmic scale for $L_{\text{bulk}} = 36\,a$. In both panels, black solid lines identify the energy of the analytical pseudo-Landau levels at the Dirac points. The corresponding density of states (DoS) are shown in panel **b** or local density of states (LDoS) in panel **d** for $\alpha_\tau = 3.255 \times 10^{-4}$ indicated by the vertical dashed lines in the panels **a** and **c**, respectively.

$$\begin{aligned}\rho(\varepsilon, x) &= \frac{1}{\pi}\sum_{\alpha=A,B} \mathrm{Im}\langle x_\alpha|G^{\mathrm{r}}(\varepsilon)|x_\alpha\rangle \\ &= \frac{1}{\pi}\sum_{\alpha=A,B}\sum_{m,n} \mathrm{Im}\langle x_\alpha\,|\psi_m\rangle\,\langle\psi_m|\,G^{\mathrm{r}}(\varepsilon)\,|\psi_n\rangle\,\langle\psi_n|\,x_\alpha\rangle \\ &= \lim_{\eta\to 0}\frac{\eta}{\pi}\sum_{\varepsilon_n,\alpha}\frac{|\psi_n^\alpha(x)|^2}{\eta^2+(\varepsilon_n-\varepsilon)^2}.\end{aligned} \tag{3.26}$$

By integrating it in energy up to the Fermi level, one obtains the particle density per unit cell,

$$\tilde{n}(x) = \int_{-\infty}^{\mu_{\mathrm{F}}} \rho(\varepsilon, x) d\varepsilon. \tag{3.27}$$

From the definition of the bulk density (3.22), by using the previous relation and exchanging the summation and the integral, one can naturally define the local density of states projected in the bulk, denoted by ρ_{bulk},

$$\begin{aligned} \tilde{n}_{\text{bulk}} &= \frac{1}{N_{\text{bulk}}} \sum_{x \in \text{bulk}} n(x) \\ &= \frac{1}{N_{\text{bulk}}} \sum_{x \in \text{bulk}} \int_{-\infty}^{\mu_{\mathrm{F}}} \rho(\varepsilon, x) d\varepsilon \\ &= \int_{-\infty}^{\mu_{\mathrm{F}}} \frac{1}{N_{\text{bulk}}} \sum_{x \in \text{bulk}} \rho(\varepsilon, x) d\varepsilon \\ &\equiv \int_{-\infty}^{\mu_{\mathrm{F}}} \rho_{\text{bulk}}(\varepsilon) d\varepsilon. \end{aligned} \tag{3.28}$$

The bulk LDoS is plotted in Figure 3.3**c** as a function of the energy and α_τ, for a bulk region of width $L_{\text{bulk}} = 36a$ centered around x_{c}, which is of the order of the magnetic length ℓ_B for $\alpha_\tau = 3.255 \times 10^{-4}$. The reason for this choice of ℓ_B is explained later. For clarity, a cut for this value of α_τ (black dashed line in panel **c**) is shown in panel **d**. For this value of bulk width, the contribution from the edge modes is negligible (light color) for the first two gaps between pLLs but more pronounced in the third one (note the logarithmic scale). This reflects the deeper penetration into the bulk of the edge states arising from the $\nu = 2$ pLL, which are more delocalized than those from lower pLLs. To avoid these finite-size effects, the focus will be set on the results for the first two gaps in the rest of this section, unless otherwise specified.

Local Valley Hall response

As in the presence of strain, the particle density $\tilde{n}(x)$ is not uniform in the bulk as it would be with a real magnetic field, the (average) bulk density was introduced. To be able to compute the valley Hall response in the bulk, one can define a local valley Hall marker for each unit cell,

$$\mathfrak{S}(x) = \sigma_0 \frac{\partial \tilde{n}(x)}{\partial \alpha_\tau}\bigg|_{\mu_F}. \tag{3.29}$$

One can ask whether it is relevant to also average it over the previously defined bulk region. Figure 3.4 presents the local valley Hall marker as function of the position for the uniaxially strained system (solid lines) and compares it to the Hall conductivity for a ribbon in the presence of a real magnetic field $B = B_\tau$ (dashed lines) for $\mu_{\mathrm{F}} = \mu_1$ (μ_2) in green (blue). In the

latter case, $\mathfrak{S}$ is uniform around the center and equals to the expected quantized integer values from the theory (-1 and -3 for the first and second gaps, respectively). In the strained case, it presents a linear drift around x_c. Their dependence on space is inherited from their respective densities – see Figure 3.2. Again, the linearity allows to filter away the discrepancies by averaging over an adequate r_{bulk} as prescribed by (3.22), yielding

$$\sigma_{\text{V}} = \frac{1}{N_{\text{bulk}}} \sum_{x \in \text{bulk}} \mathfrak{S}(x). \tag{3.30}$$

Note that the deviations of $\mathfrak{S}$ from the linearity arise as soon as edge effects become significant, which is more pronounced in the second than in the first gap as the edge states from the former are more delocalized.

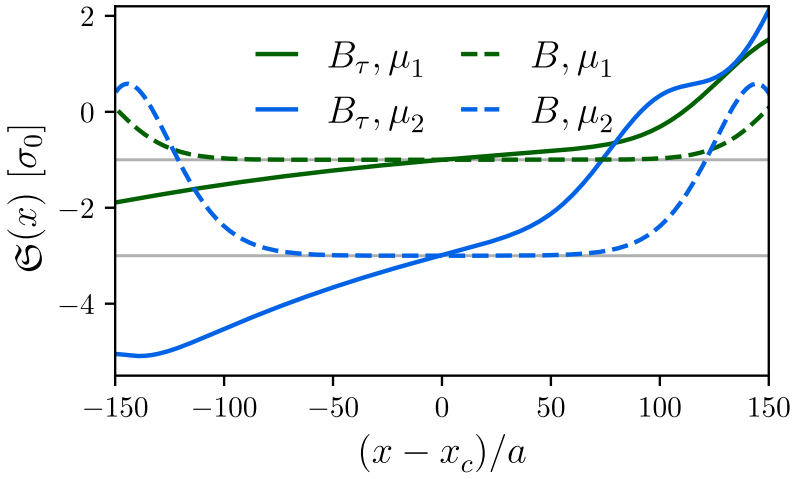

Figure 3.4: Spatial dependence of the marker $\mathfrak{S}(x)$ for the same parameters as in Figure 3.1 ($\alpha_\tau = 3.255 \times 10^{-4}$) for a strained sample (solid lines) and for a lattice with a homogeneous external magnetic field $B = B_\tau^K$ (dashed lines). Green and blue colors correspond to chemical potentials $\mu_1 = 0.02\,t$ (first gap) and $\mu_2 = 0.068\,t$ (second gap), respectively.

Following a similar reasoning as in (3.28),

$$\begin{aligned}
\sigma_{\text{V}} &= \frac{1}{N_{\text{bulk}}} \sum_{x \in \text{bulk}} \mathfrak{S}(x) \\
&= \frac{\sigma_0}{N_{\text{bulk}}} \sum_{x \in \text{bulk}} \frac{\partial \tilde{n}(x)}{\partial \alpha_\tau}\bigg|_{\mu_F} \\
&= \frac{\sigma_0}{N_{\text{bulk}}} \frac{\partial}{\partial \alpha_\tau} \sum_{x \in \text{bulk}} \int_{-\infty}^{\mu_{\text{F}}} \rho(\varepsilon, x) d\varepsilon \\
&= \sigma_0 \int_{-\infty}^{\mu_{\text{F}}} \frac{\partial \rho_{\text{bulk}}(\varepsilon)}{\partial \alpha_\tau} d\varepsilon.
\end{aligned} \tag{3.31}$$

one finds that the valley Hall response in the bulk is equal to the integral over all the occupied states of the derivative of the bulk density of states with respect to the pseudo-magnetic flux. Notice that, since the Fermi energy is kept constant, the derivation passes through the integral.

As a last step, one has to determine what is a reasonable bulk size to perform the average. The equation (3.30) is used to obtain the Figure 3.5, which presents σ_{V} (with respect to the expected quantized value) as a function of α_τ and L_{bulk} at $\mu_{\mathrm{F}} = \mu_1$ (panel **a**) and $\mu_{\mathrm{F}} = \mu_2$ (panel **b**). Clear plateaus[5] at $\sigma_{\mathrm{V}} \simeq -1$ and $\sigma_{\mathrm{V}} \simeq -3$ are visible for $L_{\mathrm{bulk}} \lesssim 100a$ (white color). At larger L_{bulk}, deviations for peculiar values of α_τ appear as horizontal stripes, stemming from μ_{F} crossing the edge states energy in Figure 3.3**a**. As the chosen bulk region broadens, the edge states contribution become more noticeable, altering the linear space dependence of $\mathfrak{S}$. This is evidenced by plotting ρ_{bulk} as a function of α_τ and L_{bulk} in Figure 3.5**c**, **d** for $\mu_{\mathrm{F}} = \mu_1$ and μ_2, respectively. Indeed, the bulk density of states also presents horizontal stripes at the same values of α_τ, reflecting the incremental contribution from the edge states as the bulk region widens. All together, the Figure 3.5 conveys that a quantized value of the valley Hall coefficient can be measured via the bulk density response as long as $\rho_{\mathrm{bulk}} \simeq 0$. When boundary effects become appreciable, ρ_{bulk} increases and the valley Hall response deviates from the quantized odd values predicted by the theory – see (3.15). Moreover, it shows that $\ell_B = \sqrt{A_{\mathrm{c}}/2\pi\alpha_\tau}$ is a suitable bulk size (black solid line in all panels) as it is well within the plateaus formed by σ_{V} for the chosen range of parameters α_τ, L_{bulk} and $L_x = 450.5a$.

As a summary, a full scan of the valley Hall fan diagram is presented in Figure 3.6**a**. The valley Hall response, obtained from (3.30) for $L_{\mathrm{bulk}} = 36a$, is plotted as a function of both the chemical potential μ_{F} and α_τ. It forms clear plateaus in regions where μ_{F} is far from the analytical ν-pLL energies $t\sqrt{\tau\nu/2}$, identified by dashed black lines. Hence, σ_{V} levels at the expected quantized odd values when the filling fraction of the pLLs is constant. On the contrary, when the bulk is metallic, i.e. when $\mu_{\mathrm{F}} \simeq t\sqrt{\tau\nu/2}$, its quantization breaks down. This phenomenon is best illustrated in Figure 3.6**b**, which shows a cut of panel **a** for $\alpha_\tau = 3.255 \times 10^{-4}$ (indicated by a horizontal solid black line). The gray shaded area represents the bulk density of states ρ_{bulk} as a function of the Fermi energy. As previously observed several times, whenever $\rho_{\mathrm{bulk}} \simeq 0$, the valley Hall response (blue dots) displays robust plateaus at -1, -3 and (close to) -5. On the other hand, σ_{V} becomes erratic as soon as ρ_{bulk} becomes finite.

We remark that if the number of particles was kept constant instead of the Fermi level, μ_{F} would be a function of α_τ, therefore by the Leibniz integral rule,

[5] See section 3.1.2 explaining the sign of the quantized values.

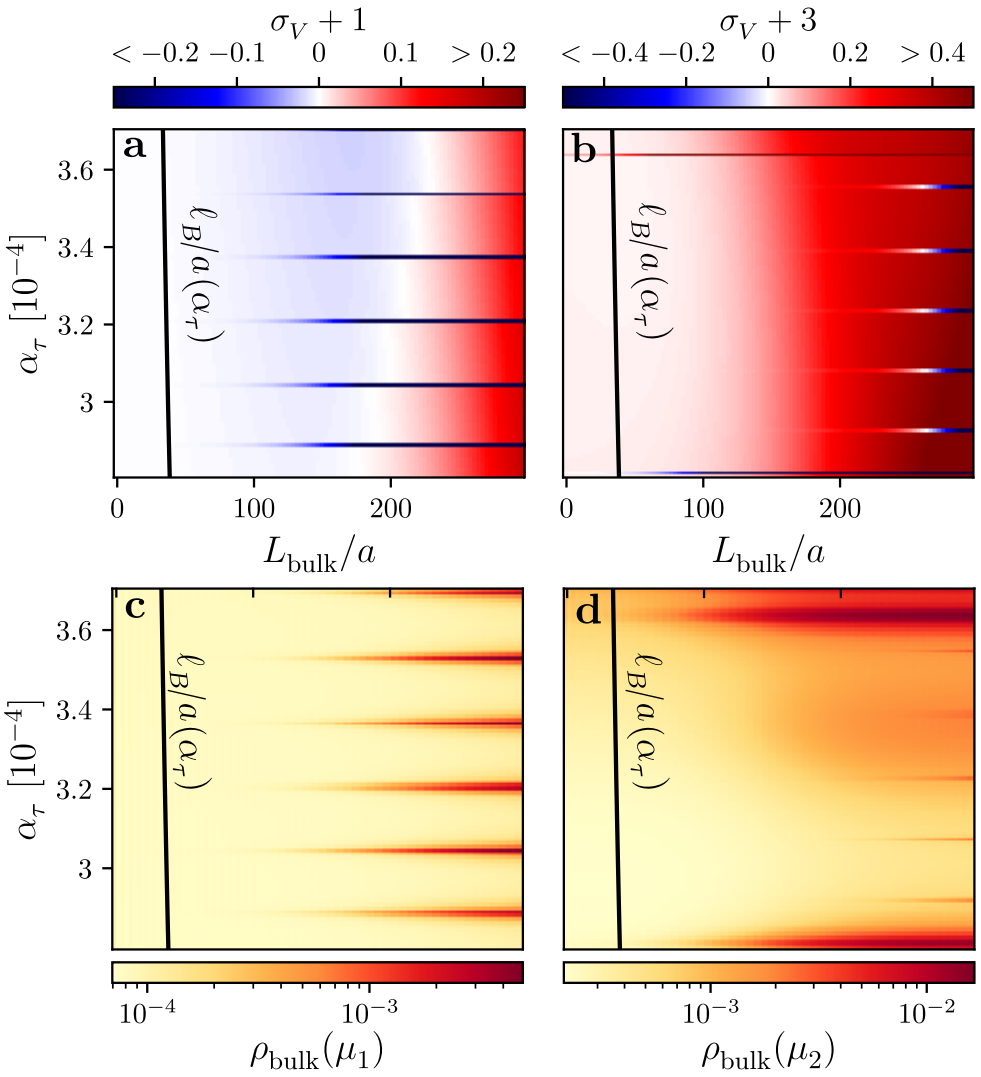

Figure 3.5: **a-b.** Valley Hall response obtained from Eq. (3.30) as a function of the flux per plaquette α_τ and the size of the bulk L_{bulk} in a system of size $L_x = 450.5a$. The chemical potential has been fixed to $\mu_1 = 0.02\,t$ in the first and $\mu_2 = 0.068\,t$ in the second gap, respectively. The colorbar shows the deviation of the valley Hall response with respect to its analytically expected value. The solid black lines represent the magnitude of the magnetic length ℓ_B for each strain intensity. **c-d.** Projected density of states $\rho_{\text{bulk}}(\mu_F)$ as a function of α_τ and L_{bulk} at the corresponding chemical potentials $\mu_{\text{F}} = \mu_1$ and $\mu_{\text{F}} = \mu_2$.

$$\begin{aligned}\sigma_{\text{V}} &= \sigma_0 \frac{\partial}{\partial \alpha_\tau} \int_{-\infty}^{\mu_{\text{F}}(\alpha_\tau)} \rho_{\text{bulk}}(\varepsilon) d\varepsilon \\ &= \sigma_0 \left[\int_{-\infty}^{\mu_{\text{F}}} \frac{\partial \rho_{\text{bulk}}(\varepsilon)}{\partial \alpha_\tau} d\varepsilon + \rho_{\text{bulk}}(\mu_{\text{F}}(\alpha_\tau)) \frac{\partial \mu_{\text{F}}}{\partial \alpha_\tau} \right].\end{aligned} \tag{3.32}$$

In this case too, it would be necessary to have $\rho_{\text{bulk}}(\mu_{\text{F}}) \simeq 0$ for the quantization to hold.

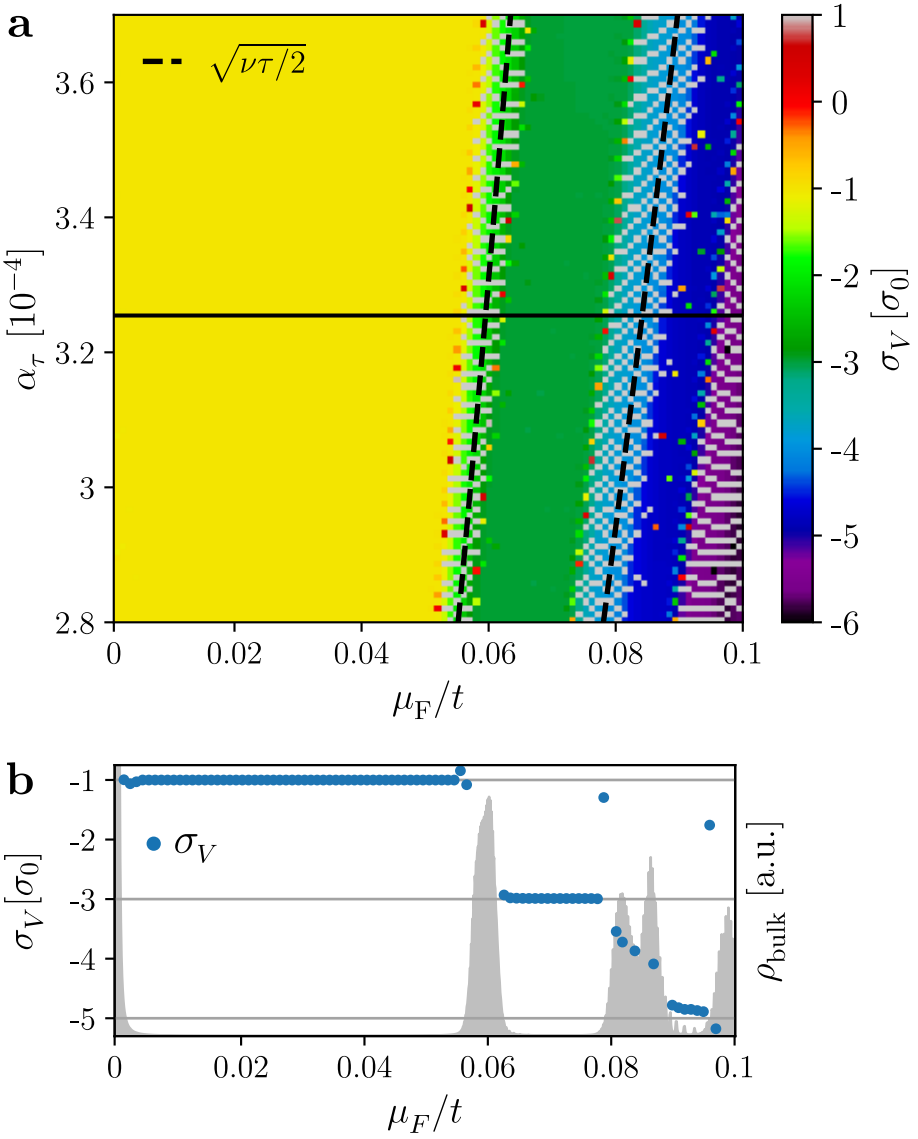

Figure 3.6: **a.** Valley Hall response obtained from Eq. (3.30) as a function of the flux per primitive cell α_τ and the Fermi energy μ_F in units of the hopping parameter t. Dashed black lines represent $\mu_F/t = \sqrt{\tau\nu/2}$ $\nu = 1$ and $\nu = 2$, where τ is the strain intensity. The size of the bulk region where we averaged the local marker is $L_{\text{bulk}} = 36\,a$. **b.** (Blue dots) Valley Hall response σ_{V} for $\alpha_\tau = 3.255 \times 10^{-4}$ (indicated by a solid black line in panel **a**). Results are restricted to the present window for clarity. (Grey area) Local density of states ρ_{bulk} from Fig. 3.3**b**.

3.2.2 Trigonal strain in a finite hexagonal flake

The cylindrical geometry of the lattice envisaged in the last section allowed to study large system sizes. It is worth asking whether the quantization of the valley Hall response obtained in this context would still hold for smaller samples with different geometries, strain configurations and edge terminations. To this end, a more realistic geometry is explored, with open boundary conditions at every edge. This is well suited for the implementation of trigonal

strain, that can be modeled by the space dependent tunneling amplitudes (2.97), yielding the Hamiltonian

$$\hat{H} = -\sum_{\mathbf{r},j} t\left(1+\tau\frac{(\mathbf{r}-\mathbf{r}_{\rm c})\cdot\boldsymbol{\delta}_j}{3a^2}\right)\hat{a}^\dagger_{\mathbf{r}}\hat{b}_{\mathbf{r}+\boldsymbol{\delta}_j} + \text{H.c.}. \tag{3.33}$$

As a reminder from section 3.2.2, the corresponding pseudo-magnetic field reads

$$\mathbf{B}^\zeta_\tau = \zeta\frac{2\hbar\tau}{3ea^2}\hat{\mathbf{z}}. \tag{3.34}$$

Notice that the pseudo-magnetic field generated by this trigonal strain has a different magnitude and an opposite sign with respect to its counterpart in the uniaxial strain. In this regard, as one could anticipate from (3.15), the bulk density response to strain variations should now be positive (negative) for $\tau > 0$ ($\tau < 0$) when the chemical potential $\mu_{\rm F}$ lies within gaps of the conduction band ($\mu_{\rm F} \geq 0$). We now numerically analyze the valley Hall response for a triaxially-stretched flake of a honeycomb lattice, shaped into the form of an hexagon – in order to preserve the trigonal symmetry. The terminations alternate between zigzag and bearded-like edges, such that the sites at the perimeter of the flake belong to the same sublattice (without loss of generality, say A sites).

The Figure 3.7 presents the spectrum of (3.33) for $\tau = 0.07$ in panel **a** and $\tau = -0.07$ in **b**. In both cases, the triaxial deformations produce dispersionless pLLs, as opposed to the pLLs obtained with the uniaxial strain. Consequently, the bulk spectral gaps are larger, helping for the detection of more precise quantized response for higher pLLs[6]. The colorscale indicates the mean distance of an eigenstate wavefunction with respect to the center $\mathbf{r}_{\rm c} = (x_{\rm c}, y_{\rm c}) \equiv (L_x/2, L_y/2)$. The procedure to obtain this valley Hall marker in this context is identical as in the preceding section.

Computing the particle density in each sublattice and the total density of states

The flatness of pLLs observed in Figure 3.7 implies that there is no energy cost in occupying one specific region rather than another in the bulk, hence the particle density per unit cell is expected to be uniform in a region of about 6-7 sites around $(x_{\rm c}, y_{\rm c}) = (30a, 35a)$ – instead of being linearly tilted around the center as in the uniaxial case. This is shown in Figure 3.8 for $\tau = 0.07$ (panel **a**) and $\tau = -0.07$ (panel **b**) at the Fermi level $\mu_{\rm F}/t = 0.1$ indicated by a dashed magenta lines in Figure 3.7 in the first pLL gap. Here, the two sublattices A and B are separated since the number of A-sites is greater than the number of B-sites, making the calculation of the particle density per unit cell irrelevant. To this end, the mirror symmetry of the flake with respect to the $y = y_{\rm c}$ axis is used to plot separately half of the A-sublattice (upper part) and

[6]The gap between the ν_1 and ν_2-pLLs is proportional to $\sqrt{\nu_2} - \sqrt{\nu_1}$ in any strain configuration envisaged here, so higher gaps become narrower. On top of that, the pLLs dispersion in the uniaxial strain case shrinks even more the gaps.

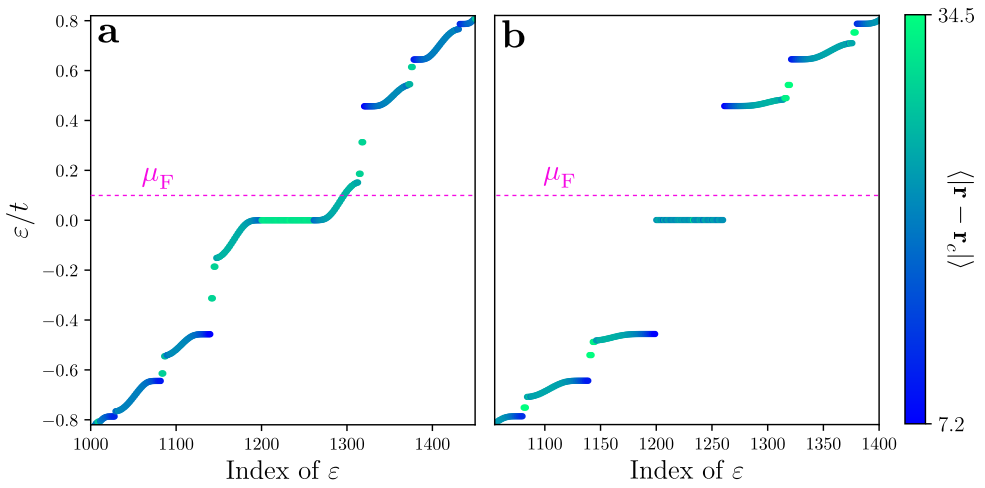

Figure 3.7: Spectrum of the Hamiltonian (3.33) of the honeycomb flake for $\tau = 0.07$ and $\tau = -0.07$ in panels **a** and **b**, respectively. The color scale indicates the mean position $\langle x \rangle$ of each state. The minimal average distance is around $7a$ (not 0) due to finite size effects from the discretization of the lattice ($\ell_B \approx 5a$) for such strain.

half of the B-sublattice (lower part). The missing pieces can be simply obtained by reflecting the corresponding portions with respect to the $y = y_c$ axis.

Surrounding these uniform bulk distributions, the boundaries can be populated or not by helical edge states depending on the sign of τ. Indeed, regarding the discussion about the existence or non-existence of propagating edge states outlined in section 2.6, this flake will support, or not support, helical edge states in the first gap (between the 0^{th} and the 1^{st} pLLs) depending on whether both sublattices are populated or not, which is related to the sign of τ. For $\tau > 0$, both sublattices are populated – see panel **a** – because the 0^{th} pLL's wavefunction is localized on the B-sublattice and mixes with the non-propagating edge state occupying the A-sublattice, thus creating a dispersive helical edge states. When $\tau < 0$, no particle (above half-filling) occupy the B-sublattice – see lower part of panel **b** – hence no dispersive mode can emerge from the 0^{th} LL as it is forbidden by the chiral symmetry – see (2.61).

The presence or absence of helical edge modes is also shown by panels **a** ($\tau > 0$) and **b** ($\tau < 0$) of Figure 3.9, where is presented the total density of states $\rho(\varepsilon)$ as a function of the energy and the strain intensity τ. As a guide to the eye, the pLL energies at the Dirac point, $\varepsilon_\nu = \pm t\sqrt{3|\tau|\nu}$ ($\nu \in \mathbb{N}$), are identified by gray dashed lines, which precisely overline the pLLs structure in both cases. One sees that for negative τ (panel **b**), the DoS remains exactly zero (light color) within the first gap, contrarily to the first gap in panel **a** where propagating helical edge modes emerge. Note that boundary modes appear in all gaps between higher pLLs ($\nu > 0$). For clarity, a cut out of panels **a** and **b** at $|\tau| = 0.07$ (vertical dashed blue line) are presented in Figure 3.9**c** and **d**, respectively.

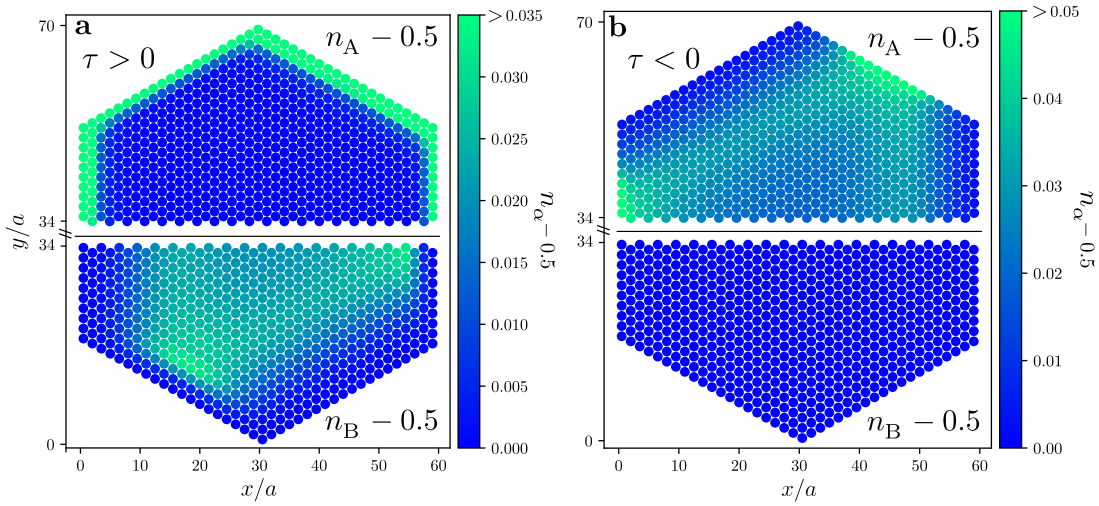

Figure 3.8: Particle density n_α (α = A,B) above half-filling on each sublattice for a strain intensity $\tau > 0$ and $\tau < 0$ in panels **a** and **b**, respectively. In the latter case, the B-sublattice (lower part) is deprived of any particle on top of half-filling. The two sublattices A and B have been separated since the number of A-sites is greater than the number of B-sites, making the calculation of the particle density per unit cell irrelevant. To this end, the mirror symmetry of the flake with respect to the $y = y_c$ axis is used to plot separately half of the A-sublattice (upper part) and half of the B-sublattice (lower part). The missing pieces can be simply obtained by reflecting the corresponding portions with respect to the $y = y_c$ axis.

Computing the local density of states

As emphasized multiple times, the quantization of the valley Hall response requires the density of states in the bulk to vanish at the chemical potentials. In the present case, this is checked by calculating the LDoS $\rho_\alpha(\varepsilon, \mathbf{r})$ at every site $\mathbf{r}_\alpha$ in the flake, where α indicates whether the site belong to the A or B-sublattice. Similarly as (3.23), it is computed from the retarded Green's function as

$$\rho_\alpha(\varepsilon, \mathbf{r}) = -\frac{1}{\pi}\mathrm{Im}\langle \mathbf{r}_\alpha | \hat{G}^r(\varepsilon) | \mathbf{r}_\alpha \rangle. \tag{3.35}$$

Figure 3.10 shows $\rho_\alpha(\mu_F, \mathbf{r})$ at the Fermi level $\mu_F = 0.1t$ for $\tau = 0.07$ (panel **a**) and $\tau = -0.07$ (panel **b**). Note that, as for the particle densities, the two sublattices are split. For $\tau > 0$, edge modes on the A-sublattice surround the entire perimeter, while delocalized states only occupy the B-sublattice closer to the center of the flake. A corresponding cut along $\mathbf{r} = x_c^\alpha \hat{\mathbf{x}} + y\hat{\mathbf{y}}$ is shown to the left of the panel, where the entire spatial distribution is restored and where x_c^α is the closest x-position of the α-sublattice to x_c. For $\tau < 0$, the LDoS remains strictly zero everywhere in the flake, consistently with the absence of the edge states. Hence, for the chosen values of parameters and independently of the sign of τ, the system's bulk density of states vanishes – irrespectively of the presence of helical edge states – which is conducive to the quantization of the valley Hall response.

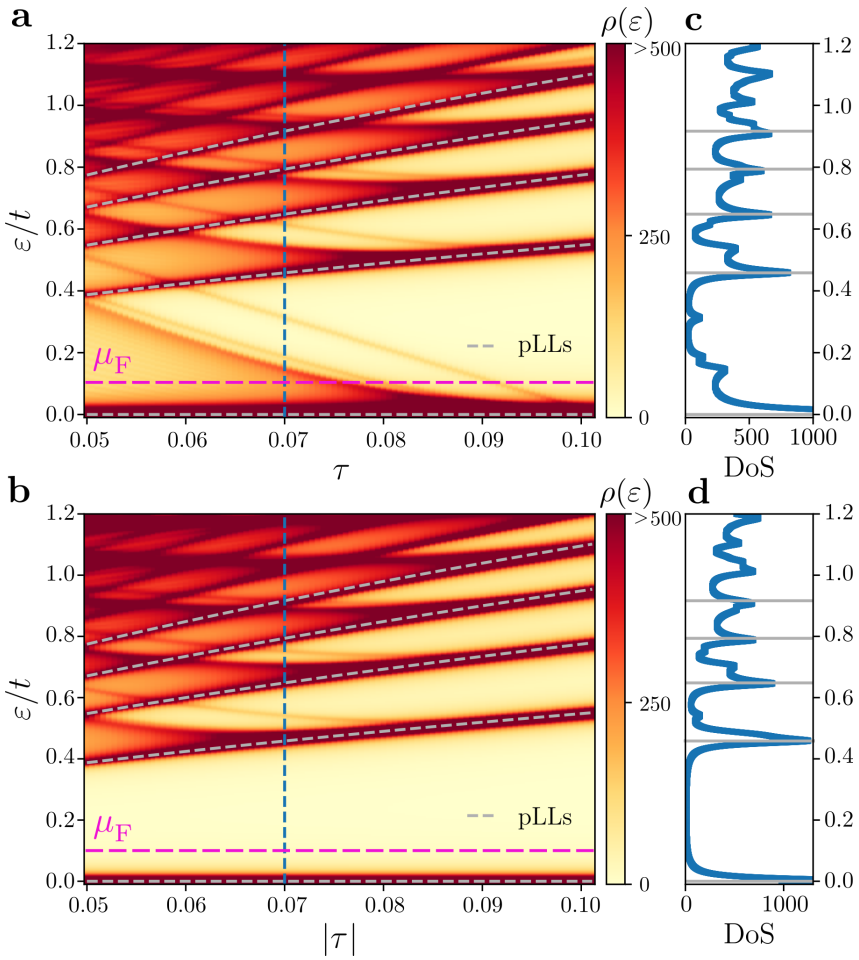

Figure 3.9: Total density of states $\rho(\varepsilon)$ (DoS) in the hexagonal flake for strain intensities **(a)** $\tau > 0$ and **(b)** $\tau < 0$. Dashed grey lines indicate the energy of the analytical pseudo-Landau levels $E_\nu = \pm v_F\sqrt{2\hbar e|\mathbf{B}_\tau^\xi|\nu} = \pm t\sqrt{3|\tau|\nu}$ for $\nu = 0, 1, 2, 3, 4$, where v_F is the Fermi velocity, $\mathbf{B}_\tau^\xi$ the pseudo-magnetic field at valley $\xi\mathbf{K}$ and ξ is the valley index (± 1). **c**,**d.** Specific cuts of panels **a** and **b** (marked with a vertical dashed blue line) for $|\tau| = 0.07$, respectively. Solid grey lines denote the analytical pseudo-Landau levels and dashed magenta lines indicate the Fermi level $\mu_F = 0.1t$ corresponding to the densities in Figure 3.8.

Local Valley Hall response

The local valley Hall response on the α-sublattice ($\alpha = $ A, B) is calculated[7] as the derivative of the dimensionless particle density at site $\mathbf{r}_\alpha$ with respect to the pseudo-magnetic flux α_τ,

$$\mathfrak{S}_\alpha(\mathbf{r}) = \sigma_0 \frac{\partial \tilde{n}_\alpha(\mathbf{r})}{\partial \alpha_\tau}\bigg|_{\mu_F} = \sigma_0 \int_{-\infty}^{\mu_F} \frac{\partial \rho_\alpha(\varepsilon, \mathbf{r})}{\partial \alpha_\tau} d\varepsilon, \tag{3.36}$$

where the development (3.31) allowed to rewrite $\mathfrak{S}_\alpha(\mathbf{r})$ in terms of the local density of states $\rho_\alpha(\varepsilon, \mathbf{r})$. Since the system presents an insulating bulk, characterized by a pseudo-Landau level spectrum, $\mathfrak{S}_\alpha(\mathbf{r})$ is expected by the theory (3.15) to be quantized when the Fermi level μ_F lies

[7] See section 3.1.2 explaining the sign of the quantized values.

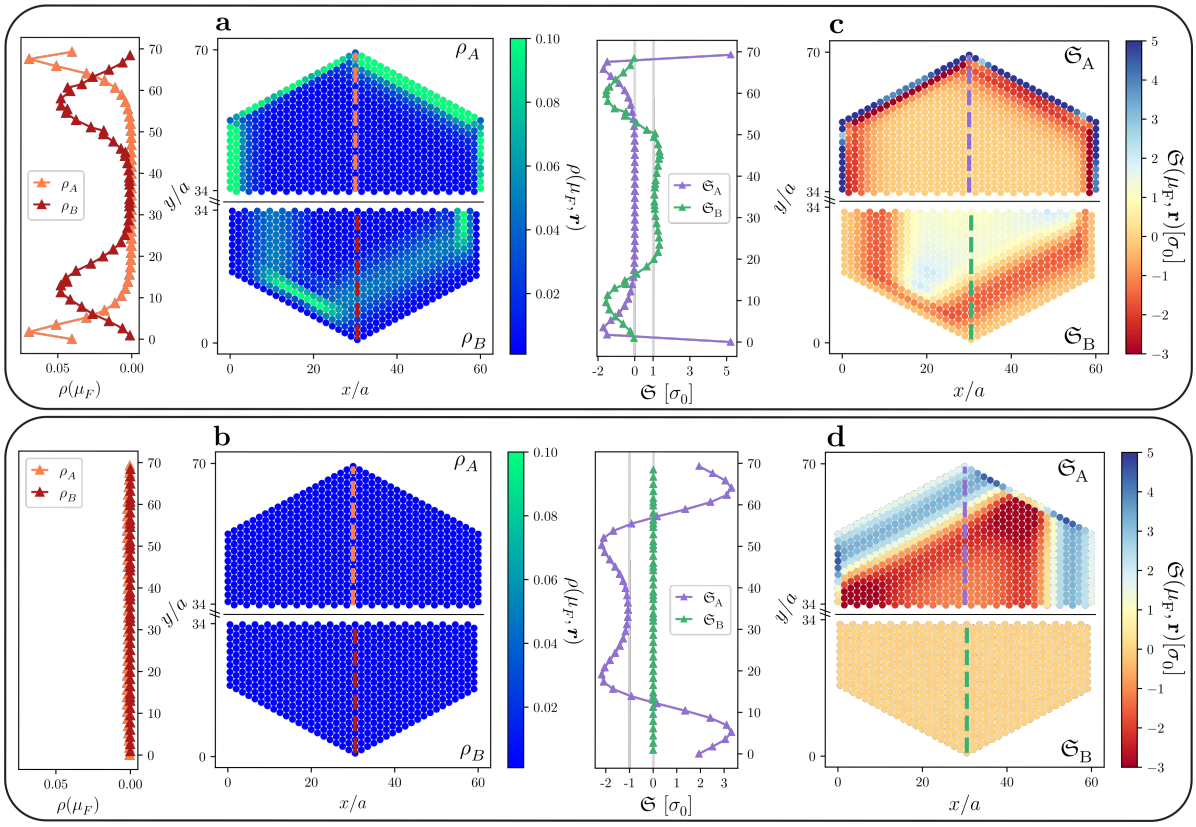

Figure 3.10: Panels **a** and **b** show the local density of states discriminated by sublattice $\rho_\alpha(\varepsilon, \mathbf{r})$ – see Eq. (3.35) – for $\tau > 0$ and $\tau < 0$, respectively. The energy has been taken to be $\varepsilon = \mu_F = 0.1\,t$ and $|\tau| = 0.07$. The terminations have been chosen so as to alternate between bearded and zigzag-like edges. The mirror symmetry of the flake with respect to the $y = y_c$ axis is exploited to plot separately half of the A-sublattice (the upper part) and half of the B-sublattice (the lower part). A corresponding cut of the panels along $\mathbf{r} = x_c\hat{\mathbf{x}} + y\hat{\mathbf{y}}$ is shown to their left, where the entire spatial distribution is restored. Panels **c** and **d** show the corresponding local marker $\mathfrak{S}_\alpha(\mathbf{r})$ differentiated by sublattice – see Eq. (3.36).

within an spectral gap. Moreover, from (3.17) the response should be quantized separately on each sublattice due to the imbalance in sublattice population of the bulk pLLs. This is exactly confirmed in Figures 3.10**c**, **d** for $\tau > 0$ and $\tau < 0$, respectively, for $\mu_{\rm F}/t = 0.1$. Around $\mathbf{r}_{\rm c}$, $\mathfrak{S}_A(\mathbf{r}) \simeq 0$ and $\mathfrak{S}_B(\mathbf{r}) \simeq 1$ in panel **c**, and in $\mathfrak{S}_B(\mathbf{r}) \simeq 0$ and $\mathfrak{S}_A(\mathbf{r}) \simeq -1$ in panel **d**. Note that, in the latter case, from the absence of helical edge states in the first gap and the localization of the 0-pLL exclusively on the A sites, the B-sublattice remains half-filled for any chemical potential within the first gap, i.e. $\tilde{n}_{\rm B}(\mathbf{r}) = 1/2$ for every $\mathbf{r}$, hence the local density on the B sites is insensitive to strain variation and $\partial\tilde{n}_{\rm B}(\mathbf{r})/\partial\alpha_\tau|_{\mu_{\rm F}} = 0$. Note that the plateau-like behavior of the marker in the bulk is inherited from the uniform particle density distribution, observed in Figure 3.8. This is emphasized by the cut along $\mathbf{r} = x_{\rm c}^\alpha\hat{\mathbf{x}} + y\hat{\mathbf{y}}$ shown to the left of each panel, where the entire spatial distribution is restored.

As before, the valley Hall coefficient $\sigma_{\rm V}$ is obtained by averaging the local marker per cell

$\mathfrak{S}(\mathbf{r}) = \mathfrak{S}_{\mathrm{A}}(\mathbf{r}) + \mathfrak{S}_{\mathrm{B}}(\mathbf{r})$ over a reasonable bulk radius $r_{\mathrm{bulk}} = L_{\mathrm{bulk}}/2$, as prescribed by (3.31). The chosen bulk size is $L_{\mathrm{bulk}} = 5a$, which corresponds to the region where the valley Hall marker is homogeneous and is on the same order as the magnetic length $\ell_B = 4.6a$ (for $|\tau| = 0.07$). Figure 3.11**a** shows the averaged response (blue dots) as a function of the Fermi level for $\tau = 0.07$. The bulk density of states is included with a gray shaded area and presents Lorentzian peaks at the pLLs energies, which are well defined contrarily to the uniaxially strained case. For μ_{F} in the first gap, σ_{V} is reasonably well quantized around 1. In the second and third gaps, finite-size effects take place because of the stronger delocalization of the edge modes associated to these energies. This is clearly revealed by the local density of states evaluated at chemical potentials $\mu_{\mathrm{F}} = 0.52t$ (panel **b**) and $\mu_{\mathrm{F}} = 0.7t$ (panel **c**), lying in these gaps and identified by vertical dashed black lines in panel **a**. Moreover, the number nodes of ρ_{bulk} differentiated by sublattices recalls that of the pLLs wavefunctions. This leads to a breakdown of the insulating character of the bulk $\rho_{\mathrm{bulk}} > 0$ and a deviation from the quantized integer values expected from (3.15). On top of that, for such high strain intensities, the magnetic length is of the order of th lattice spacing a and discretization effects emerge. Consequently the pseudo-Landau levels picture fails at correctly describing higher bulk pLLs – namely the exact positions of the nodes of the wavefunctions – causing additional discrepancies with the analytical predictions.

Importantly, the valley Hall response is quantized regardless of the edge terminations (that is effectively modified by changing the sing of τ. In other words, the quantization is independent of whether the system supports or lacks helical edge states and therefore it is not related to any counting of propagating edge modes.

3.3 Effect of disorder, defects and impurities

While the fragility of edge transport measurements to defects was a motivation to propose a probing method involving bulk density responses, the robustness to disorder of the latter has not been discussed yet. To do so, three types of defects are considered: local (or Anderson), Gaussian and off-diagonal disorders. They are introduced into the system through a general perturbation of the form

$$\begin{aligned} \hat{H}_{\mathrm{dis}} \;=\; & \sum_{\mathbf{r}\in A} V_{\mathrm{imp}}(\mathbf{r})\hat{a}^{\dagger}_{\mathbf{r}}\hat{a}_{\mathbf{r}} + \sum_{\mathbf{r}\in B} V_{\mathrm{imp}}(\mathbf{r})\hat{b}^{\dagger}_{\mathbf{r}}\hat{b}_{\mathbf{r}} \\ & - \sum_{\mathbf{r}\in A,j} \delta t_j(\mathbf{r}) \left(\hat{a}^{\dagger}_{\mathbf{r}}\hat{b}_{\mathbf{r}+\delta_j} + \mathrm{h.c.}\right), \end{aligned} \tag{3.37}$$

where $V_{\mathrm{imp}}(\mathbf{r})$ is an on-site potential resulting from the presence of defects or impurities in the lattice and can take different values on A and B sites. To include this diagonal disorder, two

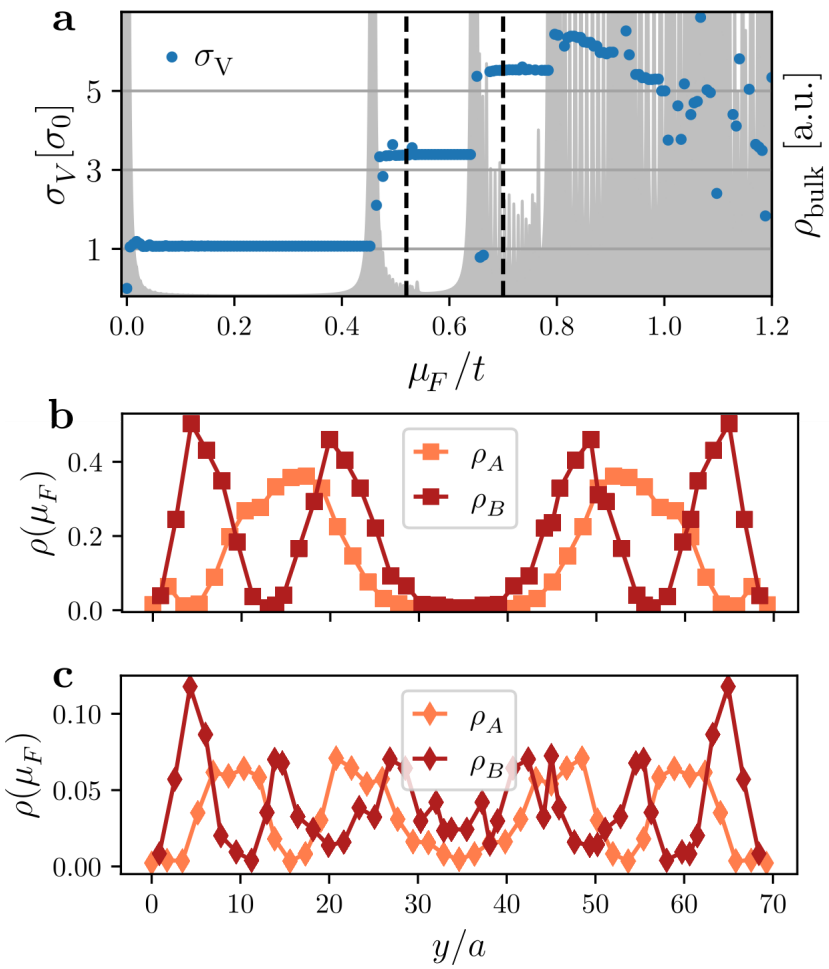

Figure 3.11: **a.** Valley Hall response σ_V (blue points) obtained from averaging the local marker per cell $\mathfrak{S}(\mathbf{r}) = \mathfrak{S}_A(\mathbf{r}) + \mathfrak{S}_B(\mathbf{r})$ in a bulk region of size $L_{\text{bulk}} = 5\,a$ (a is the lattice parameter) as a function of the chemical potential μ_F. The grey shaded area shows the density of states projected onto the bulk region at the Fermi level $\rho_{\text{bulk}}(\mu_F)$. Panels **b** and **c** show the local density of states $\rho(\mu_F, \mathbf{r})$ along $\mathbf{r} = x_c\hat{\mathbf{x}} + y\hat{\mathbf{y}}$ for $\mu_F = 0.52\,t$ and $\mu_F = 0.7\,t$, respectively, indicated by black dashed lines in **a**.

types of potentials are considered. The first one represents a short-range scattering potential that varies stochastically on the lattice spacing scale and is expressed as a sum of on-site energy offsets of intensity U_n uniformly distributed within the interval $[-W, W]$, with W being the disorder intensity. The scatterers are placed at N_{imp} out of the N_{tot} sites of the entire lattice, at positions $\mathbf{r}_n$, i.e.

$$V_{\text{imp}}(\mathbf{r}) = V^{\delta}_{\text{imp}}(\mathbf{r}) \equiv \sum_{n=1}^{N_{\text{imp}}} U_n \delta(\mathbf{r} - \mathbf{r}_n). \tag{3.38}$$

The second type of diagonal disorder has a longer range and varies smoothly on the lattice spacing scale. In this case, the potential profile around each impurity is modeled by a Gaussian

function, such that

$$V_{\text{imp}}(\mathbf{r}) = V^{\lambda}_{\text{imp}}(\mathbf{r}) \equiv \sum_{n=1}^{N_{\text{imp}}} U_n \exp\left(-\frac{|\mathbf{r}-\mathbf{r}_n|^2}{2\lambda^2}\right), \tag{3.39}$$

with λ characterizing the range of the potential. The last type of disorder is introduced by the term $\delta t_j(\mathbf{r})$, stemming from bond (off-diagonal) disorder. It is modeled along the entire flake by $\delta t_j(\mathbf{r})/t = \gamma_j(\mathbf{r})\tau$, with $\gamma_j(\mathbf{r})$ being uniformly distributed in the interval $[-\Gamma, \Gamma]$ for every position $\mathbf{r}$. This effectively imprints a lack of precision in the space dependence of the tunneling amplitudes (2.97). For concreteness, Figure 3.12 schematically shows the deviation of the flake's onsite energies (panels **a** and **b**) or tunneling amplitudes **c** with respect to the pristine case. The number of impurities in the Anderson disordered case is chosen to be equal to the number of sites. For the Gaussian defects, $N_{\text{imp}} = 0.01 N_{\text{tot}}$ and the associated range is $\lambda = 3a$.

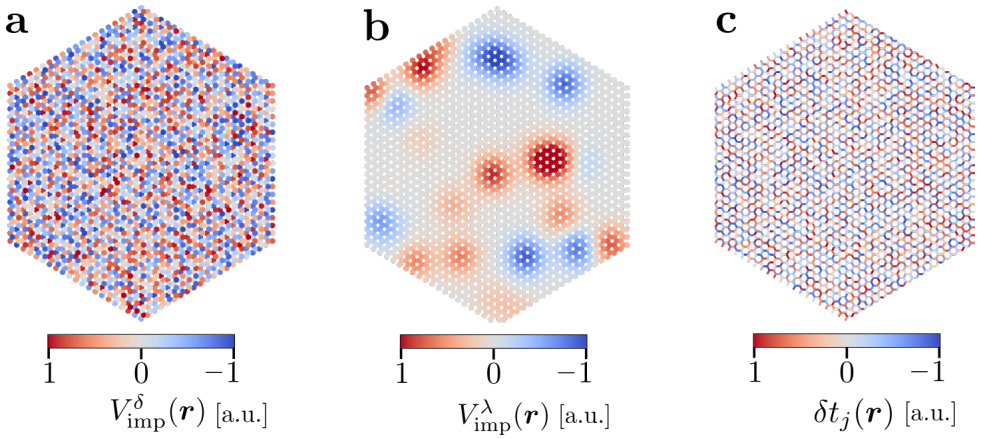

Figure 3.12: Deviations of the flake's onsite energies (panel **a** for short-range and panel **b** for Gaussian impurities) and tunneling amplitudes (panel **c**) with respect to the pristine case.

The numerical analysis of the impact of these three types of disorder is presented in Figure 3.13. Attention is focused on the density response function within the first spectral gap by setting the Fermi energy to be $\mu_{\text{F}} = 0.25t$ and $\tau = 0.07$. The left (panels **a**, **b** and **c**) and central columns (panels **d**, **e** and **f**) respectively show the effect of the onsite random potential profile (3.38) and of the Gaussian-like profile (3.39), neglecting the off-diagonal disorder, whose independent analysis appears in the right column (panels **g**, **h** and **i**). The first line (panels **a**, **d** and **g**) shows the local valley Hall marker $\mathfrak{S}_\alpha(\mathbf{r})$ discriminated by sublattice (α =A, B) along the direction $\mathbf{r} = x_{\text{c}}\hat{\mathbf{x}} + y\hat{\mathbf{y}}$ for one particular disorder configuration for each type of defect[8]. For these three plots, the disorder strengths W and Γ are chosen sufficiently weak compared to the first pLLs gap in order to preserve the insulating properties of the bulk, namely $W = 0.2t$ and $t\Gamma\tau = 0.042t$ ($\Gamma = 0.6$). In each of the three scenarios, for these moderate values of disorder, $\mathfrak{S}_\alpha$ slightly deviates from the results obtained in the perfectly ordered lattice. The

[8]The rest of the results will be presented as averages over 50 disorder configurations.

fluctuations occur at the lattice spacing scale in panels **a**, **c** and locally around a Gaussian impurity in panel **b**. Remarkably, $\mathfrak{S}_\alpha$ oscillates around the plateau-like values obtained for the ordered lattice (see Figure 3.10**c**), which is reminiscent of previous results [174]. Interestingly, when only off-diagonal disorder is added to the system, the bulk response remains polarized on the B-sublattice and $\mathfrak{S}_{\mathrm{A}}(\mathbf{r}) \simeq 0$ around y_{c}. This stems from the preservation of the chiral symmetry by bond disorder, making the 0^{th} pLL to remain polarized in the B-sublattice.

The local valley Hall marker $\mathfrak{S}(\mathbf{r}) = \mathfrak{S}_{\mathrm{A}}(\mathbf{r}) + \mathfrak{S}_{\mathrm{B}}(\mathbf{r})$ is first averaged over a bulk region of size $L_{\text{bulk}} = 4.6a$, resulting in the valley Hall coefficient σ_{V}^i – the superscript designates the i^{th} out of the N_{conf} different random disorder configurations. To account for the stochastic fluctuations arising from these randomized energy bias, it is crucial to perform calculations across multiple disorder realizations. Hence, σ_{V}^i is averaged over $N_{\text{conf}} = 50$ configurations, from which one obtains

$$\bar{\sigma}_{\mathrm{V}} = \frac{1}{50} \sum_{i=1}^{50} \sigma_{\mathrm{V}}^{(i)}. \tag{3.40}$$

Eventually, $\bar{\sigma}_{\mathrm{V}}$ is evaluated over a range of disorder strengths $W \in [0, 1]$ or $\Gamma\tau \in [0, 0.2]$, while the disorder configurations are kept the same – the magnitude of $U_n(\mathbf{r})$ and $\gamma_j(\mathbf{r})$ are related by a factor between 0 and 1 to W and Γ, respectively. Figures 3.13**b**, **e** and **h**, $\bar{\sigma}_{\mathrm{V}}$ show the deviations of $\bar{\sigma}_{\mathrm{V}}$ from the valley Hall coefficient in the pristine case, now denoted by σ_{V}^0. The standard error on this average, defined as

$$\delta\bar{\sigma} = \frac{1}{\sqrt{N_{\text{conf}} - 1}} \sqrt{\sum_{i=1}^{N_{\text{conf}}} \left(\sigma_{\mathrm{V}}^{(i)} - \bar{\sigma}_{\mathrm{V}}\right)^2}, \tag{3.41}$$

is represented by the blue shaded area. Note that, for each configuration, the positions of Gaussian impurities are aleatory changed. Commonly observed in all three panels, the discrepancies from the pristine case increase along with the disorder intensity. Overall, there exists a range of W and Γ over which $\bar{\sigma}_{\mathrm{V}}$ is close to quantization.

As encountered many times through this chapter, the bulk density of states is a relevant indicator of the quantization, or non-quantization, of the valley Hall coefficient. Figures 3.13**c**, **f** and **i** show the bulk density of states averaged over the 50 disorder configurations, denoted by $\bar{\rho}_{\text{bulk}}$, as a function of energy and the disorder intensity W or $\Gamma\tau$. From being concentrated around the pLLs (indicated by dashed gray lines), it spreads as W or Γ increases. Indeed, lattice imperfections generically lift the pLLs degeneracy, which transform them into energy bands bearing modes localized around the impurities or defects. An exception takes place for the 0^{th} in the presence of bond disorder – see panel **i**. Due to the preservation of the chiral symmetry, this pLL remains unaltered, while the gap gets filled by modes branching from the 1-pLL, whose corresponding eigenstates populate both sublattices. In general, for sufficiently high

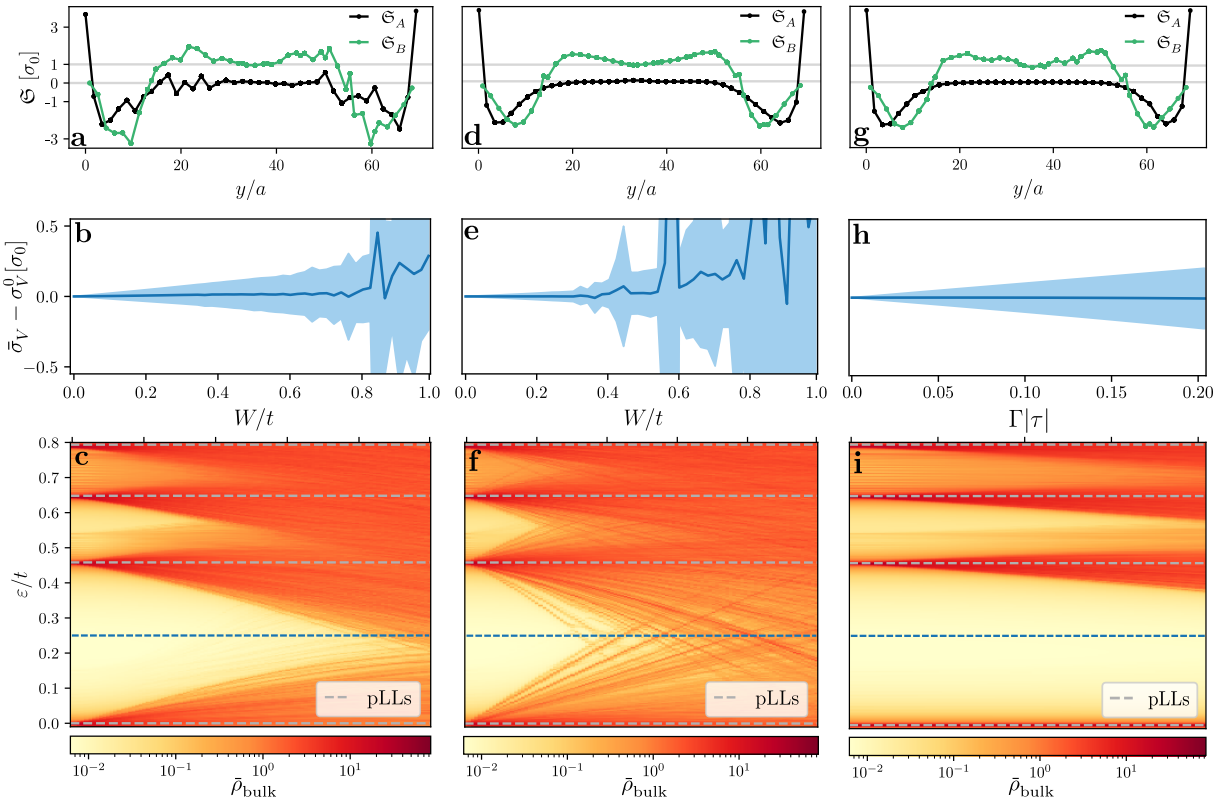

Figure 3.13: Effect of lattice imperfections on the valley Hall coefficient of the triaxially strained flake with strain intensity $\tau = 0.07 > 0$ ($\ell_B = 4.6a$) and chemical potential $\mu_{\text{F}} = 0.25\,t$ in units of the hopping parameter t. **a,b,c.** Short-range on-site potential $V^{\delta}_{\text{imp}}(\mathbf{r})$ with $N_{\text{imp}} = N_{\text{tot}}$, where N_{imp} is the number of impurities and N_{tot} is the number of sites in the flake. **d,e,f.** Gaussian impurities potential described by $V^{\lambda}_{\text{imp}}(\mathbf{r})$ with an impurity concentration of $N_{\text{imp}}/N_{\text{tot}} = 0.01$ and $\lambda = 3\,a$, where λ is the width of each Gaussian and a is the lattice spacing. **g,h,i.** Off-diagonal bond disorder. Panels **a**, **d** and **g** show a corresponding cut of the local valley Hall marker $\mathfrak{S}_{\alpha}(\mathbf{r})$, discriminated by sublattice (α =A,B), along the direction $\mathbf{r} = x_c\hat{\mathbf{x}} + y\hat{\mathbf{y}}$ for each particular disorder realization. In panels **a** and **d**, $W = 0.2\,t$ and in panel **g** $\Gamma = 0.606$. The insets schematically show the deviations of the flake's on-site energies or the tunneling amplitudes with respect to the pristine case. Panels **b**, **e** and **h** show deviations of the corresponding valley Hall response from the pristine case. The response (solid blue line) is obtained by averaging along a bulk region of size $L_{\text{bulk}} = 4.6\,a$ and over 50 different disorder configurations. The standard deviation is indicated in light blue shaded area. Panels **c**, **f** and **i** show the corresponding bulk density of states $\bar{\rho}_{\text{bulk}}$, also averaged over the different disorder realizations, as a function of energy and the disorder intensity W or Γ. Dashed gray lines indicate the energy of the pseudo Landau levels in the pristine case. The dashed blue-line shows the chemical potential μ_{F} chosen for the panels of the two top rows.

disorder intensities, the mobility gaps get entirely filled with impurity states. Consequently, $\bar{\rho}_{\text{bulk}}$ may be finite at $\mu_{\text{F}}/t = 0.25$ and the valley Hall coefficient in panels **b** and **e** lurches wildly.

3.4 Summary and outlook

This chapter introduced an alternative for measuring the valley Hall effect in strained honeycomb lattices, which relies on probing an equilibrium property of such systems locally in the bulk. Specifically, this showed that a quantized valley Hall response can be obtained by measuring a response from a fermionic density to strain variations deep within the bulk. This bulk approach is based on the Widom-Středa formula, accompanied by the introduction of a local marker $\mathfrak{S}(\mathbf{r})$, which is particularly relevant for realistic systems with open boundary conditions. The valley Hall response is the average of $\mathfrak{S}$ on a central insulating region. It remains quantized and robust as a function of the chemical potential and the pseudo-magnetic field strength, *i.e.* strain intensity. Indeed, it displays a plateau-like behavior when the probed region is incompressible, which requires large pseudo-Landau level gaps. Our numerical findings are validated by results expected from the low-energy analytical model that incorporates the effect of strain at the lowest order. In general, this holds as long as the characteristic length scale of the pLLs physics, the magnetic length, is larger than the lattice spacing and smaller than the system size. In other words, the plateaus are clearly visible when discretization and boundary effects are negligible and when the bulk density of states vanishes, which occurs when the Fermi level lies in a spectrum gap. Furthermore, the quantization is independent of the edge terminations and the existence of helical edge states living at the boundaries of a finite-size sample. This independence is rooted in the nature of the probing scheme, which extracts the valley Hall coefficient from the Fermi sea, in sharp contract with usual transport measurement, which only have access to the Fermi surface properties [27]. Eventually, these results were analyzed in regard of different lattice imperfections such as local impurities and bond-disorder in the finite honeycomb flake. Moderate disorder strengths only slightly affect the bulk density profiles, making the valley Hall marker to remain fairly robust as compared to more fragile transport observables that strongly rely on preserving the helicity of edge modes [175].

Several experimental platforms stands out as appealing testbenchs for our proposal. The first are synthetic molecular lattices [108, 176–179], where a electron gas is confined to move in a properly designed 2D-array of carbon monoxide (CO) molecules. This technique has been used to realize honeycomb [176], kagome [180] and Kekule [181] lattices. Interestingly, the CO's positions can be manipulated with atomic precision. Hence, the tunneling amplitude of electrons can be locally reduced or enhanced by separating or approaching the CO molecules, without modifying the lattice parameter [108, 178, 179]. In particular, the CO's can be properly adjusted to produce an effective strain. By employing STM probes to resolve the local density of states, the latter would be integrated in energy up to the desired Fermi level in order to reconstruct the particle density at each lattice position. Note that the strain can not be varied as a knob. Therefore, as one configuration of CO's would correspond to one value of strain imprinted onto the lattice, two lattices would have to be fabricated with two different levels

of strain. Thus, their respective particle densities deep within the bulk would have to be compared in order to extract the valley Hall response. As a by-product, STM techniques might also resolve the sublattice polarization of the valley Hall response.

An alternative is offered by ultracold Fermi gases in optical lattices, where strain could be adjusted through well-designed atom-light [74, 182] or atom-atom [76] couplings, and where the local particle density can be directly measured in-situ [46, 183–188]. Last but not least, recent advances in fabricating arbitrary two-dimensional optical tweezer arrays [189–193] open yet another route for the study of quantum gases in strained lattices, within a highly controllable and scalable environment.

Chapter 4

Strain and pseudo-magnetic fields in optical lattices from density-assisted tunneling

The proposal presented in this chapter is based on our published paper [76]. It introduces a strategy for simulating strain for cold atoms in optical honeycomb lattices. As we have seen in the previous chapters, strain can be encoded into the hopping parameters by making them dependent on space. We propose to incorporate a space-dependence via *density-assisted tunneling* [135,155,194–200], where the hopping amplitudes of one species of atoms ($\downarrow$) depend on the densities of another species ($\uparrow$) at the sites between which the $\downarrow$-atoms hop. These exotic processes can be induced by a renormalization of the hopping amplitudes of the $\downarrow$-species, generated by time-periodic modulations of the interspecies interaction – see the example in section 2.8.4. Consequently, the effective strain emerges from the interspecies interactions and results into a pseudo-magnetic field, embodied by the $\uparrow$-particles.

The following section presents the model that allows for generating effective uniaxial strain through density-assisted tunneling (DAT) and more specifically shows how a linear space-dependence of the tunneling amplitudes can be recovered. In particular, the model is investigated for $\uparrow$-particles forming a Bose-Einstein condensate (BEC) treated in the mean-field (MF) approximation. Within this framework, the BEC distribution is obtained by solving the Gross-Pitaevskii equation (GPE). Two specific regimes are explored, the non-interacting and the Thomas-Fermi (TF) regimes, for which the GPE can be solved exactly. In both cases, the analytical expression of the pseudo-magnetic field is derived. Eventually, the model is validated though a numerical analysis of the fidelity with respect to an ideal strained honeycomb lattice, introduced in section 3.2.1. Afterwards, we detail how these peculiar density-assisted tunneling (DAT) amplitudes can result from a time-periodic (Floquet) drive of the interspecies interaction. The last section further envisages various scenarios for implementing our proposal. We close the chapter by presenting the conclusions and outlooks.

4.1 Effective strain and pseudo-magnetic field from density-assisted tunneling

In order to generate uniaxial linear strain with cold atoms in optical lattices, we consider a mixture of two atomic species, denoted by $\uparrow$ and $\downarrow$ where all atoms are trapped on the same optical honeycomb lattice – see section 2.10.1. The $\downarrow$-species, whose statistics does not need to be specified, hops according to the Hamiltonian

$$\hat{H}_{\downarrow} = -t \sum_{\mathbf{r}\in \mathrm{A},j} \hat{a}^{\dagger}_{\downarrow,\mathbf{r}} \hat{b}_{\downarrow,\mathbf{r}+\boldsymbol{\delta}_j} + \mathrm{H.c.}, \tag{4.1}$$

where t is the hopping amplitude and $\hat{a}^{(\dagger)}_{\downarrow,\mathbf{r}}$ ($\hat{b}^{(\dagger)}_{\downarrow,\mathbf{r}}$) are creation/annihilation operators of a $\downarrow$ particle on $\mathbf{r} \in$ A ($\mathbf{r} \in$ B). The $\uparrow$-atoms are weakly interacting bosons, harmonically trapped, whose Bose-Hubbard Hamiltonian reads

$$\begin{aligned} \hat{H}_{\uparrow} = &- J \sum_{\mathbf{r}\in \mathrm{A},j} \left(\hat{a}^{\dagger}_{\uparrow,\mathbf{r}} \hat{b}_{\uparrow,\mathbf{r}+\boldsymbol{\delta}_j} + \mathrm{H.c.} \right) + \frac{V_x}{2} \sum_{x\in \mathrm{A,B}} (x - x_{\mathrm{c}})^2 \hat{n}_{\uparrow,\mathbf{r}} \\ &+ \frac{V_y}{2} \sum_{y\in \mathrm{A,B}} (y - y_{\mathrm{c}})^2 \hat{n}_{\uparrow,\mathbf{r}} + \frac{U}{2} \sum_{\mathbf{r}\in \mathrm{A,B}} \hat{n}_{\uparrow,\mathbf{r}} (\hat{n}_{\uparrow,\mathbf{r}} - 1) - \mu_{\uparrow} \sum_i \hat{n}_i, \end{aligned} \tag{4.2}$$

where $\hat{n}_{\uparrow,\mathbf{r}} \equiv \hat{a}^{\dagger}_{\uparrow,\mathbf{r}} \hat{a}_{\uparrow,\mathbf{r}}$ ($\hat{b}^{\dagger}_{\uparrow,\mathbf{r}} \hat{b}_{\uparrow,\mathbf{r}}$) if $\mathbf{r} \in$ A ($\in$ B) and $\mathbf{r}_{\mathrm{c}} = (x_{\mathrm{c}}, y_{\mathrm{c}})$ is the position of the system's center. The parameters J, U, $\mu_{\uparrow}$ and $V_{x,y}$ are respectively the nearest-neighbor hopping amplitude, the onsite interaction energy between bosons, the chemical potential and the strength of the harmonic confinements along x and y.

The two species are coupled through the interacting term

$$\hat{H}_{\uparrow\downarrow} = -\alpha_{\uparrow\downarrow} t \sum_{\mathbf{r}\in\mathcal{A},j} \hat{a}^{\dagger}_{\downarrow,\mathbf{r}} F_j(\hat{n}_{\uparrow,\mathbf{r}}, \hat{n}_{\uparrow,\mathbf{r}+\boldsymbol{\delta}_j}) \hat{b}_{\downarrow,\mathbf{r}+\boldsymbol{\delta}_j} + \mathrm{h.c.}, \tag{4.3}$$

where $\alpha_{\uparrow\downarrow}$ is a dimensionless parameter related to the interspecies interaction strength and the function F_j is defined as

$$F_j(\hat{n}_{\uparrow,\mathbf{r}}, \hat{n}_{\uparrow,\mathbf{r}+\boldsymbol{\delta}_j}) = \frac{1}{3} \gamma_j (\hat{n}_{\uparrow,\mathbf{r}+\boldsymbol{\delta}_j} - \hat{n}_{\uparrow,\mathbf{r}}), \qquad j \in \{1,2,3\}, \tag{4.4}$$

where $\gamma_1 = 1$ and $\gamma_2 = \gamma_3 = -1$. The hopping process of the $\downarrow$ species between two sites depends on the density difference of the $\uparrow$ particles at these sites. The coupling term $\hat{H}_{\uparrow\downarrow}$ describes the *density-assisted tunneling* (DAT) processes (also called *correlated hopping*). Overall, the tunneling processes are governed by the effective hopping operators

$$t_j^{\text{eff}} = t\left(1 - \alpha_{\uparrow\downarrow}\gamma_j \frac{\hat{n}_{\uparrow,\mathbf{r}+\boldsymbol{\delta}_j} - \hat{n}_{\uparrow,\mathbf{r}}}{3}\right). \tag{4.5}$$

As shown below, an inhomogeneous density distribution of $\uparrow$ atoms will introduce a space-dependence into the tunneling processes of the $\downarrow$ particles that will therefore be able to mimic strain. Hence, the full model reads

$$\hat{H} = \hat{H}_\downarrow + \hat{H}_\uparrow + \hat{H}_{\uparrow\downarrow}. \tag{4.6}$$

In the rest of this chapter, the model (4.6) is solved in the mean-field (MF) approximation for the $\uparrow$ particles, *i.e.* the annihilation (creation) operator $a_{\downarrow,\mathbf{r}}^{(\dagger)}$ is replaced by its average value at each site $\mathbf{r}$, evaluated on the ground state. As explained in 2.9.4, this average number is the order parameter of the BEC, as prescribed by the MF approximation. This yields $\chi_{\mathbf{r}}^{(*)} = \langle \hat{a}_{\uparrow,\mathbf{r}}^{(\dagger)} \rangle$ for $\mathbf{r} \in$ A or $\chi_{\mathbf{r}} = \langle \hat{b}_{\uparrow,\mathbf{r}} \rangle$ for $\mathbf{r} \in$ B. This regime is reached when: *i*) a shallow harmonic potential that will allow for a large number of bosons at each site of the honeycomb ribbon, that is $\bar{n}_{\uparrow,\mathbf{r}} \gg 1$; *ii*) weakly-interacting bosons ($N^\uparrow$), such that $U\bar{n}_{\uparrow,\mathbf{r}} \ll 1$ for every site (see section 2.9.4). In this MF picture, the particle distribution $\bar{n}_{\mathbf{r}} = |\chi_{\mathbf{r}}|^2$ is obtained by solving the GPE, from which the ground state and its energy are found. This will be the focus of the next section. The mean value $\bar{n}_{\mathbf{r}}$ replaces its operator counterpart $\hat{n}_{\uparrow,\mathbf{r}}$ in (4.5). The Hamiltonian of the $\uparrow$ species is replaced by the bosonic mean-field energy by neglecting Bogoliubov corrections and that of the $\downarrow$ species becomes $\hat{H}_\downarrow^{\text{eff}} = \hat{H}_\downarrow + \hat{H}_{\uparrow\downarrow}^{\text{MF}}$ that reads

$$\hat{H}_\downarrow^{\text{eff}} = -\sum_{\mathbf{r}\in\text{A},j} t_j^{\text{eff}} \hat{a}_{\mathbf{r}}^\dagger \hat{b}_{\mathbf{r}+\boldsymbol{\delta}_j} + \text{H.c.}. \tag{4.7}$$

In this 2D system, we will assume that the trap is strongly anisotropic, in the sense that the trap is stronger along x than along y, *i.e.* $V_y \ll V_x$, such that the BEC can be seen as uniform along y and harmonically trapped along x. Therefore, we can interpret that the honeycomb lattice has cylindrical boundary conditions along the y-direction – see Figure 2.8. Hence, the BEC density and, consequently, the effective tunneling amplitudes are only function of x, such that

$$\begin{aligned} t_1^{\text{eff}}(x) &= t\left[1 - \frac{\alpha_{\uparrow\downarrow}}{3}(\bar{n}_\uparrow(x) - \bar{n}_\uparrow(x-a))\right], \\ t_{2,3}^{\text{eff}}(x) &= t\left[1 - \frac{\alpha_{\uparrow\downarrow}}{3}\left(\bar{n}_\uparrow\left(x + a/2\right) - \bar{n}_\uparrow(x)\right)\right]. \end{aligned} \tag{4.8}$$

Remarkably, when $\bar{n}_\uparrow(x)$ has a parabolic profile[1]

$$\bar{n}_\uparrow(x) = -\eta_1 \frac{(x - x_c)^2}{a^2}, \tag{4.9}$$

[1] Adding a constant η_0 into the expression of the parabolic profile is irrelevant as it is automatically canceled by the density difference.

where the constants η_1 is later specified, the hopping amplitudes t_j^{eff} are linear in space,

$$\begin{aligned} t_1^{\text{eff}} &= t\left[1+\frac{2}{3}\frac{\eta_1\alpha_{\uparrow\downarrow}}{a}(x-x_c)-\frac{\alpha_{\uparrow\downarrow}\eta_1}{3}\right], \\ t_{2,3}^{\text{eff}} &= t\left[1+\frac{1}{3}\frac{\eta_1\alpha_{\uparrow\downarrow}}{a}(x-x_c)+\frac{\alpha_{\uparrow\downarrow}\eta_1}{12}\right], \end{aligned} \tag{4.10}$$

If ones defines $\tau \equiv 2\alpha_{\uparrow\downarrow}\eta_1$, these DAT amplitudes reproduce those for the uniaxial strain (2.88), where the strain τ is emulated through the interspecies interaction $\alpha_{\uparrow\downarrow}$. As discussed in section 2.5.2, a pseudo vector potential $\mathbf{A}^\zeta$ emerges from this effective strain,

$$\mathbf{A}^\zeta = \left(0, -\frac{2\zeta\alpha_{\uparrow\downarrow}\eta_1}{9a^2}(x-x_c)+\frac{5\zeta\alpha_{\uparrow\downarrow}\eta_1}{36a}\right), \tag{4.11}$$

where the charge has been absorbed into the expression of the vector potential and where the last term shifts the position of the Dirac points. The effect of this shift will not be observable in the following numerical results because $\alpha_{\uparrow\downarrow}\eta_1 \ll 1$ and can therefore be neglected. The pseudo-magnetic field $\mathbf{B}_\tau^\zeta = \nabla\times\mathbf{A}^\tau$, given by

$$e^* B_\tau^\zeta(x) = -\frac{\zeta}{2v_{\text{F}}}\partial_x(2t_1^{\text{eff}} - t_2^{\text{eff}} - t_3^{\text{eff}}), \tag{4.12}$$

which only depends on the derivatives $\partial_x t_j^{\text{eff}}(x)$, is therefore uniform and reads

$$\mathbf{B}_\tau^\zeta = -\frac{2\zeta\hbar\alpha_{\uparrow\downarrow}\eta_1}{9a^2}\,\hat{\mathbf{z}} = -\frac{\zeta\hbar\tau}{9a^2}\,\hat{\mathbf{z}}, \tag{4.13}$$

and is not affected by the shift in (4.11), neither the pLLs gaps. Note that the expression (4.13) is valid when the density profile is a parabola. Nonetheless, one can still expect to find a slowly varying pseudo-magnetic field $B_\tau^\zeta(x)$ when the density profile is sufficiently smooth.

4.2 Solving the Gross-Pitaevskii equation

In this mean-field picture, one obtains the BEC density distribution by finding the function χ that minimizes the energy functional constrained by the normalization condition $N^\uparrow = \sum_{\mathbf{r}}|\chi_{\mathbf{r}}|^2$, where the chemical potential $\mu_\uparrow$ is fixed (and plays the role of a Lagrange multiplier). This reads

$$E[\chi]-\mu_\uparrow\left(\sum_{\mathbf{r}}|\chi_{\mathbf{r}}|^2-N^\uparrow\right) = E_{\text{trap}}[\chi]+E_{\text{kin}}[\chi]+E_{\text{int}}[\chi]-\mu_\uparrow\left(\sum_{\mathbf{r}}|\chi_{\mathbf{r}}|^2-N^\uparrow\right), \tag{4.14}$$

where

$$
\begin{aligned}
E_{\text{trap}}[\chi] =& \frac{V_x}{2} \sum_{\mathbf{r}\in \text{A,B}} (x - x_c)^2 \ |\chi_{\mathbf{r}}|^2, \\
E_{\text{kin}}[\chi] =& - J \sum_{\mathbf{r}\in \text{A},j} \left(\chi^*_{\mathbf{r}} \chi_{\mathbf{r}+\boldsymbol{\delta}_j} + \text{H.c.} \right), \\
E_{\text{int}}[\chi] =& \frac{U}{2} \sum_{\mathbf{r}\in \text{A,B}} |\chi_{\mathbf{r}}|^2 (|\chi_{\mathbf{r}}|^2 - 1), \\
\mu_\uparrow =& E[\chi, N^\uparrow + 1] - E[\chi, N^\uparrow].
\end{aligned}
\tag{4.15}
$$

The minimization consists in taking the functional derivative of (4.14), which results into the GPE derived in appendix B.2 and given by equation (B.2). It was solved with the imaginary-time evolution method [173] – see appendix B.3. Its solution is the BEC wavefunction in a honeycomb ribbon of $N_x \times 2$ sites with cylindrical boundary conditions along the y coordinate. The BEC wavefunction is then plugged into the three energetic contributions in (4.15), which are calculated for various values of U and compared in Figure 4.1. For $U \to 0$, the kinetic energy[2] E_{kin} equals the trap potential energy E_{trap} and decreases for increasing values of U. Indeed, as the bosons repel each other more strongly, they counterbalance the harmonic trap and spread over the system, thus reducing the density variation and the kinetic energy. By increasing U, the original Gaussian profile widens and eventually becomes almost parabolic. At larger U, the cloud will acquire the theoretical Thomas-Fermi profile when E_{kin} can be completely neglected. However, U cannot be increased indefinitely as quantum fluctuations will be more and more relevant, invalidating the MF approximation.

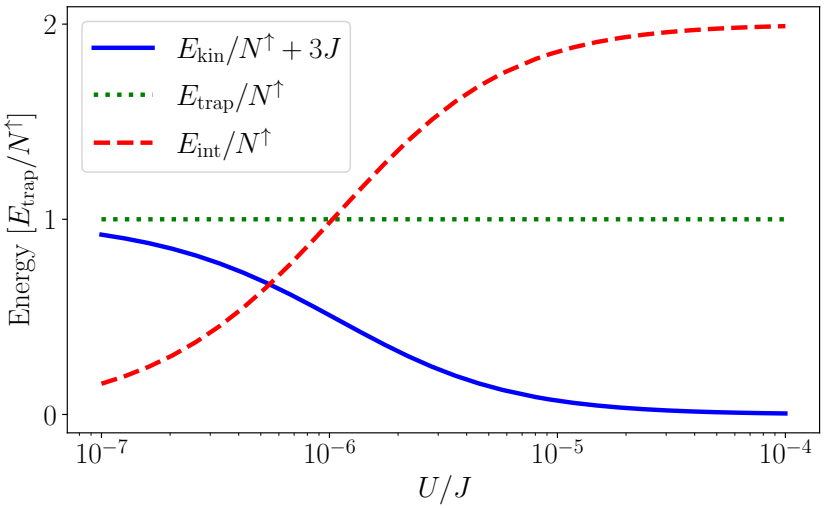

Figure 4.1: The energetic contributions are expressed in units of $E_{\text{trap}}/N^\uparrow$ as a function of the onsite interaction energy U, for $N_x = 601$, a strength of the harmonic confinement $V_x = 10^{-6} J/a^2$ and $N^\uparrow = 1.2 \times 10^5$ bosons. The $3J$-shift of the kinetic energy is due to the discretization of the Laplacian.

[2]Notice the $+3J$ in the legend of Figure 4.1 that originates from the discretization of the Laplacian.

4.2.1 Analytical limits

In this section, we explore two regimes for which the analytical expressions of the BEC density profile can be derived: the non-interacting and the Thomas-Fermi regimes. The first case occurs when $U = 0$ and the second is a regime reached when the BEC kinetic energy is negligible in comparison to the two other energetic contributions to the energy functional (4.14) [157]. In both cases, it is then possible to deduce the value of strain analytically.

Thomas-Fermi regime

The gas of $\uparrow$ atoms enters the Thomas-Fermi (TF) regime when the repulsive interacting and the trapping potential energies dominate the kinetic energy, $E_{\text{kin}} \ll E_{\text{int}}, E_{\text{trap}}$. The bosonic density is shown (blue circles) in Figure 4.2 for $V_x = 10^{-6}J/a^2$, $U = 10^{-4}J$ (using the parity symmetry with respect to $x = x_c$, only the part for $x \geq x_c$ is plotted). In general, it is accurately reproduced by the exact Thomas-Fermi distribution $\bar{n}_{\text{TF}}$ (solid orange line) obtained when E_{kin} is discarded, which reads

$$\bar{n}_{\text{TF}}(x) = \frac{1}{U}\left[\mu_\uparrow - \frac{V_x}{2}(x - x_c)^2\right]. \tag{4.16}$$

By substituting (4.16) into (4.8), the strain intensity τ^{eff} is expressed in terms of the harmonic trap parameter V_x and the interaction strength U as

$$\tau_{\text{eff}} = \frac{\alpha_{\uparrow\downarrow} V_x a^2}{U}. \tag{4.17}$$

Discrepancies between $\bar{n}_\uparrow$ and $\bar{n}_{\text{TF}}$ take place at the boundary of the cloud, located at $x = R_{\text{TF}} = \sqrt{2\mu_\uparrow/V_x}$, where the derivative of the distribution cannot be neglected anymore. The cloud's boundary therefore marks a separation between a region with strain ($|x - x_c| < R_{\text{TF}}$) and without strain ($|x - x_c| > R_{\text{TF}}$). Equivalently, it implies that a pseudo-magnetic field, identified by a dashed purple line in Figure 4.2 and given by (4.12), is present inside the cloud but vanishes at the edge. Deep in the bulk, it takes the value

$$B_0 = -\frac{\zeta\hbar\alpha_{\uparrow\downarrow} V_x}{9U}, \tag{4.18}$$

and changes abruptly near the edge before vanishing out of the cloud – see Figure 4.2.
Figure 4.3 shows the spectrum of $\hat{H}_\downarrow^{\text{eff}}$ for $U = 10^{-4}J$, which corresponds to an effective strain intensity $\tau^{\text{eff}} = 0.003$. The first five pLLs are clearly identifiable at energies predicted by (4.40) for $\tau = \tau^{\text{eff}}$, indicated by dashed red lines. Other conical structures are also visible in the spectrum, resembling those in Figure 2.9, for the unstrained honeycomb lattice, described by the Hamiltonian (4.1). They correspond to $\downarrow$ states localized outside the BEC cloud where, as expected from the $\uparrow$ distribution in Figure 4.2, there is no bosons and therefore no strain. The intermediate region around the boundary of the cloud at $x = R_{\text{TF}}$ is not a hard wall potential, allowing a penetration of the wavefunctions from both sides of this interface. This

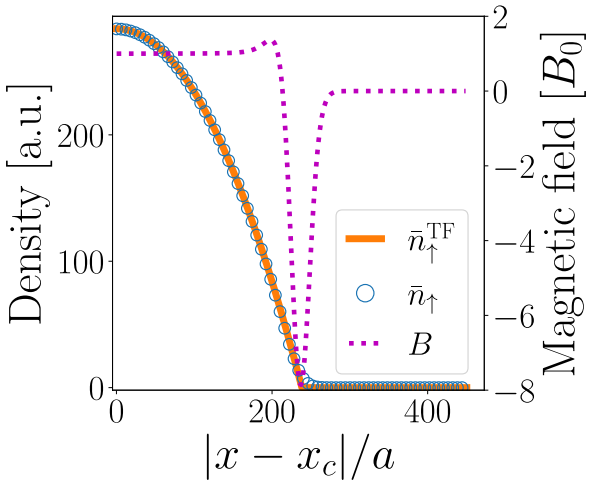

Figure 4.2: Density profile of the ↑-atoms in the Thomas-Fermi regime (blue circles) for a strength of harmonic trap $V_x = 10^{-6}J/a^2$, $N^\uparrow = 1.2 \times 10^5$ bosons and an onsite interaction $U = 10^4 J$. The orange solid line represents the analytical Thomas-Fermi distribution (4.16). The resulting magnetic field (dotted magenta line) is shown in units of B_0, the value of the magnetic field at the center of the trap, x_c.

phenomenon is emphasized by further distinguishing the contributions from the strained and unstrained parts of the ribbon. The spectrum (empty circles) of a strained lattice honeycomb, only extended over the size of the BEC ($L_x = 2R_{\mathrm{TF}}$) with the same strain intensity, is superimposed over the spectrum of $\hat{H}_\downarrow^{\mathrm{eff}}$. The pLLs plateaus are clearly identified, as well as the edge states branches on the left of the Dirac point ($k_y < K_y = 2\pi/3\sqrt{3}a = 1.21/a$). For $k_y a > 1.25$, deviations between the two spectra appear, in addition to a distinct branch, indicated by the black arrow. These discrepancies are explained by the hybridization between pLLs and planewave states living on the inside and outside of the cloud interface, respectively. The hybridization manifests itself through the gap-crossing branch and avoided crossings between pLLs and the conical structure. By plotting the wavefunctions of four states associated to the branch, one understands that it originates from modes localized at the left edge of the cloud – see Figure 4.4. The marker used to plot the wavefunctions correspond to the markers of the four dots in Figure 4.3.

Non-interacting regime

The second regime for which an analytical expression can be obtained in the non-interacting limit, *i.e.* $U = 0$. If the bosons are trapped by a weak harmonic potential such that the cloud's width is much larger than the lattice spacing and smaller than the system's size, the density profile is well approximated by a Gaussian whose expression reads

$$\bar{n}_\uparrow = \frac{3N^\uparrow}{4\sqrt{2\pi}\xi} \mathrm{e}^{-(x-x_c)^2/2\xi^2}, \qquad \xi \equiv \left(\frac{3Ja^2}{8V_x}\right)^{1/4}, \tag{4.19}$$

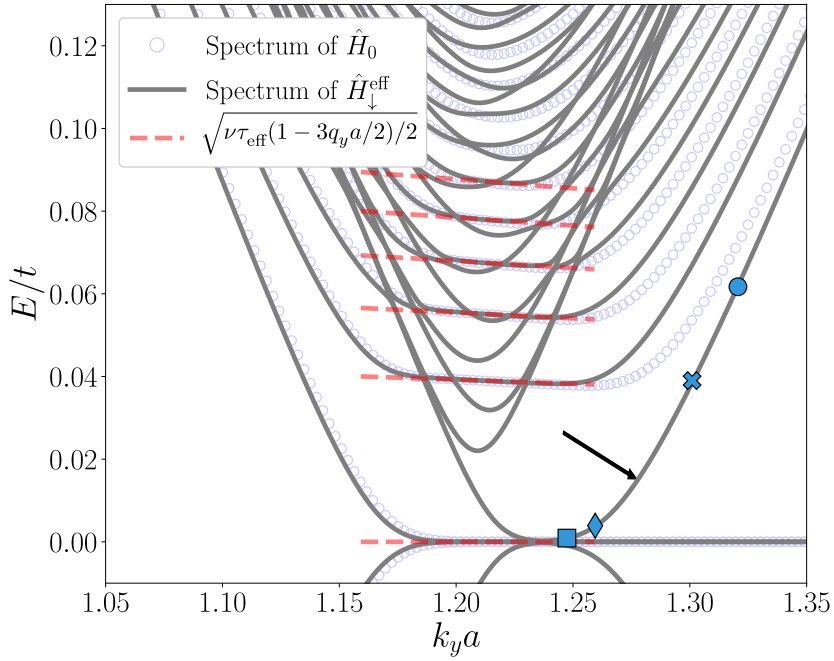

Figure 4.3: Spectrum of $\hat{H}_\downarrow^{\text{eff}}$ when the Bose-Einstein condensate of $\uparrow$-atoms is in the Thomas-Fermi regime, including a comparison with the spectrum of the strained honeycomb Hamiltonian $\hat{H}_0$ (empty circles) – see (3.19) – and the pseudo-Landau levels predicted by (2.94) (dashed lines). The number of sites along x is $N_x = 601$, the onsite interaction is $U = 10^{-4}J$, the strength of the harmonic trap is $V_x = 10^{-6}J/a^2$, the number of condensed bosons is $N^\uparrow = 1.2 \times 10^5$, and the interspecies interaction strength is $\alpha_{\uparrow\downarrow} = 0.3$. The strain intensity is $\tau_{\text{eff}} = 0.003$. The four dots with different markers correspond to representative eigenstates of the energy branch indicated by the arrow that will be shown in a separate figure.

where ξ is the cloud's width centered at x_c and the factor $3/4$ is a consequence of the honeycomb geometry – see Appendix B.1. The agreement between the Gaussian (solid orange line) and the (numerically obtained) BEC distribution is shown Figure 4.5.

Obviously, substituting $\bar{n}_\uparrow$ will not induce the hopping amplitudes (4.8) to be linear in x. Nevertheless, near x_c, i.e. $|x - x_c| \ll \xi$, the density can be approximated by the parabola

$$\bar{n}_\uparrow = \frac{3N^\uparrow}{4\sqrt{2\pi}\xi}\left[1 - \frac{(x-x_c)^2}{2\xi^2}\right]. \tag{4.20}$$

The corresponding effective strain intensity reads

$$\tau_{\text{eff}} = \frac{3N^\uparrow \alpha_{\uparrow\downarrow} a^3}{4\sqrt{2\pi}\xi^3}. \tag{4.21}$$

As shown in Figure 4.6, differently from the TF regime, the analytical prediction (2.94) for the pLLs is in good agreement with the numerical spectrum only very close to the **K** point. Away from the latter, noticeable differences between the spectra of these two regimes appear. They can directly be inferred from the inspection of their respective density profiles in Figures 4.2

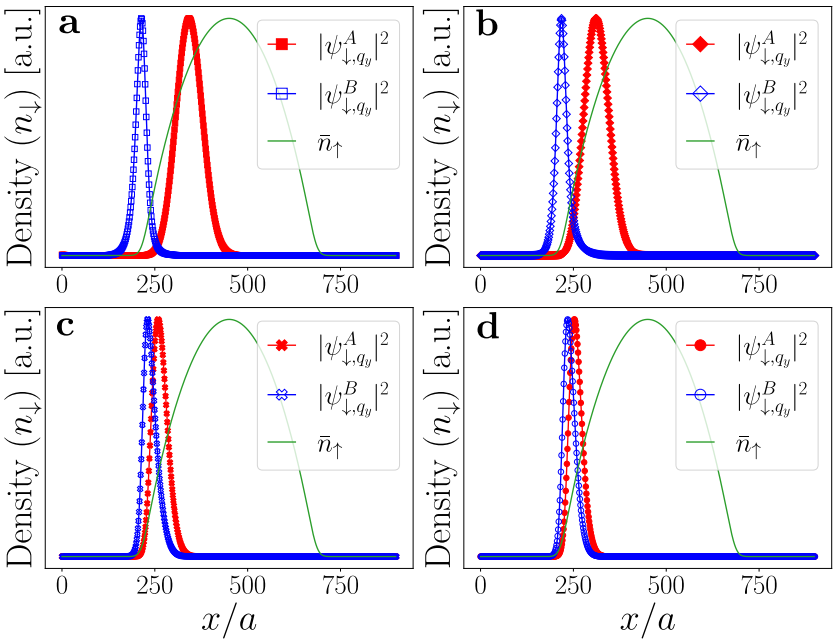

Figure 4.4: Density of the $\downarrow$ atoms corresponding to the four markers indicated in Figure 4.3. The A and B components of the eigenvectors of $\hat{H}^{\text{eff}}_{\downarrow}$ are denoted by $\psi^l_{\downarrow,q_y}$ for $l = A, B$ respectively. Their respective points in the spectrum have the following coordinates $(q_y a, E)$: **a** $(0.038, 0.0009)$, **b** $(0.050, 0.0039)$, **c** $(0.091, 0.0390)$, **d** $(0.111, 0.0617)$.

and 4.5. First, the deviations from an ideal parabola in the non-interacting case implies non-linear space-dependence in the hopping amplitudes, resulting into a non-uniform magnetic field. Hence, further away from the center ($|x - x_c| \gtrsim \xi$), the pLLs picture presented earlier simply fails because it required a uniform magnetic field. Secondly, the transition between the region with bosons and the one without bosons, that is between the effectively strained region and the unstrained one, is smoother. Therefore, this sort of overlapping conical structure on top of pLLs, previously observed in Figure 4.3 for the TF regime, is barely visible in the non-interacting regime. Jointly with the avoided crossings due hybridizations between planewave states and pLLs, it prevents any clear identification of the latter.

In view of elucidating the consequences of the magnetic field's inhomogeneity, one might assume that it smoothly varies in space. This allows to apply a local-density approximation, which requires $\ell_B, |x - x_c| \ll \xi$. In this picture, one can associate to each position $x = x_0$ and its neighboring region, a magnetic field $B(x_0)$ given by (4.12). Remember that eigenvectors' wavefunctions centered at x_0 correspond to a specific momentum due to $x_0 = x_c - \zeta \ell_B^2(x_0) q_y$ – see (2.27). Their pLLs energies are proportional to $\sqrt{B(x_0)}$ and thus deviates from (2.94) away from the **K** point. Actually, the inhomogeneity of the pseudo-magnetic field translates into a bending down of the pLLs. This behavior is well captured by further expanding the Gaussian (4.19) to the fourth order in $(x - x_c)/\xi$, yielding

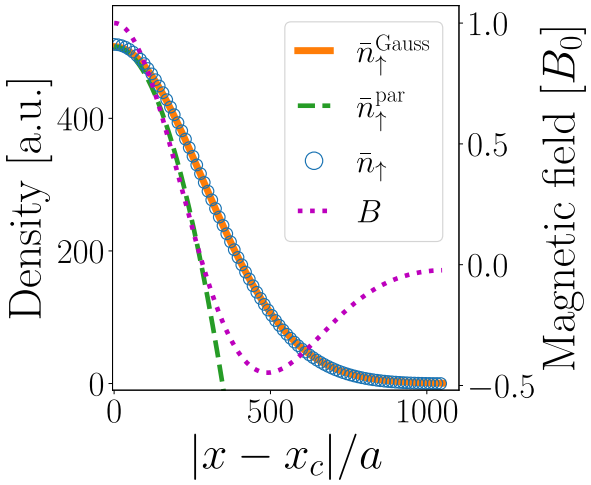

Figure 4.5: Density profile of the ↑-atoms in the non-interacting regime (blue circles) for $V_x = 5.8 \times 10^{-11} J/a^2$, $N^\uparrow = 4.8 \times 10^5$, $N_x = 1401$. The dashed green line is the approximate parabolic profile valid for $|x - x_c| \ll \xi$, where ξ is the Gaussian width (see Eq. (4.16)). The orange solid line represents the analytical Gaussian distribution (4.19) The resulting magnetic field (dotted magenta line) is shown in units of B_0, the value of the magnetic field at the center of the trap, x_c.

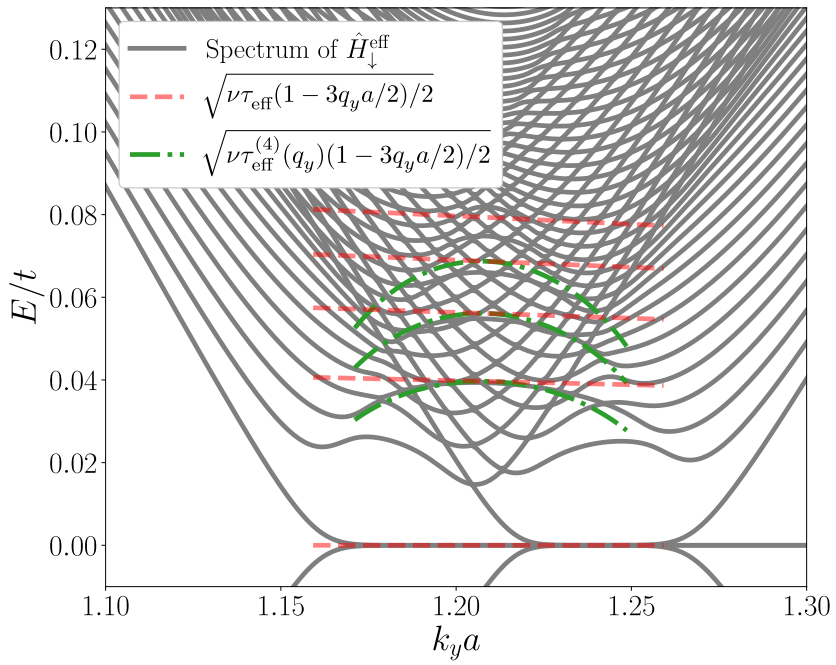

Figure 4.6: Spectrum of $\hat{H}_\downarrow^{\text{eff}}$ when the Bose-Einstein condensate of the ↑-atoms is in the non-interacting regime. The number of sites along x is $N_x = 1401$, the strength of the harmonic confinement is $V_x = 5.8 \times 10^{-11} J/a^2$, the number of bosons is $N^\uparrow = 4.8 \times 10^5$ and the interspecies interaction strength is $\alpha_{\uparrow\downarrow} = 0.49$. The strain intensity is $\tau_{\text{eff}} = 3.1 \times 10^{-3}$. Dashed red lines represent the predicted Landau energies for a homogeneous synthetic magnetic field, whereas the dashed-dotted green lines are obtained by including the leading effects of inhomogeneity.

$$\bar{n}_{\uparrow} = \frac{3N^{\uparrow}}{4\sqrt{2\pi}\xi}\left[1 - \frac{(x-x_{\rm c})^2}{2\xi^2} + \frac{(x-x_{\rm c})^4}{4\xi^4}\right]. \tag{4.22}$$

Indeed, this implies the strain parameter to be a function of space as

$$\tau_{\rm eff}^{(4)}(x) = \tau_{\rm eff}\left[1 - \frac{7a^2 - 30a(x-x_{\rm c}) + 12(x-x_{\rm c})^2}{4\xi^2}\right], \tag{4.23}$$

where $\tau_{\rm eff}$ is defined in (4.21). This results in modified pLLs,

$$\epsilon_{\nu}^{(4)} = \pm\, t\sqrt{\frac{\nu}{2}\tau_{\rm eff}\left(1 - \zeta\frac{3}{2}q_y a\right)}\sqrt{1 - \frac{7a^2}{4\xi^2} - \frac{15\zeta\ell_B^2}{2\xi^2}q_y a - \frac{3\ell_B^4}{a^2\xi^2}(q_y a)^2}\,. \tag{4.24}$$

As presented in Figure 4.6, the revised dispersion relation (4.24) (dashed green lines) captures reasonably well the bending of the lowest pLLs.

4.3 Fidelity analysis

Beyond the spectral comparison between the spectrum of the effectively strained honeycomb lattice model $\hat{H}_{\downarrow}^{\rm eff}$, and the spectrum of $\hat{H}_0$ describing the uniaxially strained honeycomb lattice – see Eq. (3.19) – one can ask how the eigenstates of both Hamiltonians compare. To establish this comparison, we employ the fidelity

$$\mathcal{F}(\nu, q_y) = |\langle\phi_{\nu,q_y}|\psi_{\downarrow,q_y}\rangle|^2, \tag{4.25}$$

where $\psi_{\downarrow,q_y}$ denotes the eigenstates of $\hat{H}_{\downarrow}^{\rm eff}$ and ϕ_{ν,q_y} those of $\hat{H}_0$ corresponding to the $\nu^{\rm th}$ pLL. As encountered in Figures 4.3 and 4.6, the spectrum of $\hat{H}_{\downarrow}^{\rm eff}$ differs from the one of $\hat{H}_0$ due to the exterior region without strain. To minimize the effects of these discrepancies, one can focus on a window $q_y \in [q_y^{\rm min}, q_y^{\rm max}]$ centered around the **K**-point that includes most of the pLLs. This interval in q_y corresponds to states localized deep in the cloud, near $x_{\rm c}$. We color each point of the spectrum with $\mathcal{F}(\nu, q_y)$ within this window in Figures 4.3 and 4.6. The results are shown in Figures 4.7**a**,**b** for $\nu = 1,\ 2,\ 3$ in the TF and the non-interacting regimes, respectively. The parameters values are chosen as in the previous section.

For both regimes, the eigenstates of $\hat{H}_{\downarrow}^{\rm eff}$ accurately reproduce those of $\hat{H}_0$ as the fidelity is larger than 0.9 in the chosen interval. Nevertheless, away from the Dirac point, it drops and even more in the non-interacting case. This is a direct consequence of the inhomogeneous magnetic field, that alters the pLL wavefunction. In particular, $B(x)$ decreases with the distance from $x_{\rm c}$, which enlarges the tail of the wavefunctions and therefore lowers the fidelity.

One can inspect how precise the LL picture remains as the (dimensionless) interspecies inter-

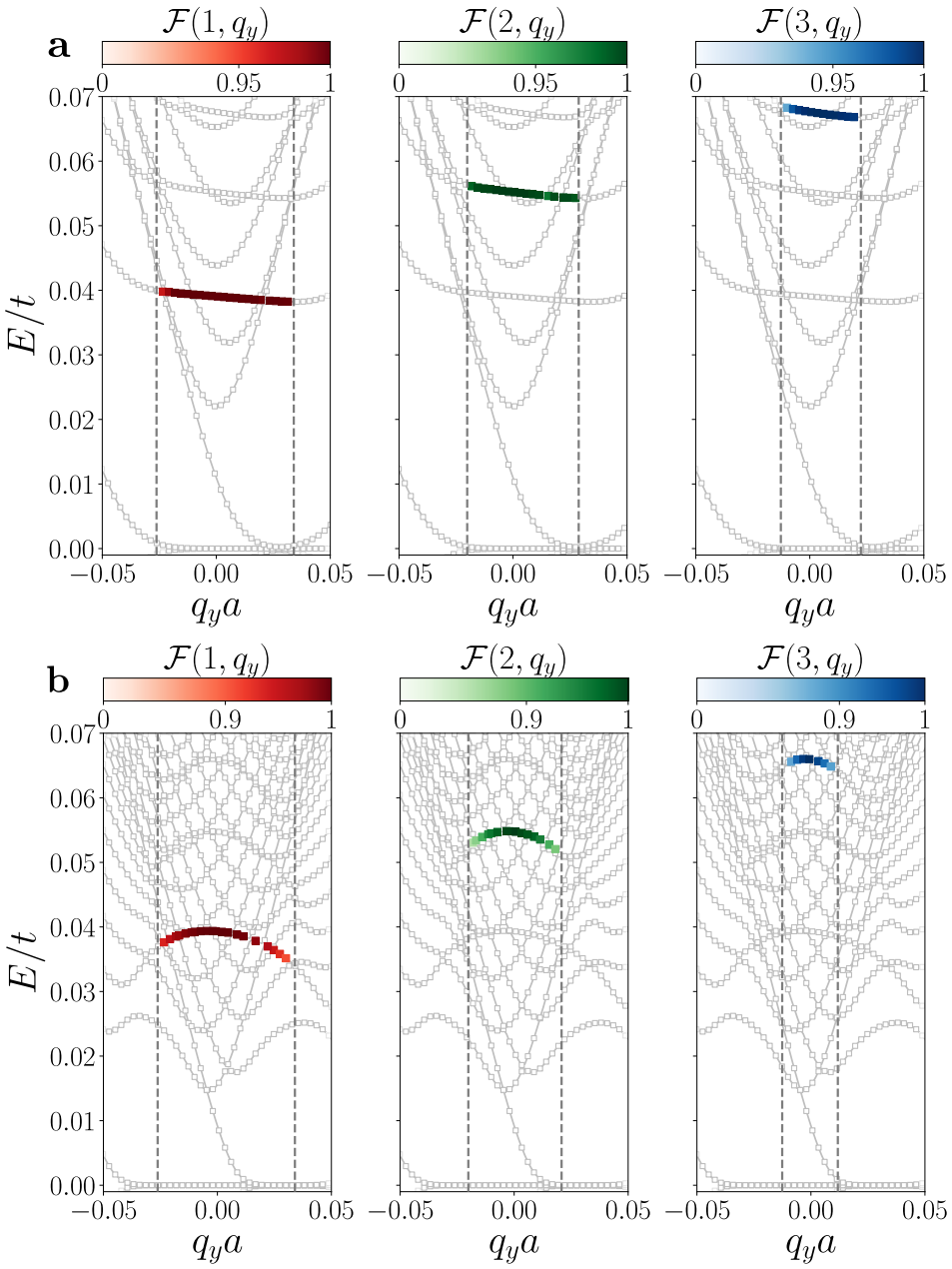

Figure 4.7: Spectra of $\hat{H}_{\downarrow}^{\text{eff}}$ around the K point obtained **a** in the Thomas-Fermi regime and **b** in the non-interacting regime, where we superimpose the fidelity $\mathcal{F}(\nu, q_y)$ with the Landau level eigenstates computed in a range of momenta delimited by the vertical dashed lines. Each panel addresses the fidelity of the ν^{th} Landau level. The parameters for the two regimes are chosen as in the previous plots. For **a**, the number of sites along x is $N_x = 601$, the onsite interaction is $U = 10^{-4}J$, the strength of the harmonic trap is $V_x = 10^{-6}J/a^2$, the number of condensed bosons is $N^{\uparrow} = 1.2 \times 10^5$, and the interspecies interaction strength is $\alpha = 0.3$. For **b**, $N_x = 1401$, $V_x = 5.8 \times 10^{-11}J/a^2$, $N^{\uparrow} = 4.8 \times 10^5$ and $\alpha_{\uparrow\downarrow} = 0.49$. As the fidelity is calculated for bulk state, the range of momenta has been chosen to avoid interface or edge-states effects.

action parameter $\alpha_{\uparrow\downarrow}$ varies, which can be reinterpreted as tuning the effective strain intensity – see (4.17) and (4.21). To do so, one inspects how the fidelity changes with $\alpha_{\uparrow\downarrow}$. Concretely,

for each value of $\alpha_{\uparrow\downarrow}$ while keeping the other parameters fixed, we extract the maximal value of the fidelity on each of the first three pLLs within the q_y-window introduced above, i.e.

$$\mathcal{F}_M(\nu) = \max_{q_y} \mathcal{F}(\nu, q_y). \tag{4.26}$$

The results are presented in Figure 4.8**a** and **b** for the TF and non-interacting regimes, respectively. These plots can be understood through a lengthscale analysis. The smallest scale is the lattice spacing a and the largest (apart from the system size L_x) is the cloud's width R_{TF} or ξ. These have to be compared to the magnetic length ℓ_B, which is the relevant scale of the LL physics. In both regimes, at high $\alpha_{\uparrow\downarrow}$ the fidelity $\mathcal{F}_M$ tends to 1. When $\alpha_{\uparrow\downarrow}$ decreases, $\mathcal{F}_M$ is reduced and even more for $\nu \geq 2$. Indeed, as shown in Figure 4.9, while the 1^{st}-LL wavefunctions of $\hat{H}_{\downarrow}^{\text{eff}}$ are well localized around x_{c} (see the solid red lines in panels **a** and **b** for the TF and non-interacting regimes, respectively), higher-LL wavefunctions are broader, thus cross the interface and hybridize with planewave solutions of the unstrained region – see panels **c** and **d** for the TF and non-interacting regimes, respectively. As expected from the discussion about Figure 4.7, it is clear that reaching the interface changes the tails of the wavefunctions due to the inhomogeneity of the pseudo-magnetic field, which itself stems from deviations of the $\uparrow$-particle distribution from the ideal parabolic profile (depicted by the double-dotted blue line). For concreteness, the counterpart wavefunction in the ideal strain case (dotted-dashed black lines) and the BEC density (dotted-dashed green line) have been added. In the TF regime (panel **c**), while an hybridization occurs at both cloud edges, the abrupt increase of $|B_\tau(x)|$ around $x = R_{\text{TF}}$ is expected to shrink the tail of the $\downarrow$-particle distribution. This is visible to the right end of the cloud but not to its left as competing hybridization mechanisms deform the left tail. In the non-interacting case (panel **d**), the overall decrease of $|B_\tau(x)|$ widens the tails of the $\downarrow$-particle distribution.

Besides, if $\alpha_{\uparrow\downarrow}$ is too large, the LL picture breaks down because $\ell_B \propto 1/\sqrt{\alpha_{\uparrow\downarrow}}$ becomes comparable to the lattice spacing a and discretization effects take place. This is shown in Figure 4.10**a** and **b** for the TF and non-interacting regimes, respectively, where we show the maximum fidelity (for the ν^{th} LL)

$$\mathcal{F}'_M(\nu) = \max_{q_y} |\langle \psi_{\nu,q_y} | \varphi_{\nu,q_y} \rangle|^2 \tag{4.27}$$

between eigenstates of $\hat{H}_{\downarrow}^{\text{eff}}$ and the analytical relativistic LLs (2.71), now denoted by φ_{ν,q_y}. Indeed, $\mathcal{F}'_M(\nu)$ decreases when $\alpha_{\uparrow\downarrow}$ increases. Furthermore, the discretization effects get even more detrimental for higher ν since more nodes, that are resolved at a precision of the order of a, constraint the width ($\ell_B \sim a$) and the shape of the wavefunctions' lobes. Another reason for the drop in fidelity, already discussed in [142], arises from the asymmetry of the wavefunctions with respect to x_{c}, as presented in Figure 4.9, whereas the analytical LL states are symmetric. This difference, negligible for low values of τ, would fade away by including neglected terms

in the effective Dirac model, such as the space-dependence of the Fermi velocity v_{F}. Hence, $\alpha_{\uparrow\downarrow}$ must be kept sufficiently low such that $\ell_B \gg a$ is ensured. In conclusion, the ideal scenario to recover the LL physics is $a \ll \ell_B \ll R_{\mathrm{TF}}, \xi$.

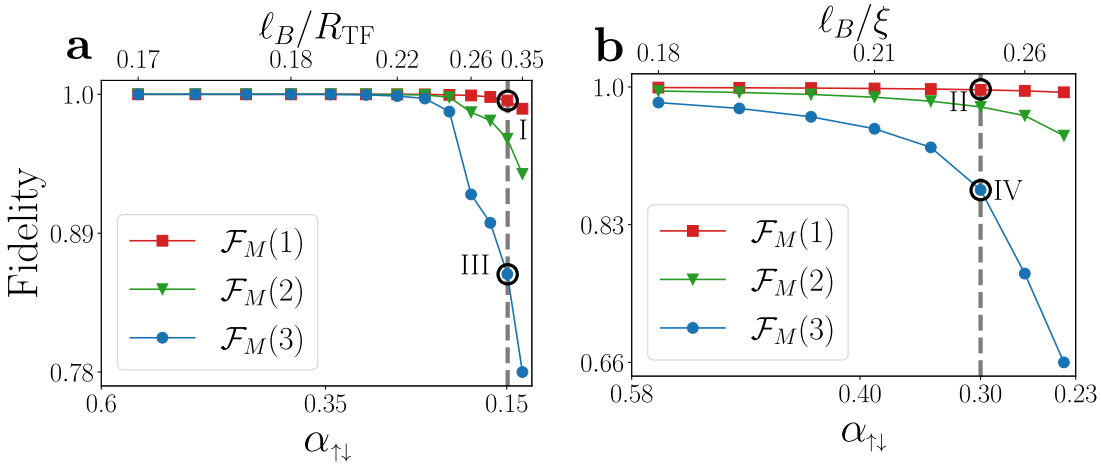

Figure 4.8: Fidelity $\mathcal{F}_M$ as a function of $\alpha_{\uparrow\downarrow}(\ell_B)$ for **a** the Thomas-Fermi regime with an onsite interaction $U = 10^{-4}J$, a strength of harmonic confinement $V_x = 10^{-6}J/a^2$ and a number of bosons $N^{\uparrow} = 1.2 \times 10^5$ and for **b** the non-interacting regime with $U = 0$, $V_x = 5.8 \times 10^{-11}J/a^2$, $N^{\uparrow} = 4.8 \times 10^5$. The wavefunctions of the dots indicated by roman numbers are taken as representative examples that are shown in Figure 4.9.

4.4 Density-assisted tunneling from Floquet engineering

We now explain how to generate the density-assisted tunneling amplitudes of the $\downarrow$ species – see Eq. (4.5). In the following, the strategy to create these DAT terms is first presented for a double-well system and is then generalized to the full honeycomb lattice.

4.4.1 Density-assisted tunneling from resonant Floquet engineering in a double-well

In order to obtain these DAT amplitudes, one needs to adapt the resonant Floquet scheme introduced with a simple example in section 2.8.4, to the case of a periodically-driven inter-species interaction. In the double-well system sketched in Figure 4.11, two species of atoms, $\uparrow$ and $\downarrow$, are trapped in the same double-well. Their respective Hamiltonians read

$$\begin{aligned} \hat{H}_{\uparrow} &= -J\hat{c}^{\dagger}_{\uparrow,0}\hat{c}_{\uparrow,1} - J\hat{c}^{\dagger}_{\uparrow,1}\hat{c}_{\uparrow,0} + \frac{U}{2}\sum_{i=0}^{1}\hat{n}_{\uparrow,i}(\hat{n}_{\uparrow,i}-1), \\ \hat{H}_{\downarrow} &= -t\hat{c}^{\dagger}_{\downarrow,0}\hat{c}_{\downarrow,1} - t\hat{c}^{\dagger}_{\downarrow,1}\hat{c}_{\downarrow,0} + \Delta\hat{n}_{\downarrow,1}, \end{aligned} \tag{4.28}$$

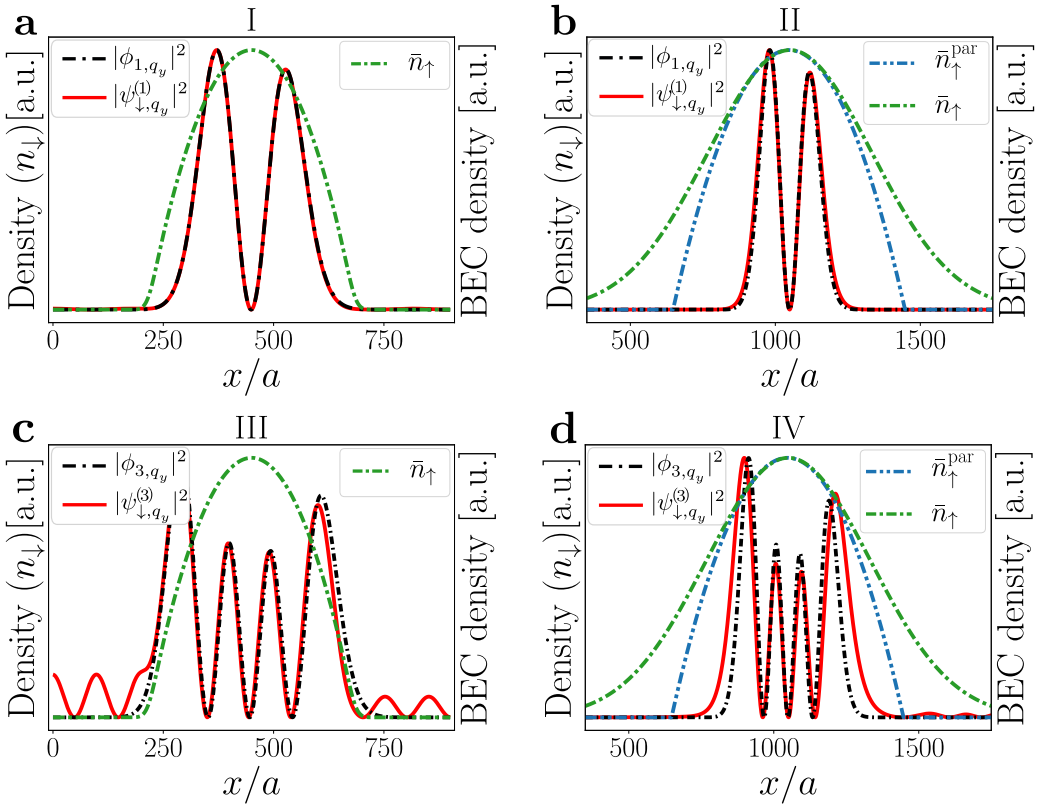

Figure 4.9: Density from the eigenvectors of (dashed red lines) $\hat{H}^{\rm eff}_\downarrow$ and (solid black lines) $\hat{H}_0$ corresponding to the circles indicated in Figures 4.8**a**,**b** for $q_y a = 0$ in **a**,**b** and $q_y a = -0.00067$ in **c**,**d**. In all panels are plotted only the A components. The single-dashed and double-dashed lines represent the numerical solution of the Gross-Pitaevskii equation $\bar{n}_\uparrow$ and the parabolic profile $\bar{n}_{\rm par}$ that approximates the Gaussian at its maximum, respectively.

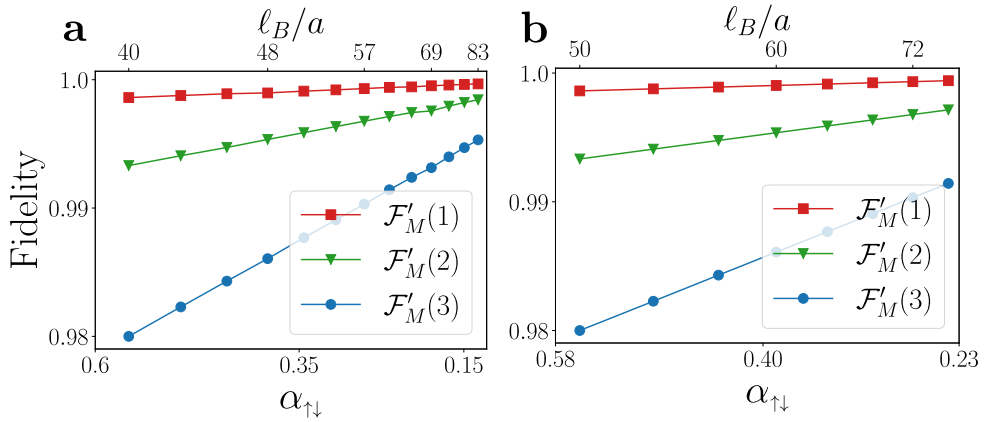

Figure 4.10: Fidelity $\mathcal{F}'_M$ as a function of $\alpha_{\uparrow\downarrow}(\ell_B)$ for **a** the Thomas-Fermi regime and for **b** the non-interacting regime with for the same values of parameters as in Figure 4.8**a**,**b**, respectively.

where $\hat{c}^\dagger_{\sigma,i}$ ($\hat{c}_{\sigma,i}$) is the creation (annihilation) operator of the $\sigma =\uparrow,\downarrow$ particle at site $i = 0, 1$ and $\hat{n}_{\sigma,i}$ their number operator. The parameters t and J are the tunneling amplitudes of the $\downarrow$ and $\uparrow$-atoms, respectively, whereas U is the interaction strength between $\uparrow$-atoms. The

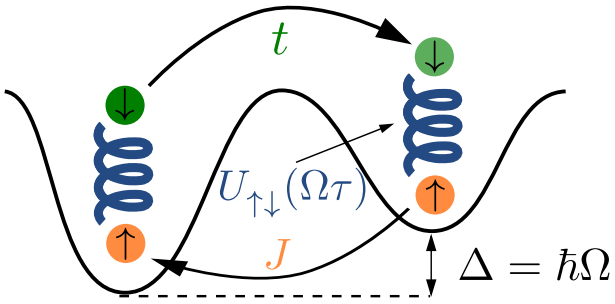

Figure 4.11: Sketch of the system described by the Hamiltonian (4.29). The parameters Δ and $U_{\uparrow\downarrow}$ are the energy imbalance between the wells and the interspecies interaction strength, respectively. The parameters t and J are the tunneling amplitudes of the $\downarrow$ and $\uparrow$-atoms, respectively, whereas U is the interaction strength between bosons

parameter Δ is an energy imbalance between the two sites, only experienced by the $\downarrow$-species that suppresses its hopping process. The two species are coupled by

$$\hat{\mathcal{V}}(\tau) = U_{\uparrow\downarrow}\cos(\Omega\tau)\left(\hat{n}_{\uparrow,0}\hat{n}_{\downarrow,0} + \hat{n}_{\uparrow,1}\hat{n}_{\downarrow,1}\right) \tag{4.29}$$

that corresponds to periodically-driven onsite interspecies interactions, at frequency Ω. The parameter $U_{\uparrow\downarrow}$ is the interspecies interaction strength. We add another time-dependent onsite energy term $\Delta_0\cos(\Omega\tau)\hat{n}_{\downarrow,0}$, whose role will soon become clear. The hopping process of the $\downarrow$-particle from one well to the other can be restored by a resonant drive $\hbar\Omega \simeq \Delta$. Following the same reasoning as in section 2.8.3 where $\mathcal{K}_{0(1)} = U_{\uparrow\downarrow}\hat{n}_{\uparrow,0(1)}$, the transformation[3] to the rotating frame

$$\hat{\mathcal{R}} = \exp\left\{\mathrm{i}\left[\frac{U_{\uparrow\downarrow}\hat{n}_{\uparrow,0}}{\hbar\Omega}\sin(\Omega\tau)\hat{n}_{\downarrow,0} + \frac{U_{\uparrow\downarrow}\hat{n}_{\uparrow,1}}{\hbar\Omega}\sin(\Omega\tau)\hat{n}_{\downarrow,1} + \Omega\tau\hat{n}_{\downarrow,1} + \Delta_0\hat{n}_{\downarrow,0}\sin(\Omega\tau)\right]\right\}, \tag{4.30}$$

yields

$$\begin{aligned}\hat{H}_{\mathrm{F}}^{(0)} = &-t\,\mathcal{J}_1\left(\frac{U_{\uparrow\downarrow}(\hat{n}_{\uparrow,0}-\hat{n}_{\uparrow,1})+\Delta_0}{\hbar\Omega}\right)\hat{c}^\dagger_{\downarrow,0}\hat{c}_{\downarrow,1}\\ &- J\mathcal{J}_0\left(\frac{U_{\uparrow\downarrow}(\hat{n}_{\downarrow,0}-\hat{n}_{\downarrow,1})}{\hbar\Omega}\right)\hat{c}^\dagger_{\uparrow,0}\hat{c}_{\uparrow,1} + \mathrm{H.c.}\\ &+ \frac{U}{2}\sum_{i=0}^{1}\hat{n}_{\uparrow,i}(\hat{n}_{\uparrow,i}-1),\end{aligned} \tag{4.31}$$

which is the 0^{th}-order term of the high-frequency expansion. The Bessel functions $\mathcal{J}_0(x) \approx 1$

[3] See appendix B.4 for the full derivation.

and $\mathcal{J}_1(x) \approx x/2$ when $x \ll 1$, which is satisfied when $\Delta_0 \ll \hbar\Omega$ and

$$\begin{aligned}
&\frac{U_{\uparrow\downarrow}}{\hbar\Omega}\left|\left\langle\{n'_{\downarrow,i}\}\right|\left(\hat{n}_{\downarrow,0}-\hat{n}_{\downarrow,1}\right)\left|\{n_{\downarrow,i}\}\right\rangle\right| \ll 1,\\
&\frac{U_{\uparrow\downarrow}}{\hbar\Omega}\left|\left\langle\{n'_{\uparrow,i}\}\right|\hat{n}_{\uparrow,0}-\hat{n}_{\uparrow,1}\left|\{n_{\uparrow,i}\}\right\rangle\right| \ll 1,
\end{aligned} \tag{4.32}$$

where $\{n_{\sigma,i}\}$ labels the Fock states for the $\sigma = \uparrow, \downarrow$ species. These two conditions impose that there is no large population imbalance between the wells. Increasing the driving frequency and reducing the interaction also help to satisfy this condition. Once $\mathcal{J}_0$ and $\mathcal{J}_1$ are expanded to first order, the Hamiltonian (4.31) reads

$$\begin{aligned}
\hat{H}_{\mathrm{F}}^{(0)} = &-t\left(\frac{\Delta_0}{2\hbar\Omega}+\frac{U_{\uparrow\downarrow}}{2\hbar\Omega}(\hat{n}_{\uparrow,0}-\hat{n}_{\uparrow,1})\right)\hat{c}^{\dagger}_{\downarrow,0}\hat{c}_{\downarrow,1}\\
&-J\hat{c}^{\dagger}_{\uparrow,0}\hat{c}_{\uparrow,1}+\frac{U}{2}\sum_{i=0}^{1}\hat{n}_{\uparrow,i}(\hat{n}_{\uparrow,i}-1)+\mathrm{H.c.},
\end{aligned} \tag{4.33}$$

where the parameters Δ_0 allows to restore the dominant part of the hopping amplitudes (2.87). By redefining the energy scale $t \to 2t\hbar\Omega/\Delta_0$, one gets

$$\begin{aligned}
\hat{H}_{\mathrm{F}}^{(0)} = &-t\left(1+\frac{U_{\uparrow\downarrow}}{\Delta_0}(\hat{n}_{\uparrow,0}-\hat{n}_{\uparrow,1})\right)\hat{c}^{\dagger}_{\downarrow,0}\hat{c}_{\downarrow,1}-J\hat{c}^{\dagger}_{\uparrow,0}\hat{c}_{\uparrow,1}+\mathrm{H.c.}\\
&+\frac{U}{2}\sum_{i=0}^{1}\hat{n}_{\uparrow,i}(\hat{n}_{\uparrow,i}-1).
\end{aligned} \tag{4.34}$$

Introducing a new parameter $\alpha_{\uparrow\downarrow} \equiv 3U_{\uparrow\downarrow}/\Delta_0$, one finally ends up with

$$\begin{aligned}
\hat{H}_{\mathrm{F}}^{(0)} = &-t\left(1+\frac{\alpha_{\uparrow\downarrow}}{3}(\hat{n}_{\uparrow,0}-\hat{n}_{\uparrow,1})\right)(\hat{c}^{\dagger}_{\downarrow,0}\hat{c}_{\downarrow,1}+\hat{c}^{\dagger}_{\downarrow,1}\hat{c}_{\downarrow,0})\\
&-J(\hat{c}^{\dagger}_{\uparrow,0}\hat{c}_{\uparrow,1}+\hat{c}^{\dagger}_{\uparrow,1}\hat{c}_{\uparrow,0})+\frac{U}{2}\sum_{i=0}^{1}\hat{n}_{\uparrow,i}(\hat{n}_{\uparrow,i}-1).
\end{aligned} \tag{4.35}$$

Applying the mean-field approximation for bosons, the second line of (4.35) becomes a simple energy shift and one gets the desired hopping amplitudes of Eq. (4.8) for the $\downarrow$-atoms (only for a double-well system at this point),

$$\hat{H}_{\mathrm{F}}^{(0)} = E_{\mathrm{MF}}-t\left(1+\frac{\alpha_{\uparrow\downarrow}}{3}(\bar{n}_{\uparrow,0}-\bar{n}_{\uparrow,1})\right)\hat{c}^{\dagger}_{\downarrow,0}\hat{c}_{\downarrow,1}+\mathrm{H.c.} \tag{4.36}$$

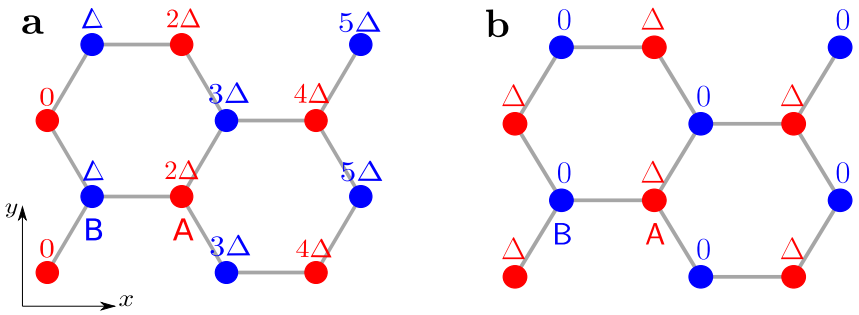

Figure 4.12: Two possible Floquet engineering schemes of strain as described in the main text. **a** Energy offset Δ linearly growing in the x direction. **b** Homogeneous energy offsets Δ only on the A sites.

4.4.2 Density-assisted tunneling from Floquet engineering in a honeycomb lattice

In order to reproduce the uniaxial strain scheme, the results obtained for the double-well system in the preceding section must be extended to a honeycomb lattice. To do so, one applies on each site an energy offset that grows along the x-axis, as sketched in Figure 4.12**a**. Then, one identifies the site 1 of the double-well as the one with the highest energy offset and the site 0 as the one with the lowest offset. Importantly, the tunneling processes to next-neighboring sites can be neglected in the high-frequency limit as they would appear at the second order in the Magnus expansion, allowing to simply view the honeycomb lattice as a set of connected double-wells. The generalization of the hopping term in Eq. (4.35) to each position $\mathbf{r}$ in the honeycomb lattice is therefore

$$t_j^{\text{eff}} = t\left(1 + \frac{\alpha_{\uparrow\downarrow}}{3}\gamma_j(\hat{n}_{\uparrow,\mathbf{r}+\boldsymbol{\delta}_j} - \hat{n}_{\uparrow,\mathbf{r}})\right), \quad \mathbf{r} \in \text{A}, \tag{4.37}$$

which exactly reproduces the desired hopping amplitudes (4.5) for $\gamma_1 = 1$ and $\gamma_2 = \gamma_3 = -1$. Notice that the sign γ_j stems from the sign of the energy offset between nearest-neighboring sites. For example, along the $\boldsymbol{\delta}_1$-link, the energy imbalance between the right and left sites is Δ, whereas along the $\boldsymbol{\delta}_2$ and $\boldsymbol{\delta}_3$-links, it is $-\Delta$.

Interestingly, by applying another type of energy offset, slightly different DAT amplitudes can be generated. Indeed, if one only offsets the A-sublattice, as depicted by Figure 4.12**b**, and naturally associates the A-sites to the site 1 of the double-well and the B-sites to the site 0, then the effective hopping amplitude in this case reads

$$t_j^{\text{eff}} = t\left(1 + \frac{\alpha_{\uparrow\downarrow}}{3}(\hat{n}_{\uparrow,\mathbf{r}} - \hat{n}_{\uparrow,\mathbf{r}+\boldsymbol{\delta}_j})\right), \quad \mathbf{r} \in \text{A}, \tag{4.38}$$

where all $\gamma_j = 1$. Therefore, by following the same reasoning as the one leading to Eq. (4.11), the effective vector potential $\mathbf{A}$ reads

$$\mathbf{A} = \left(0, -\frac{\zeta\hbar\tau_{\text{eff}}}{3a^2}(x - x_c) + \frac{\zeta\hbar\tau_{\text{eff}}}{12a}\right), \tag{4.39}$$

hence the effective magnetic field from the strain scheme in panel **b** ends up being three times larger than the one from scheme in panel **a**, whose expression is given by Eq. (4.13). The pLLs energies are

$$\epsilon_\nu^{\text{LL}}(q_y) = \pm t\sqrt{\nu\frac{3\tau_{\text{eff}}}{2}}\sqrt{1 - \zeta\frac{3}{2}q_y a}, \qquad \nu \in \mathbb{N}, \tag{4.40}$$

For $\nu = 1$, the energy gap is thus larger by a factor $\sqrt{3}$ for staggered onsite potentials shown in **b**, in comparison to the energy gaps obtained with the increasing onsite potentials presented in panel **a**. As this scheme provides larger gaps, it is expected to ease the experimental detection of LL physics.

4.5 Further effects and probing methods

In the analysis, the renormalization of the hopping parameter J of the $\uparrow$-species due to the Floquet driving of the interspecies interaction has not been considered. Similarly as in ref. [195] and assumed in the model (4.28)-(4.29), the absence of energy offset for the $\uparrow$-atoms between the wells leads to the zeroth Bessel function when $\hbar\Omega \gg U_{\uparrow\downarrow}, J$. Hence, when the density of $\downarrow$-atoms is small or uniform, the hopping amplitude of the $\uparrow$-species is unaffected by the back-action from the $\downarrow$-species. Besides, the possible depletion of the BEC due to interactions between $\uparrow$-particles has also been overlooked. Together with the back-action of the $\downarrow$-atoms, they could lead to quantum fluctuations of the BEC. Including them will provide a distinct opportunity to enrich the strain picture with dynamical effects.

A few aspects of the model's implementation have yet to be discussed as they will affect the back-action or the choice for probing methods. The first is the statistics of the $\downarrow$- particles. For fermionic $\downarrow$-atoms, the small density imbalance $\hat{n}_{\downarrow,0} - \hat{n}_{\downarrow,1}$ is readily satisfied thanks to the Pauli exclusion principle that forbids more than one fermion to be localized on a single site. For bosonic $\downarrow$-particles, one has to enforce a low or homogeneous distribution. A second aspect concerns the trapping potential of the $\uparrow$-atoms. The strain model previously analyzed requires a strongly anisotropic harmonic trap experienced by the BEC, namely $\omega_x \gg \omega_y$, where $\omega_{x,y}$ are the harmonic trapping frequencies in the two spatial directions. Note that the model assumes $\omega_y \to 0$ to simplify the theoretical analysis. Besides, no trap acts on the $\downarrow$-atoms, assuming that the confinements of the two atomic species can be separately controlled. However, adding a strong trapping potential for fermionic $\downarrow$-atoms would give the opportunity to reveal the presence of LL physics through the jumps in the density profile occurring when the Fermi level lies within spectral gaps, conferring to it the typical wedding-cake structure [74].

Moreover, valley-dependent edge modes should exist around these jumps. Nonetheless, one would have to limit the local density variations to mitigate back-action effects onto the BEC. Fortunately, the slope of the pLLs would partly smear out the ↓-density steps, *i.e.* the density gradient.

Several techniques can be employed to directly probe the LLs properties and the nature of the pseudo-magnetic field. A first possibility would be to monitor the real space dynamics of a wave packet of ↓-atoms, initially prepared in the vicinity of a Dirac point, that would exhibit a cyclotron motion [74, 201]. Since the chirality of the cyclotron orbit is different at opposite valley, this represents a direct sign of the valley-dependence of the pseudo-magnetic field (and of the time-reversal invariance of the system). Similarly, acting on the wave packet with a constant force will generate a Hall drift [137] whose direction is also valley-dependent. Particularizing the ↓-atoms to fermions, the probing method based on the adapted Středa formula presented in chapter 3 offers a local and direct measurement of the quantum valley Hall effect expected in pLLs systems, where variations of artificial strain intensity would effectively be performed through changes of the amplitude of the interspecies interaction $U_{\uparrow\downarrow}$, via Feshbach resonances. Another approach employing fermions consists in preparing a uniform fermionic gas of ↓-atoms at half-filling and employing circular shaking to spectroscopically resolve the pLLs by measuring the absorbed energy. Moreover, valley-dependent absorption processes are identifiable thanks to band mapping techniques, enabling to extract the valley Hall conductivity through the corresponding valley circular dichroism [202].

4.6 Summary and outlook

This chapter presented a novel strategy to emulate strain field in optical lattices by coupling an atomic species to a trapped BEC via well-tailored density-assisted tunneling terms generated by an external Floquet drive. By changing the shape of the BEC distribution and the Floquet scheme, different strain profiles can be implemented. The focus was set on producing uniaxial strain in the honeycomb lattice along one of the three crystalline axes of the lattice, obtained by considering a strongly anisotropic harmonic trapping potential. Two limits of interest were discussed, namely the non-interacting and the Thomas-Fermi limits. After investigating the spectral features of the ↓-atoms, the Thomas-Fermi appears as the most suitable regime to reproduce the ideal linear strain configuration. Indeed, this regime minimizes the effects of regions with inhomogeneous pseudo-magnetic field and requires smaller atomic clouds.

Furthermore, the Thomas-Fermi regime may set the ground for studying quantum fluctuations effects originating from the phonon modes (Bogoliubov quasi-particles) of the BEC or from exciting the BEC collective modes, allowing to include time-dependence to the synthetic gauge-field. This correspondence with lattice vibrations in solid-state systems motivates an

approach from polaron theory, where the ↓-species and the Bogoliubov excitations of the ↑-atomic gas respectively play the role of the electrons and the phonons that dress them [203], reducing the many-body problem to a single-particle problem. Concretely, we suggest to start by studying a single fermion coupled to weakly-interacting bosons via DAT in a double-well, a scenario for which analytical and numerical calculations can be performed exactly. These results need to be compared to those obtained with polaron theory [203] that predicts that the fermionic impurity is slowed down because of the dressing by phonons. Such insights should ease the generalization of our results to a 1D-lattice and then to a honeycomb lattice, where a dynamical pseudo-magnetic field will finally reemerge along with its quantum excitations in the form of BEC phononic modes.

Another interesting regime specific to cold atoms could be reached for strongly-interacting bosons (↑) near the Mott insulator phase. In this case, low-filling and quantum fluctuations would be the breeding ground for a physics different from solid-states systems. This suggests a distinct direction to investigate the interplay of dynamical gauge field theories on lattices (LGTs) from the previous one realized through synthetic strain fields and ultracold matter.

Chapter 5

Conclusions and perspectives

Relativistic Landau levels physics emerging in strained honeycomb lattices was central in this thesis. On the one hand, we focused on a probing method exploiting the valley Hall response enabling the detection of the Landau level physics. On the other hand, we proposed a model that reproduces this physics with an ultracold atomic mixture in a optical honeycomb lattice.

Chapter 2 introduced key notions at the core of this work. After introducing the Hall effect,the Landau levels, as well as the Widom-Středa formula, we have described the tight-binding model in a honeycomb lattice and how the latter (near-half filling) is intimately linked to effective Dirac models. We also showed how to exploit this effective description in order to derive the relativistic Landau level spectrum of the low-energy excitations of a half-filled honeycomb lattice pierced by a magnetic field. We then showed that strain can be employed to generate a pseudo-magnetic field and its associated (dispersive) relativistic Landau levels. We also introduced the valley Hall effect and existing methods for its measurements. Afterwards, we briefly presented the Floquet theory and showed two basic examples illustrating the renormalization of tunneling amplitudes, one of which leading to density-assisted tunneling. We continue on weakly-interacting Bose gas and detail the necessary conditions to invoke the mean-field approximation leading to the Gross-Pitaevskii equation. This introductory chapter ended on a derivation of the Hubbard model and the discrete Gross-Pitaevskii equation for ultracold bosons in optical lattices.

In chapter 3, we presented our proposal regarding a new probing technique based on a variant of the Widom-Středa formula that relates the valley Hall response of a bulk density to strain variations in a honeycomb lattice. We demonstrated that it is quantized in the regime of small strain intensities (and that separately on each sublattice), and numerically proved it for different geometries and strain configurations. We also demonstrated that the quantization is robust against disorder and independent of the presence of helical edge modes.

Chapter 4 has been dedicated to our model meant to generate a pseudo-magnetic field induced by artificial strain in rigid optical lattices. The strain is created through the coupling of two atomic species, of which one is bosonic, living on a honeycomb lattice. The interspecies interaction is expressed by density-assisted tunneling processes that are responsible for inducing the space-dependence into the hopping amplitudes of the other species, *i.e.* the strain. Assuming that the bosons form a static BEC, a uniform and constant pseudo-magnetic field emerges and the spectrum of the other species reproduces relativistic Landau levels. This is confirmed by a numerical analysis where we compared this atomic mixture system to the usual strained honeycomb lattice discussed in the two previous chapters. Then, we detailing the protocol to Floquet-engineer the density-assisted tunneling amplitudes.

Perspectives

This thesis opens new research routes in different domains of condensed matter physics. The probing method employing the adapted Widom-Středa formula described in chapter 3 calls for experimental realizations in synthetic platforms such as molecular graphene [108, 179], optical tweezers arrays [189–193] or cold atoms in optical lattices [46, 74, 182–188]. Moreover, to our knowledge, direct measurements of the valley Hall effect are still missing and the topological nature of the valley Hall effect still sparks intense discussions in the scientific community [30, 204]. Being able to measure this fundamental observable is primordial to deepen our understanding of electrical and optical properties of valley-materials [205, 206] such as mono- and multi-layer graphene, TMDs or ferro-electrics, notably employed for devices based on valley-dependent (valleytronics [19, 20]) and strain-engineered (straintronics [207–209]) quantum Hall logical gates. Neglected so far, the effects of strained-induced electric fields or non-linear strain could be analyzed [120, 210–213]. Another possible path would be to include particles interactions and investigate their consequences on the quantization of the valley Hall response. Furthermore, it would be interesting to adapt our method in the context of fractional Chern insulators produced in strained lattices [60–62].

While this thesis has focused on the two-dimensional honeycomb lattice which can effectively be described by a spin-1/2 relativistic theory, interesting effects originating from pseudo-gauge fields in higher-dimensional systems (*e.g.* Weyl semimetals [214] or high-order topological insulators [215]) or taking place in higher-spin effective theories [216], may emerge. Therefore, it offers the opportunity to explore consequences of strain and pseudo-gauge fields beyond the paradigmatic honeycomb lattice (graphene-type) case. It could also be adapted to other proposals for strain in square lattices [217]. Eventually, by further developing techniques to realize tunable tunneling amplitudes in optical lattices in arbitrary geometries [218, 219], it would allow to imprint any space-dependence into the tunneling amplitudes, leading not only to new strain schemes and gauge field theories but also to effective models in curved spacetime and quantum gravity [220, 221].

Appendix A

Appendices of chapter 2

A.1 Derivation of $\hat{H}_{\mathbf{F}}^{(k)}[t_0]$

By expanding both sides of equation (2.107), the left hand side yields, up to the second order of the exponent,

$$\begin{aligned}
\hat{U}(t_0+T,t_0) &= \mathcal{T}\left\{e^{-\frac{\mathrm{i}}{\hbar}\int_{t_0}^{t_0+T}\hat{H}(t)dt}\right\} \\
&\simeq \mathcal{T}\left\{1-\frac{\mathrm{i}}{\hbar}\int_{t_0}^{t_0+T}\hat{H}(t_1)dt_1 \right. \\
&\qquad \left. +\frac{1}{2}\left(\frac{-\mathrm{i}}{\hbar}\right)^2\int_{t_0}^{t_0+T}dt_1\int_{t_0}^{t_0+T}dt_2\hat{H}(t_1)\hat{H}(t_2)\right\} \\
&= 1-\frac{\mathrm{i}}{\hbar}\int_{t_0}^{t_0+T}\hat{H}(t)dt \\
&\qquad +\frac{1}{2}\left(\frac{-\mathrm{i}}{\hbar}\right)^2\int_{t_0}^{t_0+T}dt_1\int_{t_0}^{t_0+T}dt_2\mathcal{T}\left\{\hat{H}(t_1)\hat{H}(t_2)\right\}
\end{aligned} \tag{A.1}$$

Focusing only on the second order term, the time-ordering splits the integral as

$$\begin{aligned}
\int_{t_0}^{t_0+T}dt_1\int_{t_0}^{t_0+T}dt_2\mathcal{T}\left\{\hat{H}(t_1)\hat{H}(t_2)\right\} &= \int_{t_2}^{t_0+T}dt_1\int_{t_0}^{t_0+T}dt_2\hat{H}(t_1)\hat{H}(t_2) \\
&\quad +\int_{t_0}^{t_2}dt_1\int_{t_0}^{t_0+T}dt_2\hat{H}(t_2)\hat{H}(t_1).
\end{aligned} \tag{A.2}$$

From $\hat{H}(t_2)\hat{H}(t_1) = [\hat{H}(t_2),\hat{H}(t_1)] + \hat{H}(t_1)\hat{H}(t_2)$, the full interval of integration in the first

integral is recovered, as

$$\begin{aligned}\int_{t_0}^{t_0+T} dt_1 \int_{t_0}^{t_0+T} dt_2 \mathcal{T}\left\{\hat{H}(t_1)\hat{H}(t_2)\right\} =& \int_{t_0}^{t_0+T} dt_1 \int_{t_0}^{t_0+T} dt_2 \hat{H}(t_1)\hat{H}(t_2) \\ &+ \int_{t_0}^{t_2} dt_1 \int_{t_0}^{t_0+T} dt_2 [\hat{H}(t_2), \hat{H}(t_1)] \\ =& \left(\int_{t_0}^{t_0+T} dt \hat{H}(t)\right)^2 \\ &+ \int_{t_0}^{t_2} dt_1 \int_{t_0}^{t_0+T} dt_2 [\hat{H}(t_2), \hat{H}(t_1)].\end{aligned} \tag{A.3}$$

Taking the Fourier transform of $\hat{H}(t)$, that is

$$\hat{H}(t) = \sum_{l\in\mathbb{Z}} H_l \mathrm{e}^{\mathrm{i}l\Omega t}, \tag{A.4}$$

terms in orders of Ω appear.

$$\begin{aligned}-\frac{\mathrm{i}}{\hbar}\int_{t_0}^{t_0+T} \hat{H}(t)dt =& -\frac{\mathrm{i}}{\hbar}\sum_{l\in\mathbb{Z}} H_l \int_{t_0}^{t_0+T} \mathrm{e}^{\mathrm{i}l\Omega t}dt = -\frac{\mathrm{i}T}{\hbar}H_0, \\ \frac{1}{2}\int_{t_0}^{t_2} dt_1 \int_{t_0}^{t_0+T} dt_2 [\hat{H}(t_2), \hat{H}(t_1)] =& \frac{1}{2}\sum_{l,m\in\mathbb{Z}} [H_m, H_l] \int_{t_0}^{t_0+T} dt_2 \int_{t_0}^{t_2} dt_1 \mathrm{e}^{\mathrm{i}\Omega(lt_1+mt_2)} \\ =& \frac{-T}{\mathrm{i}\Omega}\sum_{l=1}^{\infty}\frac{1}{l}\left([H_l, H_{-l}]\right. \\ &\left. -[H_0, H_l]\mathrm{e}^{\mathrm{i}l\Omega t_0} + [H_0, H_{-l}]\mathrm{e}^{-\mathrm{i}l\Omega t_0}\right).\end{aligned} \tag{A.5}$$

Therefore,

$$\begin{aligned}\hat{U}(t_0+T, t_0) =& 1 - \frac{\mathrm{i}T}{\hbar}H_0 + \frac{1}{2}\left(\frac{-\mathrm{i}T}{\hbar}H_0\right)^2 - \\ & \frac{T}{\mathrm{i}\Omega}\left(\frac{-\mathrm{i}}{\hbar}\right)^2 \sum_{l=1}^{\infty}\frac{1}{l}\left([H_l, H_{-l}] + [H_0, H_l]\mathrm{e}^{\mathrm{i}l\Omega t_0} - [H_0, H_{-l}]\mathrm{e}^{-\mathrm{i}l\Omega t_0}\right)\end{aligned} \tag{A.6}$$

The right hand side of (2.107) yields

$$\begin{aligned}\mathrm{e}^{-\mathrm{i}\hat{H}_\mathrm{F}[t_0]T/\hbar} =& \mathrm{e}^{-\mathrm{i}(\hat{H}_\mathrm{F}^{(0)}[t_0] + \hat{H}_\mathrm{F}^{(1)}[t_0]/\Omega + \ldots)T/\hbar} \\ =& 1 - \frac{\mathrm{i}\,\mathrm{T}}{\hbar}\hat{H}_\mathrm{F}^{(0)}[t_0] - \frac{\mathrm{i}T}{\hbar\Omega}\hat{H}_\mathrm{F}^{(1)}[t_0] \\ &+ \frac{1}{2}\left(\frac{-\mathrm{i}T}{\hbar}\hat{H}_\mathrm{F}^{(0)}[t_0]\right)^2 + \frac{1}{2}\left(\frac{-\mathrm{i}T}{\hbar\Omega}\right)^2\left(\hat{H}_\mathrm{F}^{(1)}[t_0]\right)^2 \\ &+ \frac{1}{2\Omega}\left(\frac{-\mathrm{i}T}{\hbar}\right)^2\left(\hat{H}_\mathrm{F}^{(1)}[t_0]\hat{H}_\mathrm{F}^{(0)}[t_0] + \hat{H}_\mathrm{F}^{(0)}[t_0]\hat{H}_\mathrm{F}^{(1)}[t_0]\right) + \ldots\end{aligned} \tag{A.7}$$

By identifying terms in both expansions (A.6) and (A.7) in the following way,

$$\begin{aligned}\hat{H}_{\mathrm{F}}^{(0)}[t_0] &= H_0 = \frac{1}{T}\int_{t_0}^{t_0+T}\hat{H}(t),\\ \hat{H}_{\mathrm{F}}^{(1)}[t_0] &= \sum_{l=1}^{\infty}\frac{1}{\hbar l}\left([H_l, H_{-l}] + [H_0, H_l]\mathrm{e}^{\mathrm{i}l\Omega t_0} - [H_0, H_{-l}]\mathrm{e}^{-\mathrm{i}l\Omega t_0}\right),\end{aligned} \tag{A.8}$$

one obtains the first order correction $\hat{H}_{\mathrm{F}}^{(1)}[t_0]$ of the stroboscopic Floquet Hamiltonian. Notice that the remaining terms in (A.7) correspond to terms from a further expansion in (A.6). The same reasoning can be applied to the (t_0) gauge-independent Hamiltonian $\hat{H}_{\mathrm{eff}}$, following [143]. Then, $\hat{H}_{\mathrm{eff}}^{(0)} = H_0$ and the first-order correction terms reads

$$\hat{H}_{\mathrm{eff}}^{(1)} = \sum_{l=1}^{\infty}\frac{1}{\hbar l}[H_l, H_{-l}]. \tag{A.9}$$

A.2 Derivation of the renormalization of t

Here is presented the derivation of Hamiltonian $\hat{H}_{\mathrm{rot}}$ (2.115) after the rotation

$$\hat{\mathcal{R}}(\tau) = \mathrm{e}^{\mathrm{i}\left[\frac{\mathcal{K}_0}{\hbar\Omega}\sin(\Omega\tau)\hat{n}_0 + \frac{\mathcal{K}_1}{\hbar\Omega}\sin(\Omega\tau)\hat{n}_1 + m\Omega\tau\hat{n}_1\right]} \tag{A.10}$$

applied on $\hat{H}(\tau) = \hat{H}_0 + \hat{\mathcal{V}}(\tau)$, where

$$\begin{aligned}\hat{H}_0 &= -t\hat{c}_0^\dagger\hat{c}_1 - t\hat{c}_1^\dagger\hat{c}_0 + \Delta\hat{n}_1,\\ \hat{\mathcal{V}}(\tau) &= \mathcal{K}_0\cos(\Omega\tau)\hat{n}_0 + \mathcal{K}_1\cos(\Omega\tau)\hat{n}_1.\end{aligned} \tag{A.11}$$

From the Baker-Campbell-Hausdorff lemma and since $[\hat{n}_i, n_j] = 0,\ \forall i, j = 0, 1$,

$$\hat{\mathcal{R}}^\dagger\hat{H}\hat{\mathcal{R}} = -t\hat{\mathcal{R}}^\dagger(\hat{c}_0^\dagger\hat{c}_1 + \hat{c}_1^\dagger\hat{c}_0)\hat{\mathcal{R}} + \hat{\mathcal{V}}(\tau) + \Delta\hat{n}_1. \tag{A.12}$$

The matrix representations of $\hat{\mathcal{R}}$ and of the hopping terms of $\hat{H}_0$ are respectively given by

$$\begin{aligned}\hat{\mathcal{R}}(\tau) &= \exp\left[\begin{pmatrix}\hat{c}_0\\ \hat{c}_1\end{pmatrix}^\dagger\begin{pmatrix}\mathrm{i}\frac{\mathcal{K}_0}{\hbar\Omega}\sin(\Omega\tau) & 0\\ 0 & \mathrm{i}\left(\frac{\mathcal{K}_1}{\hbar\Omega}\sin(\Omega\tau) + m\Omega\tau\right)\end{pmatrix}\begin{pmatrix}\hat{c}_0\\ \hat{c}_1\end{pmatrix}\right]\\ &= \begin{pmatrix}\mathrm{e}^{\mathrm{i}\mathcal{K}_0\sin(\Omega\tau)/\hbar\Omega} & 0\\ 0 & \mathrm{e}^{\mathrm{i}\mathcal{K}_1\sin(\Omega\tau)/\hbar\Omega + \mathrm{i}m\Omega\tau}\end{pmatrix},\\ \hat{H}_0 &= \begin{pmatrix}0 & -t\\ -t & \Delta\end{pmatrix}.\end{aligned} \tag{A.13}$$

Therefore,

$$\begin{aligned}\hat{H}_{\text{rot}} &= -t\hat{\mathcal{R}}^{\dagger}(\hat{c}_0^{\dagger}\hat{c}_1 + \hat{c}_1^{\dagger}\hat{c}_0 + \Delta\hat{c}_1^{\dagger}\hat{c}_1)\hat{\mathcal{R}} - \mathrm{i}\hbar\mathcal{R}\partial_t\mathcal{R}^{\dagger} \\ &= \begin{pmatrix} 0 & -t\mathrm{e}^{-\mathrm{i}(\mathcal{K}_0-\mathcal{K}_1)\sin(\Omega\tau)/\hbar\Omega - \mathrm{i}m\Omega\tau} \\ -t\mathrm{e}^{\mathrm{i}(\mathcal{K}_0-\mathcal{K}_1)\sin(\Omega\tau)/\hbar\Omega + \mathrm{i}m\Omega\tau} & 0 \end{pmatrix}\end{aligned} \tag{A.14}$$

By averaging in time over one period T, we find

$$\hat{H}_{\text{eff}}^{(0)} = -t\mathcal{J}_m\left(\frac{\mathcal{K}_0 - \mathcal{K}_1}{\hbar\Omega}\right)(\hat{c}_0^{\dagger}\hat{c}_1 + \hat{c}_1^{\dagger}\hat{c}_0). \tag{A.15}$$

A.3 Identities used to derive Eq. (2.119)

In order to deduce the rotating Hamiltonian (2.119), we have employed the following identities:

$$\mathrm{e}^{\mathrm{i}\beta\hat{n}_j}\,\hat{b}_j\,\mathrm{e}^{-\mathrm{i}\beta\hat{n}_j} = \mathrm{e}^{-\mathrm{i}\beta}\hat{b}_j, \qquad \mathrm{e}^{\mathrm{i}\beta\hat{n}_j}\,\hat{b}_j^{\dagger}\,\mathrm{e}^{-\mathrm{i}\beta\hat{n}_j} = \mathrm{e}^{\mathrm{i}\beta}\hat{b}^{\dagger} \qquad (j = 0, 1). \tag{A.16}$$

where $\hat{b}_j^{(\dagger)}$ is a bosonic annihilation (creation) operator at site j and

$$\mathrm{e}^{\mathrm{i}\beta\hat{n}_j\hat{n}_j}\,\hat{b}_\sigma\,\mathrm{e}^{-\mathrm{i}\beta\hat{n}_j\hat{n}_j} = \mathrm{e}^{-\mathrm{i}\beta(2\hat{n}_j+1)}\hat{b}_j, \qquad \mathrm{e}^{\mathrm{i}\beta\hat{n}_j\hat{n}_j}\,\hat{b}_j^{\dagger}\,\mathrm{e}^{-\mathrm{i}\beta\hat{n}_j\hat{n}_j} = \mathrm{e}^{\mathrm{i}\beta(2\hat{n}_j+1)}\hat{b}_j^{\dagger}. \tag{A.17}$$

Appendix B

Appendices of chapter 4

B.1 Honeycomb geometry and normalization

In continuum space, the normalization, say to $\mathcal{N}$, of a Gaussian ψ is defined as the integral of the latter over space, as

$$\mathcal{N} = \int dx |\psi(x)|^2. \tag{B.1}$$

In a honeycomb lattice, this integral transforms into a sum, which can be split based on the sublattices, that is

$$\mathcal{N} = \sum_{x_{\mathrm{A}}} |\psi_{\mathrm{A}}(x_{\mathrm{A}})|^2 \Delta x_{\mathrm{A}} + \sum_{x_{\mathrm{B}}} |\psi_{\mathrm{B}}(x_{\mathrm{A}})|^2 \Delta x_{\mathrm{B}}, \tag{B.2}$$

where $\Delta x_{\mathrm{A}} = \Delta x_{\mathrm{B}} = 3a/2$. Then, remembering that

$$\sum_{x_{\mathrm{A}}} |\psi_{\mathrm{A}}(x_{\mathrm{A}})|^2 = \sum_{x_{\mathrm{B}}} |\psi_{\mathrm{B}}(x_{\mathrm{B}})|^2 = \frac{N^{\uparrow}}{2}, \tag{B.3}$$

because half of the particles live on each sublattice, one finds $\mathcal{N} = 3N^{\uparrow}/4$. Therefore, the honeycomb geometry can be taken into account by simply absorbing this 3/4 into the Gaussian distribution, as done in Eq. (4.22).

B.2 Gross-Pitaevskii equation in the honeycomb lattice

Here is deduced the Gross-Pitaevskii equation in a ribbon $N_x \times 2$ sites of the honeycomb lattice with cylindrical boundary conditions along the y-direction – see Figure 2.8. The bosons are described by the Bose-Hubbard Hamiltonian

$$\begin{aligned}\hat{H}_{\uparrow} =& -J\sum_{\mathbf{r}\in\mathrm{A},j}\left(\hat{a}^{\dagger}_{\uparrow,\mathbf{r}}\hat{b}_{\uparrow,\mathbf{r}+\boldsymbol{\delta}_j}+\mathrm{H.c.}\right)+\frac{V_x}{2}\sum_{\mathbf{r}\in\mathrm{A,B}}(x-x_c)^2\hat{n}_{\uparrow,\mathbf{r}}\\&+\frac{U}{2}\sum_{\mathbf{r}\in\mathrm{A,B}}\hat{n}_{\uparrow,\mathbf{r}}(\hat{n}_{\uparrow,\mathbf{r}}-1)-\mu_{\uparrow}\sum_{\mathbf{r}}\hat{n}_{\mathbf{r}},\end{aligned}\tag{B.4}$$

where $\mathbf{r}=(x,y)$, $\boldsymbol{\delta}_1=(-a,0)$, $\boldsymbol{\delta}_2=\left(\frac{a}{2},\frac{\sqrt{3}a}{2}\right)$ and $\boldsymbol{\delta}_3=\left(\frac{a}{2},-\frac{\sqrt{3}a}{2}\right)$, U is the intensity of the repulsive interaction ($U\geq 0$) between two bosons, V_x is a parameter related to the frequency of the harmonic trap imposed along x and $\mu_{\uparrow}$ is the chemical potential. Enforcing periodic boundary conditions along y, we can apply the Fourier transform (2.93). Substituting into (B.4) we obtain

$$\begin{aligned}\hat{H} =& -J\sum_{x\in\mathrm{A},k_y}\left[\hat{a}^{\dagger}_{x,k_y}\left(\sum_j \mathrm{e}^{\mathrm{i}k_y\delta_{j,y}}\hat{b}_{z_j,k_y}\right)+\mathrm{H.c.}\right]+\frac{V_x}{2}\sum_{x\in\mathrm{A},k_y}(x-x_{\mathrm{c}})^2\,\hat{a}^{\dagger}_{x,k_y}\hat{a}_{x,k_y}\\&+\frac{V_x}{2}\sum_{x\in\mathrm{B},k_y}(x-x_{\mathrm{c}})^2\,\hat{b}^{\dagger}_{x,k_y}\hat{b}_{x,k_y}+\frac{U}{2N_y}\sum_{\substack{x\in\mathrm{A}\\k_y^1,k_y^2,k_y^3,k_y^4}}\delta_{k_y^1+k_y^2,k_y^3+k_y^4}\,\hat{a}^{\dagger}_{x,k_y}\hat{a}^{\dagger}_{x,k_y}\hat{a}_{x,k_y}\hat{a}_{x,k_y}\\&+\frac{U}{2L_y}\sum_{\substack{x\in\mathrm{B}\\k_y^1,k_y^2,k_y^3,k_y^4}}\delta_{k_y^1+k_y^2,k_y^3+k_y^4}\,\hat{b}^{\dagger}_{x,k_y}\hat{b}^{\dagger}_{x,k_y}\hat{b}_{x,k_y}\hat{b}_{x,k_y}\\&-\mu_{\uparrow}\sum_{x\in\mathrm{A},k_y}\hat{a}^{\dagger}_{x,k_y}\hat{a}_{x,k_y}-\mu_{\uparrow}\sum_{x\in\mathrm{B},k_y}\hat{b}^{\dagger}_{x,k_y}\hat{b}_{x,k_y}\end{aligned}\tag{B.5}$$

where we defined $z_j\equiv x+\delta_{j,x}\in\mathrm{B}$ when $x\in\mathrm{A}$ and x_{c} as the position of the system center. We apply the mean-field approximation $\hat{a}_{x,k_y}\to\chi_{\mathrm{A}}(x,k_y)$ and $\hat{b}_{x,k_y}\to\chi_{\mathrm{B}}(x,k_y)$, yielding

$$\begin{aligned}E[\chi] =& -J\sum_{x\in\mathrm{A},k_y}\left[\chi^*_{\mathrm{A}}(x,k_y)\left(\sum_j e^{ik_y\delta_{j,y}}\chi_{\mathrm{B}}(z_j,k_y)\right)+\mathrm{H.c.}\right]\\&+\frac{V_x}{2}\sum_{x\in\mathrm{A},k_y}(x-x_{\mathrm{c}})^2\,\chi^*_{\mathrm{A}}(x,k_y)\chi_{\mathrm{A}}(x,k_y)\\&+\frac{V_x}{2}\sum_{x\in\mathrm{B},k_y}(x-x_{\mathrm{c}})^2\,\chi^*_{\mathrm{B}}(x,k_y)\chi_{\mathrm{B}}(x,k_y)\\&+\frac{U}{2L_y}\sum_{\substack{x\in\mathrm{A}\\k_y^1,k_y^2,k_y^3,k_y^4}}\delta_{k_y^1+k_y^2,k_y^3+k_y^4}\,\hat{\chi}^*_{\mathrm{A}}(x,k_y^1)\chi^*_{\mathrm{A}}(x,k_y^2)\chi_{\mathrm{A}}(x,k_y^3)\chi_{\mathrm{A}}(x,k_y^4)\\&+\frac{U}{2L_y}\sum_{\substack{x\in\mathrm{B}\\k_y^1,k_y^2,k_y^3,k_y^4}}\delta_{k_y^1+k_y^2,k_y^3+k_y^4}\,\chi^*_{\mathrm{B}}(x,k_y^1)\chi^*_{\mathrm{B}}(x,k_y^2)\chi_{\mathrm{B}}(x,k_y^3)\chi_{\mathrm{B}}(x,k_y^4),\end{aligned}\tag{B.6}$$

Assuming that the condensed bosons all occupy the zero-momentum state ($k_y = 0$), the energy per unit length along the y-direction reads

$$\begin{aligned}\frac{E[\chi_{\mathrm{A}},\chi_{\mathrm{B}}]}{L_y} =& -J\sum_{x\in\mathrm{A}}\left[\chi^*_{\mathrm{A}}(x)\left(\sum_j \chi_{\mathrm{B}}(z_j)\right)+\mathrm{H.c.}\right]+\frac{V_x}{2}\sum_{x\in\mathrm{A}}(x-x_{\mathrm{c}})^2\ |\chi_{\mathrm{A}}(x)|^2 \\ &+\frac{V_x}{2}\sum_{x\in\mathrm{B}}(x-x_{\mathrm{c}})^2\ |\chi_{\mathrm{B}}(x)|^2+\frac{U}{2}\sum_{x\in\mathrm{A}}\ |\chi_{\mathrm{A}}(x)|^4+\frac{U}{2}\sum_{x\in\mathrm{B}}|\chi_{\mathrm{B}}(x)|^4.\end{aligned} \tag{B.7}$$

where the factor $1/L_y$ has been easily eliminated by defining $\chi(x) \to \sqrt{L_y}\chi(x)$. The remaining L_y in the denominator to the left hand side reabsorbed into the energy functional by defining $E[\chi] \to L_y E[\chi]$. Minimizing each energy contribution with respect to χ^*_A and χ^*_B leads to

$$\begin{aligned}\left.\frac{\delta E_{\mathrm{kin}}}{\delta\chi^*_{\mathrm{A}}(z)}\right|_{z=x} &= -J\sum_j \chi_{\mathrm{B}}(x+\delta_{x,j}) \\ \left.\frac{\delta E_{\mathrm{pot}}}{\delta\chi^*_{\mathrm{A}}(z)}\right|_{z=x} &= \frac{V_x}{2}(x-x_{\mathrm{c}})^2\chi_{\mathrm{A}}(x) \\ \left.\frac{\delta E_{\mathrm{int}}}{\delta\chi^*_{\mathrm{A}}(z)}\right|_{z=x} &= U|\chi_{\mathrm{A}}(x)|^2\chi_{\mathrm{A}}(x) \\ \left.\frac{\delta E_{\mathrm{kin}}}{\delta\chi^*_{\mathrm{B}}(z)}\right|_{z=x+\delta_{i,x}} &= -J\sum_j \chi_{\mathrm{A}}(x+\delta_{x,i}-\delta_{x,j}) \\ \left.\frac{\delta E_{\mathrm{pot}}}{\delta\chi^*_{\mathrm{B}}(z)}\right|_{z=x+\delta_{i,x}} &= \frac{V_x}{2}(x+\delta_{x,i}-x_{\mathrm{c}})^2\chi_{\mathrm{B}}(x+\delta_{x,i}) \\ \left.\frac{\delta E_{\mathrm{int}}}{\delta\chi^*_{\mathrm{B}}(z)}\right|_{z=x+\delta_{i,x}} &= U|\chi_{\mathrm{B}}(x+\delta_{x,i})|^2\chi_{\mathrm{B}}(x+\delta_{x,i}).\end{aligned} \tag{B.8}$$

Therefore the equation of motion is

$$\begin{cases} -J\sum_j \chi_{\mathrm{B}}(z_j)+\frac{V_x}{2}(x-x_{\mathrm{c}})^2\chi_{\mathrm{A}}(x)+U|\chi_{\mathrm{A}}(x)|^2\chi_{\mathrm{A}}(x)=\mu_\uparrow\chi_{\mathrm{A}}(x) \\ -J\sum_j \chi_{\mathrm{A}}(z_i-\delta_{j,x})+\frac{V_x}{2}(z_i-x_{\mathrm{c}})^2\chi_{\mathrm{B}}(z_i)+U|\chi_{\mathrm{B}}(z_i)|^2\chi_{\mathrm{B}}(x)=\mu_\uparrow\chi_{\mathrm{B}}(z_i)\end{cases} \tag{B.9}$$

for every position x in the A-sublattice and $z_j \equiv x+\delta_{j,x}$ $z_k \equiv x+\delta_{k,x}$ in the B-sublattice.

B.3 Numerically solving the Gross-Pitaevskii equation: imaginary-time evolution method

To solve the time-independent GPE (B.9) on the honeycomb lattice and find the BEC distribution, we have employed the *imaginary-time evolution* method [173]. Here, we explain the general idea of this method: how it converges to the ground state and extracts its energy. For that, take a state $\phi(x,t)$ (t is the time here) and express it in terms of the eigenvectors φ_i of the Hamiltonian H_{GP}, defined by rewriting the GPE into a matrix form $H_{\text{GP}}\varphi_0 = \mu\varphi_0$. Hence, at $t = 0$,

$$\phi(x,0) = \sum_i c_i\varphi_i(x) \qquad \text{with} \quad c_i \in \mathbb{C}, \quad H_{\text{GP}}\varphi_i = \epsilon_i\varphi_i. \tag{B.10}$$

Besides, the wavefunction evolves in time as

$$\begin{aligned}\phi(x,t) &= e^{-\mathrm{i}H_{\text{GP}}t}\phi(x,0) = \sum_j e^{-\mathrm{i}t\epsilon_j}c_j\varphi_j(x) \\ &= e^{-\mathrm{i}t\epsilon_0}\left[c_0\varphi_0(x) + \sum_{j>0} e^{-\mathrm{i}t(\epsilon_j-\epsilon_0)}c_j\varphi_j(x)\right].\end{aligned} \tag{B.11}$$

By operating a Wick rotation $\tau = it$, we see that at long times, $\tau \to \infty$, the second term within the brackets will be exponentially small compared to the first term $c_0\varphi_0$ since $\epsilon_j > \epsilon_0$, thus

$$\phi(x,-i\tau) = e^{-\tau\epsilon_0}c_0\varphi_0(x) + \mathcal{O}(e^{-2\tau}). \tag{B.12}$$

However, note that in complex time, the evolution is not unitary anymore since $e^{-\tau H_{GP}}$ is not a unitary operator. We therefore need to enforce the normalization of the wavefunction during the whole evolution. This method proposes to use the non-linear Schrödinger equation (after a Wick rotation)

$$\partial_\tau\phi(x,-i\tau) = -H_{\text{GP}}[\phi]\phi(x,-i\tau), \tag{B.13}$$

to find the BEC wavefunction. We implemented an algorithm, whose pseudocode is shown in Algorithm 1, to solve equation (B.13) starting from an initial state to the lowest energy-state of $H_{\text{GP}}[\phi]$, where ϕ_0 is, for example, a Gaussian. Using a 4^{th}-order Runge-Kutta (RK4) algorithm, we calculate the time evolution of the wavefunction ϕ from τ to $\tau + d\tau$. Remembering that H_{GP} depends on ϕ at time τ, we plug ϕ_τ at each time step in order to compute $\phi_{\tau+d\tau}$. For the sake of concreteness, at first order in $d\tau$, this reads

$$\begin{aligned}\phi_{\tau+d\tau} &= e^{-H_{\mathrm{GP}}[\phi_\tau]d\tau}\phi_\tau \\ &= \phi_\tau - H_{\mathrm{GP}}[\phi_\tau]\phi_\tau d\tau + \mathcal{O}((d\tau)^2).\end{aligned} \tag{B.14}$$

The time-evolution stops when the maximum values of the particle densities are closer than an arbitrary threshold ϵ.

Algorithm 1 Imaginary-time algorithm

Pick initial, normalized state ϕ_{old}, convergence limit ϵ and time-step $d\tau$
while true:
  $\phi_{\mathrm{new}} \leftarrow \mathrm{RK4}(\tau, \phi_{\mathrm{old}}, d\tau)$
  $\phi_{\mathrm{new}} \leftarrow \frac{\phi_{\mathrm{new}}}{\sum \|\phi_{\mathrm{new}}\|^2}$
  $\delta_r \leftarrow |\max(\|\phi_{\mathrm{new}}\|^2) - \max(\|\phi_{\mathrm{old}}\|^2)| / \max(\|\phi_{\mathrm{new}}\|^2)$
  if $\delta_r < \epsilon$:
    break
  endif
  $\phi_{\mathrm{old}} \leftarrow \phi_{\mathrm{new}}$
end while
$\phi_{\mathrm{new}} \leftarrow e^{-H[\phi_{\mathrm{new}}]d\tau}\phi_{\mathrm{new}} = e^{-\epsilon_0 d\tau}\phi_{\mathrm{new}}$
$\epsilon_0 = -\frac{\ln \|\phi_{\mathrm{new}}\|}{d\tau}$
returns $\epsilon_0, \phi_{\mathrm{new}}$

Note that convergence conditions of the method have to be satisfied, which in our case summarize to $\epsilon_{\max} d\tau \ll 1$ [173], where $\epsilon_{\max}$ is the largest eigenvalue of H_{GP}. In conclusion, starting from an arbitrary ϕ_0, the state occupied by the system tends to the eigenvector of H_{GP} associated to the lowest eigenvalue when $\tau \to \infty$, *i.e.* $\phi_\infty \to \varphi_0$. Therefore we find

$$\phi_{\tau+d\tau} = e^{-Hd\tau}\phi_\tau = e^{-\epsilon_0 d\tau}\phi_\tau. \tag{B.15}$$

By taking the norm at both hand sides, since $\sum_i |\phi_{\mathrm{old}}^{(i)}|^2 = 1$ (ϕ_{new} is not renormalized yet), we find

$$\|\phi_{\mathrm{new}}\|^2 = e^{-2\epsilon_0 d\tau}, \tag{B.16}$$

thus

$$\epsilon_0 = -\frac{\ln \|\phi_{\mathrm{new}}\|}{d\tau}. \tag{B.17}$$

B.4 Density-assisted tunneling in the case of a mixture in a double-well

The Hamiltonian of the mixture in the double-well investigated in section 4.4.1 reads

$$\begin{aligned}\hat{H}_\uparrow &= -J\hat{c}^\dagger_{\uparrow,0}\hat{c}_{\uparrow,1} - J\hat{c}^\dagger_{\uparrow,1}\hat{c}_{\uparrow,0} + \frac{U}{2}\sum_{i=0}^{1}\hat{n}_{\uparrow,i}(\hat{n}_{\uparrow,i}-1),\\ \hat{H}_\downarrow &= -t\hat{c}^\dagger_{\downarrow,0}\hat{c}_{\downarrow,1} - t\hat{c}^\dagger_{\downarrow,1}\hat{c}_{\downarrow,0} + \Delta\hat{n}_{\downarrow,1} + \Delta_0\cos(\Omega\tau)\hat{n}_{\downarrow,0},\\ \hat{\mathcal{V}}(\tau) &= U_{\uparrow\downarrow}\cos(\Omega\tau)\left(\hat{n}_{\uparrow,0}\hat{n}_{\downarrow,0} + \hat{n}_{\uparrow,1}\hat{n}_{\downarrow,1}\right),\end{aligned} \tag{B.18}$$

with $\hat{c}^\dagger_{\sigma,i}$ ($\hat{c}_{\sigma,i}$) the creation (annihilation) operator of the $\sigma = \downarrow,\uparrow$ particle. The parameters Δ and $U_{\uparrow\downarrow}$ are the energy imbalance between the wells and the interspecies interaction strength, respectively. Following a similar reasoning as in section 2.8.3, the transformation to the rotating frame reads

$$\hat{\mathcal{R}} = \exp\left\{\mathrm{i}\left[\frac{U_{\uparrow\downarrow}\hat{n}_{\uparrow,0}}{\hbar\Omega}\sin(\Omega\tau)\hat{n}_{\downarrow,0} + \frac{U_{\uparrow\downarrow}\hat{n}_{\uparrow,1}}{\hbar\Omega}\sin(\Omega\tau)\hat{n}_{\downarrow,1} + \Omega\tau\hat{n}_{\downarrow,1} + \frac{\Delta_0}{\hbar\Omega}\hat{n}_{\downarrow,0}\sin(\Omega\tau)\right]\right\}. \tag{B.19}$$

Applied on the Hamiltonian (B.18) as prescribed by (2.115), it results into

$$\begin{aligned}\hat{H}_{\mathrm{rot}}(\tau) =& \hat{\mathcal{R}}\hat{H}(\tau)\hat{\mathcal{R}}^\dagger - \mathrm{i}\hbar\hat{\mathcal{R}}\partial_\tau\hat{\mathcal{R}}^\dagger\\ =& -t\,\mathrm{e}^{\mathrm{i}U_{\uparrow\downarrow}\sin(\Omega\tau)(\hat{n}_{\uparrow,0}-\hat{n}_{\uparrow,1})/\hbar\Omega - \mathrm{i}\Omega\tau + \mathrm{i}\Delta_0\sin(\Omega\tau)/\hbar\Omega}\hat{c}^\dagger_{\downarrow,0}\hat{c}_{\downarrow,1}\\ & - J\,\mathrm{e}^{\mathrm{i}U_{\uparrow\downarrow}\sin(\Omega\tau)(\hat{n}_{\downarrow,0}-\hat{n}_{\downarrow,1})/\hbar\Omega}\hat{c}^\dagger_{\uparrow,0}\hat{c}_{\uparrow,1} + \mathrm{H.c.}\\ & + \frac{U}{2}\sum_{i=0}^{1}\hat{n}_{\uparrow,i}(\hat{n}_{\uparrow,i}-1),\end{aligned} \tag{B.20}$$

after using the identities (A.16), which are identical for fermionic operators. After averaging over a driving period $T = 2\pi/\Omega$, one eventually finds

$$\begin{aligned}\hat{H}^{(0)}_{\mathrm{F}} =& -t\,\mathcal{J}_1\left(\frac{U_{\uparrow\downarrow}(\hat{n}_{\uparrow,0}-\hat{n}_{\uparrow,1})+\Delta_0}{\hbar\Omega}\right)\hat{c}^\dagger_{\downarrow,0}\hat{c}_{\downarrow,1}\\ & - J\mathcal{J}_0\left(\frac{U_{\uparrow\downarrow}(\hat{n}_{\downarrow,0}-\hat{n}_{\downarrow,1})}{\hbar\Omega}\right)\hat{c}^\dagger_{\uparrow,0}\hat{c}_{\uparrow,1} + \mathrm{H.c.}\\ & + \frac{U}{2}\sum_{i=0}^{1}\hat{n}_{\uparrow,i}(\hat{n}_{\uparrow,i}-1).\end{aligned} \tag{B.21}$$

Bibliography

[1] R. P. Feynman, "Simulating Physics with Computers," *International Journal of Theoretical Physics*, vol. 21, no. 6/7, 1982. 1

[2] I. M. Georgescu, S. Ashhab, and F. Nori, "Quantum simulation," *Reviews of Modern Physics*, vol. 86, no. 1, pp. 153–185, 2014. 1, 2

[3] E. Altman, K. R. Brown, G. Carleo, L. D. Carr, E. Demler, C. Chin, B. DeMarco, S. E. Economou, M. A. Eriksson, K.-M. C. Fu, *et al.*, "Quantum simulators: Architectures and opportunities," *PRX quantum*, vol. 2, no. 1, p. 017003, 2021. 1

[4] J. I. Cirac and P. Zoller, "Goals and opportunities in quantum simulation," *Nature physics*, vol. 8, no. 4, pp. 264–266, 2012. 1, 2

[5] I. Bloch, "Quantum simulations come of age," *Nature Physics*, vol. 14, no. 12, pp. 1159–1161, 2018. 1, 2

[6] M. I. Katsnelson, K. S. Novoselov, and A. K. Geim, "Chiral tunnelling and the Klein paradox in graphene," *Nature physics*, vol. 2, no. 9, pp. 620–625, 2006. 1, 16

[7] A. F. Young and P. Kim, "Quantum interference and Klein tunnelling in graphene heterojunctions," *Nature Physics*, vol. 5, no. 3, pp. 222–226, 2009. 1, 16

[8] C. Beenakker, "Colloquium: Andreev reflection and Klein tunneling in graphene," *Reviews of Modern Physics*, vol. 80, no. 4, pp. 1337–1354, 2008. 1, 16

[9] A. Schmitt, P. Vallet, D. Mele, M. Rosticher, T. Taniguchi, K. Watanabe, E. Bocquillon, G. Feve, J.-M. Berroir, C. Voisin, *et al.*, "Mesoscopic Klein-Schwinger effect in graphene," *Nature Physics*, vol. 19, no. 6, pp. 830–835, 2023. 1, 16

[10] A. Cortijo and M. A. Vozmediano, "Effects of topological defects and local curvature on the electronic properties of planar graphene," *Nuclear Physics B*, vol. 763, no. 3, pp. 293–308, 2007. 1, 16

[11] F. de Juan, M. Sturla, and M. A. Vozmediano, "Space dependent Fermi velocity in strained graphene," *Physical review letters*, vol. 108, no. 22, p. 227205, 2012. 1, 16

[12] Z. Jiang, L. Tung, Y.-J. Wang, M. Schwartz, and P. Kim, "Infrared spectroscopy of Landau levels of graphene," *Physical review letters*, vol. 98, no. 19, p. 197403, 2007. 1

[13] F. Wendler, A. Knorr, and E. Malic, "Ultrafast carrier dynamics in Landau-quantized graphene," *Nanophotonics*, vol. 4, no. 3, pp. 224–249, 2015. 1

[14] L.-J. Yin, Y. Zhang, J.-B. Qiao, S.-Y. Li, and L. He, "Experimental observation of surface states and Landau levels bending in bilayer graphene," *Physical Review B*, vol. 93, no. 12, p. 125422, 2016. 1

[15] Y. Zhang, Y.-W. Tan, H. L. Stormer, and P. Kim, "Experimental observation of the quantum Hall effect and Berry's phase in graphene," *nature*, vol. 438, no. 7065, pp. 201–204, 2005. 1, 24

[16] K. S. Novoselov, Z. Jiang, Y. Zhang, S. V. Morozov, H. L. Stormer, U. Zeitler, J. C. Maan, G. S. Boebinger, P. Kim, and A. K. Geim, "Room-Temperature Quantum Hall Effect in Graphene," *Science*, vol. 315, no. 5817, pp. 1379–1379, 2007. 1

[17] K. I. Bolotin, F. Ghahari, M. D. Shulman, H. L. Stormer, and P. Kim, "Observation of the fractional quantum Hall effect in graphene," *Nature*, vol. 462, no. 7270, pp. 196–199, 2009. 1

[18] D. Xiao, W. Yao, and Q. Niu, "Valley-Contrasting Physics in Graphene: Magnetic Moment and Topological Transport," *Phys. Rev. Lett.*, vol. 99, p. 236809, Dec 2007. 2, 37

[19] J. R. Schaibley, H. Yu, G. Clark, P. Rivera, J. S. Ross, K. L. Seyler, W. Yao, and X. Xu, "Valleytronics in 2D materials," *Nature Reviews Materials*, vol. 1, p. 16055, Aug 2016. 2, 37, 101

[20] S. A. Vitale, D. Nezich, J. O. Varghese, P. Kim, N. Gedik, P. Jarillo-Herrero, D. Xiao, and M. Rothschild, "Valleytronics: Opportunities, Challenges, and Paths Forward," *Small*, vol. 14, no. 38, p. 1801483, 2018. 2, 37, 101

[21] R. V. Gorbachev, J. C. W. Song, G. L. Yu, A. V. Kretinin, F. Withers, Y. Cao, A. Mishchenko, I. V. Grigorieva, K. S. Novoselov, L. S. Levitov, and A. K. Geim, "Detecting topological currents in graphene superlattices," *Science*, vol. 346, no. 6208, pp. 448–451, 2014. 2, 37, 38

[22] K. F. Mak, K. L. McGill, J. Park, and P. L. McEuen, "The valley Hall effect in MoS2 transistors," *Science*, vol. 344, no. 6191, pp. 1489–1492, 2014. 2, 37

[23] G. Kirczenow, "Valley currents and nonlocal resistances of graphene nanostructures with broken inversion symmetry from the perspective of scattering theory," *Phys. Rev. B*, vol. 92, p. 125425, Sep 2015. 2, 37

[24] J. Lee, K. F. Mak, and J. Shan, "Electrical control of the valley Hall effect in bilayer MoS2 transistors," *Nature nanotechnology*, vol. 11, no. 5, pp. 421–425, 2016. 2, 38

[25] M. J. Zhu, A. V. Kretinin, M. D. Thompson, D. A. Bandurin, S. Hu, G. L. Yu, J. Birkbeck, A. Mishchenko, I. J. Vera-Marun, K. Watanabe, T. Taniguchi, M. Polini, J. R. Prance, K. S. Novoselov, A. K. Geim, and M. Ben Shalom, "Edge currents shunt the insulating bulk in gapped graphene," *Nature Communications*, vol. 8, p. 14552, Feb 2017. 2, 37

[26] T. Aktor, J. H. Garcia, S. Roche, A.-P. Jauho, and S. R. Power, "Valley Hall effect and nonlocal resistance in locally gapped graphene," *Phys. Rev. B*, vol. 103, p. 115406, Mar 2021. 2, 37

[27] J. M. Marmolejo-Tejada, J. H. García, M. D. Petrović, P.-H. Chang, X.-L. Sheng, A. Cresti, P. Plecháč, S. Roche, and B. K. Nikolić, "Deciphering the origin of nonlocal resistance in multiterminal graphene on hexagonal-boron-nitride with ab initio quantum transport: Fermi surface edge currents rather than Fermi sea topological valley currents," *Journal of Physics: Materials*, vol. 1, p. 015006, sep 2018. 2, 37, 77

[28] A. Aharon-Steinberg, A. Marguerite, D. J. Perello, K. Bagani, T. Holder, Y. Myasoedov, L. S. Levitov, A. K. Geim, and E. Zeldov, "Long-range nontopological edge currents in charge-neutral graphene," *Nature*, vol. 593, pp. 528–534, May 2021. 2, 37

[29] L. F. Torres and S. O. Valenzuela, "A valley of opportunities," *Physics World*, vol. 34, no. 11, p. 43, 2021. 2

[30] S. Roche, S. R. Power, B. K. Nikolić, J. H. García, and A.-P. Jauho, "Have mysterious topological valley currents been observed in graphene superlattices?," *Journal of Physics: Materials*, vol. 5, p. 021001, Jan. 2022. 2, 101

[31] D. Jaksch, C. Bruder, J. I. Cirac, C. W. Gardiner, and P. Zoller, "Cold Bosonic Atoms in Optical Lattices," *Phys. Rev. Lett.*, vol. 81, pp. 3108–3111, Oct 1998. 2, 50

[32] I. Bloch, J. Dalibard, and W. Zwerger, "Many-body physics with ultracold gases," *Reviews of Modern Physics*, vol. 80, pp. 885–964, 07 2008. 2

[33] I. Bloch, J. Dalibard, and S. Nascimbène, "Quantum simulations with ultracold quantum gases," *Nature Physics*, vol. 8, no. 4, pp. 267–276, 2012. 2

[34] M. Lewenstein, A. Sanpera, and V. Ahufinger, "Ultracold Atoms in Optical Lattices: Simulating quantum many-body systems," 2012. 2, 43, 49, 50, 51

[35] C. Gross and I. Bloch, "Quantum simulations with ultracold atoms in optical lattices," *Science*, vol. 357, no. 6355, pp. 995–1001, 2017. 2

[36] F. Schäfer, T. Fukuhara, S. Sugawa, Y. Takasu, and Y. Takahashi, "Tools for quantum simulation with ultracold atoms in optical lattices," *Nature Reviews Physics*, vol. 2, no. 8, pp. 411–425, 2020. 2

[37] J. Argüello-Luengo, U. Bhattacharya, A. Celi, R. W. Chhajlany, T. Grass, M. Płodzień, D. Rakshit, T. Salamon, P. Stornati, L. Tarruell, *et al.*, "Synthetic dimensions for topological and quantum phases," *Communications Physics*, vol. 7, no. 1, p. 143, 2024. 2

[38] T. Esslinger, "Fermi-Hubbard physics with atoms in an optical lattice," *Annu. Rev. Condens. Matter Phys.*, vol. 1, no. 1, pp. 129–152, 2010. 2

[39] L. Tarruell and L. Sanchez-Palencia, "Quantum simulation of the Hubbard model with ultracold fermions in optical lattices," *Comptes Rendus Physique*, vol. 19, no. 6, pp. 365–393, 2018. 2, 50

[40] M. Greiner, O. Mandel, T. Esslinger, T. W. Hänsch, and I. Bloch, "Quantum phase transition from a superfluid to a Mott insulator in a gas of ultracold atoms," *Nature*, vol. 415, no. 6867, pp. 39–44, 2002. 2, 50

[41] Q. Chen, J. Stajic, S. Tan, and K. Levin, "BCS–BEC crossover: From high temperature superconductors to ultracold superfluids," *Physics Reports*, vol. 412, no. 1, pp. 1–88, 2005. 2

[42] D.-W. Zhang, Y.-Q. Zhu, Y. Zhao, H. Yan, and S.-L. Zhu, "Topological quantum matter with cold atoms," *Advances in Physics*, vol. 67, no. 4, pp. 253–402, 2018. 2, 50

[43] M. Aidelsburger, M. Atala, M. Lohse, J. T. Barreiro, B. Paredes, and I. Bloch, "Realization of the Hofstadter Hamiltonian with Ultracold Atoms in Optical Lattices," *Phys. Rev. Lett.*, vol. 111, p. 185301, Oct 2013. 2, 50

[44] G. Jotzu, M. Messer, R. Desbuquois, M. Lebrat, T. Uehlinger, D. Greif, and T. Esslinger, "Experimental realization of the topological Haldane model with ultracold fermions," *Nature*, vol. 515, pp. 237–240, 11 2014. 2, 50

[45] M. Aidelsburger, M. Lohse, C. Schweizer, M. Atala, J. T. Barreiro, S. Nascimbène, N. R. Cooper, I. Bloch, and N. Goldman, "Measuring the Chern number of Hofstadter bands with ultracold bosonic atoms," *Nature Physics*, vol. 11, no. 2, pp. 162–166, 2015. 2, 50

[46] J. Léonard, S. Kim, J. Kwan, P. Segura, F. Grusdt, C. Repellin, N. Goldman, and M. Greiner, "Realization of a fractional quantum Hall state with ultracold atoms," *Nature*, vol. 619, no. 7970, pp. 495–499, 2023. 2, 9, 50, 78, 101

[47] A. de Paz, A. Sharma, A. Chotia, E. Maréchal, J. H. Huckans, P. Pedri, L. Santos, O. Gorceix, L. Vernac, and B. Laburthe-Tolra, "Nonequilibrium Quantum Magnetism in a Dipolar Lattice Gas," *Phys. Rev. Lett.*, vol. 111, p. 185305, Oct 2013. 2

[48] B. Yan, S. A. Moses, B. Gadway, J. P. Covey, K. R. Hazzard, A. M. Rey, D. S. Jin, and J. Ye, "Observation of dipolar spin-exchange interactions with lattice-confined polar molecules," *Nature*, vol. 501, no. 7468, pp. 521–525, 2013. 2

[49] S. Baier, M. J. Mark, D. Petter, K. Aikawa, L. Chomaz, Z. Cai, M. Baranov, P. Zoller, and F. Ferlaino, "Extended Bose-Hubbard models with ultracold magnetic atoms," *Science*, vol. 352, no. 6282, pp. 201–205, 2016. 2

[50] D. M. Weld and W. Ketterle, "Towards quantum magnetism with ultracold atoms," in *Journal of Physics: Conference Series*, vol. 264, p. 012017, IOP Publishing, 2011. 2, 50

[51] B.-Y. Sun, N. Goldman, M. Aidelsburger, and M. Bukov, "Engineering and probing non-abelian chiral spin liquids using periodically driven ultracold atoms," *PRX Quantum*, vol. 4, no. 2, p. 020329, 2023. 2, 50

[52] K. G. Wilson, "Confinement of quarks," *Physical review D*, vol. 10, no. 8, p. 2445, 1974. 2, 50

[53] S. Taie, R. Yamazaki, S. Sugawa, and Y. Takahashi, "An SU(6) Mott insulator of an atomic Fermi gas realized by large-spin Pomeranchuk cooling," *Nature Physics*, vol. 8, no. 11, pp. 825–830, 2012. 2, 50

[54] X. Zhang, M. Bishof, S. L. Bromley, C. V. Kraus, M. S. Safronova, P. Zoller, A. M. Rey, and J. Ye, "Spectroscopic observation of SU(N)-symmetric interactions in Sr orbital magnetism," *Science*, vol. 345, no. 6203, pp. 1467–1473, 2014. 2, 50

[55] E. Zohar, J. I. Cirac, and B. Reznik, "Quantum simulations of lattice gauge theories using ultracold atoms in optical lattices," *Reports on Progress in Physics*, vol. 79, p. 014401, dec 2015. 2

[56] M. C. Banuls and K. Cichy, "Review on novel methods for lattice gauge theories," *Reports on Progress in Physics*, vol. 83, no. 2, p. 024401, 2020. 2, 50

[57] N. Levy, S. A. Burke, K. L. Meaker, M. Panlasigui, A. Zettl, F. Guinea, A. H. C. Neto, and M. F. Crommie, "Strain-Induced Pseudo–Magnetic Fields Greater Than 300 Tesla in Graphene Nanobubbles," *Science*, vol. 329, no. 5991, pp. 544–547, 2010. 2, 25

[58] H. Shioya, S. Russo, M. Yamamoto, M. F. Craciun, and S. Tarucha, "Electron states of uniaxially strained graphene," *Nano letters*, vol. 15, no. 12, pp. 7943–7948, 2015. 2, 25

[59] S.-Y. Li, K.-K. Bai, L.-J. Yin, J.-B. Qiao, W.-X. Wang, and L. He, "Observation of unconventional splitting of Landau levels in strained graphene," *Physical Review B*, vol. 92, no. 24, p. 245302, 2015. 2, 25

[60] Z. Bi, N. F. Yuan, and L. Fu, "Designing flat bands by strain," *Physical Review B*, vol. 100, no. 3, p. 035448, 2019. 2, 101

[61] Q. Ji, B. Li, J. Christensen, C. Wang, and M. Kadic, "Unconventional superconductivity in magic-strain graphene superlattices," *arXiv preprint arXiv:2407.16044*, 2024. 2, 101

[62] Y. Liu and Z. Zhu, "Engineering Fractional Chern Insulators through Periodic Strain in Monolayer Graphene and Transition Metal Dichalcogenides," 2024. 2, 101

[63] N. Goldman, G. Juzeliūnas, P. Öhberg, and I. B. Spielman, "Light-induced gauge fields for ultracold atoms," *Reports on Progress in Physics*, vol. 77, no. 12, p. 126401, 2014. 2

[64] J. Dalibard, "Introduction to the physics of artificial gauge fields," in *Quantum Matter at Ultralow Temperatures*, pp. 1–61, IOS Press, 2016. 2

[65] M. Aidelsburger, S. Nascimbène, and N. Goldman, "Artificial gauge fields in materials and engineered systems," *Comptes Rendus Physique*, vol. 19, no. 6, pp. 394–432, 2018. 2

[66] N. R. Cooper, J. Dalibard, and I. B. Spielman, "Topological bands for ultracold atoms," *Rev. Mod. Phys.*, vol. 91, p. 015005, Mar 2019. 2

[67] Y. Li, J. Zhang, Y. Wang, H. Du, J. Wu, W. Liu, F. Mei, J. Ma, L. Xiao, and S. Jia, "Atom-optically synthetic gauge fields for a noninteracting Bose gas," *Light: Science & Applications*, vol. 11, no. 1, p. 13, 2022. 2

[68] W. Wang, Z. Zhang, G.-X. Tang, and T. Wang, "Floquet engineering tunable periodic gauge fields and simulating real topological phases in a cold-alkaline-earth-metal-atom optical lattice," *Physical Review A*, vol. 110, no. 2, p. 023308, 2024. 2

[69] J. Struck, C. Ölschläger, M. Weinberg, P. Hauke, J. Simonet, A. Eckardt, M. Lewenstein, K. Sengstock, and P. Windpassinger, "Tunable Gauge Potential for Neutral and Spinless Particles in Driven Optical Lattices," *Phys. Rev. Lett.*, vol. 108, p. 225304, May 2012. 2

[70] J. Struck, M. Weinberg, C. Ölschläger, P. Windpassinger, J. Simonet, K. Sengstock, R. Höppner, P. Hauke, A. Eckardt, M. Lewenstein, *et al.*, "Engineering Ising-XY spin-models in a triangular lattice using tunable artificial gauge fields," *Nature Physics*, vol. 9, no. 11, pp. 738–743, 2013. 2

[71] K. Jimenez-Garcia, L. J. LeBlanc, R. A. Williams, M. C. Beeler, A. R. Perry, and I. B. Spielman, "Peierls substitution in an engineered lattice potential," *Physical review letters*, vol. 108, no. 22, p. 225303, 2012. 2

[72] N. Goldman, I. Satija, P. Nikolic, A. Bermudez, M. A. Martin-Delgado, M. Lewenstein, and I. Spielman, "Realistic time-reversal invariant topological insulators with neutral atoms," *Physical review letters*, vol. 105, no. 25, p. 255302, 2010. 3

[73] A. Klein and D. Jaksch, "Phonon-induced artificial magnetic fields in optical lattices," *Europhysics Letters*, vol. 85, no. 1, p. 13001, 2009. 3

[74] B. Tian, M. Endres, and D. Pekker, "Landau Levels in Strained Optical Lattices," *Phys. Rev. Lett.*, vol. 115, p. 236803, Dec 2015. 3, 50, 78, 97, 98, 101

[75] M. Jamotte, L. Peralta Gavensky, C. Morais Smith, M. Di Liberto, and N. Goldman, "Quantized valley Hall response from local bulk density variations," *Communications Physics*, vol. 6, no. 1, p. 264, 2023. 4, 22, 28, 52

[76] M. Jamotte, N. Goldman, and M. Di Liberto, "Strain and pseudo-magnetic fields in optical lattices from density-assisted tunneling," *Communications Physics*, vol. 5, no. 1, pp. 1–12, 2022. 4, 22, 28, 29, 43, 78, 79

[77] E. H. Hall, "On a new action of the magnet on electric currents," *American Journal of Mathematics*, vol. 2.3, pp. 287–292, 1879. 6

[78] K. v. Klitzing, G. Dorda, and M. Pepper, "New Method for High-Accuracy Determination of the Fine-Structure Constant Based on Quantized Hall Resistance," *Phys. Rev. Lett.*, vol. 45, pp. 494–497, Aug 1980. 7, 9

[79] M. Paalanen, D. Tsui, and A. Gossard, "Quantized Hall effect at low temperatures," *Physical Review B*, vol. 25, no. 8, p. 5566, 1982. 8

[80] D. J. Thouless, M. Kohmoto, M. P. Nightingale, and M. den Nijs, "Quantized Hall Conductance in a Two-Dimensional Periodic Potential," vol. 49, no. 6, p. 6, 1982. 8

[81] D. J. Thouless, "Quantization of particle transport," *Phys. Rev. B*, vol. 27, pp. 6083–6087, May 1983. 8

[82] C. L. Kane and E. J. Mele, "Quantum spin Hall effect in graphene," *Physical review letters*, vol. 95, no. 22, p. 226801, 2005. 8

[83] B. A. Bernevig, T. L. Hughes, and S.-C. Zhang, "Quantum spin Hall effect and topological phase transition in HgTe quantum wells," *science*, vol. 314, no. 5806, pp. 1757–1761, 2006. 8

[84] M. Konig, S. Wiedmann, C. Brune, A. Roth, H. Buhmann, L. W. Molenkamp, X.-L. Qi, and S.-C. Zhang, "Quantum spin Hall insulator state in HgTe quantum wells," *Science*, vol. 318, no. 5851, pp. 766–770, 2007. 8

[85] D. C. Tsui, H. L. Stormer, and A. C. Gossard, "Two-Dimensional Magnetotransport in the Extreme Quantum Limit," *Phys. Rev. Lett.*, vol. 48, pp. 1559–1562, May 1982. 8

[86] R. B. Laughlin, "Anomalous Quantum Hall Effect: An Incompressible Quantum Fluid with Fractionally Charged Excitations," *Phys. Rev. Lett.*, vol. 50, pp. 1395–1398, May 1983. 9

[87] F. Wilczek, "Quantum mechanics of fractional-spin particles," *Physical review letters*, vol. 49, no. 14, p. 957, 1982. 9

[88] A. Khare, *Fractional statistics and quantum theory*. World Scientific, 2005. 9

[89] J.-M. Berroir, Q. Dong, *et al.*, "Fractional statistics in anyon collisions," *Science*, vol. 368, no. 6487, pp. 173–177, 2020. 9

[90] J. Nakamura, S. Liang, G. C. Gardner, and M. J. Manfra, "Direct observation of anyonic braiding statistics," *Nature Physics*, vol. 16, no. 9, pp. 931–936, 2020. 9

[91] C. Nayak, S. H. Simon, A. Stern, M. Freedman, and S. Das Sarma, "Non-Abelian anyons and topological quantum computation," *Reviews of Modern Physics*, vol. 80, no. 3, pp. 1083–1159, 2008. 9

[92] P. Streda, "Theory of quantised Hall conductivity in two dimensions," *Journal of Physics C: Solid State Physics*, vol. 15, no. 22, 1982. 9

[93] A. Widom, "Thermodynamic derivation of the Hall effect current," *Physics Letters A*, vol. 90, no. 9, p. 474, 1982. 9

[94] H. M. Price, O. Zilberberg, T. Ozawa, I. Carusotto, and N. Goldman, "Four-Dimensional Quantum Hall Effect with Ultracold Atoms," *Phys. Rev. Lett.*, vol. 115, p. 195303, Nov 2015. 9

[95] C. Repellin, J. Léonard, and N. Goldman, "Fractional Chern insulators of few bosons in a box: Hall plateaus from center-of-mass drifts and density profiles," *Phys. Rev. A*, vol. 102, p. 063316, Dec 2020. 9

[96] L. Peralta Gavensky, S. Sachdev, and N. Goldman, "Connecting the many-body Chern number to Luttinger's theorem through Středa's formula," *Physical review letters*, vol. 131, no. 23, p. 236601, 2023. 9

[97] D. Vanderbilt, *Berry phases in electronic structure theory: electric polarization, orbital magnetization and topological insulators*. Cambridge University Press, 2018. 9

[98] C. Cohen-Tannoudji, B. Diu, and F. Laloë, *Quantum Mechanics Volume 1*. Hermann, 1977. 10

[99] M. O. Goerbig, "Electronic properties of graphene in a strong magnetic field," *Rev. Mod. Phys.*, vol. 83, pp. 1193–1243, Nov 2011. 11, 13, 22, 24

[100] D. Boukhvalov, M. Katsnelson, and A. Lichtenstein, "Hydrogen on graphene: Electronic structure, total energy, structural distortions and magnetism from first-principles calculations," *Physical Review B—Condensed Matter and Materials Physics*, vol. 77, no. 3, p. 035427, 2008. 13

[101] P. R. Wallace, "The band theory of graphite," *Physical review*, vol. 71, no. 9, p. 622, 1947. 14

[102] A. H. Castro Neto, F. Guinea, N. M. R. Peres, K. S. Novoselov, and A. K. Geim, "The electronic properties of graphene," *Rev. Mod. Phys.*, vol. 81, pp. 109–162, Jan 2009. 16

[103] A. Shytov, M. Rudner, N. Gu, M. Katsnelson, and L. Levitov, "Atomic collapse, Lorentz boosts, Klein scattering, and other quantum-relativistic phenomena in graphene," *Solid state communications*, vol. 149, no. 27-28, pp. 1087–1093, 2009. 16

[104] Z. Zhang, Y. Feng, F. Li, S. Koniakhin, C. Li, F. Liu, Y. Zhang, M. Xiao, G. Malpuech, and D. Solnyshkov, "Angular-dependent Klein tunneling in photonic graphene," *Physical Review Letters*, vol. 129, no. 23, p. 233901, 2022. 16

[105] A. W. Ludwig, "Topological phases: classification of topological insulators and superconductors of non-interacting fermions, and beyond," *Physica Scripta*, vol. 2016, no. T168, p. 014001, 2015. 16

[106] C.-K. Chiu, J. C. Teo, A. P. Schnyder, and S. Ryu, "Classification of topological quantum matter with symmetries," *Reviews of Modern Physics*, vol. 88, no. 3, p. 035005, 2016. 16, 18, 19

[107] A. Altland and M. R. Zirnbauer, "Nonstandard symmetry classes in mesoscopic normal-superconducting hybrid structures," *Physical Review B*, vol. 55, no. 2, p. 1142, 1997. 16

[108] K. K. Gomes, W. Mar, W. Ko, F. Guinea, and H. C. Manoharan, "Designer Dirac fermions and topological phases in molecular graphene," *Nature*, vol. 483, no. 7389, pp. 306–310, 2012. 25, 77, 101

[109] M. C. Rechtsman, J. M. Zeuner, Y. Plotnik, Y. Lumer, D. Podolsky, F. Dreisow, S. Nolte, M. Segev, and A. Szameit, "Photonic Floquet topological insulators," *Nature*, vol. 496, pp. 196–200, 04 2013. 25, 38

[110] G. Montambaux, "Artificial graphenes: Dirac matter beyond condensed matter," *Comptes Rendus Physique*, vol. 19, no. 5, pp. 285–305, 2018. 25

[111] T. S. Gardenier, J. J. Van Den Broeke, J. R. Moes, I. Swart, C. Delerue, M. R. Slot, C. M. Smith, and D. Vanmaekelbergh, "p-orbital Flat Band and Dirac Cone in the Electronic Honeycomb Lattice," *ACS nano*, vol. 14, no. 10, pp. 13638–13644, 2020. 25

[112] H. Abbaszadeh, A. Souslov, J. Paulose, H. Schomerus, and V. Vitelli, "Sonic Landau Levels and Synthetic Gauge Fields in Mechanical Metamaterials," *Phys. Rev. Lett.*, vol. 119, p. 195502, Nov 2017. 25

[113] C. Brendel, V. Peano, O. J. Painter, and F. Marquardt, "Pseudomagnetic fields for sound at the nanoscale," *Proceedings of the National Academy of Sciences*, vol. 114, no. 17, pp. E3390–E3395, 2017. 25

[114] X. Wen, C. Qiu, Y. Qi, L. Ye, M. Ke, F. Zhang, and Z. Liu, "Acoustic Landau quantization and quantum-Hall-like edge states," *Nature Physics*, vol. 15, no. 4, pp. 352–356, 2019. 25

[115] O. Jamadi, E. Rozas, G. Salerno, M. Milićević, T. Ozawa, I. Sagnes, A. Lemaître, L. Le Gratiet, A. Harouri, I. Carusotto, J. Bloch, and A. Amo, "Direct observation of photonic Landau levels and helical edge states in strained honeycomb lattices," *Light: Science & Applications*, vol. 9, no. 1, p. 144, 2020. 25

[116] M. Bellec, C. Poli, U. Kuhl, F. Mortessagne, and H. Schomerus, "Observation of supersymmetric pseudo-Landau levels in strained microwave graphene," *Light: Science & Applications*, vol. 9, no. 1, p. 146, 2020. 25

[117] J. Deng, H. Dong, C. Zhang, Y. Wu, J. Yuan, X. Zhu, F. Jin, H. Li, Z. Wang, H. Cai, C. Song, H. Wang, J. Q. You, and D.-W. Wang, "Observing the quantum topology of light," *Science*, vol. 378, no. 6623, pp. 966–971, 2022. 25

[118] A. Castro Neto and F. Guinea, "Electron-phonon coupling and Raman spectroscopy in graphene," *Physical Review B—Condensed Matter and Materials Physics*, vol. 75, no. 4, p. 045404, 2007. 25

[119] V. M. Pereira, A. Castro Neto, and N. Peres, "Tight-binding approach to uniaxial strain in graphene," *Physical Review B—Condensed Matter and Materials Physics*, vol. 80, no. 4, p. 045401, 2009. 25

[120] E. Lantagne-Hurtubise, X.-X. Zhang, and M. Franz, "Dispersive Landau levels and valley currents in strained graphene nanoribbons," *Phys. Rev. B*, vol. 101, p. 085423, Feb 2020. 27, 28, 31, 101

[121] G. Salerno, T. Ozawa, H. M. Price, and I. Carusotto, "How to directly observe Landau levels in driven-dissipative strained honeycomb lattices," *2D Materials*, vol. 2, p. 034015, sep 2015. 29

[122] S. Ryu and Y. Hatsugai, "Topological origin of zero-energy edge states in particle-hole symmetric systems," *Physical review letters*, vol. 89, no. 7, p. 077002, 2002. 34

[123] P. Delplace, D. Ullmo, and G. Montambaux, "Zak phase and the existence of edge states in graphene," *Physical Review B*, vol. 84, no. 19, p. 195452, 2011. 34

[124] G. Salerno, T. Ozawa, H. M. Price, and I. Carusotto, "Propagating edge states in strained honeycomb lattices," *Phys. Rev. B*, vol. 95, p. 245418, Jun 2017. 35

[125] M. Kohmoto and Y. Hasegawa, "Zero modes and edge states of the honeycomb lattice," *Physical Review B—Condensed Matter and Materials Physics*, vol. 76, no. 20, p. 205402, 2007. 35

[126] A. K. Geim and I. V. Grigorieva, "Van der Waals heterostructures," *Nature*, vol. 499, no. 7459, pp. 419–425, 2013. 37

[127] A. Rodin, L. C. Gomes, and A. C. Neto, "Valley physics in tin (II) sulfide," *Physical Review B*, vol. 93, no. 4, p. 045431, 2016. 37

[128] K. Chang, B. J. Miller, H. Yang, H. Lin, S. S. Parkin, S. Barraza-Lopez, Q.-K. Xue, X. Chen, and S.-H. Ji, "Standing waves induced by valley-mismatched domains in ferroelectric SnTe monolayers," *Physical Review Letters*, vol. 122, no. 20, p. 206402, 2019. 37

[129] D. Xiao, M.-C. Chang, and Q. Niu, "Berry phase effects on electronic properties," *Reviews of modern physics*, vol. 82, no. 3, pp. 1959–2007, 2010. 37

[130] M. Yamamoto, Y. Shimazaki, I. V. Borzenets, and S. Tarucha, "Valley hall effect in two-dimensional hexagonal lattices," *Journal of the Physical Society of Japan*, vol. 84, no. 12, pp. 1–11, 2015. 37

[131] D. A. Abanin, S. V. Morozov, L. A. Ponomarenko, R. V. Gorbachev, A. S. Mayorov, M. I. Katsnelson, K. Watanabe, T. Taniguchi, K. S. Novoselov, L. S. Levitov, and A. K. Geim, "Giant Nonlocality Near the Dirac Point in Graphene," *Science*, vol. 332, no. 6027, pp. 328–330, 2011. 37

[132] J. Yin, C. Tan, D. Barcons-Ruiz, I. Torre, K. Watanabe, T. Taniguchi, J. C. W. Song, J. Hone, and F. H. L. Koppens, "Tunable and giant valley-selective Hall effect in gapped bilayer graphene," *Science*, vol. 375, no. 6587, pp. 1398–1402, 2022. 38

[133] C. Weitenberg and J. Simonet, "Tailoring quantum gases by Floquet engineering," *Nature Physics*, vol. 17, no. 12, pp. 1342–1348, 2021. 38

[134] N. Tsuji, "Floquet states," *arXiv preprint arXiv:2301.12676*, 2023. 38, 39

[135] F. Meinert, M. J. Mark, K. Lauber, A. J. Daley, and H.-C. Nägerl, "Floquet Engineering of Correlated Tunneling in the Bose-Hubbard Model with Ultracold Atoms," *Phys. Rev. Lett.*, vol. 116, p. 205301, May 2016. 38, 79

[136] A. Eckardt, "Colloquium: Atomic quantum gases in periodically driven optical lattices," *Rev. Mod. Phys.*, vol. 89, p. 011004, Mar 2017. 38

[137] K. Wintersperger, C. Braun, F. N. Ünal, A. Eckardt, M. D. Liberto, N. Goldman, I. Bloch, and M. Aidelsburger, "Realization of an anomalous Floquet topological system with ultracold atoms," *Nature Physics*, vol. 16, no. 10, pp. 1058–1063, 2020. 38, 39, 98

[138] L. J. Maczewsky, J. M. Zeuner, S. Nolte, and A. Szameit, "Observation of photonic anomalous Floquet topological insulators," *Nature communications*, vol. 8, no. 1, p. 13756, 2017. 38

[139] T. Ozawa, H. M. Price, A. Amo, N. Goldman, M. Hafezi, L. Lu, M. C. Rechtsman, D. Schuster, J. Simon, O. Zilberberg, *et al.*, "Topological photonics," *Reviews of Modern Physics*, vol. 91, no. 1, p. 015006, 2019. 38

[140] T. Oka and S. Kitamura, "Floquet engineering of quantum materials," *Annual Review of Condensed Matter Physics*, vol. 10, no. 1, pp. 387–408, 2019. 38

[141] R. Fleury, A. B. Khanikaev, and A. Alu, "Floquet topological insulators for sound," *Nature communications*, vol. 7, no. 1, p. 11744, 2016. 38

[142] G. Salerno, *Artificial gauge fields in photonics and mechanical systems.* PhD thesis, University of Trento, 2016. 38, 91

[143] M. Bukov, L. D'Alessio, and A. Polkovnikov, "Universal high-frequency behavior of periodically driven systems: from dynamical stabilization to Floquet engineering," *Advances in Physics*, vol. 64, no. 2, pp. 139–226, 2015. 39, 40, 41, 104

[144] M. S. Rudner, N. H. Lindner, E. Berg, and M. Levin, "Anomalous Edge States and the Bulk-Edge Correspondence for Periodically Driven Two-Dimensional Systems," *Physical Review X*, vol. 3, no. 3, p. 031005, 2013. 39

[145] K. Plekhanov, G. Roux, and K. Le Hur, "Floquet engineering of Haldane Chern insulators and chiral bosonic phase transitions," *Physical Review B*, vol. 95, no. 4, p. 045102, 2017. 39

[146] F. Görg, K. Sandholzer, J. Minguzzi, R. Desbuquois, M. Messer, and T. Esslinger, "Realization of density-dependent Peierls phases to engineer quantized gauge fields coupled to ultracold matter," *Nature Physics*, vol. 15, no. 11, pp. 1161–1167, 2019. 39, 42

[147] C. Schweizer, F. Grusdt, M. Berngruber, L. Barbiero, E. Demler, N. Goldman, I. Bloch, and M. Aidelsburger, "Floquet approach to $\mathbb{Z}_2$ lattice gauge theories with ultracold atoms in optical lattices," *Nature Physics*, vol. 15, no. 11, pp. 1168–1173, 2019. 39, 42

[148] M. Arnal, G. Chatelain, M. Martinez, N. Dupont, O. Giraud, D. Ullmo, B. Georgeot, G. Lemarié, J. Billy, and D. Guéry-Odelin, "Chaos-assisted tunneling resonances in a synthetic Floquet superlattice," *Science advances*, vol. 6, no. 38, p. eabc4886, 2020. 39

[149] M. Benito, A. Gómez-León, V. Bastidas, T. Brandes, and G. Platero, "Floquet engineering of long-range p-wave superconductivity," *Physical Review B*, vol. 90, no. 20, p. 205127, 2014. 39

[150] H. Liu, T.-S. Xiong, W. Zhang, and J.-H. An, "Floquet engineering of exotic topological phases in systems of cold atoms," *Physical Review A*, vol. 100, no. 2, p. 023622, 2019. 39

[151] G. Floquet, "Sur les équations différentielles linéaires à coefficients périodiques," in *Annales scientifiques de l'École normale supérieure*, vol. 12, pp. 47–88, 1883. 39

[152] N. Goldman, J. Dalibard, M. Aidelsburger, and N. R. Cooper, "Periodically driven quantum matter: The case of resonant modulations," *Phys. Rev. A*, vol. 91, p. 033632, Mar 2015. 41

[153] O. Dutta, M. Gajda, P. Hauke, M. Lewenstein, D.-S. Lühmann, B. A. Malomed, T. Sowiński, and J. Zakrzewski, "Non-standard Hubbard models in optical lattices: a review," *Reports on Progress in Physics*, vol. 78, p. 066001, may 2015. 42

[154] L. Barbiero, C. Schweizer, M. Aidelsburger, E. Demler, N. Goldman, and F. Grusdt, "Coupling ultracold matter to dynamical gauge fields in optical lattices: From flux attachment to $\mathbb{Z}_2$ lattice gauge theories," *Science Advances*, vol. 5, no. 10, 2019. 42

[155] A. Rapp, X. Deng, and L. Santos, "Ultracold Lattice Gases with Periodically Modulated Interactions," *Phys. Rev. Lett.*, vol. 109, p. 203005, Nov 2012. 42, 79

[156] C. Pethick and H. Smith, *Bose–Einstein condensation in dilute gases*. Cambridge university press, 2008. 43, 44, 47, 49, 50

[157] L. Pitaevskii and S. Stringari, *Bose-Einstein condensation and superfluidity*, vol. 164. Oxford University Press, 2016. 43, 44, 47, 49, 84

[158] M. Horvath, S. Dhar, A. Das, M. D. Frye, Y. Guo, J. M. Hutson, M. Landini, and H.-C. Nägerl, "Bose-Einstein condensation of non-ground-state caesium atoms," *Nature Communications*, vol. 15, no. 1, p. 3739, 2024. 44

[159] A. Einstein, "Quantum theory of the monatomic ideal gas," *Sitzungsberichte der Preussischen Akademie der Wissenschaften, Physikalisch-mathematische Klasse*, vol. 261, 1924. 44

[160] M. H. Anderson, J. R. Ensher, M. R. Matthews, C. E. Wieman, and E. A. Cornell, "Observation of Bose-Einstein condensation in a dilute atomic vapor," *science*, vol. 269, no. 5221, pp. 198–201, 1995. 44

[161] K. B. Davis, M.-O. Mewes, M. R. Andrews, N. J. van Druten, D. S. Durfee, D. Kurn, and W. Ketterle, "Bose-Einstein condensation in a gas of sodium atoms," *Physical review letters*, vol. 75, no. 22, p. 3969, 1995. 44

[162] A. J. Leggett, "Bose-Einstein condensation in the alkali gases: Some fundamental concepts," *Reviews of modern physics*, vol. 73, no. 2, p. 307, 2001. 44

[163] R. Grimm, M. Weidemüller, and Y. B. Ovchinnikov, "Optical dipole traps for neutral atoms," in *Advances in atomic, molecular, and optical physics*, vol. 42, pp. 95–170, Elsevier, 2000. 49

[164] P. W. Anderson, "The resonating valence bond state in La2CuO4 and superconductivity," *science*, vol. 235, no. 4793, pp. 1196–1198, 1987. 50

[165] M. Köhl, H. Moritz, T. Stöferle, K. Günter, and T. Esslinger, "Fermionic Atoms in a Three Dimensional Optical Lattice: Observing Fermi Surfaces, Dynamics, and Interactions," *Phys. Rev. Lett.*, vol. 94, p. 080403, Mar 2005. 50

[166] U. Schneider, L. Hackermüller, S. Will, T. Best, I. Bloch, T. A. Costi, R. W. Helmes, D. Rasch, and A. Rosch, "Metallic and Insulating Phases of Repulsively Interacting Fermions in a 3D Optical Lattice," *Science*, vol. 322, no. 5907, pp. 1520–1525, 2008. 50

[167] W. Hofstetter, J. I. Cirac, P. Zoller, E. Demler, and M. D. Lukin, "High-Temperature Superfluidity of Fermionic Atoms in Optical Lattices," *Phys. Rev. Lett.*, vol. 89, p. 220407, Nov 2002. 50

[168] M. Boll, T. A. Hilker, G. Salomon, A. Omran, J. Nespolo, L. Pollet, I. Bloch, and C. Gross, "Spin- and density-resolved microscopy of antiferromagnetic correlations in Fermi-Hubbard chains," *Science*, vol. 353, no. 6305, pp. 1257–1260, 2016. 50

[169] A. Mazurenko, C. S. Chiu, G. Ji, M. F. Parsons, M. Kanász-Nagy, R. Schmidt, F. Grusdt, E. Demler, D. Greif, and M. Greiner, "A cold-atom Fermi–Hubbard antiferromagnet," *Nature*, vol. 545, no. 7655, pp. 462–466, 2017. 50

[170] P. T. Brown, D. Mitra, E. Guardado-Sanchez, R. Nourafkan, A. Reymbaut, C.-D. Hébert, S. Bergeron, A.-M. S. Tremblay, J. Kokalj, D. A. Huse, P. Schauß, and W. S. Bakr, "Bad metallic transport in a cold atom Fermi-Hubbard system," *Science*, vol. 363, no. 6425, pp. 379–382, 2019. 50

[171] M. P. Fisher, P. B. Weichman, and D. S. Fisher, "Boson localization and the superfluid-insulator transition," *Physical Review B*, vol. 40, no. 1, p. 546, 1989. 50

[172] D. Jaksch and P. Zoller, "The cold atom Hubbard toolbox," *Annals of Physics*, vol. 315, no. 1, pp. 52 – 79, 2005. Special Issue. 51

[173] A. Minguzzi, S. Succi, F. Toschi, M. Tosi, and P. Vignolo, "Numerical methods for atomic quantum gases with applications to Bose–Einstein condensates and to ultracold fermions," *Physics reports*, vol. 395, no. 4-5, pp. 223–355, 2004. 51, 83, 109, 110

[174] R. Bianco and R. Resta, "Mapping topological order in coordinate space," *Phys. Rev. B*, vol. 84, p. 241106, Dec 2011. 75

[175] T. Low and F. Guinea, "Strain-Induced Pseudomagnetic Field for Novel Graphene Electronics," *Nano Letters*, vol. 10, pp. 3551–3554, Sep 2010. 77

[176] M. R. Slot, T. S. Gardenier, P. H. Jacobse, G. C. P. van Miert, S. N. Kempkes, S. J. M. Zevenhuizen, C. M. Smith, D. Vanmaekelbergh, and I. Swart, "Experimental realization and characterization of an electronic Lieb lattice," *Nature Physics*, vol. 13, no. 7, pp. 672–676, 2017. 77

[177] R. Drost, T. Ojanen, A. Harju, and P. Liljeroth, "Topological states in engineered atomic lattices," *Nature Physics*, vol. 13, pp. 668–671, Jul 2017. 77

[178] A. A. Khajetoorians, D. Wegner, A. F. Otte, and I. Swart, "Creating designer quantum states of matter atom-by-atom," *Nature Reviews Physics*, vol. 1, pp. 703–715, Dec 2019. 77

[179] M. Polini, F. Guinea, M. Lewenstein, H. C. Manoharan, and V. Pellegrini, "Artificial honeycomb lattices for electrons, atoms and photons," *Nature Nanotechnology*, vol. 8, no. 9, pp. 625–633, 2013. 77, 101

[180] S. N. Kempkes, M. R. Slot, J. J. van den Broeke, P. Capiod, W. A. Benalcazar, D. Vanmaekelbergh, D. Bercioux, I. Swart, and C. Morais Smith, "Robust zero-energy modes in an electronic higher-order topological insulator," *Nature Materials*, vol. 18, pp. 1292–1297, Dec 2019. 77

[181] S. E. Freeney, J. J. van den Broeke, A. J. J. Harsveld van der Veen, I. Swart, and C. Morais Smith, "Edge-Dependent Topology in Kekulé Lattices," *Phys. Rev. Lett.*, vol. 124, p. 236404, Jun 2020. 77

[182] E. Alba, X. Fernandez-Gonzalvo, J. Mur-Petit, J. J. Garcia-Ripoll, and J. K. Pachos, "Simulating Dirac fermions with Abelian and non-Abelian gauge fields in optical lattices," *Annals of Physics*, vol. 328, pp. 64–82, 2013. 78, 101

[183] W. S. Bakr, J. I. Gillen, A. Peng, S. Folling, and M. Greiner, "A quantum gas microscope for detecting single atoms in a Hubbard-regime optical lattice," *Nature*, vol. 462, pp. 74–77, 11 2009. 78, 101

[184] J. F. Sherson, C. Weitenberg, M. Endres, M. Cheneau, I. Bloch, and S. Kuhr, "Single-atom-resolved fluorescence imaging of an atomic Mott insulator," *Nature*, vol. 467, no. 7311, pp. 68–72, 2010. 78, 101

[185] M. F. Parsons, F. Huber, A. Mazurenko, C. S. Chiu, W. Setiawan, K. Wooley-Brown, S. Blatt, and M. Greiner, "Site-Resolved Imaging of Fermionic ^{6}Li in an Optical Lattice," *Phys. Rev. Lett.*, vol. 114, p. 213002, May 2015. 78, 101

[186] L. W. Cheuk, M. A. Nichols, M. Okan, T. Gersdorf, V. V. Ramasesh, W. S. Bakr, T. Lompe, and M. W. Zwierlein, "Quantum-Gas Microscope for Fermionic Atoms," *Phys. Rev. Lett.*, vol. 114, p. 193001, May 2015. 78, 101

[187] A. Omran, M. Boll, T. A. Hilker, K. Kleinlein, G. Salomon, I. Bloch, and C. Gross, "Microscopic Observation of Pauli Blocking in Degenerate Fermionic Lattice Gases," *Phys. Rev. Lett.*, vol. 115, p. 263001, Dec 2015. 78, 101

[188] E. Haller, J. Hudson, A. Kelly, D. A. Cotta, B. Peaudecerf, G. D. Bruce, and S. Kuhr, "Single-atom imaging of fermions in a quantum-gas microscope," *Nature Physics*, vol. 11, no. 9, pp. 738–742, 2015. 78, 101

[189] D. Barredo, S. de Léséleuc, V. Lienhard, T. Lahaye, and A. Browaeys, "An atom-by-atom assembler of defect-free arbitrary two-dimensional atomic arrays," *Science*, vol. 354, no. 6315, pp. 1021–1023, 2016. 78, 101

[190] Y. Wang, S. Shevate, T. M. Wintermantel, M. Morgado, G. Lochead, and S. Whitlock, "Preparation of hundreds of microscopic atomic ensembles in optical tweezer arrays," *npj Quantum Information*, vol. 6, p. 54, Jun 2020. 78, 101

[191] K.-N. Schymik, V. Lienhard, D. Barredo, P. Scholl, H. Williams, A. Browaeys, and T. Lahaye, "Enhanced atom-by-atom assembly of arbitrary tweezer arrays," *Phys. Rev. A*, vol. 102, p. 063107, Dec 2020. 78, 101

[192] S. Ebadi, T. T. Wang, H. Levine, A. Keesling, G. Semeghini, A. Omran, D. Bluvstein, R. Samajdar, H. Pichler, W. W. Ho, S. Choi, S. Sachdev, M. Greiner, V. Vuletić, and M. D. Lukin, "Quantum phases of matter on a 256-atom programmable quantum simulator," *Nature*, vol. 595, pp. 227–232, Jul 2021. 78, 101

[193] B. M. Spar, E. Guardado-Sanchez, S. Chi, Z. Z. Yan, and W. S. Bakr, "Realization of a Fermi-Hubbard Optical Tweezer Array," *Phys. Rev. Lett.*, vol. 128, p. 223202, Jun 2022. 78, 101

[194] J. Gong, L. Morales-Molina, and P. Hänggi, "Many-body coherent destruction of tunneling," *Phys. Rev. Lett.*, vol. 103, no. 13, p. 133002, 2009. 79

[195] M. D. Liberto, C. E. Creffield, G. I. Japaridze, and C. M. Smith, "Quantum simulation of correlated-hopping models with fermions in optical lattices," *Phys. Rev. A*, vol. 89, p. 013624, Jan 2014. 79, 97

[196] L. Cardarelli, S. Greschner, and L. Santos, "Engineering interactions and anyon statistics by multicolor lattice-depth modulations," *Phys. Rev. A*, vol. 94, p. 023615, Aug 2016. 79

[197] C. Sträter, S. C. L. Srivastava, and A. Eckardt, "Floquet Realization and Signatures of One-Dimensional Anyons in an Optical Lattice," *Phys. Rev. Lett.*, vol. 117, p. 205303, Nov 2016. 79

[198] O. Jürgensen, F. Meinert, M. J. Mark, H.-C. Nägerl, and D.-S. Lühmann, "Observation of Density-Induced Tunneling," *Phys. Rev. Lett.*, vol. 113, p. 193003, Nov 2014. 79

[199] F. Görg, M. Messer, K. Sandholzer, G. Jotzu, R. Desbuquois, and T. Esslinger, "Enhancement and sign change of magnetic correlations in a driven quantum many-body system," *Nature*, vol. 553, no. 7689, pp. 481–485, 2018. 79

[200] V. Lienhard, P. Scholl, S. Weber, D. Barredo, S. de Léséleuc, R. Bai, N. Lang, M. Fleischhauer, H. P. Büchler, T. Lahaye, *et al.*, "Realization of a density-dependent Peierls phase in a synthetic, spin-orbit coupled Rydberg system," *Physical Review X*, vol. 10, no. 2, p. 021031, 2020. 79

[201] M. Di Liberto, A. Kruckenhauser, P. Zoller, and M. A. Baranov, "Topological phonons in arrays of ultracold dipolar particles," *Quantum*, vol. 6, p. 731, June 2022. 98

[202] L. Asteria, D. T. Tran, T. Ozawa, M. Tarnowski, B. S. Rem, N. Fläschner, K. Sengstock, N. Goldman, and C. Weitenberg, "Measuring quantized circular dichroism in ultracold topological matter," *Nature Physics*, vol. 15, no. 5, pp. 449–454, 2019. 98

[203] H. W. Privitera, A., "Polaronic slowing of fermionic impurities in lattice Bose-Fermi mixtures," *Physical Review A—Atomic, Molecular, and Optical Physics*, vol. 82, no. 6, p. 063614, 2010. 99

[204] L. F. Torres and S. O. Valenzuela, "A valley of opportunities," *Physics World*, vol. 34, p. 43, dec 2021. 101

[205] G. G. Naumis, S. Barraza-Lopez, M. Oliva-Leyva, and H. Terrones, "Electronic and optical properties of strained graphene and other strained 2D materials: a review," *Reports on Progress in Physics*, vol. 80, no. 9, p. 096501, 2017. 101

[206] P. Sinha, P. K. Panigrahi, and B. Chittari, "Strain induced tunable band gap and optical properties of graphene on hexagonal boron nitride," 2024. 101

[207] S.-M. Choi, S.-H. Jhi, and Y.-W. Son, "Effects of strain on electronic properties of graphene," *Physical Review B—Condensed Matter and Materials Physics*, vol. 81, no. 8, p. 081407, 2010. 101

[208] A. A. Bukharaev, A. K. Zvezdin, A. P. Pyatakov, and Y. K. Fetisov, "Straintronics: a new trend in micro-and nanoelectronics and materials science," *Physics-Uspekhi*, vol. 61, no. 12, p. 1175, 2018. 101

[209] I. Y. Sahalianov, T. M. Radchenko, V. A. Tatarenko, G. Cuniberti, and Y. I. Prylutskyy, "Straintronics in graphene: Extra large electronic band gap induced by tensile and shear strains," *Journal of Applied Physics*, vol. 126, no. 5, 2019. 101

[210] H. Suzuura and T. Ando, "Phonons and electron-phonon scattering in carbon nanotubes," *Physical review B*, vol. 65, no. 23, p. 235412, 2002. 101

[211] J. Manes, "Symmetry-based approach to electron-phonon interactions in graphene," *Physical Review B—Condensed Matter and Materials Physics*, vol. 76, no. 4, p. 045430, 2007. 101

[212] F. Guinea, M. I. Katsnelson, and A. K. Geim, "Energy gaps and a zero-field quantum Hall effect in graphene by strain engineering," *Nature Physics*, vol. 6, no. 1, pp. 30–33, 2010. 101

[213] F. Shayeganfar, "Strain engineering of electronic properties and anomalous valley hall conductivity of transition metal dichalcogenide nanoribbons," *Scientific Reports*, vol. 12, no. 1, p. 11285, 2022. 101

[214] S. Roy, M. Kolodrubetz, N. Goldman, and A. G. Grushin, "Tunable axial gauge fields in engineered Weyl semimetals: semiclassical analysis and optical lattice implementations," *2D Materials*, vol. 5, p. 024001, jan 2018. 101

[215] Y.-Q. Zhu, Z. Zheng, G. Palumbo, and Z. Wang, "Topological electromagnetic effects and higher second chern numbers in four-dimensional gapped phases," *Physical Review Letters*, vol. 129, no. 19, p. 196602, 2022. 101

[216] Z. Lan, N. Goldman, A. Bermudez, W. Lu, and P. Öhberg, "Dirac-Weyl fermions with arbitrary spin in two-dimensional optical superlattices," *Phys. Rev. B*, vol. 84, p. 165115, Oct 2011. 101

[217] J. Sun, X. Zhu, T. Liu, S. Feng, and H. Guo, "Pseudomagnetic fields in square lattices," *Physical Review B*, vol. 108, no. 20, p. 205149, 2023. 101

[218] R. Saint-Jalm, P. C. Castilho, É. Le Cerf, B. Bakkali-Hassani, J.-L. Ville, S. Nascimbene, J. Beugnon, and J. Dalibard, "Dynamical symmetry and breathers in a two-dimensional Bose gas," *Physical Review X*, vol. 9, no. 2, p. 021035, 2019. 101

[219] G. M. Nixon, F. N. Unal, and U. Schneider, "Individually tunable tunnelling coefficients in optical lattices using local periodic driving," *arXiv preprint arXiv:2309.12124*, 2023. 101

[220] A. Benhemou, G. Nixon, A. Deger, U. Schneider, and J. K. Pachos, "Probing quantum properties of black holes with a Floquet-driven optical lattice simulator," *arXiv preprint arXiv:2312.14058*, 2023. 101

[221] P. Salgado-Rebolledo and J. K. Pachos, "Emerging D massive graviton in graphene-like systems," *New Journal of Physics*, vol. 25, no. 3, p. 033019, 2023. 101